

The Journal of Healthcare Engineering

Medical Mechatronics for Healthcare

Lead Guest Editor: Yi-Hung Liu

Guest Editors: David Moratal, Javier Escudero, and Han-Pang Huang





Medical Mechatronics for Healthcare

Journal of Healthcare Engineering

Medical Mechatronics for Healthcare

Lead Guest Editor: Yi-Hung Liu

Guest Editors: David Moratal, Javier Escudero,
and Han-Pang Huang



Copyright © 2018 Hindawi. All rights reserved.

This is a special issue published in “Journal of Healthcare Engineering.” All articles are open access articles distributed under the Creative Commons Attribution License, which permits unrestricted use, distribution, and reproduction in any medium, provided the original work is properly cited.

Editorial Board

Saverio Affatato, Italy
Hasan Ayaz, USA
William Bertucci, France
Olivier Beuf, France
Daniel H.K. Chow, Hong Kong
Tiago H. Falk, Canada
Mostafa Fatemi, USA
Jesus Favela, Mexico
Joseph Finkelstein, USA
Jesus Fontecha, Spain
Antonio Gloria, Italy
Kheng-Lim Goh, Singapore
Pedro Gomes, Portugal
Carlos Gómez, Spain
Philippe Gorce, France
Sophia Z. Gu, Australia
Vincenzo Guarino, Italy

Valentina Hartwig, Italy
Andreas H. Hielscher, USA
Norio Iriguchi, Japan
Zhongwei Jiang, Japan
John S. Katsanis, Greece
Terry K.K. Koo, USA
Panagiotis Kosmas, UK
Michel Labrosse, Canada
Jui-Yang Lai, Taiwan
Feng-Huei Lin, Taiwan
Yuan-Pin Lin, Taiwan
Maria Lindén, Sweden
Francisco Lopez-Valdes, Spain
Zufu Lu, Australia
Andreas Maier, Germany
Mehran Moazen, UK
Rafael Morales, Spain

David Moratal, Spain
Angkoon Phinyomark, Canada
Vincenzo Positano, Italy
Alessandro Reali, Italy
Jose Joaquin Rieta, Spain
Sébastien Roth, France
Hélder A. Santos, Finland
Emiliano Schena, Italy
Maurizio Schmid, Italy
Jiann-Shing Shieh, Taiwan
Jinshan Tang, USA
Vinoy Thomas, USA
Ioannis G. Tollis, Greece
Damon W.K. Wong, Singapore
Ping Zhou, USA
Loredana Zollo, Italy

Contents

Medical Mechatronics for Healthcare

Yi-Hung Liu , David Moratal , Javier Escudero , and Han-Pang Huang
Editorial (3 pages), Article ID 9675482, Volume 2018 (2018)

Development of a New Robotic Ankle Rehabilitation Platform for Hemiplegic Patients after Stroke

Quanguan Liu , Chunbao Wang , Jian Jun Long , Tongyang Sun , Lihong Duan, Xin Zhang ,
Bo Zhang , Yajing Shen , Wanfeng Shang , Zhuohua Lin , Yulong Wang , Jinfeng Xia ,
Jianjun Wei , Weiguang Li , and Zhengzhi Wu 
Research Article (12 pages), Article ID 3867243, Volume 2018 (2018)

Modelling and Experiment Based on a Navigation System for a Cranio-Maxillofacial Surgical Robot

Xingguang Duan, Liang Gao, Yonggui Wang , Jianxi Li, Haoyuan Li, and Yanjun Guo
Research Article (14 pages), Article ID 4670852, Volume 2018 (2018)

Efficient Active Sensing with Categorized Further Explorations for a Home Behavior-Monitoring Robot

Wenwei Yu, Keigo Nakahata, Guang Hao Sun, Akio Namiki, Sayuri Suwa, Mayuko Tsujimura, Le Xie,
Jinwu Wang, and Shao Ying Huang
Research Article (16 pages), Article ID 6952695, Volume 2017 (2018)

A 3D Scan Model and Thermal Image Data Fusion Algorithms for 3D Thermography in Medicine

Adam Chromy and Ondrej Klima
Research Article (9 pages), Article ID 5134021, Volume 2017 (2018)

The Efficacy of a Haptic-Enhanced Virtual Reality System for Precision Grasp Acquisition in Stroke Rehabilitation

Shih-Ching Yeh, Si-Huei Lee, Rai-Chi Chan, Yi Wu, Li-Rong Zheng, and Sheryl Flynn
Research Article (9 pages), Article ID 9840273, Volume 2017 (2018)

Development of a Blood Pressure Measurement Instrument with Active Cuff Pressure Control Schemes

Chung-Hsien Kuo, Chun-Ju Wu, Hung-Chyun Chou, Guan-Ting Chen, and Yu-Cheng Kuo
Research Article (15 pages), Article ID 9128745, Volume 2017 (2018)

Analysis of the Biceps Brachii Muscle by Varying the Arm Movement Level and Load Resistance Band

Nuradebah Burhan, Mohammad 'Afif Kasno, Rozaimi Ghazali, Md Radzai Said, Shahrum Shah Abdullah,
and Mohd Hafiz Jali
Research Article (8 pages), Article ID 1631384, Volume 2017 (2018)

Development of an Automatic Dispensing System for Traditional Chinese Herbs

Chi-Ying Lin and Ping-Jung Hsieh
Research Article (12 pages), Article ID 9013508, Volume 2017 (2018)

Realization of a CORDIC-Based Plug-In Accelerometer Module for PSG System in Head Position Monitoring for OSAS Patients

Wen-Yen Lin, Wen-Cheng Chou, Tsu-Hui Shiao, Guang-Ming Shiao, Chin-Shan Luo, and Ming-Yih Lee
Research Article (9 pages), Article ID 4728187, Volume 2017 (2018)



Research on Safety and Compliance of a New Lower Limb Rehabilitation Robot

Yongfei Feng, Hongbo Wang, Hao Yan, Xincheng Wang, Zhennan Jin, and Luige Vladareanu
Research Article (11 pages), Article ID 1523068, Volume 2017 (2018)

Mechanical Bed for Investigating Sleep-Inducing Vibration

Hitoshi Kimura, Akisue Kuramoto, Yuma Inui, and Norio Inou
Research Article (9 pages), Article ID 2364659, Volume 2017 (2018)

Editorial

Medical Mechatronics for Healthcare

Yi-Hung Liu ¹, David Moratal ², Javier Escudero ³, and Han-Pang Huang⁴

¹Department of Mechanical Engineering, National Taipei University of Technology, Taipei, Taiwan

²Department of Electronics Engineering, Universitat Politècnica de València, Valencia, Spain

³School of Engineering, Institute for Digital Communications, University of Edinburgh, Edinburgh, UK

⁴Department of Mechanical Engineering, National Taiwan University, Taipei, Taiwan

Correspondence should be addressed to Yi-Hung Liu; yhliu@ntut.edu.tw

Received 27 November 2017; Accepted 27 November 2017; Published 18 April 2018

Copyright © 2018 Yi-Hung Liu et al. This is an open access article distributed under the Creative Commons Attribution License, which permits unrestricted use, distribution, and reproduction in any medium, provided the original work is properly cited.

1. Introduction

Advances in the healthcare technology have positioned biomedical technology as a major driver in global knowledge-based economies. A successful healthcare intervention depends on not only the capability or experience of clinicians but also the adequacy of medical instruments and assistive devices. In addition, the technical aids and assistive devices for elderly or people with severe motor disability are getting more attention due to our aging society all over the world, and they are widely used in daily life. As a result, medical mechatronics becomes an important emerging technology to improve healthcare. Medical mechatronics is the integration of technologies and knowledge from various domains [1], including biosignal sensing fusion, real-time clinical data analysis, electric and mechanical system design, assistive/rehabilitation robot development, and machine/deep learning algorithms. Although medical mechatronics has proven to be successful in healthcare applications, there still remain difficulties and challenges to overcome. For example, most previous assistive devices/robots were developed to provide patients with rehabilitation training in hospitals. With the rapid growth of aging population, these assistive devices are required to have smaller size and cheaper production cost and be safer in order to meet the requirement of in-house rehabilitation [2]. As a result, the medical mechatronic components in these assistive devices/robots need to be redesigned.

The goal of this special issue is to bring together the researchers in these fields and present high-quality research on recent developments on medical mechatronics and

novel applications of medical mechatronics in healthcare, as well as the relevant prospect on opportunities and challenges. The selected eleven papers underwent a rigorous refereeing and revision process. Most of the studies were carried out on clinical data, which provides the results reported in this special issue a high confidence level. Moreover, most of the papers in this special issue include mechatronics and healthcare experts as coauthors, which is beneficial to open new methods and issues to medical experts in this multidisciplinary field.

2. The Special Issue

Stroke is a leading cause of long-term disability, and virtual reality- (VR-) based stroke rehabilitation is effective in increasing motivation and the functional performance in people with stroke. Although much of the functional reach and grasp capabilities of the upper extremities is regained, the pinch movement remains impaired following stroke. In the study by S.-C. Yeh et al., a haptic-enhanced VR system is proposed to simulate haptic pinch tasks in order to assist in long-term poststroke recovery of upper extremity fine motor function. Their results also suggest that this system is also effective under certain challenging conditions such as being in the chronic stroke phase or a coside of lesion and dominant hand (nondominant hand impaired).

In addition to VR-assisted rehabilitation, rehabilitation/mobile robot plays also a critical role in healthcare. This special issue collects a set of papers involving rehabilitation/healthcare robots. Ankle rehabilitation exercises act an important role in recovering walking ability of patients after

stroke. Currently, patients mainly perform ankle exercise to reobtain range of motion (ROM) and strength of ankle joint under therapist assistance by manual operation. However, most of the rehabilitation devices focus on ankle functional training and ignore the importance of neurological rehabilitation in the early hemiplegic stage. Q. Liu et al. developed a novel robotic ankle rehabilitation platform to assist patients in executing ankle exercise. This robotic platform consists of two three-DOF symmetric layer-stacking mechanisms, which can execute ankle internal/external rotation, dorsiflexion/plantarflexion, and inversion/eversion exercises while the rotation center of the distal end of the robotic platform always coincides with patient's ankle pivot center. Y. Feng et al. proposed a new applicable and effective sitting/lying lower limb rehabilitation robot (LLR-Ro), which has a mechanical limit protection, an electrical limit protection, and a software protection to prevent the patient from being secondary damaged. As a new type of the rehabilitation robots, its hip joint rotation ranges are different in the patient sitting training posture and lying training posture. The mechanical leg of the robot has a variable workspace to work in both training postures. In addition, to eliminate accident interaction force between patients and LLR-Ro in the process of the passive training, an amendment impedance control strategy based on position control is also proposed to improve the compliance of the LLR-Ro. On the other hand, mobile robotics is a potential solution to home behavior monitoring for the elderly. For a mobile robot, there are several types of uncertainties for its perceptions, such as the ambiguity between a target object and the surrounding objects. The problem could be more serious for a home behavior monitoring system, which aims to accurately recognize the activity of a target person, in spite of these uncertainties. W. Yu et al. proposed a new strategy of active sensing, called active sensing with categorized further explorations. It detects irregularities and categorizes situations requiring further explorations, which strategically maximizes the information needed for activity recognition while minimizing the costs. Two schemes of active sensing, based on two irregularity detections, namely, heuristic-based and template-matching-based irregularity detection, were implemented and examined for body contour-based activity recognition. Their proposed approach can guide the robot system to sense the target person actively and achieve high accuracy of activity recognition.

Biceps brachii muscle illness is one of the common physical disabilities that requires rehabilitation exercises in order to build up the strength of the biceps brachii muscle after surgery. It is also important to monitor the condition of that muscle during the treatment or rehabilitation exercise. Electromyography (EMG) is one of the preferred methods for measuring and recording the activity of the biceps brachii muscle, and wavelet transform (WT) has been widely used as a temporal-spectral analysis method for monitoring EMG signals. However, WT parameter selection remains a challenging task. N. Burhan et al. analyzed and investigated the selection of the best mother wavelet (MWT) function and depth of the decomposition level in the wavelet denoising EMG signals of the biceps brachii muscle. The efficacy

of the wavelet denoising signal was determined through an analysis of the activity of the biceps brachii muscle for vicinarians during the rehabilitation exercise.

Overnight polysomnography (PSG) is a standard diagnostic procedure for obstructive sleep apnea (OSA). However, there are no sensor systems to hook up with PSG for accurate head position monitoring available clinically. W.-Y. Lin et al. presented a CORDIC- (COordinate Rotation DIGital Computer-) based tilting sensing algorithm to quickly and accurately convert accelerometer raw data into the desired head position tilting angles. Their system can hook up with PSG devices for diagnosis to have head position information integrated with other PSG-monitored signals. It has been applied in an IRB test in Taipei Veterans General Hospital and been proved that it can meet the medical needs of accurate head position monitoring for PSG diagnosis. In addition to the head-posture monitoring during sleep, vibration condition monitoring is also a crucial factor in sleep study. H. Kimura et al. developed a new mechanical bed for inducing sleep to investigate the effects of different vibration conditions. The new bed has two active DOFs, vertical and horizontal directions, to examine the anisotropy of sensation. The bed includes three main parts: a vertical driver unit, horizontal driver unit, and unique 2-DOF counterweight system. Due to the new counterweight system, the required torque is extremely small and the driving sound is suppressed to less than 40 dB. Their results have suggested the ability of appropriate vibration to induce sleep.

C.-H. Kuo et al. proposed an oscillometric blood pressure (BP) measurement approach based on the active control schemes of cuff pressure. Compared with conventional electronic BP instruments, their proposed BP measurement approach is based on the utilization of a variable-volume chamber which can better actively and stably alter the cuff pressure during inflating or deflating cycles, because the variable-volume chamber could significantly eliminate the air turbulence disturbance during the air injection stage when compared to an air pump mechanism. C.-Y. Lin and P.-J. Hsieh developed an automatic dispensing system for Chinese herbal decoctions with the aim of reducing manpower costs and the risk of mistakes. They employed machine vision in conjunction with a robot manipulator to facilitate the grasping of ingredients. An offline least square curve fitting method was used to calculate the amount of material grasped by the claws and thereby improve system efficiency as well as the accuracy of individual dosages. Their experiments on the dispensing of actual ingredients have demonstrated the feasibility of their proposed system.

In the study of A. Chromy and O. Klima, a 3D scan model and thermal image data fusion algorithms are presented. At present, medical thermal imaging is still considered a mere qualitative tool enabling us to distinguish between but lacking the ability to quantify the physiological and nonphysiological states of the body. Such a capability would, however, facilitate solving the problem of medical quantification. Accordingly, they proposed a generally applicable method to enhance captured 3D spatial data carrying temperature-related information. Their method can be utilized for high-density point clouds or detailed meshes at a

high resolution but is conveniently usable in large objects with sparse points. Also, the technique offers a wide application potential in medicine and multiple technological domains, including electrical and mechanical engineering.

Acknowledgments

The guest editors of this special issue would like to thank all authors of the submitted papers, as well as all reviewers for their hard work and detailed reviews that led to eleven accepted papers.

*Yi-Hung Liu
David Moratal
Javier Escudero
Han-Pang Huang*

References

- [1] S. Katsura, W. Iida, and K. Ohnishi, "Medical mechatronics—an application to haptic forceps," *Annual Reviews in Control*, vol. 29, no. 2, pp. 237–245, 2005.
- [2] H. P. Huang, Y. H. Liu, W. C. Lee, J. Y. Kuan, and T. H. Huang, "Medical mechatronics: part I - rehabilitation robotic prostheses for upper extremity," in *Contemporary Issues in System Science and Engineering*, M. C. Zhou, H.-X. Li, and M. Weijnen, Eds., Wiley-IEEE Press, New York, USA, 2015.

Research Article

Development of a New Robotic Ankle Rehabilitation Platform for Hemiplegic Patients after Stroke

Quanquan Liu ^{1,2,3,4,5}, Chunbao Wang ^{1,2,3,4,5}, Jian Jun Long ², Tongyang Sun ³,
Lihong Duan,¹ Xin Zhang ², Bo Zhang ^{4,6}, Yajing Shen ⁷, Wanfeng Shang ¹,
Zhuohua Lin ⁴, Yulong Wang ², Jinfeng Xia ⁵, Jianjun Wei ⁵, Weiguang Li ³,
and Zhengzhi Wu ¹

¹Shenzhen Institute of Geriatrics, Shenzhen, China

²The Second People's Hospital of Shenzhen, Shenzhen, China

³The School of Mechanical & Automotive Engineering, South China University of Technology, Guangzhou, China

⁴Faculty of Science and Engineering, Waseda University, Tokyo, Japan

⁵The School of Mechanical Engineering, Guangxi University of Science and Technology, Liuzhou, China

⁶The Beijing Advanced Innovation Center for Intelligent Robots and Systems, Beijing Institute of Technology, Beijing, China

⁷Mechanical and Biomedical Engineering Department, City University of Hong Kong, Hong Kong

Correspondence should be addressed to Yulong Wang; ylwang66@126.com and Zhengzhi Wu; szwzz001@163.com

Received 26 April 2017; Accepted 13 November 2017; Published 15 March 2018

Academic Editor: Saverio Affatato

Copyright © 2018 Quanquan Liu et al. This is an open access article distributed under the Creative Commons Attribution License, which permits unrestricted use, distribution, and reproduction in any medium, provided the original work is properly cited.

A large amount of hemiplegic survivors are suffering from motor impairment. Ankle rehabilitation exercises act an important role in recovering patients' walking ability after stroke. Currently, patients mainly perform ankle exercise to reobtain range of motion (ROM) and strength of the ankle joint under a therapist's assistance by manual operation. However, therapists suffer from high work intensity, and most of the existed rehabilitation devices focus on ankle functional training and ignore the importance of neurological rehabilitation in the early hemiplegic stage. In this paper, a new robotic ankle rehabilitation platform (RARP) is proposed to assist patients in executing ankle exercise. The robotic platform consists of two three-DOF symmetric layer-stacking mechanisms, which can execute ankle internal/external rotation, dorsiflexion/plantarflexion, and inversion/eversion exercise while the rotation center of the distal zone of the robotic platform always coincides with patients' ankle pivot center. Three exercise modes including constant-speed exercise, constant torque-impedance exercise, and awareness exercise are developed to execute ankle training corresponding to different rehabilitation stages. Experiments corresponding to these three ankle exercise modes are performed, the result demonstrated that the RARP is capable of executing ankle rehabilitation, and the novel awareness exercise mode motivates patients to proactively participate in ankle training.

1. Introduction

Recently, a large number of stroke survivors are suffering from motor impairment. The recovery of motor loss function is difficult conducted only by biomedical treatment [1]. Generally, ankle rehabilitation after stroke consists of three stages [2]. In the first stage, known as the first month after stroke, patients mainly play simple and passive training in bed. In the second stage, patients begin to participate in active

rehabilitation exercises, including balance and coordination training to strengthen the affected ankle. In the third stage, patients try to reobtain their healthy state through intensive rehabilitation training. The first two stages aim to avoid patient muscle atrophy, and the third stage focuses on improving patients' life quality. To stroke survivors, rehabilitation at the first two stages plays an important role in recovering their walk ability by exercising the affected muscles [3, 4].

In the traditional ankle exercise, physiotherapy (PT) manually holds patients' affected ankle to carry out internal/external rotation, dorsiflexion/plantarflexion, and inversion/eversion motion during ankle rehabilitation. This manual training method makes PT exhausted, and the rehabilitation performance highly relies on a physiotherapist's experience. Furthermore, patients may act confrontation on this passive training method which reduces the rehabilitation efficiency. In order to address the manipulation challenges in ankle rehabilitation, many studies have considered the development of robotic systems to reduce a physiotherapist's workload and enhance patients' rehabilitation performance. A parallel structure robotic system and an exoskeletal structure robotic system are the two main research interests in the ankle rehabilitation assistance.

Saglia et al. reported a two-DOF foot pedal using parallel structure for ankle rehabilitation [2]. It can achieve ankle dorsiflexion/plantarflexion and inversion/eversion exercises under position control for patient-passive exercise mode or under admittance control for patient-active exercise mode. Rutgers University developed a 6-DOF ankle rehabilitation robot "Rutgers ankle" based on a Stewart platform driven by pneumatic actuation, where a 6-DOF force sensor was used to provide force and torque feedback generated between the patient's foot and the foot pedal [5]. Liu et al. announced a 3-RSS/S parallel robotic platform associated with a virtual training environment, which employed servo motor to drive its parallel links [6]. Meng et al. constructed a parallel structure ankle rehabilitation robot, where the patient's leg is fixed to the base of the robot; therefore, the robot can drive the patient's foot to generate relative movement using the ankle joint as the pivot center [7]. Muhammad and Shafriza presented a mechanical design and kinematic analysis of a parallel robot for ankle rehabilitation [8]. Yu et al. presented a 3-DOF cable-driven parallel robot for ankle rehabilitation. The mechanical design ensured that the mechanism center of the rotations can match the ankle axes of rotations [9].

Besides the parallel structure robotic ankle rehabilitation robot, a number of exoskeletal structure ankle rehabilitation robots were also developed. Jeffrey et al. presented a powered ankle-foot orthosis. The device owns only one DOF to realize ankle dorsiflexion/plantarflexion training [10]. Delaware University developed a wearable exoskeletal ankle rehabilitation robot to assist dorsiflexion/plantarflexion and inversion/eversion training [11]. Rahman and Ikeura developed a dynamic knee-ankle-foot orthosis to offer variable-impedance dorsiflexion/plantarflexion training using a wrap-spring clutch [12]. Hong et al. introduced a 3-DOF ankle rehabilitation robot, which consisted of a parallel connection of a spherical five-bar linkage and a revolute-spherical-universal serial chain to assist ankle dorsiflexion/plantarflexion and inversion/eversion training [13].

The summary of the existing state-of-the-art parallel structure ankle rehabilitation robots and exoskeletal ankle rehabilitation robots can be found in Table 1.

Through examining the existing robots for ankle rehabilitation, a few improvements could still be identified as follows: (1) the rotation center of the foot pedal should easily point to the rotation center of the ankle joint via mechanical

configuration; (2) the robot should be friendly and stimulate the patient to participate in ankle training, encouraging the patient to self-balance both their ankle joints during exercise; and (3) maintainability and modularity might be improved. Trying to achieve these improved specifications, we developed a novel robotic ankle rehabilitation platform (RARP) for hemiplegic stroke survivors, as shown in Figure 1. It consists of two 3-DOF symmetric layer-stacking structure platforms; therefore, the mechanical configuration allows the patient to use his/her sound side ankle joint to teach the affected side ankle joint for ankle exercises under a physiotherapist's instructions.

This paper is organized as follows. The design specification of the RARP is presented in Section 2.1, while Section 2.2 is dedicated to the mechanical design of the RARP. And the control architecture of the RARP is described in Section 2.4. The experimental results are reported in Section 3, while the discussion is in Section 3.4. Finally, the conclusions are reported.

2. Materials and Methods

2.1. Design Specification of the RARP. Figure 2 demonstrates the anatomical characteristics of the human ankle joint. The rotation of the ankle joint can be projected to three orthogonal planes and divided into three different rotating movements with the corresponding axes. The ankle joint can be simplified as a spherical joint, and the rotation along the x -axis is to achieve inversion/eversion movement, while the rotation along the y -axis is to obtain dorsiflexion/plantarflexion movement and the rotation along the z -axis is to realize internal/external rotation. Considering the individual difference of ankle physiological characteristics, the range of each ankle motion is shown in Table 2 [14, 15].

2.2. Design Consideration and Iterations. The final design of the RARP mechanism was obtained after several rounds of design iterations. The following considerations led to the convergence of the final design.

2.2.1. Exercise Mode. Corresponding to the different sources of tractive force for ankle movement, ankle rehabilitation can be sorted into patient-passive exercise and patient-active exercise. In the early stage of ankle therapy, the patient can hardly self-move his/her foot; therefore, a passive exercise with constant-speed movement to avoid muscle atrophy is necessary. This kind of task can be accomplished after the patient has carried out delicate movement by himself/herself. In order to allow the patient to fully reobtain his/her motor function, constant torque-impedance exercises can be executed with the device to enhance the strength of the patient's affected muscles.

To the above exercise modes, researchers pay most attentions to recover the range of motion and force strength of the patient's affected ankle; however, ankle exercise content should consider the balance and the coordination between the sound side ankle and the affected side ankle due to the individual differences. Hence, in this paper, we propose a new ankle exercise mode, named as awareness exercise that

TABLE 1: Existing state-of-the-art ankle rehabilitation robots.

Catalog	System or developer	DOFs	Payload
Parallel structure	Saglia et al. [2]	2	≤ 120 Nm
	Rutgers University [5]	6	≤ 35 Nm
	Liu et al. [6]	3	—
	Meng et al. [7]	6	—
	Muhammad and Shafriza [8]	3	—
	Yu et al. [9]	3	—
Exoskeletal structure	Jeffrey et al. [10]	1	≤ 30 Nm
	Delaware University [11]	2	—
	Rahman and Ikeura [12]	1	≤ 60 Nm
	Hong et al. [13]	3	—

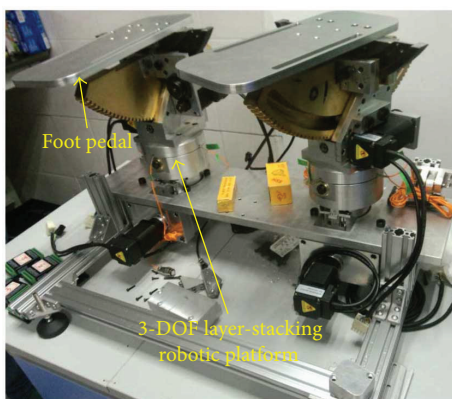


FIGURE 1: Constructed ankle rehabilitation robotic platform.

allows the patient to train his/her affected side ankle using the motor parameters obtained from his/her sound side ankle. With this exercise mode, the motor capability of the affected side ankle will approach that of the sound side ankle; therefore, it allows the patient to regain symmetric balance capability for walking after ankle exercise.

2.2.2. Mechanical Configuration. A 3-DOF robotic platform is proposed to assist the ankle to achieve inversion/eversion, dorsiflexion/plantarflexion, and internal/external rotation. As shown in Figure 2(b), the joints of inversion/eversion and dorsiflexion/plantarflexion are independent, while located behind the movement of internal/external rotation. Three mechanical structures to realize 3-DOF ankle exercises are illustrated in Figure 3.

In the first design solution (Figure 3(a)), the rotation generated by motor M1 and motor M2 will be transferred to linear motion through a ball screw pair mechanism and then drives the foot pedal to obtain internal/external rotation and dorsiflexion/plantarflexion exercise, respectively. Motor M3 is directly mounted to the pedal mechanism; therefore, the rotation generated by M3 will drive the ankle joint to execute inversion/eversion ankle exercise.

In the second design solution (Figure 3(b)), the 3-DOF mechanism is constructed based on a serial mechanism structure. The coronal axis and the sagittal axis are located

in the same plane to form a cross structure, while driven by motors M2 and M3, respectively. The base of motor M2 is fixed at the output shaft of motor M1; therefore, the rotation of motor M1 will drive the whole distal mechanism movement. Careful geometric dimensional design of the robotic platform can allow that the pivot point of the ankle joint coincides with the rotation center of the pedal.

In the third design solution (Figure 3(c)), the 3-DOF mechanism is stacked up layer by layer. In order to ensure that the rotation center of the pedal always points to the pivot center of the ankle joint, a circular plate is fitted in the worm gear pair mechanism; therefore, the rotation of the worm will drive the circular plate to rotate along its central axis. Since platform II and platform III are orthogonally mounted with each other, the rotation center of the foot pedal will automatically point to the pivot center of the ankle joint (Figure 3(f)). A torque sensor (FT20, Forsentek Co., Shenzhen, China) is mounted at the mechanism for internal/external rotation exercise, and two force sensors (FL25-100 kg, Forsentek Co., Shenzhen, China) are mounted under the foot pedal to detect the interaction force between patients' foot and the foot pedal.

All the three design solutions can accomplish ankle exercises with motion of inversion/eversion, dorsiflexion/plantarflexion, and internal/external rotation. In the first solution, the use of a screw pair mechanism can increase systematic rigidity; however, the volume is hard to be compacted. In the second solution, although the serial mechanism is easy for a compact design, the payload on the pedal will generate a large torque at the serial structure robotic joint; hence, high-torque motor is needed to execute ankle exercise and the cantilever needs to be strengthened. In the third solution, the rotation of the motor passes through the combination of gear pairs to drive the circular plate rotating along its central axis. This layer-stacking mechanism design takes use of the advantage that the high-torque transmission of worm gear pair and the payload on the pedal can be transmitted to the ground through the circular plates. Finally, the third solution is used in our robotic platform.

2.3. Component Description. As shown in Figure 3, the ankle rehabilitation robotic platform consists of three parts

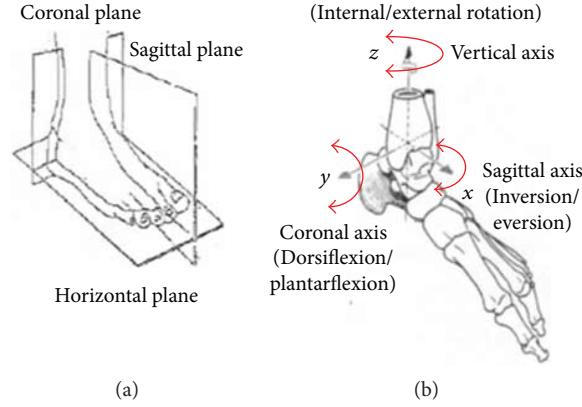


FIGURE 2: The anatomical planes and terms of location and orientation; (a) projection planes; (b) rotational axes.

TABLE 2: Ankle physiological data.

Axis	Motion	Angle range (degree)	Torque (Nm)	Angular velocity (degrees/s)
x	Inversion	0~30	10	≤100
	Eversion	-20~0		
y	Dorsiflexion	0~30	45	≤80
	Plantarflexion	-40~0		
z	Internal rot.	0~20	20	≤80
	External rot.	-30~0		

corresponding to inversion/eversion, dorsiflexion/plantarflexion, and internal/external rotation, respectively. We employ the combination of the gear pairs to execute a power transmission from the motor to the actuator.

2.3.1. Mechanism for Internal/External Rotation Exercise. The mechanism that activates ankle exercise of internal/external rotation (Figure 4) consists of gear pair I and worm gear pair II. Spur gear a1 transmits motor's rotation to the shaft s1 through gear pair I. Due to spur a2 and worm a3 being coaxial, the mechanism allows us to transmit the mechanical power to the worm gear pair I. Define the gear ratio $N_{i,j}$ between two consecutive gears as

$$N_{i,j} = \frac{z_i}{z_j}, \quad (1)$$

where z is the number of teeth and i and j are the leading and follower gears, and the equation relating joint movement θ_{j1} to the rotation $\theta_{in,1}$ can be expressed as follows:

$$\theta_{j1} = \theta_{in,1} N_{reducer} N_{a1,a2} N_{a3,a4}, \quad (2)$$

where $N_{reducer} = 5.2$, $N_{a1,a2} = 1.88$, and $N_{a3,a4} = 20$.

The input spur gear a1 is actuated by a brushless DC motor (MT8N42P06V2E), which is a 60 W motor coupled with the 5.2:1 gearhead, and the rated speed of the motor is 3000 RPM, while the rated torque is 0.2 Nm. By substituting the rated parameters into (2), the output of the robotic joint J1 can exert an angular velocity of 92 degrees/s. The output torque can be computed by

$$T_{1out} = T_1 N_{reducer} N_{a1,a2} N_{a3,a4} \prod_{i=1}^4 \eta_i, \quad (3)$$

where T_{1out} is the output torque, T_1 is the rated torque of motor I, η_1 is the transmission efficiency of the planetary reducer and equals to 0.8, η_2 is the transmission efficiency of the cylindrical gear pair and equals to 0.98, η_3 is the transmission efficiency of the worm gear pair and equals to 0.75, and η_4 is the transmission efficiency of the ball bearing and equals to 0.99. By substituting these parameters into (3), the output torque can exert a value of 22.76 Nm. Compared with the system specification, the mechanism design of the joint for internal/external rotation exercise can satisfy the requirement.

2.3.2. Mechanism for Dorsiflexion/Plantarflexion Exercise. The mechanism for dorsiflexion/plantarflexion exercise, corresponding to J2 in Figure 5, is actuated by a brushless DC motor. The movement is transmitted from the motor II axis to the perpendicular joint axis by means of the combination of the spur gear pair and worm gear pair. The actuator is MT8N42P10V2E, able to provide 100 W of power with a rated torque of 0.32 Nm and a rated speed of 3000 RPM. The shaft of motor II is parallel with that of the worm rod, while executing power transmission through an intermediate wheel. Two guider rods are used to ensure that platform II works in the plate paralleled with shaft s2. The equation relating joint movement θ_{j2} to the rotation $\theta_{in,2}$ can be expressed as follows:

$$\theta_{j2} = \theta_{in,2} N_{b1,b2} N_{b2,b3} N_{b3,b4}, \quad (4)$$

where $N_{b1,b2} = 1.68$, $N_{b2,b3} = 0.595$, and $N_{b3,b4} = 172$. By substituting the rated parameters of motor II into (4), the movement of the robotic joint J2 can execute a maximum angular velocity of 104.6 degrees/s. The output torque of the robotic joint J2 can be calculated by

$$T_{2out} = T_2 N_{b1,b2} N_{b2,b3} N_{b3,b4} (\eta_2 \eta_3 \eta_4), \quad (5)$$

where T_{2out} represents the output torque of motor II, T_2 is the rated torque of motor II, η_2 is the transmission efficiency of the cylindrical gear pair and equals to 0.98, η_3 is the transmission efficiency of the worm gear pair and equals to 0.75, and η_4 is the transmission efficiency of the ball bearing and

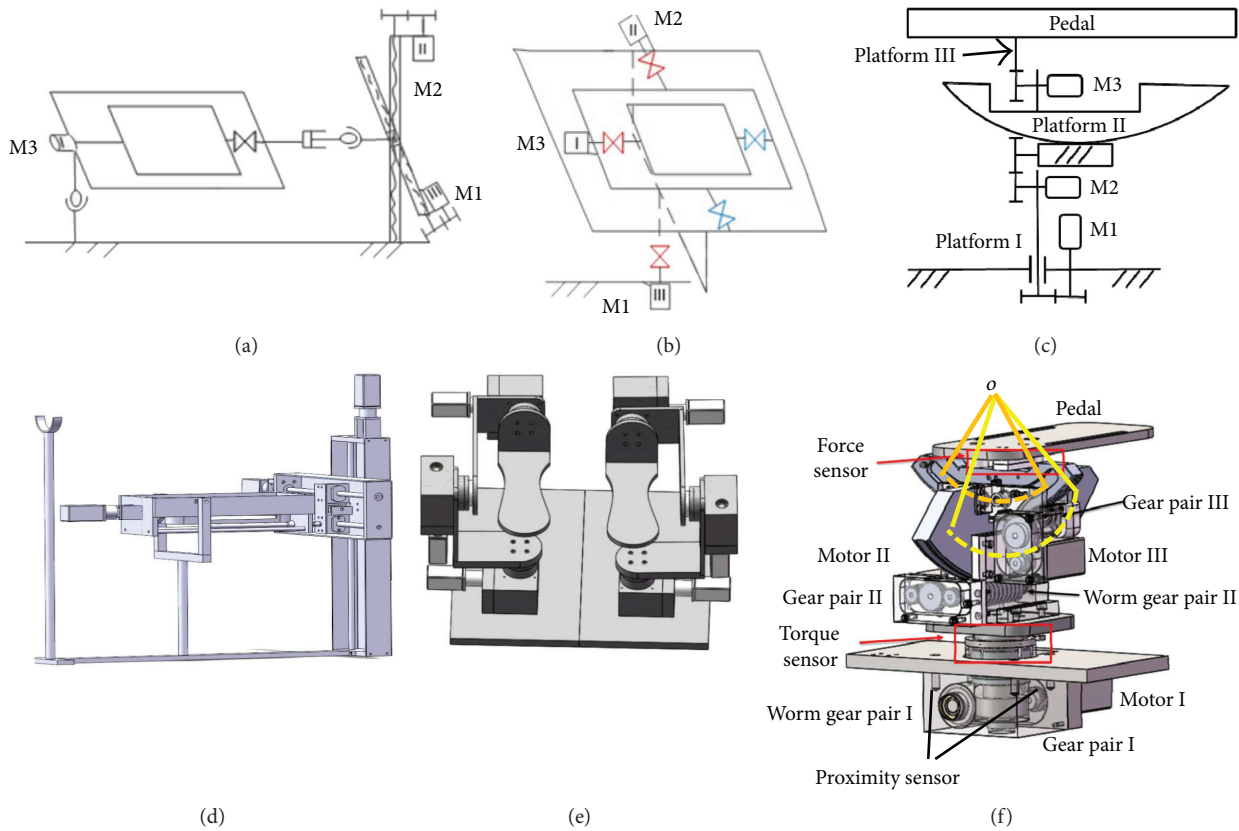


FIGURE 3: Three design solutions of the 3-DOF ankle rehabilitation robotic platform: (a) mechanical diagram of solution I; (b) mechanical diagram of solution II; (c) mechanical diagram of solution III; (d) 3D model of solution I; (e) 3D model of solution II; (f) 3D model of solution III.

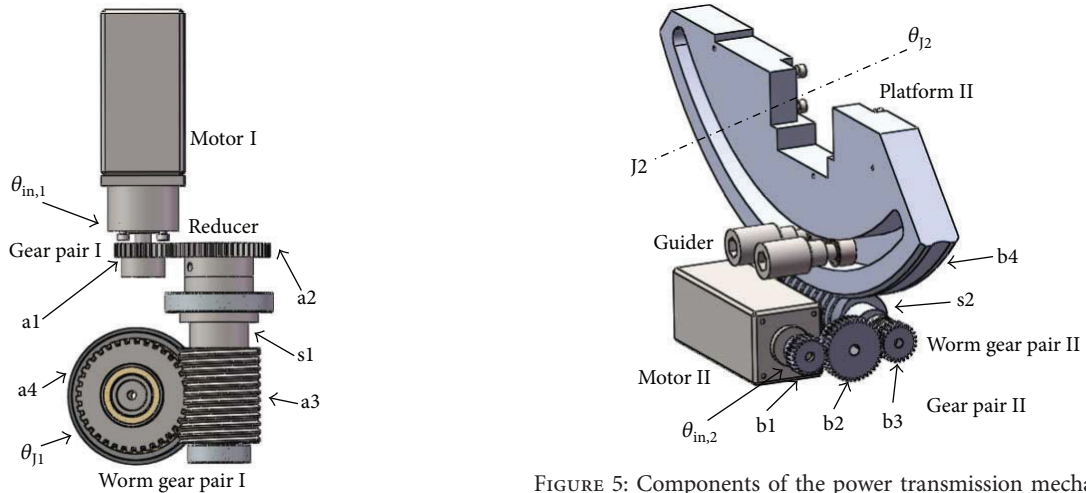


FIGURE 4: Components of the power transmission mechanism for internal/external rotation exercise.

equals to 0.99. By substituting these parameters into (5), platform II can execute a torque of 55.04 Nm, which can meet the design requirement.

2.3.3. Mechanism for Inversion/Eversion Exercise. As presented previously, the mechanism for inversion/eversion

FIGURE 5: Components of the power transmission mechanism for dorsiflexion/plantarflexion exercise.

exercise is located at the top layer and fitted a foot pedal at the distal zone, as shown in Figure 6. Three gear pairs are employed to execute the power transmission from the motor shaft to the foot pedal. Gear c1 is mounted directly at the motor shaft. Gear c2 and gear c3 are mounted at the both sides of shaft s3 while gear c4 and gear c5 are installed at the both ends of shaft s4.

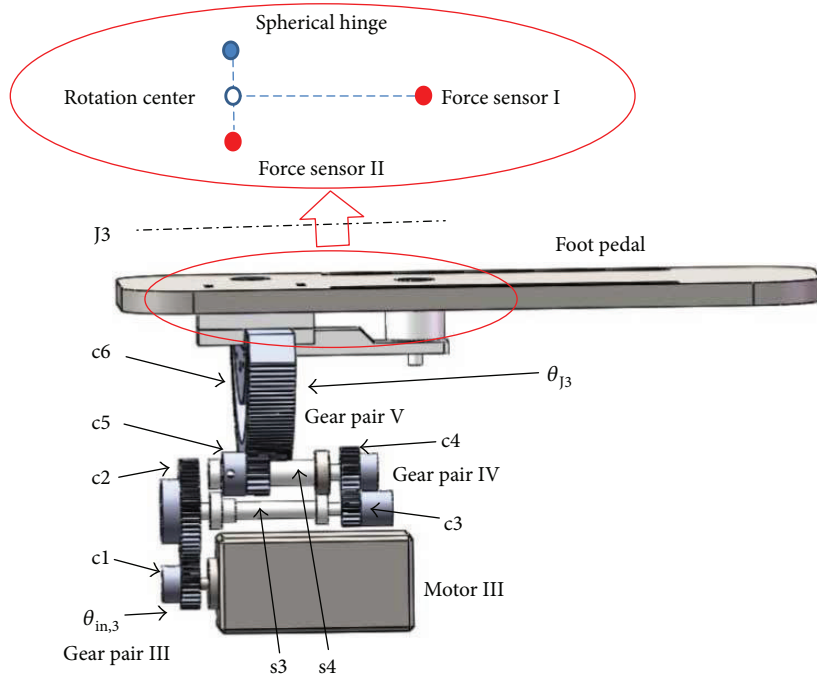


FIGURE 6: Components of the power transmission mechanism for inversion/eversion exercise.

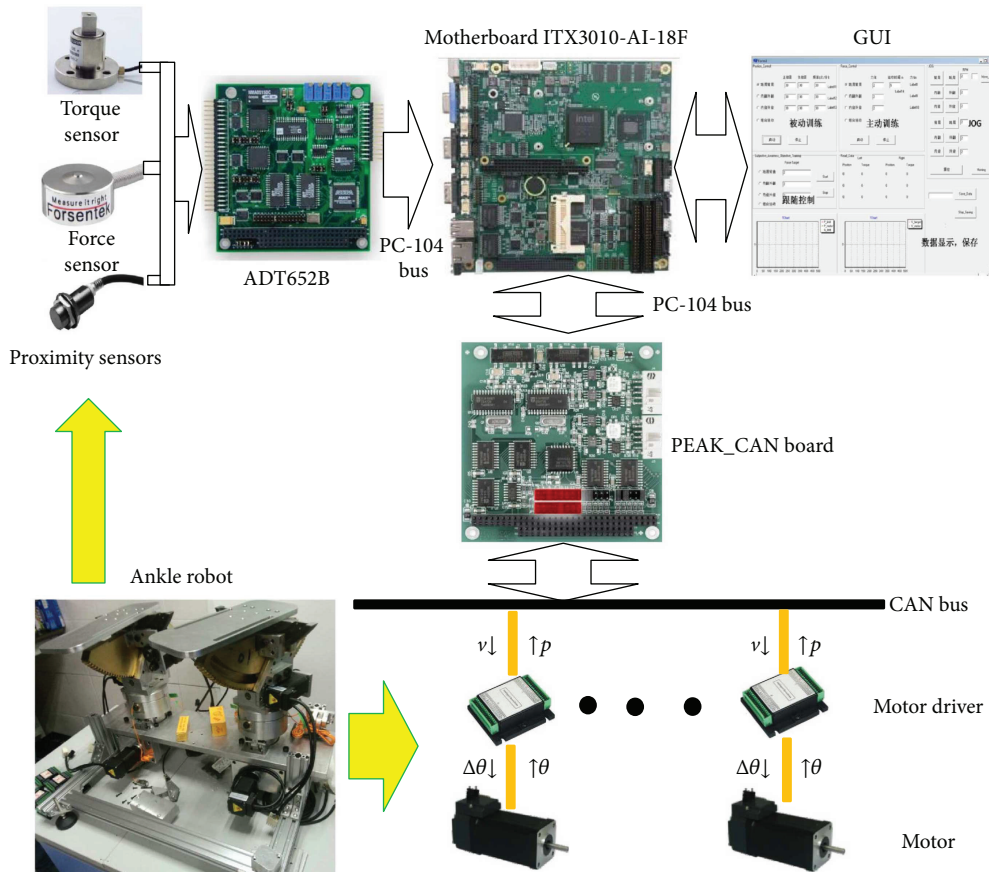


FIGURE 7: Control architecture of the ankle rehabilitation robotic system.

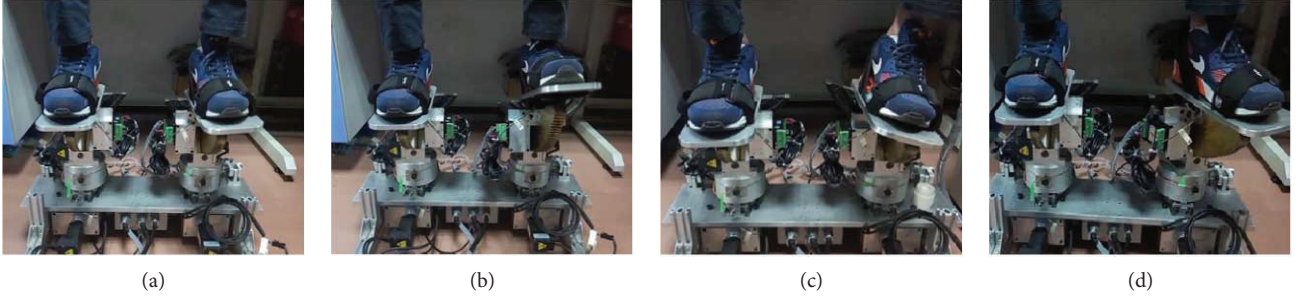


FIGURE 8: Experimental scenarios under patient-passive exercise mode: (a) initial posture; (b) dorsiflexion/plantarflexion exercise; (c) inversion/eversion exercise; (d) internal/external rotation exercise.

TABLE 3: Parameters for constant-speed ankle exercise.

Parameter joint	Angular velocity (degrees/s)	Range (degrees)
Dor./plantar.	60	-30~30
Inv./ev.	36	-20~20
Int./ex. rot.	60	-20~20

Gear c_1 , actuated by a brushless DC motor (MT8N42P06V2E), bites with gear c_2 in gear pair III, and the similar configuration was constructed in gear pair IV and gear pair V. The equation bridging joint movement θ_{j_3} to the rotation $\theta_{in,3}$ can be expressed as follows:

$$\theta_{j_3} = \theta_{in,3} N_{c_1,c_2} N_{c_3,c_4} N_{c_5,c_6}, \quad (6)$$

where $N_{c_1,c_2} = 2.2$, $N_{b_2,b_3} = 1.5$, and $N_{b_3,b_4} = 17.1$. Based on the known parameters, we can obtain that the robotic joint J3 can achieve a maximum angular velocity of 319 degrees/s; the output torque of the robotic joint J3 can be described as

$$T_{3out} = T_3 N_{c_1,c_2} N_{c_2,c_3} N_{c_3,c_4} (\eta_2^3 \eta_4^2), \quad (7)$$

where T_{3out} is the output torque of motor III, T_3 is the rated torque of motor III, η_2 is the transmission efficiency of the cylindrical gear pair and equals to 0.98, and η_4 is the transmission efficiency of the ball bearing and equals to 0.99. By substituting the parameters into (7), the foot pedal can achieve 10.41 Nm for inversion/eversion exercise.

Two force sensors (FL25-100 kg, Forsentek Co., Shenzhen, China) are mounted under the foot pedal, based on the lever principle; the torque generated for dorsiflexion/plantarflexion and inversion/eversion movements can be calculated by

$$\begin{aligned} T_{inv./ev.} &= 2F_2 l_1 + F_1 l_1, \\ T_{dor./plantar.} &= F_1 l_2, \end{aligned} \quad (8)$$

where $T_{inv./ev.}$ and $T_{dor./plantar.}$ represent the rotational torques of inversion/eversion and dorsiflexion/plantarflexion, respectively. F_1 and F_2 denote the measured force on sensor I and sensor II, and l_1 and l_2 are the length of the corresponding cantilevers.

2.4. Overview of the Control Architecture. For the ankle rehabilitation robotic platform, six IBL3605A motor drivers (made by Techservo Co. Ltd., Shenzhen, China) are used to drive the two 3-DOF layer-stacking robotic platforms. Encodes embedded in the motors provide the current relative angular position of each motor shaft, thus enabling a semi-closed loop position control. All the drivers communicate via CAN bus with a PC-104-based personal computer (PC). The C++ software that runs on the PC obtains control instructions from the peripheral equipment (mouse, keyboard, and sensors) and sends the desired velocity of the motors to the controllers through a CAN-PC104 card (PEAK-System Technik, Germany). The relations between each submodule of the control system are described in Figure 7.

As shown in Figure 7, the user sets the ankle exercise parameters and chooses the exercise mode via GUI on the PC. By combining the sensing data and user input from GUI, the motion amount of each joint can be calculated in the PC and delivered to the corresponding motor through CAN bus. The generated encoder data, internal/external rotation torque (torque sensor), foot pressure (force sensor), and joint range limits (proximity sensor) will be sent back to the controller as a compensation for the input.

Based on the designed ankle rehabilitation robotic platform, a healthy subject with no experience of using the robot was selected to complete three trajectories on each exercise mode mentioned in Section 2.2. The user had 5 min to familiarize himself with the operating characteristics of the robot system before executing the ankle exercises.

3. Results and Discussion

As introduced in Section 2, the ankle rehabilitation robotic platform consists of two symmetric exercise mechanisms. The mechanical configuration allows patients to execute the affected ankle exercise only or the coordination training on both feet. Three ankle exercise modes are designed to execute ankle rehabilitation corresponding to different rehabilitation stages.

3.1. Constant-Speed Ankle Exercise. In the early stage of ankle therapy, the patient is unable to move his/her foot; hence, a patient-passive training which can delicately move the patient's foot is needed. In this stage, the patient's foot is unable to provide force to move the foot pedal. Therefore,

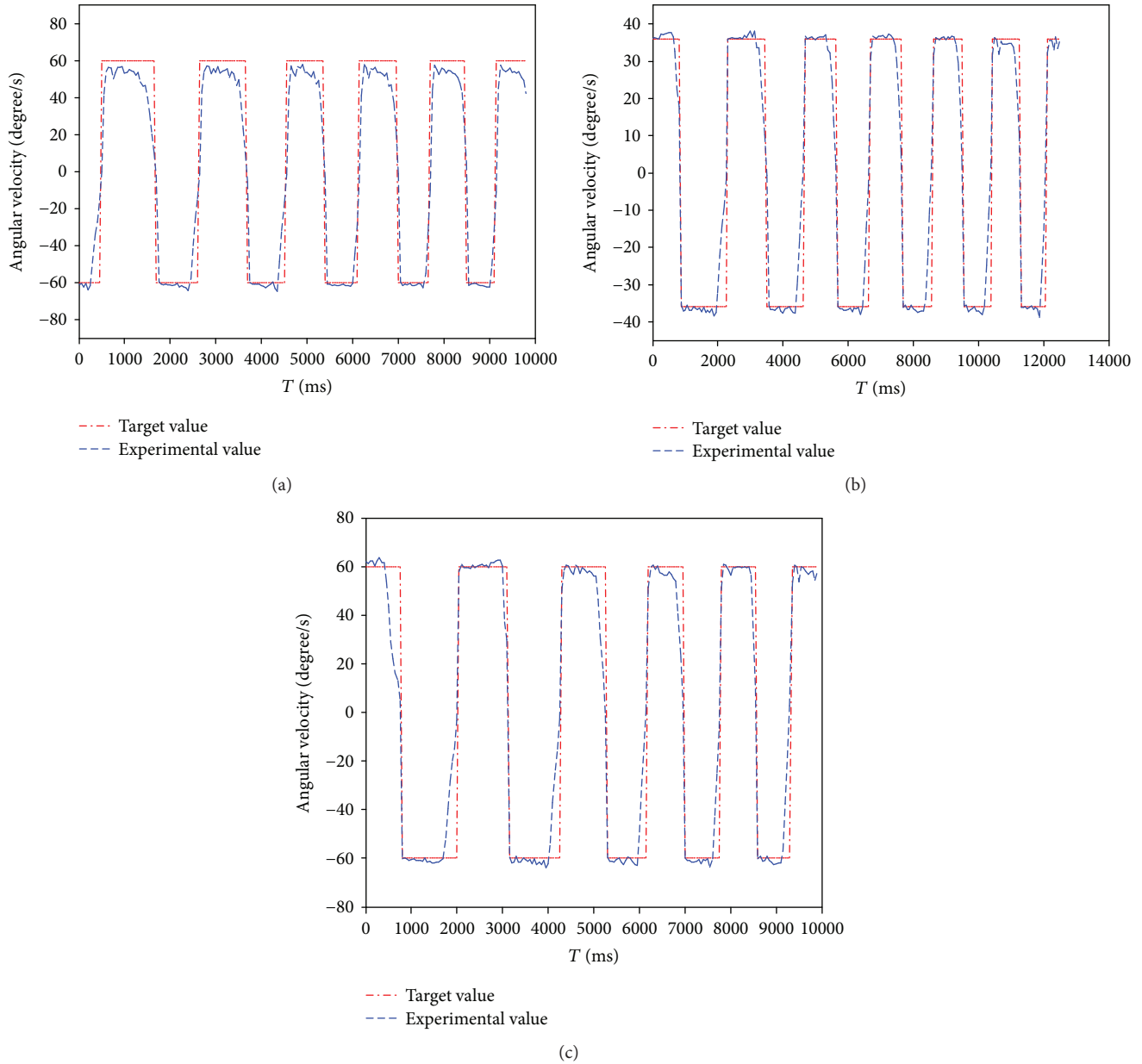


FIGURE 9: Experimental tracking result and setting parameters of patient-passive exercise: (a) dorsiflexion/plantarflexion movement; (b) inversion/eversion movement; (c) internal/external rotation.

TABLE 4: The setting parameters under constant torque-impedance ankle exercise.

Movement	Dorsiflexion/ plantarflexion	Inversion/ eversion	Internal/external rotation
Torque (Nm)	5	2	10

the objective of this rehabilitation stage is to exercise the affected muscles to avoid muscle atrophy.

In order to avoid exercise injury, the robot should provide moderate exercise with a constant speed in the early stage. The experimental scenario is shown in Figure 8. The

user sets the exercise velocity and angle of joint motion via GUI (parameters are listed in Table 3).

The trail of joint velocity was recorded during exercise, and the relation between the experimental result and the target parameter is shown in Figure 9. The experimental result demonstrated that the robotic platform can well track the target value in the inversion/eversion movement and internal/external rotation. There is a mean error of 6°/s in the dorsiflexion movement, which is caused by the payload on the foot pedal due to motor impedance on the patient's ankle.

3.2. Constant Torque-Impedance Ankle Exercise. In this exercise mode, the patient lays his/her affected side foot on the foot pedal and executes force to push the foot pedal to

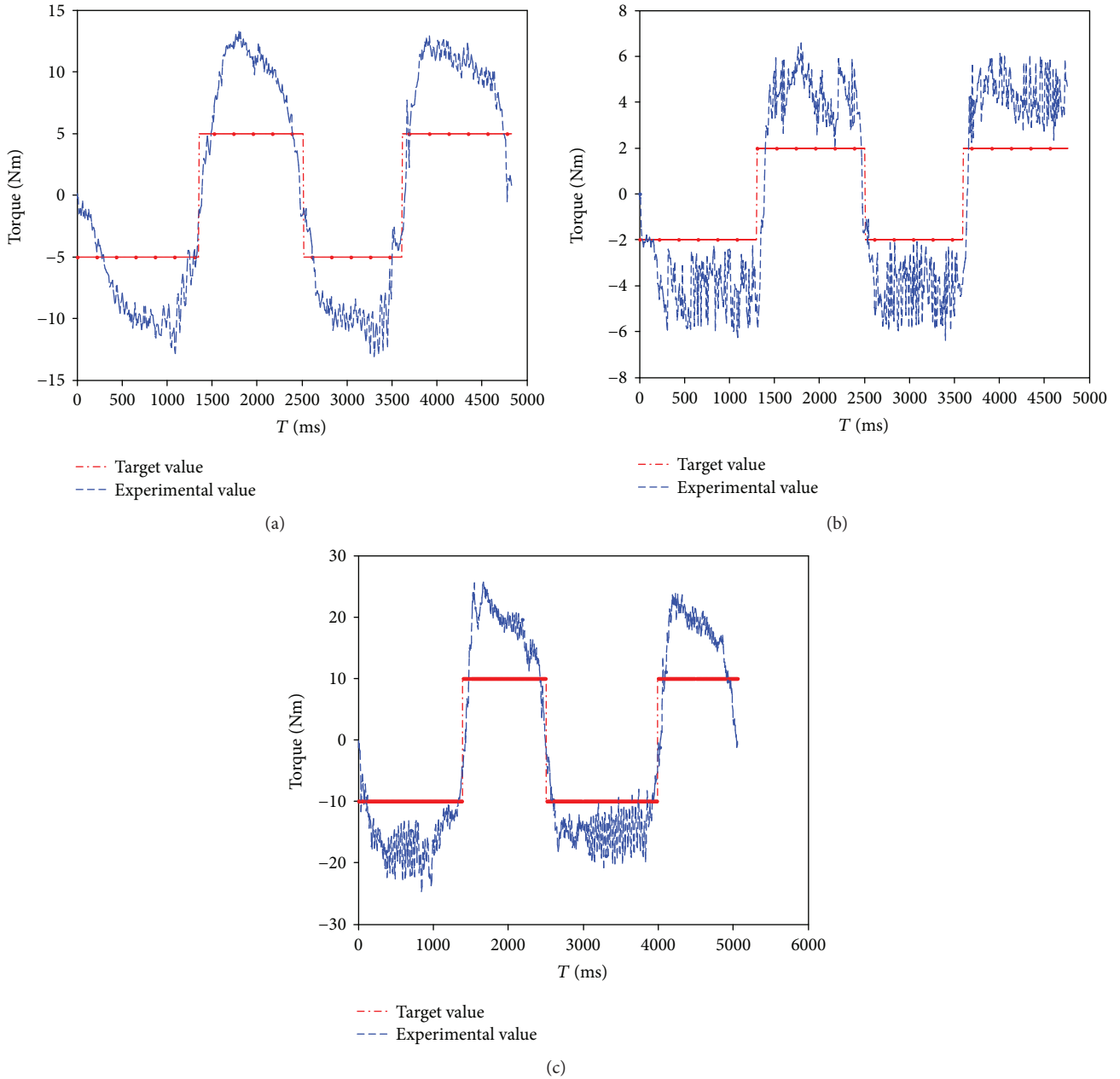


FIGURE 10: Experimental data and the target threshold under patient-active ankle exercise mode: (a) dorsiflexion/plantarflexion movement; (b) inversion/eversion movement; (c) internal/external rotation.

enhance strength of the affected side ankle. A force threshold is set through GUI, and the foot pedal will move after the detected force on the foot pedal has exceeded the threshold value. The parameters under constant torque-impedance ankle exercise are noted in Table 4.

The experimental result under constant torque-impedance ankle exercise is shown in Figure 10. The robot joint will keep on moving when the detected force is smaller than the set threshold. The foot pedal moves with the velocity proportional to the deviation of the detected torque and the threshold value. The experimental result demonstrated that the foot pedal will quickly follow the movement of the patient’s foot after the interaction torque has exceeded the threshold.

3.3. Awareness Exercise. In this training mode, the sound side of the patient’s foot will lie on the foot pedal and drive the foot pedal to move in the ankle range of motion under self-awareness control. Since the mechanism of the affected side robotic platform is symmetric to that of the sound side, the movement of the sound side will be directly mapped to drive the mechanism at the affected side under position control. The experimental scenarios are shown in Figure 11.

Corresponding to the ankle exercise shown in Figure 11, the positioning tracking trajectories are described in Figure 12. The foot pedal at the sound side is driven by the patient under awareness exercise mode, and the foot pedal at the affected side follows well the trace generated at the sound side.

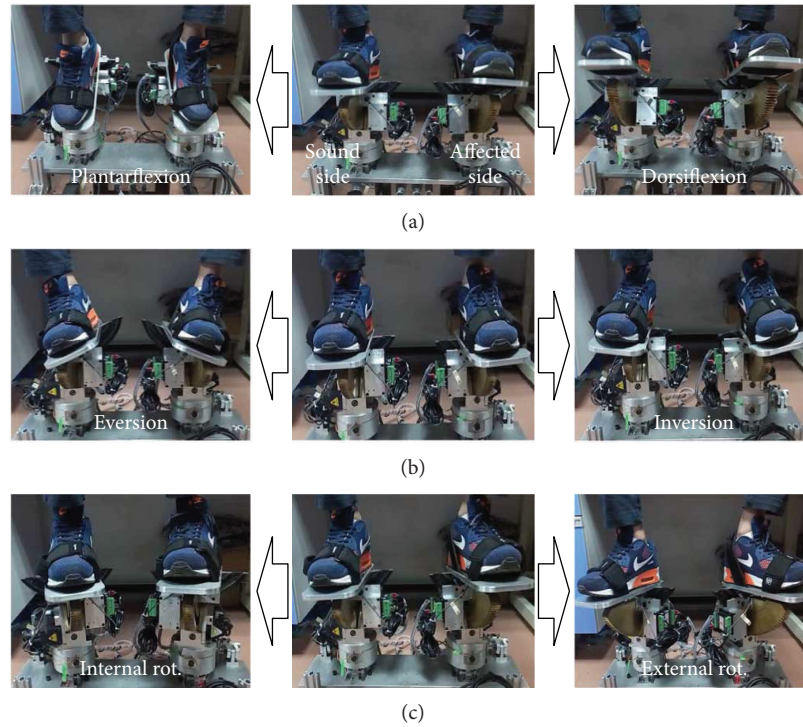


FIGURE 11: Ankle exercise under fusion of awareness and passive exercise modes: (a) movement of dorsiflexion/plantarflexion; (b) movement of inversion/eversion; (c) internal/external rotation.

3.4. Discussion. The ankle exercises under constant-speed exercise mode are described in Figures 8 and 9. The experimental result demonstrated that the velocity of the ankle rehabilitation robotic platform follows well the input value. In the constant torque-impedance exercise mode, changing the threshold of the torque can realize strength training of the affected ankle. And the foot pedal of the robot will move with the velocity proportional to the deviation of the detected torque and the target torque. In the awareness exercise mode, the sound side of the robotic platform will teach the affected side to move in the range of motion. The root mean square (RMS) in the dorsiflexion/plantarflexion is 6.55 degrees, and the maximum time delay is 80 ms. The RMS in the inversion/eversion is 1.56 degree, and the maximum time delay is 70 ms. The RMS in the internal/external rotation is 1.58 degree, and the maximum time delay is 85 ms. The mean error and standard deviations are illustrated in Table 5.

The above-proposed three exercise modes correspond to different rehabilitation stages. In the constant-speed exercise mode, the patient cannot manage the affected muscle by himself/herself; therefore, the ankle rehabilitation robotic platform will move with a constant moderate speed with the consideration of individual difference, which aims to avoid patient muscle atrophy. The constant-speed exercise mode can be replaced by a torque resistance control scheme, which is used for enhancing the strength of the patient's ankle. In this mode, the ankle rehabilitation robotic platform is controlled to provide a certain level of torque to the footplate while the patient tries to fully regain his/her range of motion.

In the awareness rehabilitation procedure, the patient can exercise his/her affected side ankle using the motion data captured from the sound side ankle under proprioceptive training. In order to reobtain the individual balance, the patient has to lay his/her sound side ankle and affected ankle on the corresponding robotic platform, respectively, and then drive the sound side to move within the range of motion under his/her awareness, while the affected side ankle robotic platform will track the same trail mapped from that of the sound side ankle robot to exercise the affected ankle.

The experimental results demonstrated that the ankle rehabilitation robotic platform is capable of executing the above three exercise modes. Based on the experimental results, several improvements are needed to be addressed as follows.

3.4.1. A Friendly Interface for the Robot User. Currently, robot users input instructions to the control system via a mouse and keyboard. A touch panel, integrated into the control architecture, will enable the robot user to easily enter the parameters and instructions. Furthermore, the touch panel is portable, which allows the user to set the rehabilitation parameters at a comfortable location.

3.4.2. Integration with Virtual Reality Scenarios. Although patients can perform ankle training under awareness exercise mode, a virtual training scenario integrated with patient rehabilitation information will stimulate the robot user to concentrate on training and make the rehabilitation become an attractive activity.

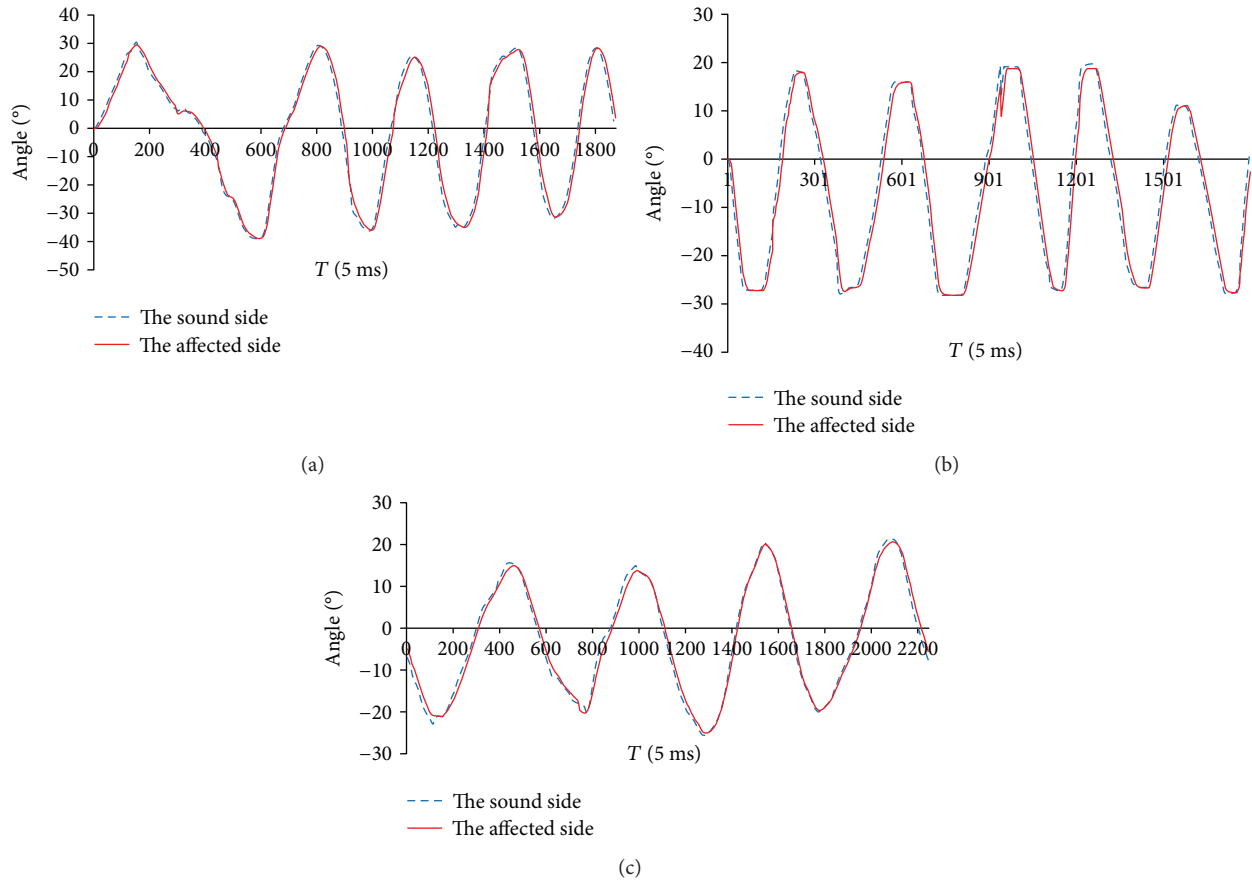


FIGURE 12: The ankle movement under awareness exercise mode: (a) dorsiflexion/plantarflexion; (b) inversion/eversion; (c) internal/external rotation.

TABLE 5: The mean error and standard deviations on the three exercise modes.

Exercise mode 1	Trail			Mean error	Standard deviation
	1	2	3		
Dorsiflexion/plantarflexion (°/s)	6.6	6.3	5.1	6	0.79
Inversion/eversion (°/s)	1.2	0.6	0.9	0.9	0.3
Internal/external rotation (°/s)	1.2	0.6	0.9	0.9	0.3
Exercise mode 2	Trail			Mean error	Standard deviation
	1	2	3		
Dorsiflexion/plantarflexion (Nm)	6.2	5.8	6.4	6.13	0.31
Inversion/eversion (Nm)	3.6	3.2	3.5	3.43	0.21
Internal/external rotation (Nm)	8.6	8.1	8.3	8.33	0.25
Exercise mode 3	Trail			Mean error	Standard deviation
	1	2	3		
Dorsiflexion/plantarflexion (°)	6.94	6.82	5.89	6.55	0.57
Inversion/eversion (°)	1.69	1.47	1.52	1.56	0.12
Internal/external rotation (°)	1.65	1.47	1.62	1.58	0.10

4. Conclusions

This paper presented a novel layer-stacking structure robotic platform used for robot-aided ankle rehabilitations. The

ankle rehabilitation robot consists of two symmetric 3-DOF robotic platforms, where one is used to detect the movement of the sound side ankle and the other is used to exercise the affected side ankle. The unique mechanical configuration

allows the patient to exercise his/her affected side ankle via the movement taught by the sound side ankle. The rehabilitation protocol has been considered the basis for design of the control architecture. Based on the designed robotic system, three exercise modes including constant-speed exercise, constant torque-impedance exercise, and awareness exercise modes have been developed to perform ankle training corresponding to different rehabilitation stages. The experimental results demonstrated that the promising performance of tracking trail between the two symmetric robotic platforms was obtained with a mean tracking error of 6°/s under constant-speed exercise mode. The robotic platform can move smoothly in the constant torque-impedance mode, and the robotic platform at the affected side can well track the movement of the sound side with the maximum mean error of 6.55°.

Future work will look at the development of a friendly human-machine interface and the integration of a virtual environment based on the robot's vision to stimulate the patient during training [16]. Rehabilitation experiments with a team of clinicians are under preparation. Further studies will also extend to the integration of the EMG and FES information in the control architecture.

Conflicts of Interest

The authors declare that there is no conflict of interest regarding the publication of this paper.

Authors' Contributions

Quanquan Liu, Chunbao Wang, and JianJun Long contributed equally to this work.

Acknowledgments

The authors would like to thank C. Wei, A. Hou, P. Chen, and Z. Lu for the prototype manufacture and thank Dr. Q. Shi for the experimental advice. This work was supported in part by the Science and Technology Foundation of Guangdong, China (nos. 2016A020220001 and 2014A020225004), Technology Research Foundation of Basic Project of Shenzhen, China (nos. JCYJ20160428110354308 and JCYJ20170413095245139), Research Foundation of Health and Family Planning Commission of Shenzhen Municipality, China (nos. SZBC2017006 and 201601054), Returned Overseas Business Foundation of Shenzhen (no. 2016001), Research Foundation of International Cooperation of Shenzhen Municipality (no. GJHZ20170331105318685), and Guangxi Key Scientific and Technological Project (no. 1598013-12).

References

- [1] M. Dombovy, "Introduction: the evolving field of neurorehabilitation," *Continuum Lifelong Learning in Neurology*, vol. 17, no. 3, pp. 443–448, 2011.
- [2] J. Saglia, N. Tsagarakis, J. Dai, and D. G. Caldwell, "Control strategies for patient-assisted training using the ankle rehabilitation robot (ARBOT)," *IEEE/ASME Transactions on Mechatronics*, vol. 18, no. 6, pp. 1799–1808, 2013.
- [3] S. Rao, J. Binder, T. Hammwek et al., "Somatotopic mapping of the human primary motor cortex with functional magnetic resonance imaging," *Neurology*, vol. 45, no. 5, pp. 919–924, 1995.
- [4] C. Weiller, F. Chollet, K. J. Friston, R. J. Wise, and R. S. Frackowiak, "Functional reorganization of the brain in recovery from striatocapsular infarction in man," *Annals of Neurology*, vol. 31, no. 5, pp. 463–472, 1992.
- [5] M. Girone, G. Burdea, M. Bouzit, V. Popescu, and J. E. Deutsch, "A Stewart platform-based system for ankle telerehabilitation," *Autonomous Robots*, vol. 10, no. 2, pp. 203–212, 2001.
- [6] G. Liu, J. Gao, H. Yue, X. Zhang, and G. Lu, "Design and kinematics analysis of parallel robots for ankle rehabilitation," in *2006 IEEE/RSJ International Conference on Intelligent Robots and Systems*, pp. 253–258, Beijing, China, 2006.
- [7] W. Meng, S. Xie, Q. Liu, C. Lu, and Q. Ai, "Robust iterative feedback tuning control of a compliant rehabilitation robot for repetitive ankle training," *IEEE/ASME Transactions on Mechatronics*, vol. 22, no. 1, pp. 173–184, 2017.
- [8] N. Muhammad and N. Shafriza, "Design and kinematic analysis of parallel robot for ankle rehabilitation," *Applied Mechanics and Materials*, vol. 446–447, pp. 1279–1284, 2013.
- [9] R. Yu, Y. Fang, and S. Guo, "Design and kinematic analysis of a novel cable-driven parallel robot for ankle rehabilitation," *Symposium of Advanced on Theory and Practice of Robots and Manipulators*, pp. , 2014293–301, 2014.
- [10] W. Jeffrey, S. Thomas, B. Alexander, S. John, and R. E. Jack, "Stroke survivor's gait adaptations to a powered ankle-foot orthosis," *Advanced Robotics*, vol. 25, no. 15, pp. 1879–1901, 2011.
- [11] A. Agrawal, S. K. Banala, S. K. Agrawal, and S. A. Binder-Macleod, "Design of a two degree-of-freedom ankle-foot orthosis for robotic rehabilitation," in *9th International Conference on Rehabilitation Robotics*, pp. 41–44, Chicago, IL, USA, 2005.
- [12] S. Rahman and R. Ikeura, "A novel variable impedance compact compliant ankle robot for overground gait rehabilitation and assistance," *Procedia Engineering*, vol. 41, pp. 522–531, 2012.
- [13] M. Hong, Y. Shin, and J. Wang, "Novel three-DOF mechanism for lower-limb exoskeleton: kinematic analysis and design of passive-type ankle module," in *2014 IEEE/RSJ International Conference on Intelligent Robots and Systems*, pp. 504–509, 2014.
- [14] *Human Characteristics Database*, <http://www.tech.nite.go.jp/human/indexeng.html>.
- [15] C. Wang, L. Wang, J. Qin et al., "Development of an ankle rehabilitation robot for ankle training," in *2015 IEEE International Conference on Information and Automation*, pp. 94–99, Lijiang, China, 2015.
- [16] Q. Shi, C. Li, C. Wang, H. Luo, Q. Huang, and T. Fukuda, "Design and implementation of an omnidirectional vision system for robot perception," *Mechatronics*, vol. 41, pp. 58–66, 2017.

Research Article

Modelling and Experiment Based on a Navigation System for a Cranio-Maxillofacial Surgical Robot

Xingguang Duan,^{1,2} Liang Gao,^{1,2} Yonggui Wang ,³ Jianxi Li,^{1,2} Haoyuan Li,^{1,2}
and Yanjun Guo^{1,2}

¹Intelligent Robotics Institute, Beijing Institute of Technology, Beijing 100081, China

²Beijing Advanced Innovation Center for Intelligent Robots and Systems, Beijing 100081, China

³Beijing Institute of Technology, Beijing 100081, China

Correspondence should be addressed to Yonggui Wang; wangyg1025@163.com

Received 7 April 2017; Revised 15 August 2017; Accepted 23 August 2017; Published 10 January 2018

Academic Editor: Yi-Hung Liu

Copyright © 2018 Xingguang Duan et al. This is an open access article distributed under the Creative Commons Attribution License, which permits unrestricted use, distribution, and reproduction in any medium, provided the original work is properly cited.

In view of the characteristics of high risk and high accuracy in cranio-maxillofacial surgery, we present a novel surgical robot system that can be used in a variety of surgeries. The surgical robot system can assist surgeons in completing biopsy of skull base lesions, radiofrequency thermocoagulation of the trigeminal ganglion, and radioactive particle implantation of skull base malignant tumors. This paper focuses on modelling and experimental analyses of the robot system based on navigation technology. Firstly, the transformation relationship between the subsystems is realized based on the quaternion and the iterative closest point registration algorithm. The hand-eye coordination model based on optical navigation is established to control the end effector of the robot moving to the target position along the planning path. The closed-loop control method, “kinematics + optics” hybrid motion control method, is presented to improve the positioning accuracy of the system. Secondly, the accuracy of the system model was tested by model experiments. And the feasibility of the closed-loop control method was verified by comparing the positioning accuracy before and after the application of the method. Finally, the skull model experiments were performed to evaluate the function of the surgical robot system. The results validate its feasibility and are consistent with the preoperative surgical planning.

1. Introduction

Cranio-maxillofacial region is the most exposed part of the human body and plays an important role in the maintenance of facial feature, speaking, swallowing, chewing, facial expressions, and so on. The congenital malformation, traumatic defect, and trauma after tumor resection of the cranio-maxillofacial region are the common clinical diseases. These diseases will bring great psychological pressure and inconvenience to people's life and work. In order to reduce the trauma of cranio-maxillofacial surgery for patients, the minimally invasive treatment is often adopted. And the cranio-maxillofacial puncture manually by surgeons is typical of minimally invasive treatment [1].

With the fast development of science and technology, computer-assisted surgery becomes the necessary supportive tool for diagnosis, operation planning, and treatment in

medicine services [2–5]. In clinical routine, surgeons have been already supported by various computer-assisted devices such as the 3D reconstruction system, preoperative planning system, and intraoperative navigation system, especially the navigation system, which has brought great convenience for surgery and attracted increasing attentions. The navigation system is composed of stereotactic medical imaging technology, computer technology, artificial intelligence technology, and minimal invasive surgery [6]. In 1881, Zernov developed a brain-measuring instrument, which is the earliest surgery navigation records. In 1908, Horsley and Clarke created brain stereotactic technology [7]. In 1990, the United States launched the StealthStation, which is the first commercial surgery navigation system in the world and can be used in the human body. After that, the Stryker (Stryker-Leibinger, Kalamazoo, MI, USA), VectorVision (BrainLab, Munich, Germany), StealthStation (Medtronic-Xomed, Jacksonville,

FL, USA), and other products have been launched, and these products can be competent in many navigation surgeries [8]. At present, the navigation system commonly used in surgery is mainly divided into the following categories, that is, the optical navigation system, ultrasonic navigation system, and electromagnetic navigation system. These navigation systems have different advantages, and the optical navigation system becomes the mainstream for its ease of use, simple operation, and high accuracy in the surgical navigation system. The navigation system establishes the dynamic relationship between virtual digital images and actual operation structure and solves the problems of clinical surgeons that need to be solved urgently, including preoperative virtual surgery planning and intraoperative lesion accurate positioning. The computer-assisted technology based on the navigation system has improved the flexibility, accuracy, and prognosis of surgery largely [9, 10].

Furthermore, the robot technology has been widely used in cranio-maxillofacial surgery for its flexibility of control, stability, and high accuracy [11, 12]. In 1994, Kavanagh carried out preclinical tests in the field of oral and maxillofacial surgery using the image-guided robot system on the temporal bone for the first time [13]. In 1998, Lueth et al. developed the first interactive surgical robot (OTTO) for cranio-maxillofacial surgery. The robot was used for inserting non-flexible catheters and implanting bone fixtures [14]. In 2006, Bale et al. installed a frameless stereotactic device on a six-degrees-of-freedom mechanical arm for the ablative treatment of trigeminal neuralgia. The average positioning accuracy can reach 1.31 ± 0.67 mm in the model, body, and clinical trials [15]. In other surgeries, many robot systems have been developed, such as Robopsy, B-Rob I, and ZEUS.

To the best of our knowledge, although robot-assisted technology has been applied in cranio-maxillofacial surgery [16], its use for biopsy of skull base lesions and radioactive particle implantation of skull base malignant tumors has not yet been reported. And the function of cranio-maxillofacial puncture robot is single, which is designed for a certain operation, such as radiofrequency thermocoagulation. This makes it necessary for surgeons to switch and adapt to different surgical systems for different surgeries, which brings inconvenience to the operation. However, according to clinical experience, some cranio-maxillofacial surgery procedures have similarities; that is, puncture is needed to be done. Therefore, in order to make the surgical robot universal, a robot system that can be used in a variety of punctures is needed.

In robot puncturing surgery, the needle can be navigated by computed tomography (CT), ultrasound, or magnetic resonance image (MRI) to ensure the positioning accuracy of the needle. The iSYS1 robot system [17], AcuBot system [18], and PAKY-RAM robot [19] guided needle puncture through CT fluoroscopy to achieve high positioning accuracy. But CT fluoroscopy exposes the patient to radiation and does some harm to the patient's health. Hong et al. proposed an ultrasound-driven needle insertion robot for percutaneous cholecystostomy, which is capable of modifying the needle path by real-time motion compensation through visual servo control before needle insertion [20].

But ultrasound can provide only two-dimensional (2D) anatomical information with poor quality. MRI is nonirradiating, but its application in a robot surgery system is limited because of its cost, tunnel size, and material compatibility constraints [21]. In order to obtain better positioning accuracy, the needle position has to be checked repeatedly. Therefore, an accurate and safe navigation system is required during operation.

Although the structure of the cranio-maxillofacial region is complex and the forms of lesions are different, some experienced surgeons performing the operation could reduce most of the potential risks and have good prognosis by using a commercialized surgery navigation system. For surgeons, flexible and precise puncture can help them reduce the operation time, risk, and fatigue. Then, a new type of a cranio-maxillofacial surgery robot system is developed to assist surgeons in performing a variety of cranio-maxillofacial puncture surgeries, such as biopsy of skull base lesions, radiofrequency thermocoagulation of the trigeminal ganglion, and radioactive particle implantation of skull base malignant tumors. This paper aims to relate the components of the entire robot system and to realize the interaction among the robot, navigation system, and patient. The "kinematics+optics" hybrid motion control method is proposed in this paper, which can form a closed-loop system to improve the positioning accuracy of the system. Then, the robot can move accurately along a predetermined trajectory and assist surgeons to complete the corresponding cranio-maxillofacial surgery.

2. System and Model

2.1. System Composition. The cranio-maxillofacial surgery robot system (Figure 1) can be divided into four parts according to the function, including the patient subsystem, robot subsystem, optical measurement subsystem, and 3D reconstruction image subsystem [22]. The patient subsystem is the object of surgical treatment, and the head of the patient is fixed and adjusted through the head clamp to coincide with the operation. The robot subsystem is a frame structure with five degrees of freedom, and the working space can reach $300 \times 400 \times 400$ mm, which can meet the needs of the operation. By switching the end effector, the robot subsystem can perform a variety of operations, such as biopsy, radiofrequency thermocoagulation, and radioactive particle implantation. The optical measurement subsystem mainly realizes the spatial registration between each subsystem and real-time tracking in the operation. The 3D reconstruction image subsystem can obtain a 3D image of the cranio-maxillofacial region by CT scanning and reconstruction, which is applied to the entire operation, and provides guarantee for preoperative operation planning, intraoperative navigation, and postoperative verification.

Here, we mainly focus on the optical measurement subsystem. The optical measurement subsystem mainly consists of a set of optical measuring instruments (NDI Polaris, Canada). The optical measuring instrument includes an optical tracker, two passive rigid bodies, and a passive probe. The two passive rigid bodies are fixed on the robot

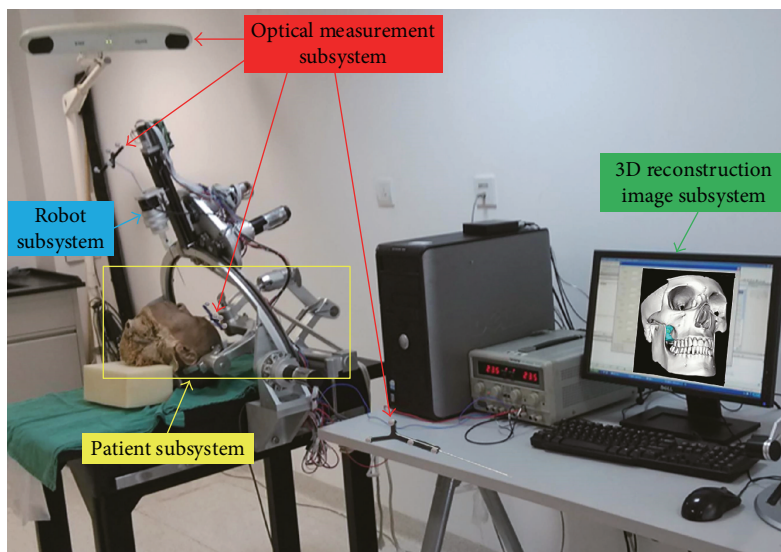


FIGURE 1: The cranio-maxillofacial surgery robot system.

and patient's head, respectively. The passive rigid bodies and probe can create the corresponding coordinate system by the position of four reflecting balls attached to them. The optical tracker can obtain the position of the reflecting balls by transmitting the infrared signal. In the range of measurement, the accuracy of the optical measuring instrument is 0.25 mm RMS.

In this paper, the relationship between the four subsystems is described, which are used to guide the movement of the robot arm. The spatial registration is firstly to realize the transformation of coordinate spaces between the four subsystems, so as to realize the integration of them. Secondly, the end effector of the robot can be controlled to a certain position in the robot work space through the hand-eye coordination method. In addition, the positioning accuracy of the end effector of the robot can be improved by the "kinematics + optics" hybrid motion control method.

2.2. System Model

2.2.1. Navigation Spatial Registration Based on an Improved ICP Algorithm. The spatial registration essentially performed the transformation matrix among the 3D image coordinate system, patient coordinate system, robotic coordinate system, and optical coordinate system [23]. The transformation relationship between coordinate systems is shown in Figure 2.

When the number of point sets is few, a classical ICP algorithm could not get the accurate and stable results, which are needed to iteratively solve the corresponding relation between two point sets. In order to reduce patient suffering caused by placing the titanium screws, the registration process could not provide enough marker points. So the classical ICP algorithm need to be improved to calculate transformation matrixes. In the improved ICP algorithm, the corresponding relation of points between two known point sets should be seen in the initial condition to avoid the iterative solution process between two unknown point sets. Then,

solve the mapping relationship by the least squares method and calculate iteratively the transformation matrixes based on the result error, until the accuracy is higher than the certain safety threshold [24–26].

The navigation spatial registration based on the improved ICP algorithm is illustrated as follows [27].

- (1) ${}^O T_p$, which is the transformation matrix from the patient space to optical measurement space, can be obtained by the optical tracker and passive rigid body on the patient skull.
- (2) ${}^P T_V$ is the transformation matrix from the 3D image space to patient space. Firstly, the coordinates of some medical marker points (titanium screws) which were fixed on the patient skull should be obtained by using the optical tracker and passive probe. Through the ${}^O T_p$, the above coordinates could be transformed into the patient space. So the coordinates of medical marker points in the patient space could be measured. Based on the coordinates of the medical marker points in the 3D image space and patient space, the transformation matrix ${}^P T_V$ could be calculated by the improved ICP algorithm.
- (3) ${}^O T_V$, which is the transformation matrix from the 3D image space to optical measurement space, could be computed from the following formula:

$${}^O T_V = {}^O T_P {}^P T_V. \quad (1)$$

- (4) ${}^O T_R$, which is the transformation matrix from the robot space to optical measurement space, can be obtained by using the optical tracker and passive rigid body on the robot. The robot coordinate system R should be established by the passive rigid body of the robot.

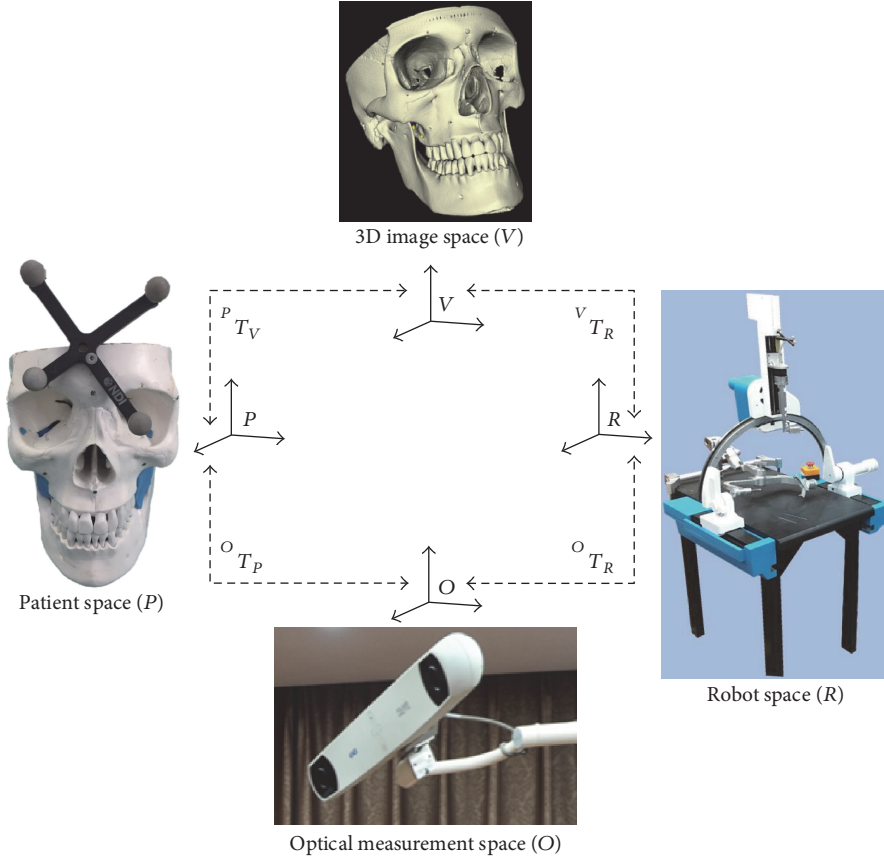


FIGURE 2: The transformation relationship between coordinate systems.

However, the kinematics and control of the robot should be realized in the robot base coordinate system R_B which is generated in the robot body. So the transformation matrix ${}^{R_B}T_O$ from the optical measurement space to the robot base coordinate system R_B should be solved.

First, the local coordinate system R_L is established through the three points, which are marked on the fixed position of the robot body. Then, the ${}^{R_B}T_{R_L}$ could be got, which is the transformation matrix from the robot local coordinate system to the robot base coordinate system. Next, the coordinate of the three points in the optical measurement space is measured by using the passive probe to touch the three points on the surface of the robot, and the transformation matrix ${}^O T_{R_L}$ from the robot local coordinate system to optical measurement space could be calculated. So the mapping relationship ${}^{R_B}T_O$ between the optical measurement space and robot base coordinate system is measured as follows:

$${}^{R_B}T_O = {}^{R_B}T_{R_L} ({}^O T_{R_L})^{-1}. \quad (2)$$

Furthermore, the transformation matrix ${}^R T_{R_B}$ from the robot base coordinate system to the robot space could be calculated by the following formula:

$${}^R T_{R_B} = ({}^O T_R)^{-1} ({}^{R_B} T_O)^{-1}. \quad (3)$$

As a result, controlling the robot to a certain position could be realized, as long as the corresponding parameters are described in the robot space.

- (5) ${}^R T_P$, which is the transformation matrix from the patient space to robot space, is calculated by ${}^O T_R$ and ${}^O T_P$ as follows:

$${}^R T_P = ({}^O T_R)^{-1} {}^O T_P. \quad (4)$$

- (6) ${}^V T_R$, which is the transformation matrix from the robot space to 3D image space, is calculated by ${}^O T_R$ and ${}^O T_V$ as follows:

$${}^V T_R = ({}^O T_V)^{-1} {}^O T_R = ({}^O T_P {}^P T_V)^{-1} {}^O T_R. \quad (5)$$

In robot-assisted surgery, the target position and orientation matrix V_{Target} , which is planned by the surgery planning system in preoperation, can be obtained in the 3D image space. The target matrix R_{Target} in the robotic space which corresponds to the target matrix V_{Target} can be obtained. According to the above matrix transformation, the equation $R_{\text{Target}} = ({}^V T_R)^{-1} V_{\text{Target}}$ could be got.

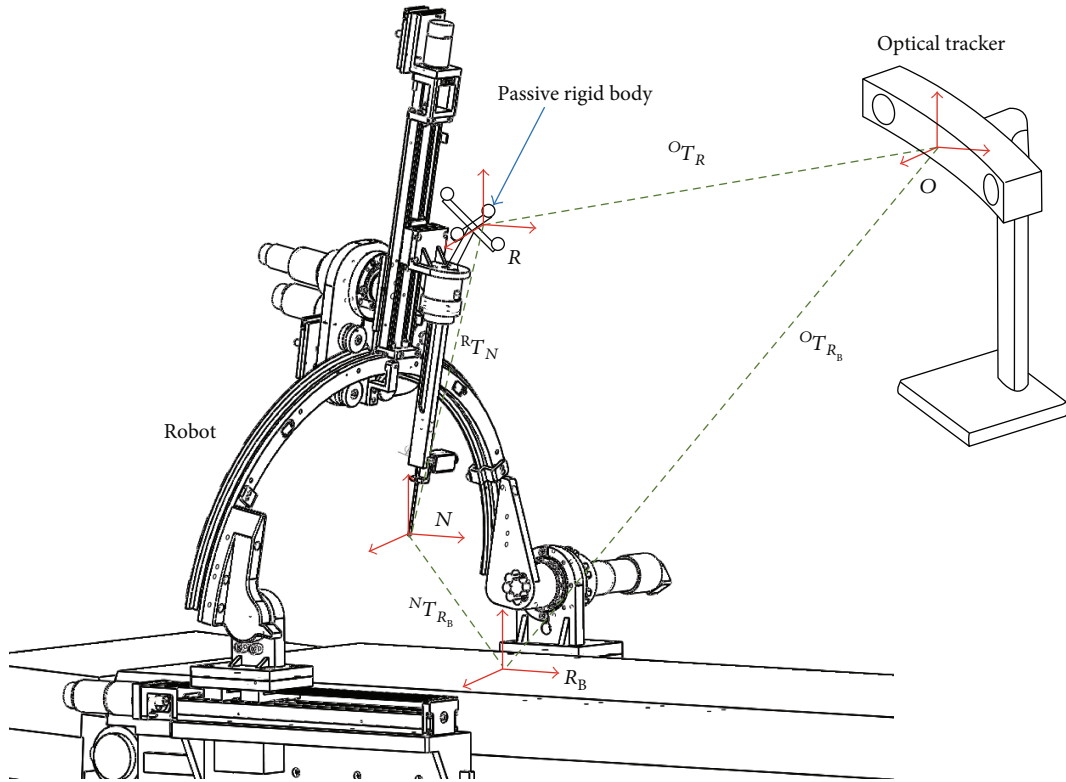


FIGURE 3: Hand-eye coordination based on optical navigation.

Then, the target matrix R_{Target} can be calculated after getting ${}^V T_R$, and the robot can move to the target position with right orientation.

2.2.2. Hand-Eye Coordination Based on Optical Positioning. To control the end effector of the robot from the current position to target position, the target position and orientation of the end effector in the robot base coordinate system must be described. After establishing the transformation relationship between the robot base coordinate system and optical measurement space, transform the position and orientation of the end effector into the robot base coordinate system in order to control the end effector to the target position and orientation. This procedure is called the robot hand-eye coordination [28, 29].

The end effector of the robot is a puncture needle. Because the position of the puncture needle will be changed with the movement of the robot, the passive rigid body is installed at the one end of the end effector. The transformation relationship between the passive rigid body coordinate system and puncture needle coordinate system is fixed. The hand-eye coordination procedure means the relative position and posture between the puncture needle and passive rigid body, which would be calculated. Through the passive rigid body, the optical tracker can get the current and target position and orientation of the puncture needle in the optical measurement space. The different types of puncture needles will be used for different surgeries; we can study the relationship between one puncture needle and the passive rigid body

here. The key of hand-eye coordination is to get the ${}^R T_N$, which is the transformation matrix from the puncture needle coordinate system to robot coordinate system. The hand-eye coordination based on optical navigation is shown in Figure 3 and described below.

First, install a needle to the end of the robot. Control the needle tip to touch a point P on the calibration block, and we can obtain the corresponding transformation matrix ${}^O T_R$. Get the coordinates of $P_1(x_1, y_1, z_1)$ and $P_2(x_2, y_2, z_2)$ on the structure of the end effector by the passive probe, and the direction of $\overrightarrow{P_1 P_2}$ is parallel with the needle. Then, remove the puncture needle and obtain the coordinate $P(x, y, z)$ in the navigation coordinate system by the passive probe. Establish a needle tip coordinate system with the origin $P(x, y, z)$ and the direction $\overrightarrow{P_1 P_2}$; then, we can obtain ${}^O T_N$, which is the transformation matrix from the puncture needle coordinate system to optical coordinate system. The transformation matrix ${}^R T_N$ can be calculated by ${}^O T_R$ and ${}^O T_N$ as follows:

$${}^R T_N = ({}^O T_R)^{-1} ({}^O T_N). \quad (6)$$

The transformation relationship between the puncture needle coordinate system and robot coordinate system can be obtained. And the real-time transformation matrix ${}^O T_R$ can be obtained through the optical tracker and passive rigid body. So the relationship between the puncture needle and optical navigation coordinate system can be obtained,

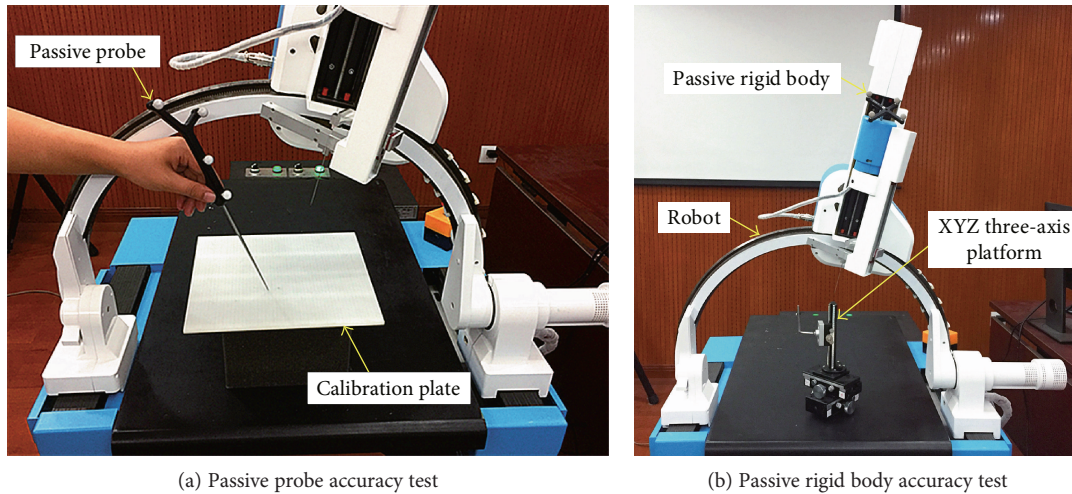


FIGURE 5: Optical measuring instrument accuracy test.

position and orientation information in the robot base coordinate system. $\Delta R_{BTarget}$ is deviation between the current position and orientation information of the current puncture point and the target position and orientation information in the robot base coordinate system. The deviation can be adjusted by a PID controller:

$$\begin{aligned} \Delta \bar{R}_{BTarget(k)} = & K_p [E_{(k)} - E_{(k-1)}] + K_I E_{(k)} \\ & + K_D [E_{(k)} - 2E_{(k-1)} + E_{(k-2)}], \end{aligned} \quad (10)$$

$$\bar{R}_{BTarget(k)} = \bar{R}_{BTarget(k-1)} + \Delta \bar{R}_{BTarget(k)},$$

where K_p is the proportional gain, K_I is the integral gain, K_D is the derivative gain, k is the sampling sequence and $k = 0, 1, 2, \dots, n$, and $E_{(k)}$ is the deviation between the target point and current position. $\Delta \bar{R}_{BTarget(k)}$ is the increment of deviation at the k sampling time. $\bar{R}_{BTarget(k)}$ is the output of the PID controller at the k sampling time. The optimal deviation is obtained by adjusting the gain parameters of the PID controller [30]. Thus, the joint angles can be calculated by inverse kinematics to control the robot to reach the target position.

4. Experiments and Results

4.1. System Model Tests

4.1.1. Optical Measuring Instrument Accuracy Test. Because the navigation system is based on optical measurement, the accuracy of the optical measuring instrument has a great influence on the performance of the navigation system. Therefore, the positioning accuracy of the optical measuring instrument has been tested as follows.

First, the positioning accuracy of the passive probe is tested, as shown in Figure 5(a). The calibration plate is used as a position-measuring device. There is a horizontal and vertical scale of 5 mm absolute spacing on the calibration plate. In the test, place the calibration plate in the measured position in any direction and angle. Any two points on the

calibration plate were selected as the test points of the passive probe. The two points are touched, respectively, by the passive probe perpendicular to the calibration plate, and the coordinates of the two points under the optical measuring device are obtained. The distance between the two points in the actual and optical measuring device is computed, respectively, and the difference of distance is the positioning error of the passive probe. Repeat the above procedure 20 times.

Then, the positioning accuracy of the passive rigid body is tested, as shown in Figure 5(b). In the test, the XYZ three-axis platform is used as a position-measuring device. The measurement accuracy of the XYZ three-axis platform is 0.1 mm. The passive rigid body is fixed at the end effector of the robot. The end effector is controlled to move a series of fixed distances, and its coordinates are recorded by the XYZ three-axis platform simultaneously. Repeat the above procedure 20 times.

In this section, the accuracy of the optical measuring instrument is verified by experiments. Experimental results show that the average positioning error of the passive probe is 0.09 mm. The average positioning error of the passive rigid body is 0.2 mm. The experimental errors of the optical measuring instrument are within the nominal error range of 0.25 mm, which can meet the needs of the surgical robot system.

4.1.2. Registration Accuracy Test. The surgical planning path can be converted to the robot puncture path through the registration between the 3D reconstructed image and patient. The registration accuracy has a great influence on the accuracy of the robot system, so it is necessary to verify the accuracy of the registration algorithm through experiment. The lesion area of puncture operation is usually in the skull base, but the registration marker points can be placed on the surface of the skull usually. Therefore, the registration can be achieved through eight marker points outside the skull, and the registration error can be verified by the other ten marker points. The eight registration marker points are located in the middle of eyebrows, anterior nasal spine, left orbit, right orbit, left infraorbital, right infraorbital, left external auditory

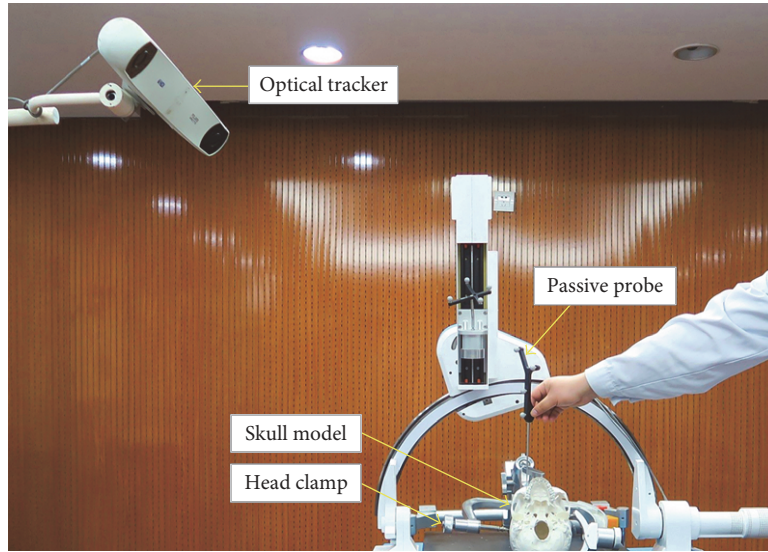


FIGURE 6: The registration accuracy test.

meatus, and right external auditory meatus. The ten registration verification marker points are located in the both sides of the subtemporal, foramen ovale, external carotid artery, jugular foramen, and styloid process.

As shown in Figure 6, the optical tracking system, which contains the optical tracker and passive probe, is used as a measurement tool in this experiment. The skull model marked with medical titanium screws (1.5 mm × 5 mm) is the experimental object. The head clamp is used for fixing the skull model. The Cone beam CT (CBCT) NewTom VG is used to obtain the patient's medical image. The graphic workstation is used for performing the 3D image reconstruction. The work flow of the registration accuracy experiment is shown as follows.

- (1) The medical titanium screws were drilled into the eight registration marker points and ten registration verification marker points of the skull model.
- (2) The medical image of the skull model was obtained by CBCT, and the image was imported into the graphic workstation for 3D image reconstruction.
- (3) Fix the skull model on the experimental platform with the head clamp, and put the navigation equipment in the right position.
- (4) The spatial coordinates of eight registration points were acquired by the passive probe.
- (5) In the 3D medical image, the coordinates of corresponding registration points are acquired in order. The conversion relationship between the 3D image coordinate space and the optical navigation coordinate space is obtained by performing the registration. And the conversion relationship can be represented by T .
- (6) The spatial coordinates of ten verification points on the skull model are obtained by using the

passive probe, and the coordinates were recorded as $A(A_x, A_y, A_z)$. In the 3D medical image, the coordinates of corresponding verification points are acquired in order and the coordinates were recorded as $B(B_x, B_y, B_z)$. The coordinates of points on the medical image are converted to the optical navigation coordinate system, and the coordinates can be recorded as follows:

$$C(C_x, C_y, C_z) = TB(B_x, B_y, B_z). \quad (11)$$

- (7) The Euclidean distance between the corresponding points A and C is analyzed and compared, and the Euclidean distance was recorded as $|AC|$. $|AC|$ is the registration error of the verification point and can be calculated as follows:

$$|AC| = \sqrt{(A_x - C_x)^2 + (A_y - C_y)^2 + (A_z - C_z)^2}. \quad (12)$$

- (8) Repeat the registration process six times, and record and analyze the registration error.

The experimental results are shown in Table 1. Mean represents the average error, and SD represents the standard deviation of errors. According to the experimental data, the average of the registration error of each target point in each group of experiments and the average of the registration error of the same target point in many groups of experiments are obtained, and they are all less than 0.75 mm. The corresponding standard deviations are small also. It can be seen that the registration algorithm can be applied to image registration between the 3D medical image and patient accurately and stably.

4.2. Positioning Accuracy Tests. In this section, two positioning accuracy tests have been implemented: (1) the positioning error of the open-loop robotic control and (2) the

TABLE 1: The results of the registration accuracy test.

The target point	The registration error (mm)						Mean \pm SD
	Group one	Group two	Group three	Group four	Group five	Group six	
Right subtemporal	0.70	0.67	0.63	0.66	0.65	0.45	0.63 \pm 0.08
Right foramen ovale	0.66	0.78	0.84	0.73	0.75	0.52	0.71 \pm 0.10
External orifice of the right carotid artery	0.42	0.62	0.50	0.55	0.63	0.72	0.57 \pm 0.10
Right jugular foramen	0.54	0.76	0.82	0.68	0.69	0.62	0.69 \pm 0.09
Right styloid process	0.35	0.93	0.41	0.72	0.77	0.55	0.62 \pm 0.20
Left subtemporal	0.51	0.86	0.73	0.35	0.59	0.77	0.64 \pm 0.17
Left foramen ovale	0.68	0.78	0.69	0.71	0.87	0.68	0.74 \pm 0.07
External orifice of the left carotid artery	0.72	0.79	0.71	0.62	0.65	0.38	0.65 \pm 0.13
Left jugular foramen	0.54	0.66	0.95	0.45	0.92	0.81	0.72 \pm 0.19
Left styloid process	0.72	0.57	0.63	0.54	0.59	0.92	0.66 \pm 0.13
Mean \pm SD	0.58 \pm 0.13	0.74 \pm 0.11	0.69 \pm 0.15	0.60 \pm 0.12	0.71 \pm 0.11	0.64 \pm 0.16	—

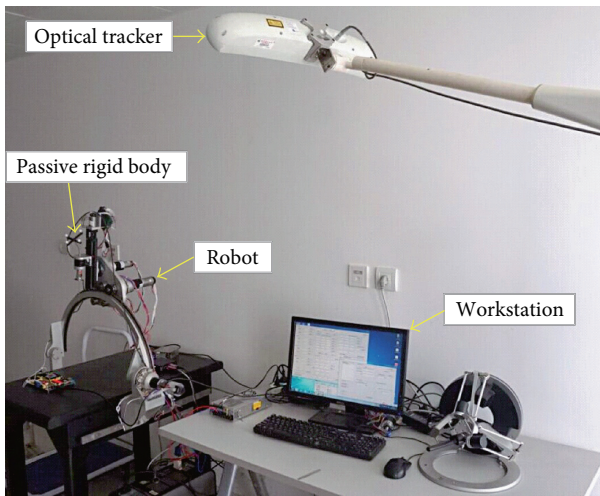


FIGURE 7: Measurement of positioning accuracy.

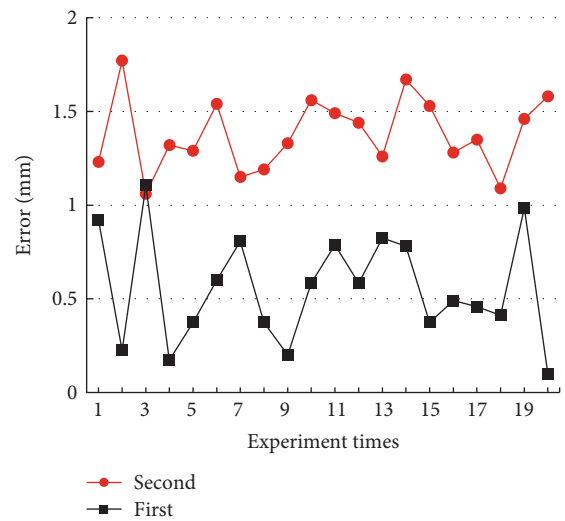


FIGURE 8: The results of the positioning accuracy test.

positioning error of the closed-loop robotic control. Test 1 can verify the work ability of the robot. By comparing tests 1 and 2, the feasibility of the proposed “kinematics + optics” hybrid motion control method can be proved.

In the first positioning accuracy test, the optical measuring instrument is used as a position-measuring device, as shown in Figure 7. Before testing, the passive rigid body is fixed at one end of the end effector and the optical tracker is placed in the corresponding position. The robot is controlled by the servo motion control system. The end effector is controlled to move a series of predetermined target positions, and its coordinates are recorded by the optical measuring instrument simultaneously. The positioning error of the robot can be calculated by the deviation between the given target point and the actual point of arrival of the end effector.

In the second positioning accuracy test, the test platform is the same as Section 4.1.1, as shown in Figure 5(b). In the test, the passive rigid body is fixed at the end effector of the robot. The optical tracker is placed in a representative

location to achieve the best positioning effect. The “kinematics + optics” hybrid motion control method is applied to the motion control of the robot. The end effector of the robot is controlled to move a series of predetermined target positions, and its coordinates are recorded by the XYZ three-axis platform simultaneously. Then, the positioning error of the robot based on the “kinematics + optics” hybrid motion control method can be obtained.

Repeat the above tests 20 times, respectively. The results of two positioning accuracy tests are shown in Figure 8. In test 1, the average positioning error E_1 is 1.38 mm and the maximum error is 1.77 mm. In test 2, the average positioning error E_2 is 0.56 mm and the maximum error is 1.10 mm. The result $E_1 > E_2$ shows that the motion control method presented in this paper can improve the average positioning accuracy at least 55%. Meanwhile, compared with test 1, the biggest experimental error is reduced from 1.77 to 1.10 mm, as shown in Figure 8. In general, 1.10 mm is smaller than the diameter of the lesion, so the risk of positioning deviation can be eliminated and the method is feasible.

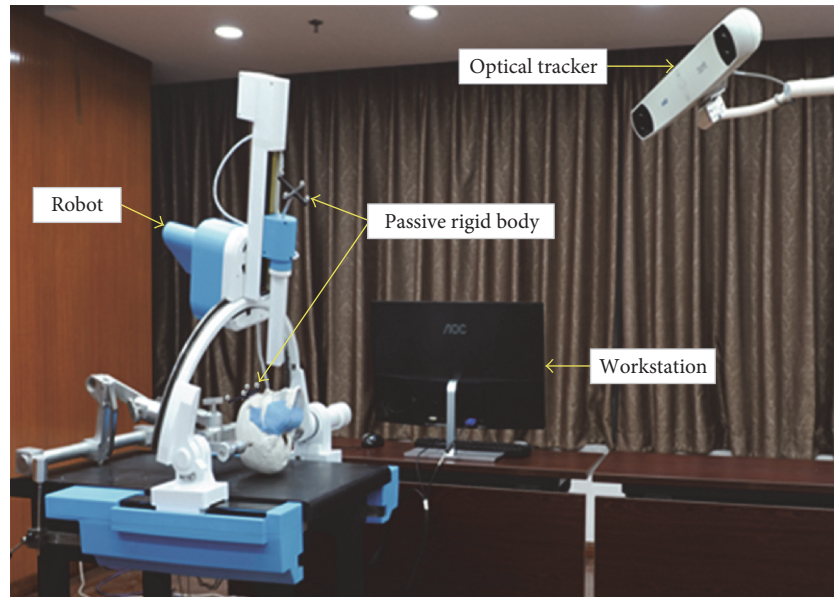


FIGURE 9: The skull model experimental platform.

4.3. Skull Model Experiment. The robot system based on optical navigation can assist surgeons to complete three kinds of surgeries, including biopsy of skull base lesions, radiofrequency thermocoagulation of the trigeminal ganglion, and radioactive particle implantation of skull base malignant tumors. In order to verify the universality and feasibility of the system model and control method based on optical navigation in the whole robot system, the skull model experiments are carried out on the three kinds of surgeries. And the skull model experiments are performed by the surgeon himself.

4.3.1. Model Experiment of Biopsy of the Skull Base Lesions. Biopsy is a common procedure in the medical field, which can effectively diagnose the lesion area. There are two major approaches for biopsy, needle biopsy and open excisional biopsy, and the needle biopsy is more attractive in surgery [31]. While in most cases the needle biopsy can be completed without difficulty, there are limitations to the accuracy obtainable using freehand techniques [32]. In order to improve the effect of needle biopsy, we use the robot system to assist surgeons to complete the needle biopsy, and the related experiment is as follows [33].

The devices and materials used in the experiment include the surgical robot, a skull model, the meatball, the Cone beam CT, the super light clay, the biopsy gun, the biopsy needle, and the medical titanium screws. And in the skull model experiment, the meatball is used as the lesion tissues. The experimental platform is shown in Figure 9. The work flow of the experiment is shown as follows.

- (1) The meatball with super light clay was fixed in the skull model as the lesion tissue. The titanium screws were fixed on the surface of the skull model as the registration marker points.

- (2) The medical image of the skull model was obtained by CBCT, and the image was imported into the graphic workstation for 3D image reconstruction.
- (3) Get the position of the meatball, and complete the surgical planning of biopsy in the 3D medical image.
- (4) Based on the optical tracker and passive probe, the registration between the robot body and the optical navigation system is completed. The end effector of the biopsy is mounted on the robot.
- (5) The skull model is fixed on the operation platform with the head clamp. The corresponding coordinates of the titanium screw marker points in the optical navigation coordinate system and the medical image coordinate system are obtained. Medical software is used to complete the registration between the medical image and optical navigation system.
- (6) According to the surgical planning, the coordinates of the puncture target and insertion point outside the skin were transferred to the robot coordinate system. The end of the robot is moved to the vicinity of the insertion point, and the automatic control model is used to realize the accurate positioning of the needle.
- (7) The robot performs the puncture operation automatically. When the robot reaches the target position, the system indicates that the puncture is over.
- (8) Press the button of the biopsy gun to complete biopsy. Remove the puncture biopsy needle from the end effector, and maintain the biopsy needle at the location where the puncture is completed. Control the end of the robot to return to its initial position.

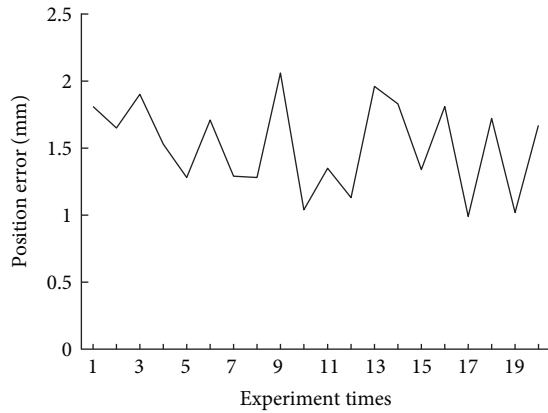


FIGURE 10: The results of 20 groups of biopsy experiment.

- (9) Scan the skull model with the puncture needle, and import the data into the medical software to reconstruct the 3D model again. The reconstructed 3D model was fused with the preoperative medical image to calculate the distance between the target point and the needle tip, and record the results.

According to the above procedure, 20 groups of biopsy experiment were performed the results are shown in Figure 10. The average puncture error of the system is 1.52 mm, and the standard deviation is 0.33 mm. In each group, the target tissue can be successfully obtained and the postoperative CT scan results are shown in Figure 11.

4.3.2. Model Experiment of Radiofrequency Thermocoagulation of the Trigeminal Ganglion. Radiofrequency thermocoagulation of the trigeminal ganglion is an effective method for the treatment of trigeminal neuralgia and is one of the common operations in cranio-maxillofacial surgery. The operation uses a puncture needle to puncture the position of the trigeminal ganglion and carries on radiofrequency thermocoagulation therapy to the target. The trigeminal ganglion is located inside the foramen ovale. During the puncture, the puncture needle must pass through a foramen ovale with a diameter of about 5 mm to reach the trigeminal ganglion [34]. Therefore, surgeons usually use the needle through the foramen ovale as a sign of successful operation.

The operation procedure of the trigeminal thermocoagulation experiment is exactly the same as that of the biopsy experiment, but the end effector is different. The procedure of operation of the trigeminal thermocoagulation can be referred to the biopsy. In the model experiment, 10 groups of trigeminal thermocoagulation experiment were performed; the experimental results are shown in Figure 12. The average puncture error of the model experiment is 1.62 mm, the standard deviation is 0.26 mm, and the puncture needle can pass through the oval hole every time. The experimental results show that the success rate of the robotic system in the model experiment of radiofrequency thermocoagulation of the trigeminal ganglion is 100%.

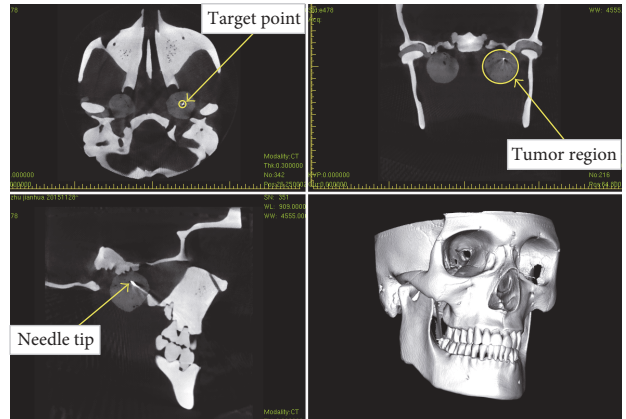


FIGURE 11: Postoperative CT scan results.

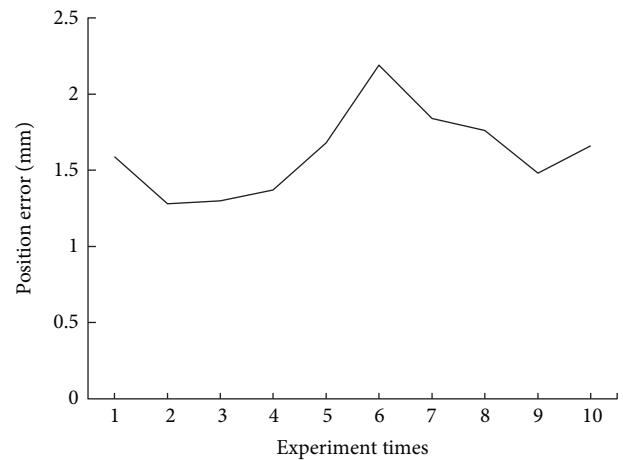


FIGURE 12: The puncture error of model experiment.

4.3.3. Model Experiment of Radioactive Particle Implantation. Radioactive particle implantation experiment of skull base malignant tumor was also performed according to the actual operation [35]. First, the tumor is segmented from the medical image, and then, the particle implantation path is automatically generated on the tumor. Surgeons can adjust the particle implantation path according to experience. The robot can carry out the implantation of radioactive particles according to path planning. In the model experiment, the meatball is also used as the tumor tissues. The radioactive particles are replaced by the steel wires of 5 mm in length, and the size of steel wires are the same as the size of radioactive particles. The particles were implanted with an automatic particle gun, and the rationality of particle implantation was verified. In addition to the basic position error, the TPS system is used to verify the rationality of particle implantation through the deviation of the radioactive dose topographic map. Due to the limited size of the meatball, three paths were designed in the model experiment and each path was implanted with 5 particles.

The devices and materials used in the experiment include the surgical robot system, the automatic particle implantation device, the steel particles, the meatball, the CBCT, the



FIGURE 13: The radioactive particle implantation experiment.

super light clay, the titanium screws, and the skull model. The work flow of the experiment is shown as follows.

- (1) Load the particles into the automatic particle implantation gun.
- (2) The meatball with super light clay was fixed in the skull model as the tumor tissues. The titanium screws were fixed on the surface of the skull model as the registration marker points.
- (3) The 3D reconstructed image of the skull model was obtained by CBCT and the graphic workstation. Find out the tumor from the 3D reconstructed image, and automatically generate the particle implantation path. Surgeons can adjust the particle implantation path according to experience.
- (4) The optical navigation system is used to complete the spatial registration of the 3D reconstructed image space, the robot space, the optical navigation space, and the patient space.
- (5) The robot was automatically controlled to reach the puncture point of the first path and complete the puncture. According to the number and spacing of particle implantation on the first path, the robot system implants particles sequentially. After the robot completes the particle implantation, it automatically returns to the insertion point, as shown in Figure 13.
- (6) Similarly, refer to the above steps to complete the implantation of particles in the other two paths.
- (7) After completion of the particle implantation, the skull model was scanned by CBCT and analyzed.

In the model experiment, 10 groups of particle implantation were performed. The average error of particle implantation is 1.51 mm, and the standard deviation is 0.50 mm. The effect of particle implantation is usually

analyzed by the TPS system. Assuming that the implanted particles are radioactive particles, the corresponding verification results of the TPS system are shown in Figure 14. The results of TPS system analysis show that the radiation dose map deviation is less than 1%, which means that particle implantation is reasonable.

5. Conclusions and Discussions

This paper presents a novel cranio-maxillofacial puncture robot system through the analysis of surgical requirements, and the system can assist surgeons to complete biopsy of skull base lesions, radiofrequency thermocoagulation of the trigeminal ganglion, and radioactive particle implantation of the maxillofacial tumor. The surgical robot system is divided into four parts, including the 3D reconstructed image subsystem, robotic subsystem, optical measurement subsystem, and patient subsystem. The spatial registration based on quaternion and the iterative closest point registration algorithm is realized to obtain the transformation relationship between four subsystems. The hand-eye coordination model is established to control the end effector of the robot moving to the target position according to preoperative planning. The “kinematics + optics” hybrid motion control method is presented to improve the positioning accuracy of the robot end effector. The accuracy of the system model was measured through the model tests. And the feasibility of the “kinematics + optics” hybrid motion control method was verified by comparing the positioning accuracy before and after the application of the method. Finally, the skull model experiments were carried out to evaluate the function of the whole robot system. The experimental results show that the feasibility and effectiveness of the robot system based on optical navigation can meet the needs of cranio-maxillofacial surgery.

During the puncture process, imaging data can provide precise navigation for precise needle placement. Along with CT fluoroscopy [17–19], intraoperative ultrasound [20], and MRI [21], optical navigation is also now an important tracking system for real-time guidance. Real-time vision feedback can verify the needle’s advancement along the planned path without intraoperative X-ray exposure to the patient. Accuracy depends on the uninterrupted update of position data acquired by optical tracking, which provides accurate vision feedback and closed-loop control. And the navigation system can track the two passive rigid bodies fixed on the robot and patient’s head, respectively, in real time. Then, the robot and head can be tracked and compensated in real time to ensure the accuracy of puncture. However, infrared signals can only be transmitted in straight lines, so the optical measuring instrument should have good visibility when used.

The accuracy requirement for cranio-maxillofacial puncture is determined by the characteristics of lesions in different surgeries. However, there is no generally agreed value currently. According to the surgeon’s clinical experience and related literature [36, 37], select 3 mm as the accuracy limit. And this is also the minimum safety distance to protect the carotid artery for this robot system in the preoperative planning. In each of the above three surgical skull model

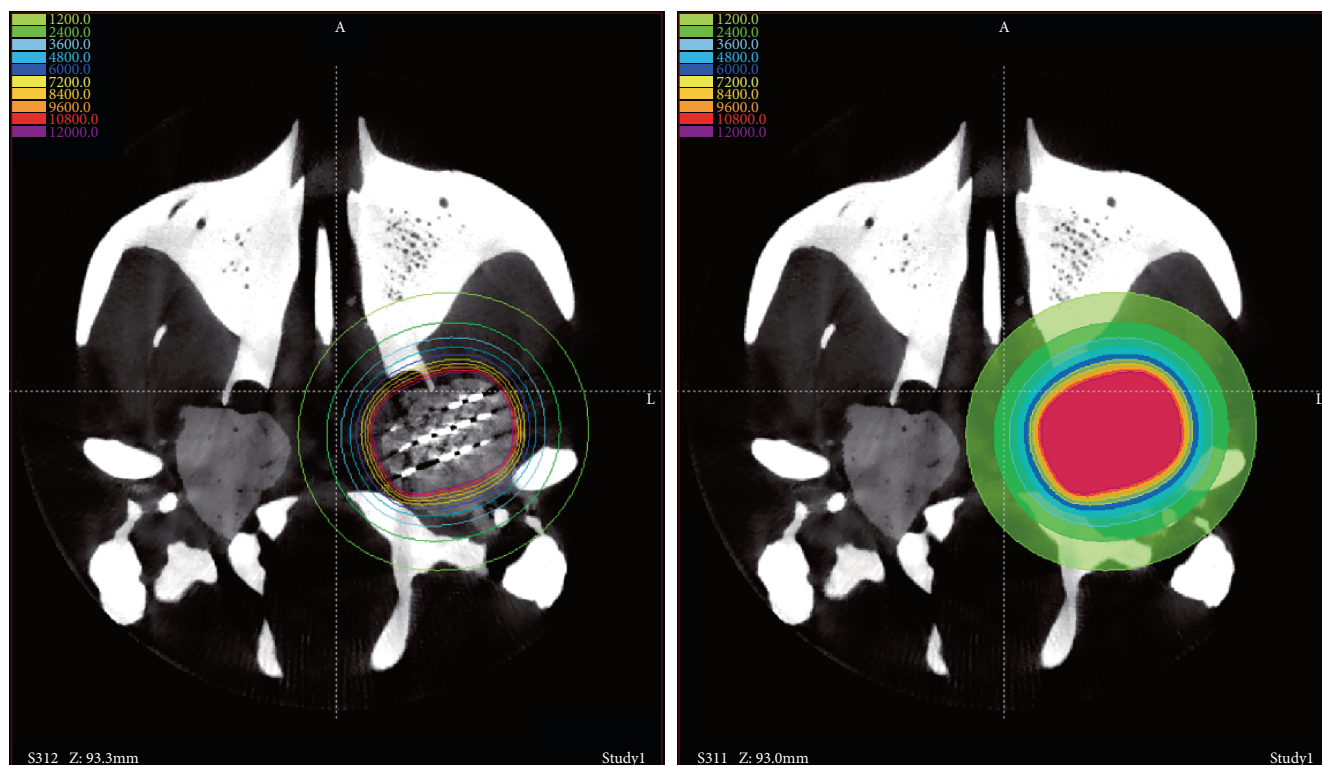


FIGURE 14: The radioactive dose topographic map.

experiments, the average puncture error of the robot system is less than 3 mm. Using the proposed navigation system and the control method in this paper, we consider our result to be meeting the accuracy requirement. The results of three skull model experiments are similar, indicating that the system has good consistency.

Although the results of this paper has showed the feasibility of the robot system based on the navigation system, there are still a number of shortcomings and designs needed to be overcome, improved, and optimized. The method of fixing titanium screws on the patient for registration is invasive, and the noninvasive methods should be proposed. In the optical tracking system, the end effectors of the robot cannot be displayed in the surgical design system in real time, which is adverse to carry out the real-time navigation of the robot for surgeons. More experiments will be done in animal models and humans to detect and evaluate the feasibility of the robot system. The safety of the robot system should be improved and optimized. More flexible robot wrist and more easy-to-use end effectors need to be designed according to clinical requirements.

Conflicts of Interest

The authors declare that there is no conflict of interest regarding the publication of this article.

Acknowledgments

This work is supported by the National Natural Science Foundation of China (Grant nos. U1613221 and 61673064).

References

- [1] R. Olszewski, "Surgical engineering in cranio-maxillofacial surgery: a literature review," *Journal of Healthcare Engineering*, vol. 3, no. 1, pp. 53–86, 2012.
- [2] X. Chen, Y. Lin, C. Wang, G. Shen, S. Zhang, and X. Wang, "A surgical navigation system for oral and maxillofacial surgery and its application in the treatment of old zygomatic fractures," *The International Journal of Medical Robotics and Computer Assisted Surgery*, vol. 7, no. 1, pp. 42–50, 2011.
- [3] S. Zachow, H. C. Hege, and P. Deuffhard, "Computer assisted planning in cranio-maxillofacial surgery," *Journal of Computing and Information Technology*, vol. 14, no. 1no. 1, pp. 53–64, 2006.
- [4] S. Hassfeld and J. Mühling, "Computer assisted oral and maxillofacial surgery – a review and an assessment of technology," *International Journal of Oral & Maxillofacial Surgery*, vol. 30, no. 1, pp. 2–13, 2001.
- [5] A. Baumann, K. Schicho, C. Klug, A. Wagner, and R. Ewers, "Computer-assisted navigational surgery in oral and maxillofacial surgery," *Atlas of the Oral & Maxillofacial Surgery Clinics*, vol. 13, no. 1, pp. 41–49, 2005.
- [6] M. Peterhans, A. vom Berg, B. Dagon et al., "A navigation system for open liver surgery: design, workflow and first clinical applications," *The International Journal of Medical Robotics and Computer Assisted Surgery*, vol. 7, no. 1, pp. 7–16, 2011.
- [7] V. Horsley and R. H. Clarke, "The structure and functions of the cerebellum examined by a new method," *Brain*, vol. 31, no. 1, pp. 45–124, 1908.
- [8] H. Kawachi, Y. Kawachi, C. Ikeda, R. Takagi, A. Katakura, and T. Shibahara, "Oral and maxillofacial surgery with computer-

- assisted navigation system," *The Bulletin of Tokyo Dental College*, vol. 51, no. 1, pp. 35–39, 2010.
- [9] C. B. Guo and Y. X. Guo, "Navigation guided needle biopsy for tumors in the skull base," *Chinese Journal of Practical Stomatology*, vol. 7, no. 6, pp. 321–324, 2014.
- [10] C. Westendorff, D. Gülicher, F. Dammann, S. Reinert, and J. Hoffmann, "Computer-assisted surgical treatment of orbitozygomatic fractures," *Journal of Craniofacial Surgery*, vol. 17, no. 5, pp. 837–842, 2006.
- [11] X. G. Zhao, T. W. Yang, J. D. Han, and W. L. Xu, "A review on the robot-assisted needle puncture technology," *Chinese Science Bulletin*, vol. 58, no. S2, pp. 20–27, 2013.
- [12] A. Garg, R. C. Dwivedi, S. Sayed et al., "Robotic surgery in head and neck cancer: a review," *Oral Oncology*, vol. 46, no. 8, pp. 571–576, 2010.
- [13] K. T. Kavanagh, "Applications of image-directed robotics in otolaryngologic surgery," *Laryngoscope*, vol. 104, no. 3, pp. 283–293, 1994.
- [14] T. C. Lueth, A. Hein, J. Albrecht et al., "A surgical robot system for maxillofacial surgery," *IECON '98. Proceedings of the 24th Annual Conference of the IEEE Industrial Electronics Society (Cat. No.98CH36200)*, 1998, pp. 2470–2475, Aachen, Germany: IEEE, 1998.
- [15] R. J. Bale, I. Laimer, A. Martin et al., "Frameless stereotactic cannulation of the foramen ovale for ablative treatment of trigeminal neuralgia," *Operative Neurosurgery*, vol. 59, no. 4, Supplement 2, pp. ONS-394-ONS-402, 2006.
- [16] J. D. Ceulaer, C. D. Clercq, and G. R. J. Swennen, "Robotic surgery in oral and maxillofacial, craniofacial and head and neck surgery: a systematic review of the literature," *International Journal of Oral & Maxillofacial Surgery*, vol. 41, no. 11, pp. 1311–1324, 2012.
- [17] B. Schulz, K. Eichler, P. Siebenhandl et al., "Accuracy and speed of robotic assisted needle interventions using a modern cone beam computed tomography intervention suite: a phantom study," *European Radiology*, vol. 23, no. 1, pp. 198–204, 2013.
- [18] D. Stoianovici, K. Cleary, A. Patriciu et al., "AcuBot: a robot for radiological interventions," *IEEE Transactions on Robotics and Automation*, vol. 19, no. 5, pp. 927–930, 2003.
- [19] S. B. Solomon, A. Patriciu, M. E. Bohlman, L. R. Kavoussi, and D. Stoianovici, "Robotically driven interventions: a method of using CT fluoroscopy without radiation exposure to the physician," *Radiology*, vol. 225, no. 1, pp. 277–282, 2002.
- [20] J. Hong, T. Dohi, M. Hashizume, K. Konishi, and N. Hata, "An ultrasound-driven needle-insertion robot for percutaneous cholecystostomy," *Physics in Medicine & Biology*, vol. 49, no. 3, pp. 441–455, 2004.
- [21] N. Hungr, C. Fouard, A. Robert, I. Bricault, and P. Cinquin, "Interventional radiology robot for CT and MRI guided percutaneous interventions," *Medical Image Computing and Computer-Assisted Intervention*, vol. 14, no. 1, pp. 137–144, 2011.
- [22] X. Z. Kong, X. G. Duan, and Y. G. Wang, "An integrated system for planning, navigation and robotic assistance for mandible reconstruction surgery," *Intelligent Service Robotics*, vol. 9, no. 2, pp. 113–121, 2016.
- [23] G. Liu, X. Yu, C. Li, G. Li, X. Zhang, and L. Li, "Space calibration of the cranial and maxillofacial robotic system in surgery," *Computer Assisted Surgery*, vol. 21, Supplement 1, pp. 55–61, 2016.
- [24] X. Kong, X. Duan, Y. Wang et al., "Navigation method for mandible reconstruction surgery robot," in *2013 IEEE International Conference on Robotics and Biomimetics (ROBIO)*, pp. 250–255, Shenzhen, China: IEEE, December 2013.
- [25] H. Tian, P. Yang, C. Su, and Z. Dong, "ICP registration technology based on the coordinate system direction fit," *International Journal of Security and its Applications*, vol. 9, no. 12, pp. 47–56, 2015.
- [26] H. Tian, D. Wu, J. Wang, Z. Du, and L. Sun, "Visualization and real-time tracking technologies of the probe used in surgical navigation based on electromagnetic positioning," *Robot*, vol. 33, no. 1, pp. 59–65, 2011.
- [27] Y. G. Wang and X. G. Duan, "Spatial registration for a three-arm robot assisted mandible reconstruction surgery," *Mathematical Problems in Engineering*, vol. 2015, pp. 1–10, 2015.
- [28] Y. Zhang, L. Li, Y. Zhou, T. Su, J.-T. Ma, and X.-M. Hu, "Multi-sensor augmented reality tracking based on robot hand-eye calibration," in *Affective Computing and Intelligent Interaction. Advances in Intelligent and Soft Computing*, vol. 137, Springer, Berlin, Heidelberg.
- [29] K. H. Strobl and G. Hirzinger, "Optimal hand-eye calibration," in *2006 IEEE/RSJ International Conference on Intelligent Robots and Systems*, pp. 4647–4653, Beijing, China, October 2006.
- [30] F. Liu and H. Chen, "Motion control of intelligent underwater robot based on CMAC-PID," in *2008 International Conference on Information and Automation*, pp. 1308–1311, Changsha, China, June 2008.
- [31] V. G. Mallapragada, N. Sarkar, and T. K. Podder, "Robot-assisted real-time tumor manipulation for breast biopsy," *IEEE Transactions on Robotics*, vol. 25, no. 2, pp. 316–324, 2009.
- [32] K. R. Cleary, "CT-directed robotic biopsy testbed: motivation and concept," *Proceedings of SPIE*, vol. 4319, pp. 231–236, 2001.
- [33] S. E. Connor and N. Chaudhary, "CT-guided percutaneous core biopsy of deep face and skull-base lesions," *Clinical Radiology*, vol. 63, no. 9, pp. 986–994, 2008.
- [34] D. R. Emril and K. Y. Ho, "Treatment of trigeminal neuralgia: role of radiofrequency ablation," *Journal of Pain Research*, vol. 3, pp. 249–254, 2010.
- [35] J. G. Zhang, J. Zhang, T. L. Song, Z. G. Cai, W. J. Sheng, and G. Y. Yu, "Radioactive seed implantation in treatment of oral and maxillofacial malignancy," *Zhonghua kou Qiang yi xue za zhi = Zhonghua Kouqiang Yixue Zazhi = Chinese Journal of Stomatology*, vol. 41, no. 8, pp. 464–466, 2006.
- [36] R. Seifabadi, N. B. Cho, S. E. Song et al., "Accuracy study of a robotic system for MRI-guided prostate needle placement," *The International Journal of Medical Robotics and Computer Assisted Surgery*, vol. 9, no. 3, pp. 305–316, 2013.
- [37] M. Li, G. Li, B. Gonenc, X. Duan, and I. Iordachita, "Towards human-controlled, real-time shape sensing based flexible needle steering for MRI-guided percutaneous therapies," *The International Journal of Medical Robotics and Computer Assisted Surgery*, vol. 13, no. 2, pp. 1–14, 2017.

Research Article

Efficient Active Sensing with Categorized Further Explorations for a Home Behavior-Monitoring Robot

Wenwei Yu,¹ Keigo Nakahata,² Guang Hao Sun,³ Akio Namiki,² Sayuri Suwa,⁴ Mayuko Tsujimura,⁴ Le Xie,⁵ Jinwu Wang,⁵ and Shao Ying Huang⁶

¹Center for Frontier Medical Engineering, Chiba University, Chiba, Japan

²Graduate School of Engineering, Chiba University, Chiba, Japan

³Graduate School of Informatics and Engineering, The University of Electro-Communications, Chofu, Japan

⁴Graduate School of Nursing, Chiba University, Chiba, Japan

⁵Research Institute of Med-X, Shanghai Jiao Tong University, Shanghai, China

⁶Engineering Product Development, Singapore University of Technology and Design, Singapore

Correspondence should be addressed to Wenwei Yu; yuwill@faculty.chiba-u.jp

Received 16 May 2017; Revised 15 August 2017; Accepted 24 September 2017; Published 28 November 2017

Academic Editor: Yi-Hung Liu

Copyright © 2017 Wenwei Yu et al. This is an open access article distributed under the Creative Commons Attribution License, which permits unrestricted use, distribution, and reproduction in any medium, provided the original work is properly cited.

Mobile robotics is a potential solution to home behavior monitoring for the elderly. For a mobile robot in the real world, there are several types of uncertainties for its perceptions, such as the ambiguity between a target object and the surrounding objects and occlusions by furniture. The problem could be more serious for a home behavior-monitoring system, which aims to accurately recognize the activity of a target person, in spite of these uncertainties. It detects irregularities and categorizes situations requiring further explorations, which strategically maximize the information needed for activity recognition while minimizing the costs. Two schemes of active sensing, based on two irregularity detections, namely, heuristic-based and template-matching-based irregularity detections, were implemented and examined for body contour-based activity recognition. Their time cost and accuracy in activity recognition were evaluated through experiments in both a controlled scenario and a home living scenario. Experiment results showed that the categorized further explorations guided the robot system to sense the target person actively. As a result, with the proposed approach, the robot system has achieved higher accuracy of activity recognition.

1. Introduction

Increasing population age turns to be a significantly serious problem in the world [1, 2]. As the population of the single-living elderly (SLE) is increasing rapidly, the demand for behavior monitoring of SLE at home is rising. This is due to the necessity to secure their safety, to know the rhythm and quality of their ADL (activity of daily living), and to make effective care plans.

In the literature, two main approaches have been reported on elderly behavior monitoring at home: wearable systems and smart houses [3]. Wearable systems may cause user discomfort which leads to discontinuous monitoring [4]. Smart houses usually require a large number of sensors

which increases the cost and the operational complexity. Even more, blind spots and dead angle due to the furniture layout may interrupt the monitoring, which threatens the safety of the person under monitoring. Recent studies have shown that robots can be an important tool for facilitating part of ADL, exercise, and rehabilitation in a home environment through interactions with the elderly [5–8].

Our studies showed that mobile robotics is a potential solution to home behavior monitoring for the elderly [9–11]. A replacement of smart house with a mobile robot reduces the number of sensors which in turn reduces the cost of implementation and the deployment complexity. Moreover and importantly, it provides seamless temporal and spatial monitoring for safe home daily living if the robot is well

controlled. It was reported in [9–11] that a mobile robot was capable of tracking a target subject and performing tasks such as observations and analyses of the environment and recognition and analyses of the behaviors of the subject, by using the location information and the extracted body contour features of the subject. The system showed an excellent performance: 98.6–99.4% as an overall correct rate of human activity recognition in testing datasets. However, the test data sets were collected in a static scenario where the activities were carried out sequentially at one place and repeated during a certain period of time.

In a real home environment, there are various types of uncertainties, such as the ambiguity between the subject under monitoring and the surrounding objects, the occlusion by furniture, difficulties in localization and movement control due to uneven floor, and frequent partial furniture layout alternations. In this study, we focused on the ambiguity between the subject under monitoring and the surrounding objects, which is a major obstacle for home behavior recognition. Active sensing is the ability to infer information under an uncertain environment by spontaneous sensing activity [12]. There are mainly two categories. The first category is the use of self-generated signals to probe the environment, such as echolocation chirps in bats. The other one uses a self-motion, such as a move to find out an object hidden in the shadows [12]. The active sensing mechanism in this study was inspired by the latter. There are various strategies for active sensing for a robot in terms of maximizing the information gain and minimizing the cost simultaneously [13–16]. In this work, we propose a strategy of active sensing that suits the aforementioned home monitoring scenario, which identifies the situation and conducts a categorization of the situations before further explorations. It is named active sensing with categorized further explorations. For identifying different situations in an uncertain scenario, the heuristic-based and the template-matching-based irregularity detections were implemented and compared. Their time cost and accuracy in activity recognition were evaluated in different uncertain situations.

This paper is organized as follows. Section 2 describes the active sensing framework briefly and the proposed strategy. Section 3 details the experiments to test the different irregularity detections for the categorization for the proposed approach. In Section 4, experimental results are presented, which is followed by discussions. Concluding remarks are stated in Section 5.

2. Methods

In this section, we present the details of the proposed active sensing with categorized further exploration for a mobile robot for home behavior monitoring, including the framework and the categorization. For the categorization, the heuristic-based and the template-matching-based methods are examined and compared in terms of time cost and recognition accuracy.

2.1. The Mobile Behavior-Monitoring Robot. The autonomous mobile behavior-monitoring robot performs the

subject tracking and activity recognition. As shown in Figure 1(a), the hardware of the robot is assembled base on Pioneer P3-DX. It includes a laser range finder (LRF) and a Kinect sensor on a rotating platform. The LRF provides data about the obstacles in the environment, and it is used to determine the location of the robot and to avoid obstacles. The Kinect sensor is used to detect and track the subject. This sensor is mounted on a rotating platform. In the robot, an algorithm is applied to integrate Kinect and Lidar (light detection and ranging) sensor data. It is for detecting and tracking novelties using the environment map of the robot as a top-down approach without the necessity of large amount of training data. Using geometric features calculated from human body contour extracted from depth images, the system can identify six different activities: standing, walking, bending, sitting, lying down, and falling [9–11].

2.2. A Framework of Active Sensing for Home Monitoring Mobile Robots. Active sensing is the ability to infer information under an uncertain environment by spontaneous sensing activities [12–17]. There are two types of active sensing, one uses self-generated signals to probe the environment, such as echolocation chirps in bats [16], and the other uses a self-motion, such as a move to find out an object hidden in the shadows [12]. The active sensing mechanism implemented in the mobile behavior-monitoring robot is inspired by the second type.

In the literature, the active sensing has been studied as a theoretic framework for understanding biological sensing mechanism [15–17]. One control framework for active sensing by the human sight is Context-Dependent Active Controller (C-DAC). C-DAC assumes that the observer aims to optimize a context-sensitive objective function that takes into account behavioral costs such as temporal delay, response error, and the cost of switching from one sensing location to another [17]. This framework allows us to derive behaviorally optimal procedures for making decisions about where to acquire sensory inputs, when to move from one observation location to another, and how to negotiate the exploration-exploitation tradeoff between collecting additional data versus terminating the observation process [17].

The implementation to the mobile robotics focused on the efficient information collection, or exploration of unknown areas [12, 13], and the locations of a team of mobile robots for efficient informative measurement [14]. In the case of home behavior monitoring, the routine tasks for the mobile robot are target person following, visual tracking, and behavior recognition. Especially, the former two tasks need reactive planning for ensuring the safety of the target person, not to obstruct the path of the target person, while not losing him/her from its visual field. Thus, it is important to identify the situations that require further explorations and determine how important it is to deal with the situation. Our categorizing and further exploration strategy for active sensing fits well to the application for high detection accuracy and time cost minimization simultaneously.

For a home monitoring robot, in the case that a subject sits down close to an object, there is ambiguity between the

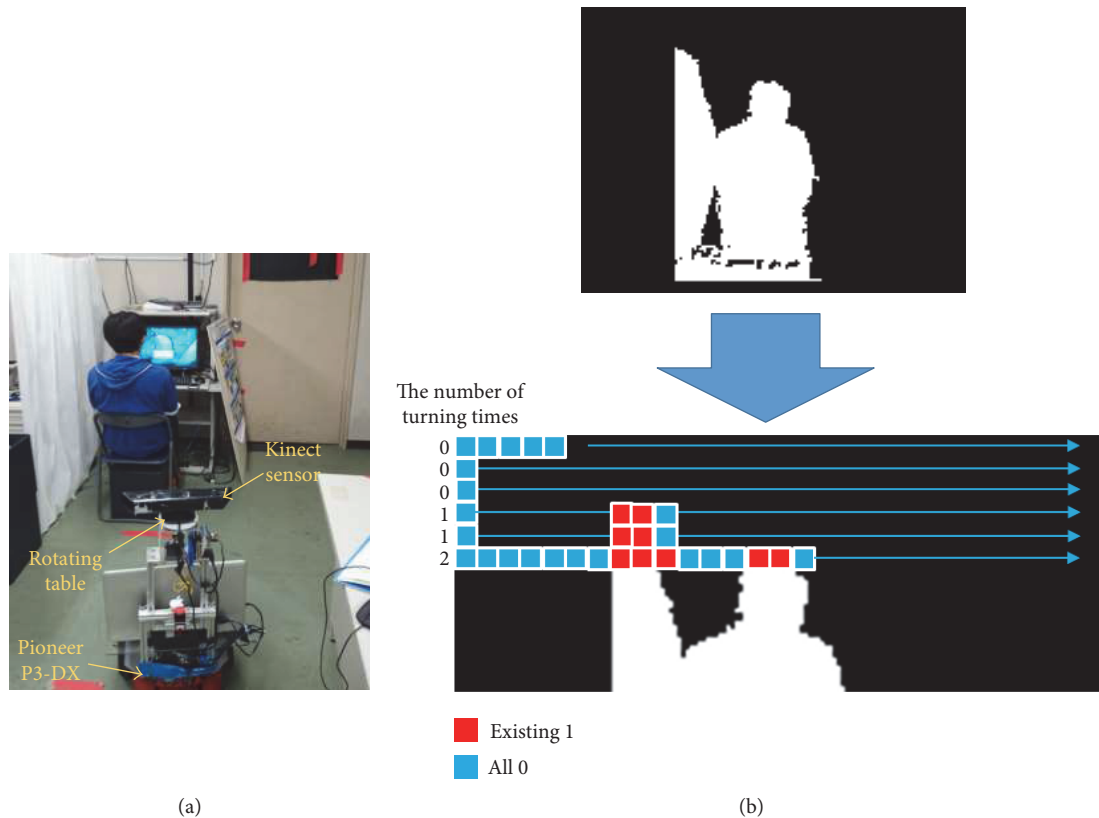


FIGURE 1: How to judge the irregularity of a feature extraction. (a) The scenario where there is an ambiguity between the target subject and the surrounding object. (b) A binary image in the human body contour region used for activity recognition.

targeted subject and the surrounding object. In the algorithm, the subject and the object are at the same depth (Figure 1(a)) where the human body contour extraction fails and part of the object is included in the subject contour. Therefore, active sensing is necessary to deal with such cases. In order to implement both the situation categorization and active sensing, three algorithms were performed in a row: (1) categorization by detecting irregularity of feature extractions, (2) further explorations by adjusting sensing parameters of the robot accordingly, and (3) avoiding excessive parameter adjustment based on a short-term memory mechanism so that the behavioral cost (the time of changing the parameter) was minimized. In the proposed approach, the first step is to identify when this situation is occurring. In this paper, both heuristic-based and template-matching-based active sensing schemes are applied for irregularity detections. They are examined and compared through experiments.

2.3. Active Sensing with Irregularity Detections. In the proposed framework, active sensing with categorized further explorations, irregularity detection is a key step for categorization of the situation and further explorations. Irregularity detections (also known as anomaly detection) which is to identify different situations in an uncertain scenario for home monitoring for the elderly are conducted using active sensing. Two types of irregularity detections were implemented and compared. One is heuristic-based

irregularity detection and the other is template-matching-based irregularity detection. The heuristic-based active sensing (H-AS) is a method specifically designed for the targeted application. The template-matching-based active sensing (TM-AS) is a clustering-based irregularity detection which is one of the machine learning-based approaches.

2.3.1. Heuristic-Based Active Sensing (H-AS). H-AS is specifically designed to detect the situation where the subject under monitoring is indistinguishable with the surrounding (e.g., a wall or a curtain) for home monitoring, which is the irregularity for detection.

Figure 1(a) shows the scenario when the robot is facing towards the subject under monitoring. The robot acquires images of the subject. The image acquired is scanned in blocks of 5×5 pixels with an aim of detecting more than one block per line where the pixels take a value of zero. When the image has one or none of this blocks per line, it is considered as a suitable image for the body contour extraction and there is no need for the robot to conduct active sensing at that location.

The human body contour region which is used for activity recognition is expressed in a binary image as shown in Figure 1(b). In the situation illustrated on the line at the bottom in the binary image in Figure 1(b), the human body contour becomes indistinguishable with part of the wall located at the left side of the subject. In this scenario, a correct feature extraction is not possible and the robot fails in activity

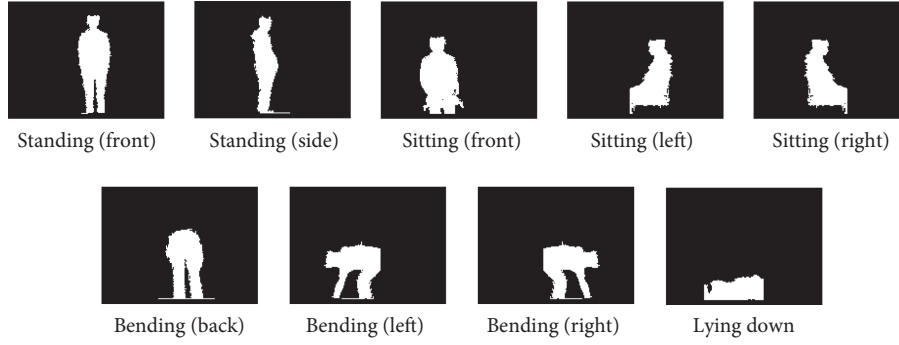


FIGURE 2: Images as templates for different activities.

recognition. This is considered as an irregularity. Further explorations are needed at this location.

Once an irregular situation is identified, a straightforward next step is to move the robot to a new location, where it will have a different viewpoint of the scene. In this study, in order to optimize the active sensing operation time, instead of moving the robot to a different location, rotational movements by rotating the rotating platform (refer to Figure 1(a)) are implemented. The rotation is done in both directions until it can identify a regular situation in the body extraction process [18].

2.3.2. Template-Matching-Based Active Sensing (TM-AS). The final technical goal of this study is to enable the robot to recognize robustly a number of behaviors aforementioned (standing, walking, bending, sitting, lying down, and falling). TM-AS is applied. For these behaviors, when the standard patterns of all the behaviors can be collected and a regular pattern space can be expanded, then this space can be used to check an arbitrary pattern to see whether it is regular or irregular. TM-AS is a clustering-based anomaly detection where machine learning is applied. Certainly, the discriminability depends on the patterns collected, features of the patterns, and discriminability indexes employed. These factors were investigated through experiments. The study will be reported in the following sessions. Note that, though the method is implemented for a specific depth sensing, the proposed idea can be applied to the other sensing modals in general.

(1) Template Preparation. Since, confusing with the environment is less possible to occur for the behaviors of walking and falling down, in this study, the templates would be at first setup for the other four behaviors (standing, sitting, lying down, and bending) which are more possible to occur near the objects (such as wall, furniture, and curtain) in the living environment.

Standard depth images were recorded for each behavior as follows: (1) the depth images were collected 1.3m away from the targeted person. (2) The numbers of templates for each different behavior were set as 2 for standing, 3 for sitting, 3 for bending, and 1 for lying down. If the patterns taken from the left and those from the right are different sufficiently, they were treated as different templates. Figure 2 shows the template patterns.

(2) Feature Selection and Similarity Indexes. Since it is easier to extract contour of depth images, three contour-related parameters were considered. They are the distance between the center of weight to the contour point ($D(i)$), and the angle of normal vector ($A_{nv}(i)$) as shown in (1), (2), and (3), respectively.

$$D(i) = \sqrt{(x_i - x_c)^2 + (y_i - y_c)^2}, \quad (1)$$

where (x_c, y_c) denotes the coordinate of the center of weight, and (x_i, y_i) denotes the i th contour point.

$$A_{tl}(i) = \tan^{-1} \left(\frac{y_{i+P} - y_{i-P}}{x_{i+P} - x_{i-P}} \right), \quad (2)$$

$$A_{nv}(i) = A_{tl}(i) - \left(\frac{\pi}{2} \right), \quad (3)$$

where the subscript tl stands for tangential line of the contour points, and nv stands for the normal vector. The accumulated difference (AD) between a template image and the one under test is expressed as

$$\begin{aligned} AD_D &= \sum_{i=1-n}^n |D_{I1}(i) - D_{I2}(i)|, \\ AD_{Anv} &= \sum_{i=1-n}^n |A_{nv_I1}(i) - A_{nv_I2}(i)|, \end{aligned} \quad (4)$$

where AD_d^{upper} and AD_d^{lower} are the accumulated difference of distance of contour points for the upper and the lower body, respectively. Points that have a difference with the top pixel along the longitudinal direction smaller than a threshold are defined as upper body contour points and the others are the lower body ones. AD_{Anv} is the accumulated difference of angle in radian of the unit principal normal vector.

The upper body feature, AD_d^{upper} , can make a difference between the class of standing and sitting and the other class including bending and lying down. The lower body feature, AD_d^{lower} , can tell the difference among the four activities. On the other hand, the angle of unit normal vector (AD_{Anv}) might be sensitive to local changes. Both of the accumulated difference in distance and angle of unit normal vector will be affected by occlusion and cluttering. In this study, either the accumulated difference in distance or angle is determined as the similarity index for template matching, by a score calculated from the

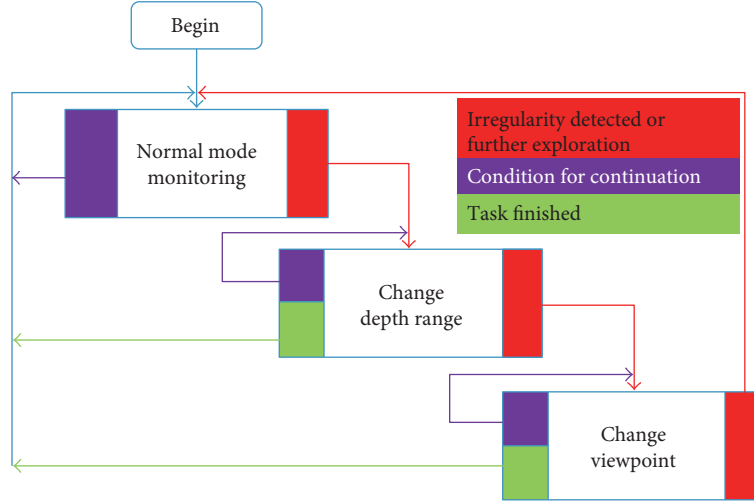


FIGURE 3: The configuration of the robot and the subject under test in experiment 1.

template patterns. In the future, they can be combined to deal with different uncertainties.

Davies-Bouldin (DB) index is a clustering index which is a ratio of intraclass distance and interclass distance. A small DB index indicates intraclass similarity and interclass difference. It is used to evaluate whether the accumulated difference of distance or that of angles is more informative for classification for TM-AS. A smaller intraclass or a larger interclass distance results in a smaller index value. That is, a feature leading to a smaller DB index value shall be a better feature.

$$DB = \frac{1}{k} \sum_{i=1-k} \max_{j \neq i} (D_{ij}), \quad (5)$$

$$D_{ij} = \frac{d_i + d_j}{d_{ij}}.$$

2.4. Modification of Sensing Parameters. Two sensing parameters can be modified by the system.

- (1) The viewpoint: the angular relative location of the robot with respect to the targeted subject as shown in one of the experimental setups shown in Figure 3. In this study, the robot rotates the sensor to change its viewpoint until the irregularity disappears.
- (2) The range of depth: the probabilistic depth map estimation [12] could be expressed by (6) and (7). D_{xy} is the raw image value from the depth camera at the coordinates x and y . I_{xy} is the extracted image value determined by the probability Prob_{xy} calculated by (6), using a threshold Th_{Prob} . This can be interpreted as the robot observes the target at a gaze distance μ , with range of depth σ .

$$\text{Prob}_{xy} = \frac{1}{\sigma\sqrt{2\pi}} \exp \left[-\frac{(D_{xy} - \mu)^2}{2\sigma^2} \right] \quad (6)$$

$$I_{xy} = \begin{cases} 1 & \text{Prob}_{xy} \geq \text{Th}_{\text{Prob}} \\ 0 & \text{Prob}_{xy} < \text{Th}_{\text{Prob}} \end{cases} \quad (7)$$

2.5. Irregularity Detections, Sensing Parameter Modification, and Behavior Recognition. Figure 4 shows a flowchart of irregularity detection, sensing parameter explorations, and behavior recognitions. Three modules, namely, normal mode monitoring, change depth range, and change viewpoint, were connected through three different types of links. The red path means irregularity detected or further explorations, the purple one shows condition for recursion, and the green one indicates the task finished and return.

In the normal mode monitoring, when a number of irregularities are detected, the system calls the module of change depth range. If the module finds a good depth range as a sensing parameter after exploration, it returns to the normal mode monitoring. Otherwise, the system shifts to change viewpoint module. Since the change of depth range does not need to change the physical position of the robot, its cost is lower than that of change viewpoint, which needs to physically change the orientation of the robot. The depth-first search strategy was employed. That is, for each viewpoint, a full span of depth range is explored. For the details of the modules, please see the appendix.

3. Experiments

This section describes the experiments for comparing and evaluating the heuristic-based and the template-matching-based active sensing schemes as well as the conventional approach without active sensing, in a controlled scenario and a daily life activity scenario. For TM-AS, the similarity index using DB index was evaluated based on the templates prepared, as shown in Section 2.3.2, item (1).

3.1. The Clustering Index (DB Index) Values for Evaluating AD_d^{upper} , AD_d^{lower} , and AD_{Anv} for TM-AS. For TM-AS, as presented in Section 2.3.2, item (1), the three features (AD_d^{upper} , AD_d^{lower} , and AD_{Anv}) for calculating similarity

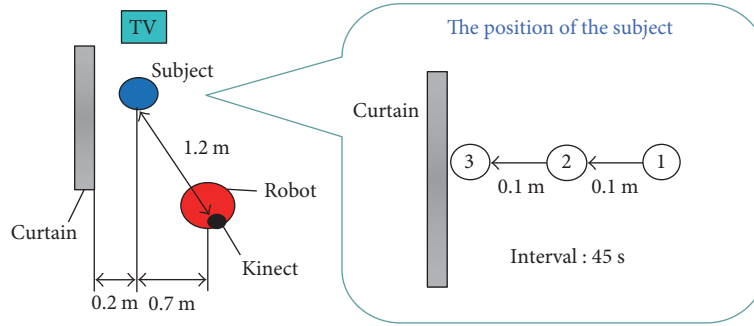


FIGURE 4: A flowchart of irregularity detection, sensing parameter explorations, and behavior recognitions.

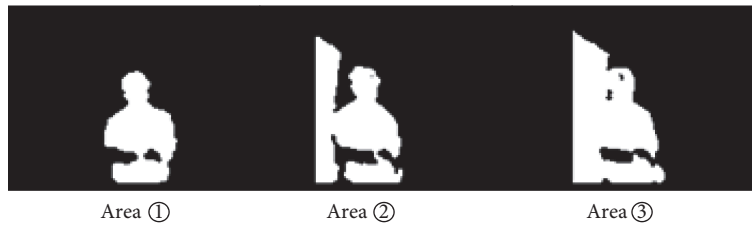


FIGURE 5: Observed and processed depth images in different areas.

indexes for template matching were evaluated by using the DB index. The one with the smallest DB index is selected as the similarity index.

3.2. Experiment 1, a Controlled Scenario. The aim of this experiment is to evaluate the performance of the two active sensing schemes when the target person is sitting close to an object in the environment and indistinguishable in depth with the object. In this scenario, the subject is sitting beside a partition curtain, with a similar sitting height of the subject, as illustrated in Figure 1(a). The similar situations may be caused by the subject standing or sitting against the wall, or bending in front of a refrigerator with its door opened as a background. The robot was located (manually) at a position where the curtain interferes with the human body contour extraction as shown in Figure 3. Note, a similar situation would happen even if a different image feature extraction (e.g., the feature from color images) is employed. The subject was required to sit at one of the three locations with a distance of 0.1 m in between as shown in the insert in Figure 3. Figure 5 shows the observed targeted person and the object in different areas.

In this scenario, we evaluated three different configurations, the conventional system (no active sensing), H-AS, and TM-AS. The evaluation includes not only the accuracy but also the number of rotations that it took for the robot to obtain the most appropriate recognition.

3.3. Experiment 2, Daily Living Activity Scenario 1. The aim of this experiment is to evaluate the active sensing performance in a flow of home living activities. In contrast with the previous experiment, the interference with surrounding objects does not necessarily happen for all the frames for all the activities. The experiment with a total duration of one hour was performed by two subjects for the conventional system (no active sensing) and by three subjects for the

proposed active sensing scheme (due to the analysis on Experiment 1, only H-AS is implemented. For detailed reasons, please find them in Section 4.2). In this experiment, the robot tracks a subject moving in a home living environment. Therefore, the place where the robot stops is not always the same.

We set up two rooms as illustrated in Figure 6. The subject moved to follow a scenario performing the following activities: initially the subject arrived at home ①. The robot was waiting at the entrance, and it started tracking the subject. Then, the subject moved towards the kitchen and washed his hands ②. He walked to the TV, took a seat, and watched TV for a while ③. After that, he stood up and picked a drink from the refrigerator ④. When he finished his drink, he went to the table and read a newspaper for a while ⑤. After that, he moved to his desk and read a book ⑥. Some minutes later, the subject went to an open area and began to walk as an exercise ⑦. When the exercise was finished, he went to bed ⑧.

During the experiment, the robot tracked the subject and identified the performed activities (standing, walking, sitting, bending, and lying down) in real time and it also logged the information for further analysis. The full experiment was recorded with a video camera. Once the experiment was over, we analyzed the log file and the video data to calculate the accuracy of the recognition for each activity.

3.4. Experiment 3, Daily Living Activity Scenario 2. The aim of this experiment is different with that of experiment 2. Multiple confusing situations were contained in this scenario, as shown in Figure 7.

The subject moved from location ① to ② while the robot moved towards the subject to monitor his behavior from its initial position. The subject sat in a deep-back chair for the first five minutes, as shown in the left part of Figure 7. This

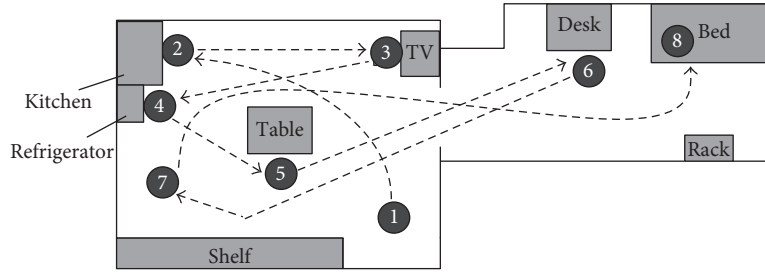


FIGURE 6: The layout of the two rooms for the planned situations and sites for experiment 2.

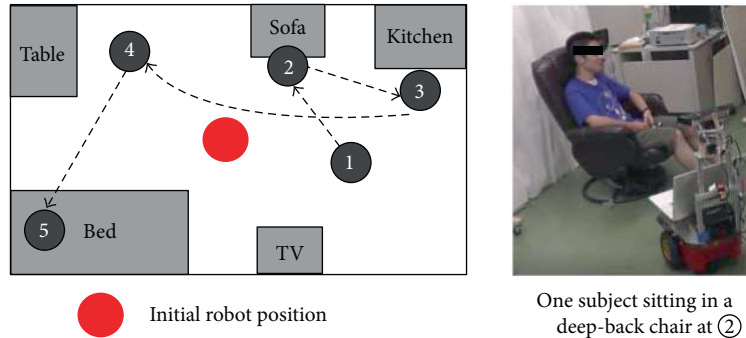


FIGURE 7: The layout of the one room for the planned situations and sites for experiment 3.

TABLE 1: DB values of the accumulated difference (AD) for different features.

Feature	DB
AD_d^{upper}	0.558
AD_d^{lower}	0.520
AD_{Anv}	0.490

deep-back chair was the source of the first confusion. Then the subject moved to ③ and stood in the kitchen for cooking for the next five minutes. The subject then moved to ④ and sat and had meal for another five minutes. In this situation, the wall was the source of confusion. Finally, the subject moved to the bed on the left lower corner at ⑤ and lied on the bed for the final five minutes. Since the subject was asked to turn over on the bed, he was very close to the wall in some cases. This is the 3rd source of confusion. Both the H-AS and TM-AS were implemented and compared with the non-AS cases. Three subjects took part in the experiment.

4. Results

4.1. The Clustering Index for Different Features (AD_d^{upper} , AD_d^{lower} , and AD_{Anv}). DB index values for all the three features, AD_d^{upper} , AD_d^{lower} , and AD_{Anv} , were calculated based on (1), (2), and (3) and are shown in Table 1. As noted in subsection 2.3.2, a smaller DB index value means better clustering, that is, a smaller intraclass distance and a larger interclass distance. As shown in Table 1, the accumulated difference of unit normal vector angle has the smallest value. Therefore, AD_{Anv} is used for further analyses next. Moreover, AD_d^{upper}

and AD_d^{lower} are larger no matter it is upper body or lower body. It is observed that $AD_d^{\text{lower}} < AD_d^{\text{upper}}$, which indicates that the contour of the lower body provides more useful information for measuring the similarity of images of different activities.

Table 2 shows the AD_{Anv} of each template image pair in Figure 2. Generally, the AD shows a smaller value for the images from the same class, for example, the standing (side) and standing (front), while those for the images from different classes, for example, standing and sitting, are larger.

According to this analysis, in experiments 1, 2, and 3, AD_{Anv} was used as the index for irregularity detection.

4.2. Experiment 1, a Controlled Scenario. The results of experiment 1 are summarized in Tables 3 and 4. Table 3 tabulates the activity recognition accuracy for sitting position for the three areas. As shown in Table 3, for different distance between the subject and the curtain, the accuracy of activity recognition varies significantly for areas ② and ③ when the subject got closer to the curtain. As shown, without AS, it shows accurate detections for area ① but low accuracy for area ② and area ③. TM-AS shows the highest accuracy of activity recognition in all the three areas whereas H-AS achieves similar accuracy of activity recognition for areas ① and ② but cannot obtain high accuracy in ③.

Figure 8 shows the change of the sensing parameters (viewpoint and depth range) and activity recognized (correct answer: sitting or incorrect answer: the others). Figure 8(a) shows the results for H-AS where only the viewpoint was changed whereas the lower graph shows those for TM-AS where both the depth range and viewpoint were changed. As shown in Figure 8(a), when the subject changed from area

TABLE 2: The accumulated difference (AD) of unit normal vector angle among the template images.

Template image	Template image								
	Standing (front)	Standing (side)	Sitting (front)	Sitting (left)	Sitting (right)	Bending (back)	Bending (left)	Bending (right)	Lying (down)
Standing (front)	0.0	20.5	17.6	42.3	41.6	25.9	63.4	62.6	52.4
Standing (side)	20.5	0.0	29.6	45.2	37.9	23.8	55.9	56.0	58.8
Sitting (front)	17.6	29.6	0.0	44.9	36.7	29.4	65.6	65.4	53.1
Sitting (left)	42.3	45.2	44.9	0.0	66.5	39.8	61.0	60.5	57.4
Sitting (right)	41.6	37.9	36.7	66.5	0.0	36.3	64.5	62.8	61.7
Bending (back)	25.9	23.8	29.4	39.8	36.3	0.0	45.0	43.0	51.9
Bending (left)	63.4	55.9	65.6	61.0	64.5	45.0	0.0	50.7	65.4
Bending (right)	62.6	56.0	65.4	60.5	62.8	43.0	50.7	0.0	70.9
Lying (down)	52.4	58.8	53.1	57.4	61.7	51.9	65.4	70.9	0.0

TABLE 3: The activity recognition accuracy for sitting position for the three areas.

		Area ①	Area ②	Area ③
w/o AS (conventional)	Average frame number	292	259	217
	Recognition accuracy (%)	100.0	16.8	0.0
H-AS	Average frame number	282	201	265
	Recognition accuracy (%)	100.0	79.6	1.4
TM-AS	Average frame number	247	250	237
	Recognition accuracy (%)	100.0	84.7	52.9

TABLE 4: The time cost of AS (unit: second), from the first irregularity detected to the last sensing parameter change.

AS trial number	Area ②		Area ③
	Heuristic-based AS	Template-matching-based AS	Template-matching-based AS
Trial 1	14.5	10.9	27.3
Trial 2	10.4	13.9	29.9
Trial 3	7.74	13.9	11.9

① to ② getting closer to the curtain, the robot misrecognized the activity. With the heuristics, the irregularity was detected and the robot changed its viewpoint to obtain a correct recognition. But for area ③, H-AS failed the irregularity detections due to the limitation of the heuristics; thus, no change of viewpoints was conducted for a correct activity recognition.

The TM-AS is a more generalized irregularity detection function. In the experiment, it explored two sensing parameters: both viewpoint and depth range. This is because that without exploring both sensing parameters, it is impossible to deal with the ambiguous situations in area ③. Whenever the subject moved from area ① to ②, or from area ② to ③, the irregularity could be detected, and the exploration was initiated. After the subject moved from ① to ②, only changing the depth range was needed, and then the right activity was recognized. However, when the subject moved from ② to ③, the robot had to explore both the viewpoint and depth range to find the right sensing parameter for activity recognition. The detection process is further illustrated using depth images in Figure 9. In Figure 9, several selected observed

images of the trial with TM-AS as the subject moved are shown. The confusion with the surrounding objects was reduced and finally disappeared, as multiple sensing parameters were explored.

Table 4 shows the time cost of both active sensing schemes in the areas ② and ③ for three trials. Although depending on small difference between the initial position, orientation, and the noise of depth images in some frames, the exploration process was different with different trials. Generally, the time cost of TM-AS is higher than that of H-AS in area ②. Here, the time cost was calculated by counting the time from the first irregularity detected to the change of the last sensing parameter. For TM-AS, the time cost in area ③ was higher than that in area ②.

Since the time efficiency is very important for real-time applications, and in the real daily living environment, the situation similar to that in area ③ would not frequently happen; thus in experiment 2, H-AS was further examined.

4.3. Experiment 2, Daily Living Activity Scenario 1. Table 5 shows the results of one subject in non-AS experiment. The walking in italic means the move from one site to another site. At ⑦ for walking exercise, since the subject was instructed to repeatedly move forward, stand, move backward, and stand slowly, two behaviors: standing (⑦-1) and walking (⑦-2), both in bold, shall be recognized. Here, we omitted transitional states, which are the short behaviors detected between two main behaviors, for example, between sitting at ③ and walking for ③-④, bending and standing as transitional states were detected for around 10 frames.

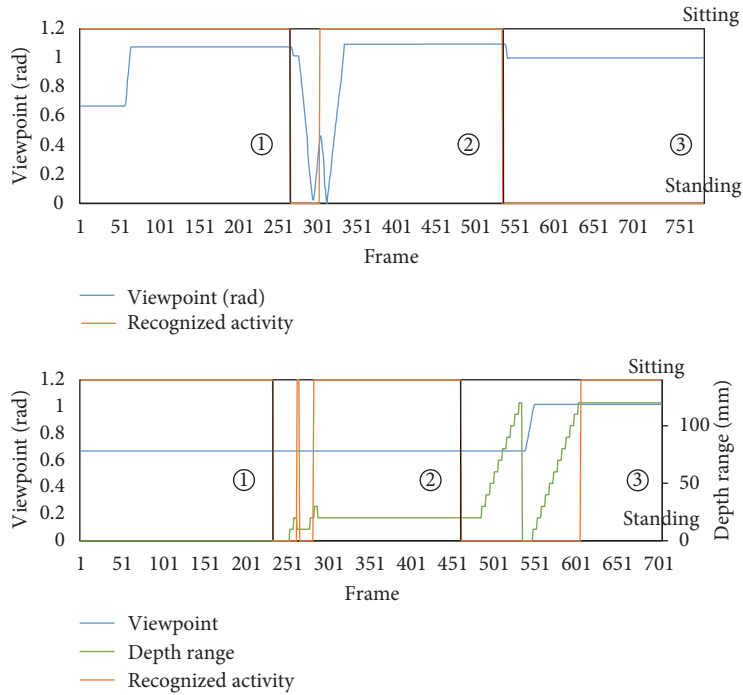


FIGURE 8: The sensing parameters and recognized activity of the two active sensing schemes. (a) H-AS; (b) TM-AS.

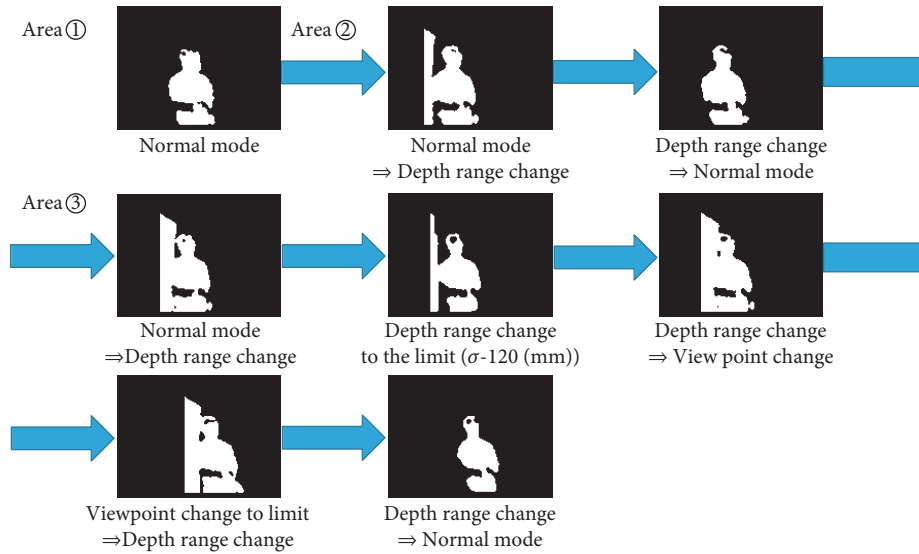


FIGURE 9: A sequence of selected image to show a TM-AS process as the subject moved.

The comparison of recognition accuracy between the system with H-AS and the conventional system (no active sensing) is shown in Figure 10. Here, all the recorded frames and true frames of walking for move between sites (marked in italic in Table 5) were summed up. And the accuracy values shown are the average of that of two subjects. As shown in the graph, recognition accuracy of all the activities except walking for move was improved by applying active sensing.

In total, the accuracy was improved by H-AS (H-AS 84.29% versus w/o AS 67.81%). The accuracy of sitting and

watching TV at ③ was improved up to 99.50%, from 68.42% by the conventional system. This significant improvement could be the result of the viewpoint change of the robot during the experiments. For the activities except sitting and walking, improvement of recognition accuracy was confirmed, too, though, for those activities, irregularity was rarely detected. This is because that, taking the connection of sitting and standing as an example, the activities are sequentially conducted, a good observing viewpoint for sitting can be also good for the next subsequent activity, such as standing.

TABLE 5: The accuracy of behavior recognition of subject 1, w/o active Sensing.

Situation number	Behavior	Video frames	True frames	Accuracy (%)	Situation number	Behavior	Video frames	True frames	Accuracy (%)
①-②	Walking	81	52	64.20	⑤	Sitting newspaper	4514	4292	95.08
②	Bending (washing)	177	164	92.66	⑤-⑥	Walking	124	75	60.48
②-③	Walking	61	43	70.49	⑥	Sitting book	5564	5075	91.21
③	Sitting (TV)	4711	1795	38.10	⑥-⑦	Walking	128	79	61.72
③-④	Walking	101	29	28.71	⑦-1	Standing	385	385	100.00
④	Bending (refrigerator)	266	175	65.79	⑦-2	Walking	1164	477	40.98
④-⑤	Walking	28	17	60.71	⑦-⑧	Walking	292	147	50.34
					⑧	Lying down	3371	2889	85.70

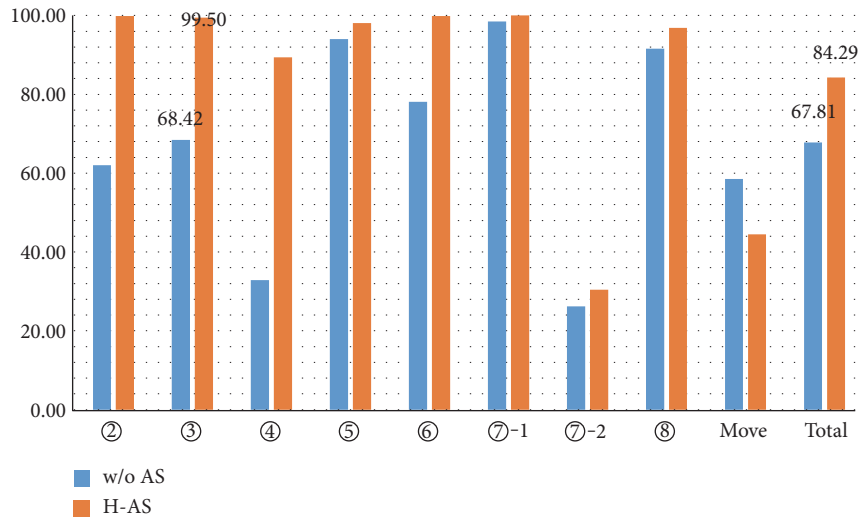


FIGURE 10: Accuracy (%) of behavior recognition of the w/o AS and H-AS. Note: the label “Move” means the walking for move behavior.

TABLE 6: Comparison of accuracy at each situation between w/o AS, H-AS, and TM-AS*.

	w/o AS				H-AS				TM-AS			
Situation ID	②	③	④	⑤	②	③	④	⑤	②	③	④	⑤
Video frame	4389	4413	4149	3248	4402	4718	4446	4540	4640	4809	4614	4185
True Frame	2950	4364	571	691	2494	4366	4089	2096	4102	4791	3524	1412
Accuracy (%)	67.2	98.9	13.8	21.3	56.7	92.5	92.0	46.2	88.4	99.6	76.4	33.7

*Note: the numbers of recorded video frame and true frame are the average of three subjects

In Figure 10, it is also observed that the recognition accuracy of both walking for exercise at ⑦ and walking for move was quite low. In fact, most frames of walking were misrecognized as standing, which may result from the low walking speed of the subject. In the activity recognition algorithm, the moving speed of subjects was also taken into consideration [11]. Basically, in the experiment, the subject walked slowly, since he was instructed to simulate the walking of the elderly. That is why the misrecognition occurred frequently. This can be further improved by adjusting behavior recognition algorithm.

Taking the accuracy values at different situations, and that of walking for move, of the 2 subjects as samples, a paired (w/o AS versus H-AS) *t*-test was performed. The *p* value is 0.0222, which means that there is significant difference between the two methods.

4.4. Experiment 3, Daily Living Activity Scenario 2. Table 6 shows a comparison between the accuracy at each simulation between the w/o AS, H-AS, and TM-AS. As shown in the table, at situation ②, accuracy by TM-AS reaches 88.2%. Comparing to 56.7% by using H-AS and 67.2% for w/o

TABLE 7: Comparison of accuracy of three subjects at situations ② and ④.

Subject ID-situation	w/o AS	H-AS	TM-AS
S1-②	64.6	96.5	90.6
S1-④	36.3	89.8	96.6
S2-②	68.9	13.0	88.6
S2-④	0.0	95.2	76.4
S3-②	68.1	52.7	85.9
S3-④	0.0	91.8	54.7
w/o AS versus H-AS	t -test: $p = 0.113$, no significant difference		
w/o AS versus T-AS	t -test: $p = 0.017$, with significant difference		
H-AS versus T-AS	t -test: $p = 0.564$, no significant difference		

AS, this shows that TM-AS effectively improves the accuracy for the situation. The deep-back chair (as shown in the right part of Figure 7) is a different challenge from that of the wall and curtain, as tested in experiment 2. Depending on the observation angle, the deep back shades the upper body completely, without showing the two-peak feature, which is a decisive factor of the heuristics in H-AS. That is why the accuracy of H-AS is even worse than w/o AS.

On the other hand, at situation ④, which is also a sitting related situation, the accuracy of TM-AS is much higher than that of w/o AS. However, it is lower than that of H-AS, which is to be analyzed later in this subsection in detail. Sitting at both situations ② and ④ is analyzed. Table 6 shows the accuracy of both situations from all the three subjects, subject 1 (S1), subject 2 (S2), and subject 3 (S3). Performing t -test to the pairs of methods, as shown in the lower part of Table 7, there is a significant difference between the TM-AS and w/o AS and no significant difference between w/o AS and H-AS, or between H-AS and TM-AS.

The fact that the accuracy of TM-AS is lower than that of H-AS at the sitting situations in Table 7 can be explained as follows. Figure 11(b) shows the illustration and photos for recognitions for situation ④. Here, the observation angle is defined as θ in Figure 11(a). At $\theta = 75^\circ$ as shown in Figure 11(b), after adjusting the sensing range, the silhouette of the subject could be acquired and matched with one of the sitting templates prepared. A successful recognition was obtained when the robot observes the subject at an angle over 75° . However, not all the angles lead to a successful recognition. Figure 11(c) shows the case when $\theta = 45^\circ$. Although by adjusting the sensing range, the silhouette of the sitting subject could be acquired clearly too, and it could not match any of the three sitting templates (front, left, and right as shown in Figure 2). Thus, the active sensing could not stop successfully within a time limit. It is reasonable to assume that an additional sitting template at around 45° will help to solve the problem.

In order to verify the aforementioned hypothesis, a 45° sitting template as shown in Figure 11(d) was added, and

an additional supporting experiment at situation ④, with one subject sitting at the site, and the robot started from three observation angles, 30° , 45° , and 60° , was done. The results are tabulated in Table 8. As shown in the table, the accuracy at $\theta = 45^\circ$ was improved for sitting for situation ④. Certainly, this raised a new question for the T-AS, that is, for each behavior, how many templates should be prepared for a recognition with good accuracy, which shall be investigated in near future.

Another result requiring further investigation is the unsatisfactory accuracy (46.2% for H-AS and 33.7% for TM-AS) at situation ③, as shown in Table 6 previously. After checking the results carefully, it is clear that, in most failed cases, the subject was lying in the bed and leaning against the wall, as shown in the illustration in Figure 12(a). Especially, when the angle between the robot and the subject θ is about 45° , this is more critical. Note, under the one-room setting of experiment 3, the distance among the furniture is small, and a 45° observation angle is more likely to happen than 90° . One example of the binary images extracted from the depth images of such cases is shown in Figure 12(b), in which, a portion of the wall (vertical part) and the lying human body (horizontal part) were merged. The upper part of this binary image is similar to the standing template (shown in Figure 12(d)). Therefore, the misrecognition of lying down on a bed as standing occurred. Figure 13 shows the time course of the recognized activity of situation ③ of the original TM-AS (the blue line). The sitting behavior was misrecognized as standing by the original TM-AS.

This problem can be dealt with by introducing the second central moment [19] and making use of the orientation of the major axis of the binary image as shown in Figure 12(c). The orientation of the major axis (the long axis of the ellipse enclosing the binary image) can differentiate the pure standing and lying down with confusion from the wall. As an example, in Figure 12(d), the orientation of the major axis of a pure standing image is -89° .

In order to validate this idea, an additional supporting experiment was performed by one subject at situation ③. The cases with the observation angles 45° and 90° were tested. Table 9 shows the results. The time course of the recognized activity by the improved TM-AS is shown by an orange line in Figure 13. Especially, the accuracy in the observation when angle was 45° was improved greatly from 0% to 64.75%, though there is still space for improvement. This will be further discussed in the next section.

5. Discussion

In this paper, an active sensing approach is proposed for a home monitoring robot where a categorization is introduced for further explorations for improving the accuracy of activity recognition with less time cost. It was targeted at uncertain situations where a subject under monitoring is indistinguishable with the surrounding objects in a real environment.

The performance of the active sensing depends greatly on the irregularity detection. H-AS is a method specifically designed for the targeted application. It is based on a heuristic

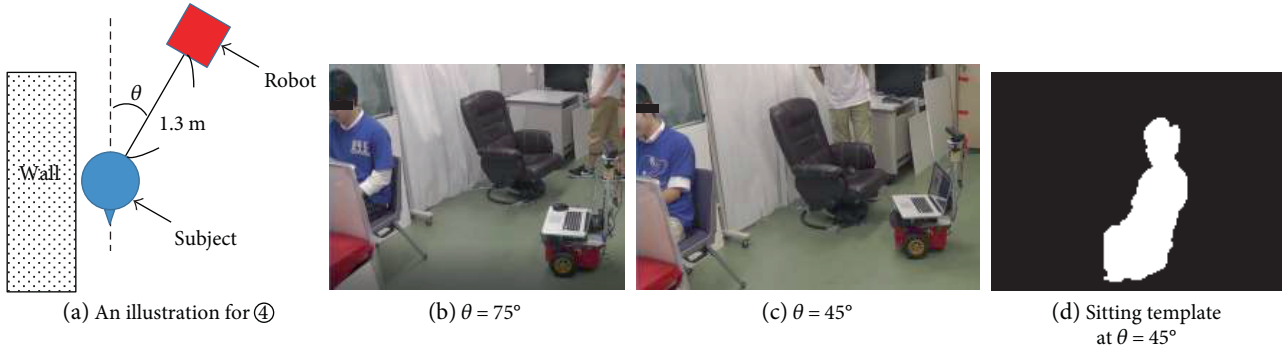


FIGURE 11: An explanation about the observation angle at situation ④.

TABLE 8: Comparison between the w/o and with a new 45° sitting template, for different initial observation angles (30° , 45° , and 60°).

Observation angle	w/o the 45° template			With the 45° template		
	30°	45°	60°	30°	45°	60°
Video frame	400	400	400	400	400	400
True frame	330	337	362	358	362	367
Accuracy (%)	82.5	84.25	90.50	89.50	90.50	91.75

for detecting a local irregular feature pattern, which depends on the activities to be recognized. Therefore, it can only categorize all the situations into two classes: regular and irregular. Through the experiments, it is found that the H-AS could deal with the ambiguous situations to a certain extent; however, when the subject was sitting very close to an object with similar sitting height as the subject, it failed to detect the irregularity. Moreover, the local irregular feature pattern could only cover a specific type of uncertain situations, thus ignore all the situations where changing the sensing parameters is needed. Despite that, the H-AS led to an improvement in the accuracy of activity recognition in a daily living activity scenario for those activities that happen frequently.

On the other hand, TM-AS realizes more general irregularity detection, in which activity-dependent templates representing normal situations were prepared for comparing with the current situations. The unmatched situations are judged as irregular for further sensing. Although TM-AS was only tested for the activity of sitting in two controlled scenarios in this study, in general cases, it could detect irregular situations against identified activity-dependent normal ones. In general, the template-matching-based irregularity detection is the nearest neighbor classifier that excludes the far data points as anomaly (irregularity). It is one of the canonical anomaly detection approaches. Other methods for anomaly detection, such as simple statistical methods and machine learning-based methods, including both the supervised learning (e.g., support vector machine) and unsupervised learning (e.g., different clustering methods), can be applied to the proposed framework. These can be further implemented and compared with the current approach in our future work.

In this study, the accuracy of recognizing the main behaviors of an elderly staying at home by a robot is examined. They are standing, walking, bending, sitting, lying down, and falling. The detection of behaviors and the change between two behaviors, such as from walking to sitting, are crucial for home monitoring for behavioral studies. The walking speed in this home monitoring scenario is set to be 1 km/hr–3 km/hr. Because of the low speed and the small change of speed, the study on walking was not further detailed into different walking speeds. Moreover, due to the low speed, it is hard to be distinguished from standing. Especially in experiment 2, at situation ⑦, the walking exercise required the subject to move forward and backward repeatedly and slowly, which makes the differentiation more difficult. Moreover, in this study, the activity recognized during the behavior changes was not counted, because the duration of behavior changes is much shorter than that of the behaviors during daily living, and real-time intervention is out of our scope. In the future, if the behavior changes need to be accurately monitored, for the purpose of, for example, real-time behavior support, then the influence of the speed on accuracy during behavior changes has to be investigated. In that case, the sampling rate and the computational efficiency of the system should be improved to meet the real-time requirement.

The aim of experiment 3 is to explore the limitation of the proposed AS algorithms. Based on the results, it is clearly shown that there are various kinds of confusing situations caused by a wall or by different types of furniture to different behaviors. These situations need to be identified by irregularity detection and further coped with by efficient active sensing. Experimentally, we have successfully shown the possibility of applying TM-AS to deal with the confusion caused at situations ④ and ⑤ in experiment 3. More systematic investigation is needed to verify the effectiveness of the improved TM-AS in a complete way. Especially, the following three issues shall be further investigated with immediate attention.

The first issue is that the accuracy of detection can considerably be affected by the number of available templates. More templates are needed for increasing the accuracy of detection. This was shown by the results and further investigation of situation ④ in experiment 3. Moreover, when the number of behaviors for detection increases, more templates are needed. Therefore, the templates for matching need to be generated carefully for expressing a complete set of normal

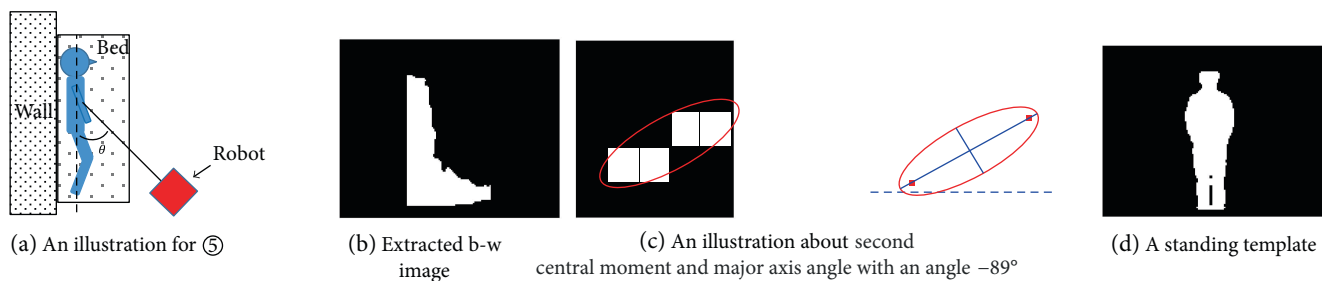


FIGURE 12: An explanation about misrecognition at situation ⑤.

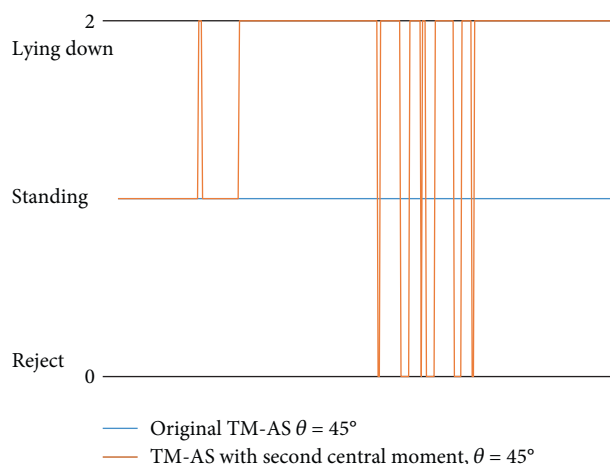


FIGURE 13: Time course of the recognized activity of the original TM-AS and an improved TM-AS.

TABLE 9: The accuracy of the original TM-AS and an improved TM-AS at situation ⑤.

	w/o the major axis angle		With the major axis angle	
	45°	90°	45°	90°
Observation angle	45°	90°	45°	90°
Video frame	400	400	400	400
True frame	0	332	259	333
Accuracy (%)	0	83	64.75	83.25

situations as required. The clustering method [20] might be useful to generate the templates in an unsupervised way.

The second issue is that, as the environment turns to be more complex, the distance (similarity) index might be insufficient to differentiate the normal and irregular situations. This was shown by the results and further investigation of situation ⑤ in experiment 3, in which, an irregular situation of one behavior (e.g., lying down) was recognized as the normal situation of another behavior (e.g., standing). Therefore, multiple similarity indexes need to be applied to avoid the false-positive judgement. Furthermore, for some location-dependent critical confusing cases, the initial recognition could be taken as a hypothesis for active sensing to confirm. Each recognition result could be attached with a location-dependent or even

behavior-dependent “belief” value, when the “belief” value is low, then an active sensing method could be initiated to confirm the first guess.

The third issue is that the efficiency of the exploration of sensing parameter shall be improved. For TM-AS, after an irregularity was identified based on a temporary activity, further explorations are encouraged by the method to explore the templates for all the activities for all the sensing parameters, which lowers its time efficiency. Therefore, for TM-AS, its time efficiency needs further improvement. This can be done by introducing a memory-based approach for the exploration of sensing parameter. If the robot could identify its situations, employ situation-dependent exploration strategy, and improve the strategy in an incremental way, more practical active sensing could be realized.

In this work, we aimed to realize the active sensing mechanism for robust sensing and behavior monitoring. In the near future, we will classify the Japanese home living environments into several types and do a set of experiments, with more subjects, to evaluate our monitoring mobile robot system in a comprehensive way.

6. Conclusion

This work is an advancement of the previously presented work based on the use of a mobile robot for monitoring the home-alone elderly. It addresses the problem of the uncertain situations, where the subject under monitoring is difficult to be distinguished from the background. A new approach is proposed where active sensing is applied for categorization of situations before further explorations for both detection accuracy improvement and cost minimization of time. For categorizing the situations, two schemes, H-AS and TM-AS, were employed for irregularity detections. Experiments were designed to compare and examine the performances of both active sensing schemes in terms of the detection accuracy and time cost for the targeted application. The proposed approach can detect ambiguities of surrounding objects and change the sensing parameters of the robot to eliminate the ambiguities. Experimental results show that significant improved accuracy of the system in both a controlled scenario and two home living scenarios has been achieved, with reasonable time cost.

For the proposed approach, remained issues are identified, analyzed, and discussed in detail. In our future work, the TM-AS is to be improved by well-prepared templates,

hybridized similarity indexes, and optimized sensing parameter exploration strategy. Moreover, other common uncertain situations, such as occlusion by furniture, difficulties of localization and movement control due to uneven terrain, and frequent partial furniture layout alternations, will be resolved.

Appendix

Consider Pseudocodes 1, 2, and 3 for exploring sensing parameters with irregularity detection based on template matching.

```

Codes
Begin_Normal_Mode_Monitoring
   $B_F = \text{recogActivity}(I_F[t])$    $B_F = 1 \sim 6$ 
  If  $\text{calAD}(I_T[B_F], I_F[t]) > \text{Th}_{AD}$ 
     $\text{Flag}_{Frame}[t] = 1$ 
  Else.
     $\text{Flag}_{Frame}[t] = 0$ 
  If  $N_{IR} = \sum_{j=1 \sim \min(t, \text{ConstBuff})} \text{Flag}_{Frame}[j] > \text{Th}_{NIR}$ 
    Goto Change_DepthRange
  Else
    Goto Begin_Normal_Mode_Monitoring
End_Normal_Mode_Monitoring

Explanation of parameters and functions
 $B_F$ : activity recognized,  $I_F[t]$ : image of frame  $t$ 
 $I_T[B_F]$ : the templates of  $B_F$ .
 $\text{Th}_{AD}$ : a threshold to decide whether irregular or not
 $\text{Flag}_{Frame}[t]$ : flag of frame  $t$ ; 1: irregular frame
                0: normal frame
 $N_{IR}$ : number of irregular frames
 $\text{Th}_{NIR}$ : a threshold to decide irregularity occurrence
 $\text{Const}_{\text{Buff}}$ : A constant denoting number of past frames for checking
Functions called
recogActivity(): activity recognition (ref. [10])
calAD(): accumulated difference calculation

```

PSEUDOCODE 1: Normal_Mode_Monitoring.

```

Codes
Begin_Change_Viewpoint
   $\text{Angle} = \text{Angle}_{Robot}[t]$ 
  If  $i\text{Rotate} > \text{Const}_{\text{Max\_rotation}}$ 
     $i\text{Rotate} = 0$ 
    Goto Begin_Normal_Mode_Monitoring
  If  $i\text{Rotate} \neq 0$ 
     $\text{Angle} = \text{Angle} + \text{Const}_{\text{Angle}} * i\text{Rotate}$ 
  Else
     $\text{Angle} = \text{Angle} - \text{Const}_{\text{Angle}} * i\text{Rotate}$ 
   $\text{Angle}_{Robot}[t] = \text{rotateRobot}(\text{Angle})$ 
  If  $\text{Angle} = \text{Angle}_{Robot}[t]$ 
    Goto Begin_Normal_Mode_Monitoring
End_Change_Viewpoint

Explanation of parameters and functions
 $\text{Angle}_{Robot}[t]$ : angle in the world coordinates at  $t$ 
 $i\text{Rotate}$ : a variable for calculating rotation angle
 $\text{Const}_{\text{Max\_rotation}}$ : a constant denoting maximal number of rotation steps
 $\text{Const}_{\text{Angle}}$ : a constant denoting angles for each rotation step
Functions called
rotateRobot(): rotate to a specified objective angle

```

PSEUDOCODE 2: Change_Viewpoint.

```

Codes
Begin_Change_DepthRange
  For i = 1: Const_Smooth
    BF = recogActivity (IF[t])  BF = 1~6
    ADSmooth[i] = calAD(IT[BF], IF[t])
    minADSmooth = min(ADSmooth [i]) {i = 1~Const_Smooth}
    σ = σrange[iDepthRange]
    ADDepthRange[iDepthRange] = minADSmooth
    If minADSmooth ≥ ThAD
      minADDepthRange = min(ADDepthRange[i]) {i = 1~ iDepthRange}
      If minADDepthRange < ThAD
        iDepthRange = argmedian(AD[i] | AD[i] < ThAD)
                          {i = 1~ iDepthRange}
        σ = σrange[iDepthRange]
        Goto Begin_Normal_Mode_Monitoring
      iDepthRange + = 1
    If iDepthRange > Const_DepthRange
      σ = σinit
      iDepthRange = 0
      Goto Begin_ChangeViewpoint
    Else
      Goto Begin_Change_DepthRange
  End_Change_DepthRange

Explanation of parameters and functions
BF: activity recognized,
IF[t]: image of frame t
IT[BF]: the templates of BF
ADSmooth: array to save AD values
σrange: sensing parameter range for exploring,
σ: current depth range
ADDepthRange: AD for each sensing parameter
minADDepthRange: minimal AD value among explored parameters
argmedian(): to get the id of the parameter with the median value among useful (AD[i] < ThAD) explored parameters
Const_DepthRange: the size of σrange
σinit: initial value of sensing parameter
Functions called recogActivity(): activity recognition (ref. [10])
calAD(): accumulated difference calculation

σrange[i] = 200-i*10 mm, {i = 1~12}; σ works for probabilistic model to extract IF(t) from raw image data
Const_DepthRange = 12
Const_Smooth = 5
Const_Angle = 20 degrees
Const_Max_rotation = 4

```

PSEUDOCODE 3: Change_DepthRange.

Conflicts of Interest

The authors declare that they have no conflicts of interest.

Acknowledgments

This work was supported by JSPS grant-in-aid for Scientific Research(B) 17H02129.

References

- [1] *Profile of Older Americans: 2014 Profile* July 2015, http://www.aoa.acl.gov/Aging_Statistics/Profile/index.aspx.
- [2] European Commission, *The Ageing Report: Underlying Assumptions and Projection Methodologies*, European Commission, Belgium, 2015.
- [3] S. C. Mukhopadhyay, "Wearable sensors for human activity monitoring: a review," *IEEE Sensors Journal*, vol. 15, no. 3, pp. 1321–1330, 2015.
- [4] L. Snidaro and G. L. Foresti, "A multi-camera approach to sensor evaluation in video surveillance," in *IEEE International Conference on Image Processing 2005*, vol. 1, p. I–1101, Italy, 2005.
- [5] J. Fasola and M. J. Mataric, "Using socially assistive human-robot interaction to motivate physical exercise for older adults," *Proceedings of the IEEE*, vol. 100, no. 8, pp. 2512–2526, 2012.

- [6] A. J. Huete, J. G. Victores, S. Martinez, A. Gimenez, and C. Balaguer, "Personal autonomy rehabilitation in home environments by a portable assistive robot," *IEEE Transactions on Systems, Man, and Cybernetics, Part C (Applications and Reviews)*, vol. 42, no. 4, pp. 561–570, 2012.
- [7] S. Bedaf, G. J. Gelderblom, and L. De Witte, "Overview and categorization of robots supporting independent living of elderly people: what activities do they support and how far have they developed," *Assistive Technology*, vol. 27, no. 2, pp. 88–100, 2015.
- [8] N. Myagmarbayar, Y. Yuki, N. Imamoglu, J. Gonzalez, M. Otake, and W. Yu, "Human body contour data based activity recognition," in *2013 35th Annual International Conference of the IEEE Engineering in Medicine and Biology Society (EMBC)*, vol. 2013, pp. 5634–5637, Japan, January 2013.
- [9] N. Imamoglu, E. Dorrnzoro, M. Sekine, K. Kita, and W. Yu, "Top-down spatial attention for visual search: novelty detection-tracking using spatial memory with a mobile robot," *Advances in Image and Video Processing*, vol. 2, no. 5, 2014.
- [10] M. Nergui, Y. Yoshida, N. Imamoglu, J. Gonzalez, M. Otake, and W. Yu, "Human activity recognition using body contour parameters extracted from depth images," *Journal of Medical Imaging and Health Informatics*, vol. 3, no. 3, pp. 455–461, 2013.
- [11] N. Imamoglu, E. Dorrnzoro, Z. Wei et al., "Development of robust behaviour recognition for an at-home biomonitoring robot with assistance of subject localization and enhanced visual tracking," *The Scientific World Journal*, vol. 2014, Article ID 280207, 22 pages, 2014.
- [12] R. Wang, M. Veloso, and S. Seshan, "Active sensing data collection with autonomous mobile robots," in *2016 IEEE International Conference on Robotics and Automation (ICRA)*, Sweden, 2016.
- [13] L. Mihaylova, T. Lefebvre, H. Bruyninckx, K. Gadeyne, and J. De Schutter, "Active sensing for robotics - a survey," *the 5th International Conference On Numerical Methods and Applications*, 2002, Bulgaria, 2002.
- [14] Z. Ke, *Active Sensing with Applications to Mobile Robotics, Ph.D. Dissertation*, the University of Minnesota, Minneapolis, MN, USA, 2012.
- [15] S. C.-H. Yang, D. M. Wolpert, and M. Lengyel, "Theoretical perspectives on active sensing," *Current Opinion in Behavioral Sciences*, vol. 11, pp. 100–108, 2016.
- [16] C. F. Moss and A. Surlykke, "Auditory scene analysis by echolocation in bats," *The Journal of the Acoustical Society of America*, vol. 110, no. 4, pp. 2207–2226, 2001.
- [17] S. Ahmad, H. Huang, and A. J. Yu, "Cost-sensitive Bayesian control policy in human active sensing," *Frontiers in Human Neuroscience*, vol. 8, p. 955, 2014.
- [18] K. Nakahata, E. Dorrnzoro, N. Imamoglu, M. Sekine, K. Kita, and W. Yu, "Active sensing for human activity recognition by a home bio-monitoring robot in a home living environment, intelligent autonomous systems 14," *Proceedings of the 14th International Conference IAS-14*, 2016, pp. 315–326, Springer International Publishing AG, Switzerland, July 3–7, 2016.
- [19] M. K. Hu, "Visual pattern recognition by moment invariants," *IRE Transactions on Information Theory*, vol. 8, pp. 179–187, 1962.
- [20] M. Christonpher, *Bishop, Pattern Recognition and Machine Learning*, Springer Science+Business Media, LLC, New York, NY, USA, 2006.

Research Article

A 3D Scan Model and Thermal Image Data Fusion Algorithms for 3D Thermography in Medicine

Adam Chromy¹ and Ondrej Klima²

¹Faculty of Electrical Engineering and Communication, Brno University of Technology, Brno, Czech Republic

²Faculty of Information Technology, IT4Innovations Centre of Excellence, Brno University of Technology, Brno, Czech Republic

Correspondence should be addressed to Adam Chromy; adam.chromy@ceitec.vutbr.cz

Received 6 April 2017; Revised 3 September 2017; Accepted 4 October 2017; Published 8 November 2017

Academic Editor: David Moratal

Copyright © 2017 Adam Chromy and Ondrej Klima. This is an open access article distributed under the Creative Commons Attribution License, which permits unrestricted use, distribution, and reproduction in any medium, provided the original work is properly cited.

Objectives. At present, medical thermal imaging is still considered a mere qualitative tool enabling us to distinguish between but lacking the ability to quantify the physiological and nonphysiological states of the body. Such a capability would, however, facilitate solving the problem of medical quantification, whose presence currently manifests itself within the entire healthcare system. **Methods.** A generally applicable method to enhance captured 3D spatial data carrying temperature-related information is presented; in this context, all equations required for other data fusions are derived. The method can be utilized for high-density point clouds or detailed meshes at a high resolution but is conveniently usable in large objects with sparse points. **Results.** The benefits of the approach are experimentally demonstrated on 3D thermal scans of injured subjects. We obtained diagnostic information inaccessible via traditional methods. **Conclusion.** Using a 3D model and thermal image data fusion allows the quantification of inflammation, facilitating more precise injury and illness diagnostics or monitoring. The technique offers a wide application potential in medicine and multiple technological domains, including electrical and mechanical engineering.

1. Introduction

In recent years, the availability of thermal imagers has moved from expensive, bulky, and cumbersome systems to affordable and practical solutions [1]. Applicable sensors and filters have been developed to such an extent that thermal cameras can be found already in smartphones at prices up to 700 EUR [2]. Due to such rapid progress, thermal imaging is being practically employed on an everyday basis also in fields and disciplines where it previously functioned as an instrument convenient exclusively for research purposes.

In the given context, a typical target field is, for example, medicine: digital medical thermal imaging (DMTI), a modality of medical imaging to monitor surface skin temperature, has been evolving over the last 50 years to contribute towards improving evidence-based diagnosis and facilitating the early detection of diseases.

Within medicine, current applications of the technique are to be sought primarily within clinical procedures centred

on assessing and monitoring peripheral vascular, neurological, and musculoskeletal conditions within multiple medical subdisciplines, including cardiology, dermatology, dentistry, obstetrics, oncology, physiotherapy, public health, surgery, and veterinary medicine, and the investigation of chronic and occupational diseases [3].

Although the 2D thermal imaging is able to quantify the temperature of the individual pixels of the image, the DMTI is still considered a mere *qualitative tool*, enabling us to distinguish between the physiological and nonphysiological states of the body but lacking the ability to *quantify* them [3, 4]. This is due to three main drawbacks of DMTI: almost impossible definition of the region of interest (ROI) in a thermal image due to lack of recognizable clearly bounded thermal features in the image, distortions caused by transforming 3D world to 2D representation, and dependence of the thermogram on the view of the camera. The first drawback makes measurements of average ROI temperature impossible, the same as differential measurements between

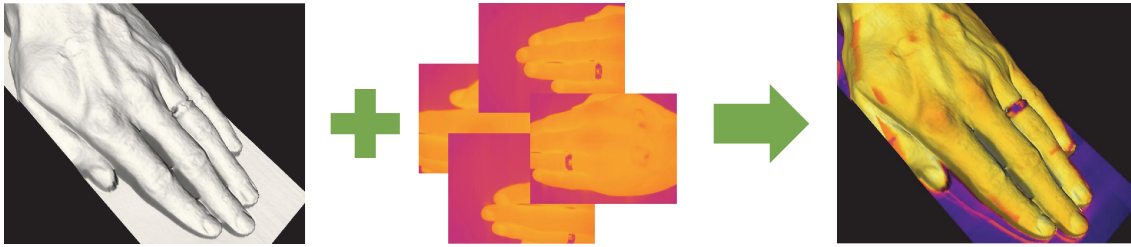


FIGURE 1: Visualizing the data fusion process: the 3D model from a 3D scanner (left) is combined with the 2D thermal images obtained using a thermal camera (middle) to produce the final 3D thermal model (right).

two ROIs, what are the main methods of medical thermal quantification (the single thermal values are not used for quantification, since the surface body temperature is influenced by previous physical activity, stress, etc. From this reason, the comparison between average temperatures of the reference area and ROI shall be used). The second drawback disallows also measurements of an affected area, and the third one disqualifies evaluation of changes during the time.

Nearly all types of injury, together with many diseases or pathological changes, are characterized by an increased blood flow and a stronger cellular metabolic rate in the affected region; the two aspects cause a local increase of temperature *proportional* to the phenomenon [5]. This proportional dependence predetermines that quantification via DMTI should be possible.

Another rapidly advancing technology consists in 3D scanning. 3D surface models find increasingly intensive use in situations where an object must be preserved in a permanent, time-invariant state. In such cases, colour-covered 3D models seem to constitute the best modality [6]. Further, at present, object cloning could also be named as a dynamically growing domain. Multiple types of 3D printers are available on the market, and each of them requires a tool to build the 3D model to be printed [7]. Finally, computer-based 3D models are, due to their plasticity, becoming ever more favoured in the visualization of objects characterized by good visibility but also a small size of major details, which then have to be enlarged plastically [8]. These solutions and applications, by definition, exhibit a strong potential to be used also in healthcare too.

If combined, the two above-outlined, state-of-the-art technologies could yield a volume of new information even higher than that obtainable through their separate use. Such data fusion would subsequently enable us to address some of the long-term challenges to be resolved within diverse medical sectors.

One such problem lies in *medical quantification*, an issue encompassing the entire healthcare system: evaluation methods excessively inaccurate, insensitive, or subjective embody a principal drawback affecting, for example, dermatology, traumatology, physiotherapy, and forensic sciences.

In dermatology, the degree of objectivity in evaluating disease severity and the extent of lesions is still insufficient, due in particular to the lack of reliable *in vivo* quantification methods to assess the concrete region of interest only.

Traumatology and forensic sciences suffer from the absence of methods to cope with the quantification of bruise severity, often through time.

In physiotherapy, techniques are unavailable for detecting early tiny changes in the body volume, a possible symptom of an emerging disease. It is also rather difficult to distinguish between physiological (e.g., muscle growth) and nonphysiological (e.g., swelling) changes, and the impact of treatment procedures on a disease cannot be quantified smoothly, because the current evaluation methods are mostly based on subjective perception, health surveys and related forms, or low-resolution scoring systems exhibiting poor interobserver correlation.

These and many other issues are solvable using 3D thermal quantification. An effective approach appears to consist in extending a 3D scanner with a thermal imaging sensor and mapping relevant thermal information onto the surface of the 3D model via data fusion algorithms (Figure 1) [9].

Such a combination of sensors generates a multilayered 3D model of the patient's body, containing the temperature at each surface point and embodying an extension of the 3D volume that constitutes the output of a standard 3D scanner. By studying the distribution of the temperatures along the surface of the body, we can then easily localize and, subsequently, quantify the inflammation foci (in the sense of the average temperature gradient in the affected region or its extent). At the following stage, the volume increment caused by swelling can be precisely measured.

Besides inflammation monitoring, merging thermal and spatial data allows several other medical applications. While inflammation increases the local temperature, necrosis leads to its decrease; thus, the device characterized herein can be used in, for example, monitoring diabetic necrotic tissues.

This paper discusses data fusion algorithms to merge a 3D model (captured by any 3D scanner) and thermal images (captured by any thermal imager). In this context, the following section introduces a generally applicable process of combining the thermal and spatial data; importantly, the related significance and usefulness for medical diagnosis are experimentally demonstrated on 3D thermal models of real patients.

2. Materials and Methods

The section outlines a procedure for merging 3D data and thermal images. The algorithms introduced below are

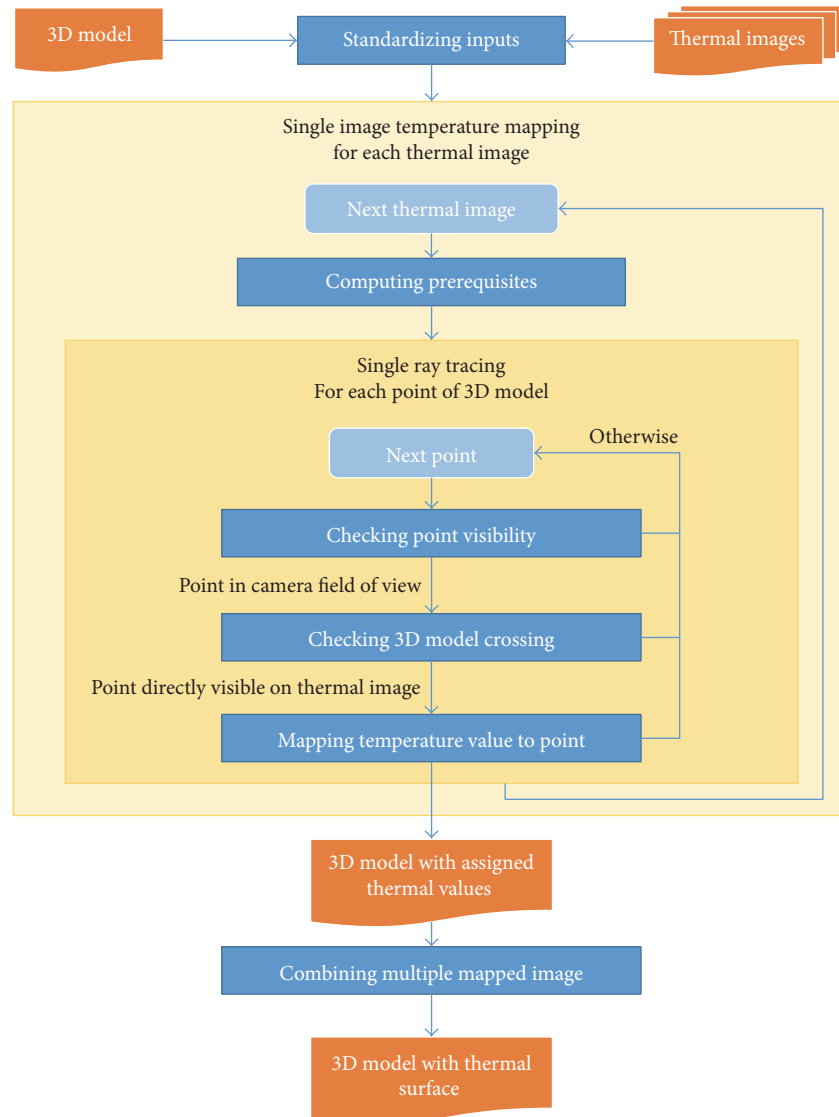


FIGURE 2: A schematic diagram of the data fusion algorithm.

applicable to a *general* digital 3D model of an object provided by *any* 3D scanner and usable with the *general* thermal data produced by *any* thermal imager. The only requirement is to know the location and orientation of the camera relevant to each captured image. After this condition has been satisfied, the data fusion algorithm is fully automatic and does not require manual assistance.

The entire algorithm is set forth within the diagram in Figure 2, and all the procedures are further explained in the following sections.

2.1. Standardizing Inputs. Various 3D scanners provide the output data in diverse, more or less standardized, digital formats. Even though the protocol, structure, and data type vary between the different forms, they share a common feature: the data can be considered a *triangle mesh*, namely, a *set of triangles* defined by three points, with each of these defined by three coordinates in the Cartesian

space. The data may assume the shapes of another polygon mesh (e.g., a quadrilateral mesh or a set of quadrilaterals) or an unordered set of points (point cloud) [10]. The first type is easily transferable to triangle mesh because every convex polygon can be divided to a number of triangles [11], and the other one enables conversion to a triangle mesh via any triangulation algorithm [12], for example, a Delaunay triangulation [13].

Thermal imagers also exhibit different file formats; in all cases, however, the thermal data are obtainable as a *2D matrix of scalar temperature values*. Some cameras supply such matrices directly, while others provide coloured images in the bitmap form. In the latter option, the transformation scale between the colour and the temperature values is yielded, whereby the colours can be translated to scalars [14]. In general terms, however, the thermal data are represented as a 2D matrix where each value refers to the temperature of a particular pixel.

The discussion below also presumes no radial and tangential distortion of the image, meaning that the input images shall be already preprocessed according to the intrinsic parameters of the camera.

Proper image alignment is achievable if the following thermal imager parameters are known:

- (1) Location of the camera focus in space (vector \vec{T}_{from})
- (2) Camera view direction (unit vector \vec{T}_{to})
- (3) Direction defining ‘‘up’’ in the camera image (unit vector \vec{T}_{up} , perpendicular to \vec{T}_{to})
- (4) Angle of view of the camera in the horizontal (δ_H) and vertical (δ_V) dimensions (in radians)
- (5) Focal distance of the camera optics (scalar T_{FD})
- (6) Number of values (resolution) in the thermal image along the horizontal (I_W) and vertical (I_H) dimensions.

The first three parameters are usually measured directly using various tracking systems [15] or estimated from scene changes (ICP-based methods, [16]). Parameters 4–6 are mostly known from the technical documentation of the camera; alternatively, they can be acquired through the calibration method published in [17].

It is important to emphasize that these 6 parameters exert a significant influence on proper matching between the thermal images and the 3D model, and we thus need to know them with a high accuracy. The calibration methods relevant to these tasks are characterized in [17–19]. The properly mutually calibrated sensors, providing these 6 parameters with high accuracy and then ensuring correct registration of thermal images onto the 3D model, are assumed in further text.

2.2. Computing Prerequisites. The computations below are associated with certain prerequisites, which can be computed once per mapped image (Figure 3) in order to keep the algorithm fast.

The position of the thermal image, located in real coordinates and defined by its top-left (\vec{I}_{TL}), top-right (\vec{I}_{TR}), bottom-left (\vec{I}_{BL}), and bottom-right (\vec{I}_{BR}) corners, is computable as

$$\begin{aligned} \vec{I}_{\text{TL}} &= T_{\text{FD}} * \vec{T}_{\text{to}} + \vec{I}_{\text{CU}} + \vec{I}_{\text{CL}}, \\ \vec{I}_{\text{TR}} &= T_{\text{FD}} * \vec{T}_{\text{to}} + \vec{I}_{\text{CU}} - \vec{I}_{\text{CL}}, \\ \vec{I}_{\text{BL}} &= T_{\text{FD}} * \vec{T}_{\text{to}} - \vec{I}_{\text{CU}} + \vec{I}_{\text{CL}}, \\ \vec{I}_{\text{BR}} &= T_{\text{FD}} * \vec{T}_{\text{to}} - \vec{I}_{\text{CU}} - \vec{I}_{\text{CL}}, \end{aligned} \quad (1)$$

where the vectors \vec{I}_{CU} and \vec{I}_{CL} point away from centre of the image, upwards or leftwards. Both the vectors are shortened by one half of a pixel size as each pixel represents the average colour on its surface. We then have

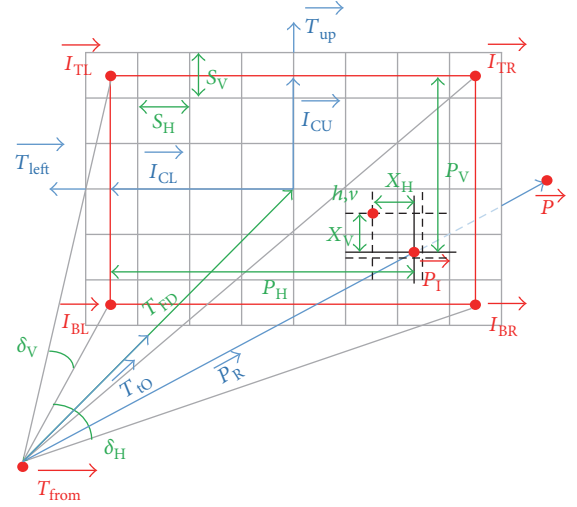


FIGURE 3: The meaning of the main variables from the thermal image mapping algorithm. Here, the red variables are the positional vectors; the blue ones denote the directional vectors; and the green values represent the scalars.

$$\begin{aligned} \vec{I}_{\text{CU}} &= \left(\vec{T}_{\text{up}} * \tan \frac{\delta_V}{2} * |T_{\text{FD}} * \vec{T}_{\text{to}}| \right) * \left(1 - \frac{1}{I_H} \right), \\ \vec{I}_{\text{CL}} &= \left(\vec{T}_{\text{left}} * \tan \frac{\delta_H}{2} * |T_{\text{FD}} * \vec{T}_{\text{to}}| \right) * \left(1 - \frac{1}{I_W} \right), \\ \vec{T}_{\text{left}} &= \text{norm} \left(\vec{T}_{\text{up}} \times \vec{T}_{\text{to}} \right). \end{aligned} \quad (2)$$

The size of a single pixel in the horizontal (S_H) and vertical (S_V) dimensions can be derived as follows:

$$\begin{aligned} S_H &= 2 \frac{\left(\tan (\delta_H/2) * |T_{\text{FD}} * \vec{T}_{\text{to}}| \right)}{I_W}, \\ S_V &= 2 \frac{\left(\tan (\delta_V/2) * |T_{\text{FD}} * \vec{T}_{\text{to}}| \right)}{I_H}. \end{aligned} \quad (3)$$

2.3. Single Image Temperature Mapping. The central concept of the mapping algorithm is to trace the rays between the thermal imager’s origin and each point of the scanned 3D model. For each point of the 3D model, the steps to be taken are as shown in the following portion of the article: this single mapping procedure is performed for each thermal image, resulting in the assignment of several thermal values to each point of the 3D model (the number of the thermal values assigned to a single point is given by the number of those images where the particular point is directly visible).

2.3.1. Checking the Point Visibility. In the initial phase, we need to check whether the point (\vec{P}) lies within the imager’s field of view, namely, if the ray $\vec{P}_R = \vec{P} - \vec{T}_{\text{from}}$ from the imager’s focus to the point intersects the plane in which the thermal image is located (the plane is defined by three arbitrary points from the image corner points \vec{I}_{TL} , \vec{I}_{TR} , \vec{I}_{BL} , and \vec{I}_{BR}).

If we find an intersection point (\vec{P}_1), the algorithm is left to continue; otherwise, we skip the related following steps and continue with step 1 for the next point of the 3D model.

Then, it has to be established whether \vec{P}_1 lies within the thermal image rectangle. This is true when all the following conditions are satisfied [20]:

$$\begin{aligned} \text{norm}(\vec{I}_{BR} - \vec{I}_{BL}) \cdot \text{norm}(\vec{P}_1 - \vec{T}_{\text{from}} - \vec{I}_{BL}) &> 0, \\ \text{norm}(\vec{I}_{TR} - \vec{I}_{BR}) \cdot \text{norm}(\vec{P}_1 - \vec{T}_{\text{from}} - \vec{I}_{BR}) &> 0, \\ \text{norm}(\vec{I}_{TL} - \vec{I}_{TR}) \cdot \text{norm}(\vec{P}_1 - \vec{T}_{\text{from}} - \vec{I}_{TR}) &> 0, \\ \text{norm}(\vec{I}_{BL} - \vec{I}_{TL}) \cdot \text{norm}(\vec{P}_1 - \vec{T}_{\text{from}} - \vec{I}_{TL}) &> 0. \end{aligned} \quad (4)$$

If, however, the above items are not fulfilled, we skip again.

2.3.2. Checking the 3D Model Crossing. Satisfying the conditions above does not suffice to determine if a point is *directly* visible, as that point can be hidden behind a part of the 3D model. Thus, we are obliged to check if the ray \vec{P}_R intersects the 3D model or not.

The simplest procedure to find the intersection consists in verifying whether the ray \vec{P}_R intersects *any* of the triangles which constitute the 3D model. To check the ray-triangle intersection, the algorithm from source [21] is used.

The algorithm iterates throughout all the triangles. When the ray-triangle intersection is located, the iteration stops, and we skip. With all the triangles checked without the intersection found, the point \vec{P} is *directly* visible from \vec{T}_{from} , and we continue with the last step; otherwise, the stage is skipped.

2.3.3. Mapping the Temperature Values to the Point. After the direct visibility has been proved, the temperature value for the given point is computed as the linear interpolation between the 4 nearest neighbouring pixels, taking into account the distance from the intersection \vec{P}_1 to the pixels.

The indices (the horizontal index h and vertical index v) of the nearest pixel from \vec{P}_1 in the top-left direction are determined as follows:

$$\begin{aligned} h &= \text{floor}\left(\frac{P_H}{S_H}\right), \\ v &= \text{floor}\left(\frac{P_V}{S_V}\right), \\ P_H &= \left| \text{norm}(\vec{I}_{BL} - \vec{I}_{TL}) \times (\vec{P}_1 - \vec{T}_{\text{from}} - \vec{I}_{TL}) \right|, \\ P_V &= \left| \text{norm}(\vec{I}_{TL} - \vec{I}_{TR}) \times (\vec{P}_1 - \vec{T}_{\text{from}} - \vec{I}_{TR}) \right|. \end{aligned} \quad (5)$$

The distance of the intersection \vec{P}_1 from this pixel (expressed as a percentage of the pixel size) in the horizontal (X_H) and vertical (X_V) directions is

$$\begin{aligned} X_H &= \frac{P_H \bmod S_H}{S_H}, \\ X_V &= \frac{P_V \bmod S_V}{S_V}. \end{aligned} \quad (6)$$

The temperature t_p belonging to the point P is then interpolated from the temperatures of the neighbouring pixels $t_{h,v}$, $t_{h+1,v}$, $t_{h,v+1}$, and $t_{h+1,v+1}$:

$$t_p = \text{interp}(\text{interp}(t_{h,v}, t_{h,v+1}, X_H), \text{interp}(t_{h+1,v}, t_{h+1,v+1}, X_H), X_V), \quad (7)$$

$$\text{interp}(t_1, t_2, d) = (1 - d) * t_1 + d * t_2.$$

2.4. Combining Multiple Mapped Images. The temperature mapping procedure outlined in the previous section assigns several temperature values to each point visible in the thermal image. If more overlapping thermal images are mapped, then a correspondingly increased count of values is assigned to a single point of the 3D model.

Pursuing the development of medical thermography, we use long-wave infrared thermal imagers (LWIR) to detect the thermal radiation from the scene; such radiation consists of the reflected and the emitted forms [22]. The typical emissivity of a naked human body ranges between 0.93 and 0.96 [23], meaning that the major part of the radiation detected by a thermal imager consists in the emitted form; reflected radiation thus plays a minor role.

Our experiments also show the validity of this claim in that the values belonging to a single point of the 3D model, acquired via the images captured from several different orientations, varied at the sensor noise level only. Thus, the thermal radiation reflection can be considered negligible.

The final point temperature value is thus simply computable as the average temperature from all the values associated with the particular point.

2.5. Optimizing the Algorithm Performance. Even though the algorithm to check the ray-triangle intersection [21] is very fast, iterating throughout the entire set of triangles remains significantly slow.

The procedure execution time can be markedly decreased by a hierarchical structure allowing us not to check triangles remote from the ray. The presented algorithm exploits a modification of the octree data structure, facilitating the partitioning of the 3D space by recursive subdivision into eight octants [24, 25].

The minimal rectangular spatial area aligned with the axes into which the model extends is divided into a number of same-sized cubes. The triangles of the 3D model are split to form cubes respecting their relevant locations in the 3D space. To enable the assignment to a cube, at least one point of a triangle shall be in its spatial area.

Every eight neighbouring cubes are encapsulated in a bounding box with a double-length edge; such boxes are then encapsulated in another bounding box and so forth. If a cube does not have an assigned triangle, it is completely removed, similarly to a bounding box with no child cube. If a bounding

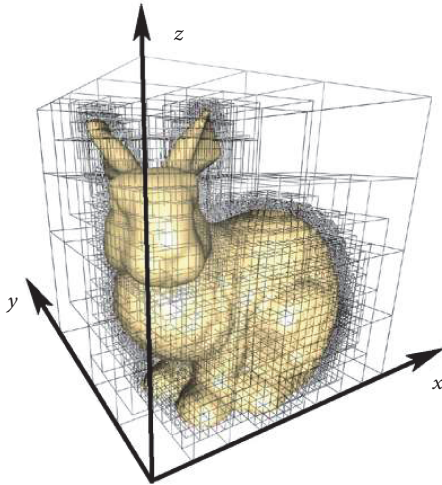


FIGURE 4: The spatial division employed in the octree hierarchical cubes.

box has only one child, it is substituted by that single child. The result is a tree hierarchical structure (Figure 4).

When testing the 3D model intersection, we start at the top-level bounding box, checking the intersection; if a ray crosses, we check the intersection with the 8 subboxes and so on. Using this approach, we finally reach the cubes at the lowest levels, which are intersected by the ray. Only the triangles belonging to these cubes are tested for intersection. The method distinctly decreases the number of tested triangles, exerting a positive effect on the image mapping performance.

As the algorithm computational time depends on multiple parameters, including, for example, the complexity of a particular 3D model, its resolution, thermal image capturing directions, and the order of the points stored in the memory, it is impossible to estimate the computational effort.

To obtain a rough estimate of the optimization performance, we conducted an experiment where an object was scanned by means of a 3D scanner and a thermal imager in exactly the same manner but at different resolutions. The scanned area corresponded to 100×100 mm, with the fixed resolution of 64 points per mm in one axis and the variable resolution of from 0.2 to 20 points in the other. As a result, the number of points fluctuated between 14 thousand and 2.5 million. The results are presented in Figure 5. Here, the grey line indicates the performance without optimization, which grows rapidly even when the resolution still remains very low. The blue line shows the performance in the condition where the octree cube size fixed at 5 mm, a solution linear from the beginning but also exhibiting the tendency towards fast growth with the increasing number of points. The orange line then represents the optimization performance in the scenario of the octree tube adapted according to the average distance between the neighbouring points; this configuration has approximately linear characteristics, pointing to the fact that octree optimization reduces the computational complexity.

3. Results

The result of the data fusion method described above lies in a 3D point cloud or a mesh in the same form as that captured by the 3D scanner, enhanced through the thermal information linked with each point of the digital model.

The experiments showed that combining the 3D spatial and thermal data will yield new diagnostic outcomes unavailable with the 3D scanner and thermal imager used separately.

The algorithms were verified in detailed high-resolution meshes captured via RoScan, a robotic 3D scanner able to provide 3D models having a resolution better than 0.1 mm [8, 26, 27]. The thermal images were taken using a LWIR thermal camera Xenics GOBI1954 with the resolution of 384×288 pixels, pixel pitch of $25 \mu\text{m}$, and spectral response in the wavelength range of 8–14 μm . To establish a computational unit, we employed a desktop computer having an Intel Core i7-4790K processor at 4.00 GHz; 32 GB RAM; and an NVIDIA GeForce GTX 970 GPU.

Due to the octree optimization, the data fusion was quick: the 3D models with 500,000 points merged with the 10 thermal images in only 27 seconds. The resulting data were conveyed in the standard PLY format [28, 29], facilitating the import to multiple 3D analysing software tools; in our experiments, the CloudCompare opensource software was used [30].

The screenshots from the temperature-mapped 3D models are shown in the related images. Figure 6 introduces a high-density 3D model of a hand in the physiological condition, with the thermal 3D image displaying even the tiniest details.

Figure 7 presents an inflamed toe after the injury and following the recovery. The injury induced merely light pain, and no other symptoms were observed. A significant temperature increment of 5.12°C is visible in the 3D scan of the afflicted toe; this bodily part also exhibited the volume increment of 5%. Seventy-four hours later, after the recovery, no symptoms or pain was observed; however, the increased temperature was still present in the toe, indicating that the subject had not fully recovered by then. In this context, let us note that the inflammation appears to be determinable and measurable in its very roots, *before* becoming painful. This finding can benefit, for example, top-class athletes and other sportsmen in their efforts to prevent injuries.

Figure 8 demonstrates the ability to measure objects inside the inner tissue, which are otherwise not observable or measurable via traditional approaches. The subject informed us of the injury approximately 2 months ago, and he mentioned an unusual feeling perceived when touching a hard surface with the afflicted finger. The suspected cause consisted in an encapsulated glass shard of unknown dimensions. Although this location could be examined via MRI or CT, these methods are too expensive if employed for the given purpose. Our approach, then, was significantly cheaper while providing the same information; the thermal data served towards defining the boundaries of the encapsulated shard, and the 3D model facilitated precise measurement of the item's dimensions.

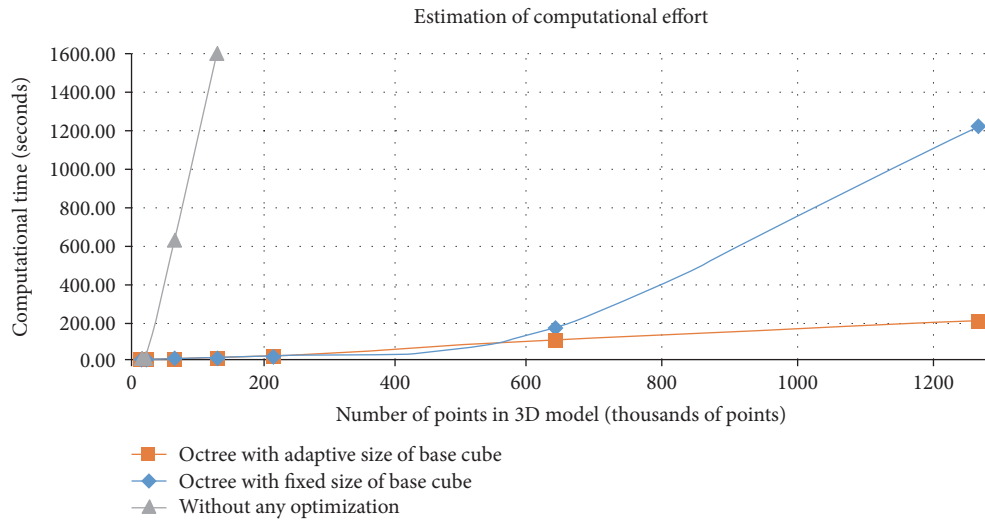


FIGURE 5: A rough estimation of the optimization performance.

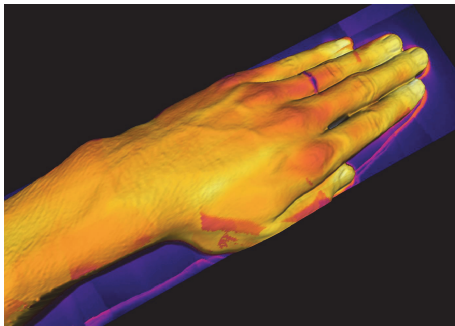


FIGURE 6: A temperature-mapped 3D model of a hand in the physiological condition. Higher temperatures are observable in the vicinity of the vessels and veins, while lower ones can be located around the joints. The high thermal conductivity of the ring cools the element down, even when put on the finger.

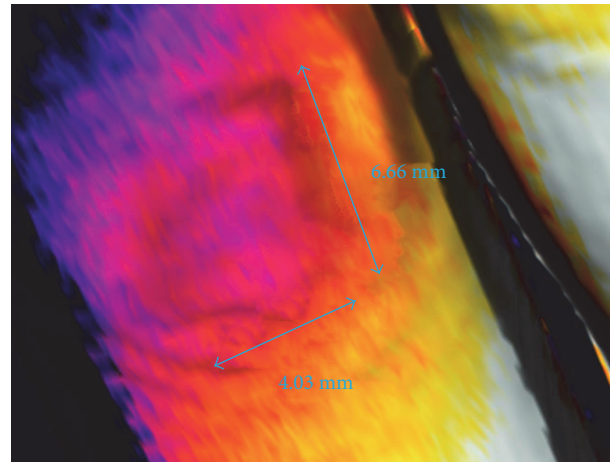


FIGURE 8: Measuring the dimensions of a glass shard encapsulated in the inner tissue of the finger, unobservable via traditional methods.

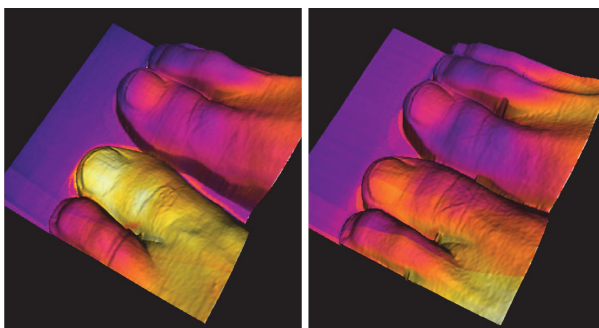


FIGURE 7: (a) A stubbed toe captured 2 hours after the injury; a precise 3D scan enables us to measure the inflamed area and the swelling-induced volume increase. (b) The same scene 74 hours after the injury; the volume and temperature of the toe have decreased.

It has to be stressed that all the diagnostic information acquired in the cases displayed in Figures 7 and 8, that is, the average temperature and dimensions of the selected region, would not have been available without merging the thermal images and the 3D model. This fact then aptly demonstrates the benefits of the proposed technique.

4. Discussion

The described method to merge sets of 2D thermal images with a digital 3D model appears to contribute new diagnostic data unobtainable via traditional methods or through using thermal imaging or 3D scanning separately. The present paper characterizes an algorithm for a general 3D model and images, regardless of the data format. This approach allows us to employ the algorithms also in other research applications or medical diagnostic tools.

Considering its principles, the method is suitable for rendering high-density point clouds or detailed meshes at a

high resolution; conversely, the technique cannot be conveniently utilized in large objects with sparse points.

The benefits of creating 3D thermal models have already been demonstrated on practical experiments with injured subjects. The findings published within article [31] show that thermal imagers constitute a useful, versatile diagnostic tool which, when combined with 3D scanners, significantly increases the amount of data to facilitate precise diagnostics or monitoring.

This method finds use within not only the medical but also the technological domain: the data fusion between thermal imagers and 3D scanners will bring numerous advantages in, for example, robotic rescue systems [32, 33], where the potential of the technique may be exploited for augmented reality [18].

Additional Points

Main Messages. (i) 3D thermal imaging facilitates quantification, a step not performable with 2D thermal imaging. (ii) Combining 3D and thermal imaging yields more useful diagnostic data. (iii) Practical experiments on injured subjects display possible target application cases. (iv) A general recipe for fusing a thermal image and a 3D model is proposed, offering broad usability with common data types.

Conflicts of Interest

The authors declare no competing interest, confirming that the experiments reported in the manuscript were performed pursuant to the ethical standards set forth in the Declaration of Helsinki.

Authors' Contributions

Adam Chromy carried out the research related to 3D scanning and thermal imaging and prepared the corresponding portion of this manuscript. Ondrej Klima researched the data processing optimization, designed and evaluated the experiments, and prepared the corresponding portion of the manuscript. The authors have read, reviewed, and approved the final manuscript.

Acknowledgments

The research was supported by Grants no. FEKT-S-17-4234 ("Industry 4.0 in automation and cybernetics") and no. FEKT/FIT-J-17-4745 ("Intermodal 3D data registration in healthcare"), both funded by the Internal Science Fund of Brno University of Technology.

References

- [1] V. C. Coffey, "Multispectral imaging moves into the mainstream," *Optics & Photonics News*, vol. 23, no. 4, pp. 18–24, 2012.
- [2] J. T. Hardwicke, O. Osmani, and J. M. Skillman, "Detection of perforators using smartphone thermal imaging," *Plastic and Reconstructive Surgery*, vol. 137, no. 1, pp. 39–41, 2016.
- [3] R. Vardasca and R. Simoes, "Current issues in medical thermography," in *Topics in Medical Image Processing and Computational Vision*, pp. 223–237, Springer, Dordrecht, 2013.
- [4] X. Ju, J.-C. Nebel, and J. P. Siebert, "3D thermography imaging standardization technique for inflammation diagnosis," in *Proceedings Volume 5640, Infrared Components and Their Applications*, p. 266, 2005.
- [5] T.-C. Chang, Y.-L. Hsiao, and S.-L. Liao, "Application of digital infrared thermal imaging in determining inflammatory state and follow-up effect of methylprednisolone pulse therapy in patients with Graves' ophthalmopathy," *Graefes Archive for Clinical and Experimental Ophthalmology*, vol. 246, no. 1, pp. 45–49, 2008.
- [6] J. H. Park, "Digital restoration of Seokguram Grotto: the digital archiving and the exhibition of South Korea's representative UNESCO world heritage," in *2012 International Symposium on Ubiquitous Virtual Reality (ISUVR)*, vol. 2012, pp. 26–29, Adaejeon, South Korea, 2012.
- [7] S. Klein, M. Avery, G. Adams, A. Guy, P. Stephen, and S. Steve, "From scan to print: 3D printing as a means for replication," in *2014 International Conference on Digital Printing Technologies*, 2014.
- [8] A. Chromy and L. Zalud, "Robotic 3D scanner as an alternative to standard modalities of medical imaging," *SpringerPlus*, vol. 3, no. 1, p. 13, 2014.
- [9] L. Zalud and P. Kocmanova, "Fusion of thermal imaging and CCD camera-based data for stereovision visual telepresence," in *2013 IEEE International Symposium on Safety, Security, and Rescue Robotics (SSRR)*, Linkoping, Sweden, 2013.
- [10] F. Bernardini and H. Rushmeier, "The 3D model acquisition pipeline," *Computer Graphics Forum*, vol. 21, no. 2, pp. 149–172, 2002.
- [11] M. de Berg, M. van Kreveld, and M. Overmars, *Computational Geometry: Algorithms and Applications*, Springer, Berlin, 3rd edition, 2008.
- [12] Z. C. Marton, R. B. Rusu, and M. Beetz, "On fast surface reconstruction methods for large and noisy point clouds," in *2009 IEEE International Conference on Robotics and Automation*, pp. 3218–3223, Kobe, Japan, 2009.
- [13] M.-B. Chen, "A parallel 3D Delaunay triangulation method," in *2011 IEEE Ninth International Symposium on Parallel and Distributed*, pp. 52–56, Busan, South Korea, 2011.
- [14] T. Williams, *Thermal Imaging Cameras: Characteristics and Performance*, CRC Press, 2009.
- [15] A. Chromy, "Application of high-resolution 3D scanning in medical volumetry," *International Journal of Electronics and Telecommunications*, vol. 62, no. 1, pp. 23–31, 2016.
- [16] S. Rusinkiewicz and M. Levoy, "Efficient variants of the ICP algorithm," in *Proceedings Third International Conference on 3-D Digital Imaging and Modeling*, 2001, pp. 145–152, Quebec City, Quebec, Canada, 2001.
- [17] A. Chromy, *Mutual Calibration of Sensors for Multispectral 3D Scanning of Surface*, 2017.
- [18] P. Kocmanova and L. Zalud, "Spatial calibration of TOF camera, thermal imager and CCD camera," *Mendel 2013: 19th International Conference on Soft Computing*, 2013, pp. 343–348, 2013.
- [19] F. Burian, P. Kocmanova, and L. Zalud, "Robot mapping with range camera, CCD cameras and thermal imagers," in *2014 19th International Conference On Methods and*

- Models in Automation and Robotics (MMAR)*, pp. 200–205, Miedzzydroje, Poland, 2014.
- [20] R. Szeliski, *Computer Vision: Algorithms and Applications*, Springer Science & Business Media, 2010.
- [21] T. Möller and B. Trumbore, “Fast, minimum storage ray/triangle intersection,” in *Proceeding SIGGRAPH '05 ACM SIGGRAPH 2005 Courses*, Los Angeles, California, July-August, 2005.
- [22] J. S. Trefil, *The Nature of Science: An A-Z Guide to the Laws and Principles Governing Our Universe*, Houghton Mifflin Harcourt, 2003.
- [23] P. O. Fanger, *Thermal Comfort. Analysis and Applications in Environmental Engineering*, 1970.
- [24] T. L. Kunii, *Frontiers in Computer Graphics: Proceedings of Computer Graphics Tokyo '84*, Springer Science & Business Media, 2012.
- [25] P. Kocmanova, L. Zalud, and A. Chromy, “3D proximity laser scanner calibration,” in *2013 18th International Conference on Methods and Models in Automation & Robotics (MMAR)*, pp. 742–747, Miedzzydroje, Poland, 2013.
- [26] A. Chromy, P. Kocmanova, and L. Zalud, “Creating three-dimensional computer models using robotic manipulator and laser scanners,” in *12th IFAC Conference on Programmable Devices and Embedded Systems*, pp. 268–273, Elsevier B.V, Velke Karlovice, 2013.
- [27] A. Chromy and L. Zalud, “Novel 3D modelling system capturing objects with sub-millimetre resolution,” *Advances in Electrical and Electronic Engineering*, vol. 12, no. 5, pp. 476–487, 2014.
- [28] P. Bourke, “PLY - polygon file format,” 2009, November 2016, <http://paulbourke.net/dataformats/ply/>.
- [29] M. Isenburg and P. Lindstrom, “Streaming meshes,” in *VIS 05. IEEE Visualization, 2005*, pp. 231–238, Minneapolis, MN, USA, 2005.
- [30] D. Girardeau-Montaut, “CloudCompare - open source project,” 2016, November 2016, <http://www.danielgm.net/cc/>.
- [31] G. Melvin, “Thermography gallery,” *Thermal Imaging of the Southwest*, 2016.
- [32] L. Zalud, “ARGOS - system for heterogeneous mobile robot teleoperation,” in *2006 IEEE/RSJ International Conference on Intelligent Robots and Systems*, pp. 211–216, Beijing, China, 2006.
- [33] L. Zalud, L. Kopecny, and F. Burian, “Orpheus reconnaissance robots,” in *2008 IEEE International Workshop on Safety, Security and Rescue Robotics, SSRR 2008*, pp. 31–34, Sendai, Japan, 2008.

Research Article

The Efficacy of a Haptic-Enhanced Virtual Reality System for Precision Grasp Acquisition in Stroke Rehabilitation

Shih-Ching Yeh,¹ Si-Huei Lee,² Rai-Chi Chan,² Yi Wu,³ Li-Rong Zheng,¹ and Sheryl Flynn⁴

¹School of Information Science and Technology, Fudan University, Shanghai City, China

²Department of Physical Medicine and Rehabilitation, Taipei Veterans General Hospital, Taiwan and National Yang-Ming University, Taipei, Taiwan

³Department of Rehabilitation Medicine, Huashan Hospital, Fudan University, Shanghai, China

⁴Blue Marble Game Ltd., Los Angeles, USA

Correspondence should be addressed to Si-Huei Lee; leesihuei@gmail.com

Received 2 June 2017; Revised 18 August 2017; Accepted 20 September 2017; Published 5 November 2017

Academic Editor: Yi-Hung Liu

Copyright © 2017 Shih-Ching Yeh et al. This is an open access article distributed under the Creative Commons Attribution License, which permits unrestricted use, distribution, and reproduction in any medium, provided the original work is properly cited.

Stroke is a leading cause of long-term disability, and virtual reality- (VR-) based stroke rehabilitation is effective in increasing motivation and the functional performance. Although much of the functional reach and grasp capabilities of the upper extremities were regained, the pinch movement remains impaired following stroke. In this study, we developed a haptic-enhanced VR system to simulate haptic pinch tasks to assist the recovery of upper-extremity fine motor function. We recruited 16 adults with stroke to verify the efficacy of this new VR system. Each patient received 30 min VR training sessions 3 times per week for 8 weeks. Outcome measures, Fugl-Meyer assessment (FMA), Test Evaluant les Membres superieurs des Personnes Agees (TEMPA), Wolf motor function test (WMFT), Box and Block test (BBT), and Jamar grip dynamometer, showed statistically significant progress from pretest to posttest and follow-up, indicating that the proposed system effectively promoted fine motor recovery of function. Additionally, our evidence suggests that this system was also effective under certain challenging conditions such as being in the chronic stroke phase or a coside of lesion and dominant hand (nondominant hand impaired). System usability assessment indicated that the participants strongly intended to continue using this VR-based system in rehabilitation.

1. Introduction

Stroke is a leading cause of long-term disability [1] with up to 76% of people with stroke experiencing a paralysis of the upper limbs at onset [2]. Although rehabilitation programs can enhance the recovery of upper-limb function, the effectiveness of therapeutic interventions is generally less pronounced in the upper limbs than in the lower limbs [3]; 55%–75% of stroke survivors continue to experience functional limitations in their upper extremities 3–6 months after a stroke [4–7]. Functional recovery in the paretic upper limbs typically exhibits a proximal-to-distal gradient, which results in hand function being poorer than arm function [8]. However, functional recovery of the upper limbs after a stroke is primarily determined by the improvement of the paretic hand. Faria-Fortini et al. [9] reported that in people with

chronic stroke, grip and pinch strength are more related to upper-limb function than to proximal-end strength. Thus, efforts to improve hand and finger strength should be emphasized in rehabilitation programs. Although stroke survivors often regain most of the functional reach and grasp capabilities in their upper extremities, the recovery of the pinch skill remains incomplete in the majority of patients. Pinch movements represent an important upper-extremity motor skill [10, 11], and impaired pinch substantially affects a persons' dexterity after a stroke.

Regarding the mechanism of motor improvement, recent evidence indicates that highly repetitive and task-specific trainings may induce cortical reorganization and improve motor recovery. Functional magnetic resonance imaging- (MRI-) based research has demonstrated that VR training systems induce cortical reorganization in stroke patients

[12, 13]. The mere repetition of simple tasks that lie within the capability of the performer, however, is unlikely to induce neural plasticity and learning [14]. Thus, task-oriented training programs should be (1) adequately challenging to require new learning, (2) progressive and optimally adapted to each person's capability, and (3) sufficiently stimulating to invite active participation. Creating realistic and demanding practice environments, however, is often challenging and can be limited by a facility's financial resources. Consequently, virtual reality (VR) offers numerous advantages in rehabilitation settings. VR can be used to transform tedious repetitive tasks into engaging, functional, and challenging activities, and the difficulty of tasks can be graded according to a person's ability. By providing engaging skill training and immediate appropriate and accurate performance feedback through visual and auditory rewards, virtual rehabilitation increases a person's motivation to practice tasks [15].

Although numerous VR training systems have been developed for retraining upper-extremity functions post stroke, only a few systems have been designed to retrain hand function [16–20]. Furthermore, among the VR systems developed to retrain hand function, several designs are excessively complex for clinical use [16–18]. Installing hardware is also technically challenging, and people with stroke may require help donning the hand-tracking apparatus, which can make the process time-consuming. Moreover, the hardware used in VR systems, such as haptic devices and hand-tracking gloves, is expensive, which limits the use of these systems in rehabilitation settings. Furthermore, several VR systems do not incorporate haptics for the provision of sensory feedback [20, 21]. Sensory feedback obtained from the performance of everyday tasks is crucial for improving hand function. Incorporating haptic feedback into VR systems not only enables users to observe how they are manipulating virtual objects but also helps them experience a realistic sense of touch in the virtual environment. Moreover, VR systems integrated with haptics that provide users the feedback of proprioception can potentially help with the enhancement of motor control and muscle strength.

Novint Falcon™ (Novint Technologies Inc®, US) [22] is a commercially available, cost-effective robot arm that serves as a haptic interface. By generating forces that exhibit 3 degrees of freedom, Novint Falcon can simulate complex mechanics and produce force sensations that users perceive to be real. In this study, we employed dual-Novint Falcon devices to create a novel haptic interface to develop a stroke rehabilitation system that simulates pinch tasks and strengthens the hands and fingers to enhance the therapeutic benefit. Our objectives in this study were to (1) develop a novel haptic-enhanced VR training system for use in stroke rehabilitation, (2) determine the efficacy of the proposed system, and (3) examine the usability of the proposed system. Our hypothesis was that the proposed VR system integrated with haptics is able to improve fine motor functions effectively.

2. Method and Materials

2.1. Haptic-Enhanced Virtual Reality System. Developing the system described here involved implementing 3 subsystems

that covered VR tasks, haptic simulation, and a user-machine interface. The system architecture is shown in Figure 1. Based on a task-oriented therapy design, the VR tasks were formulated to ensure that pinch movements were required to complete each task and that the patients experienced finger strengthening. Two VR tasks were implemented using the 3D game engine Unity™ (Unity Technologies@US), which is a state-of-the-art toolkit used for developing 3D games deployed on multiple operating systems. The first task was a “pinch strengthening” task, in which participants were required to grip a virtual box by using 2 fingers, the thumb+each finger. The participants gradually increased their pinch strength until the default strength setting used for the simulation was achieved. The second task was a “pinch and lift” task, in which participants were required to grip a virtual box with two fingers (thumb+index and thumb+middle fingers) and lift the weighted box to a default height. In the proposed system, 2 Novint Falcon devices operated in coordination to simulate the haptic perceptions of 2 fingertips. In both tasks, the haptic simulation was implemented in such a manner that the participants perceived the reaction force of the surface and/or the weight of the box. A maximum of 20 seconds was allowed for each trial. A series of dynamically adjusted hierarchical challenges was also incorporated into the two VR tasks, based upon the severity of the participant's motor injury. In this study, we designed a user-machine interface that separately linked two of the participants' fingers with Novint Falcon, which allowed the participants to perform the pinch-skill tasks naturally, without exerting additional effort and to fully experience the effects of the haptic simulations. This user-machine interface is adaptable to various finger combinations.

2.2. Study Participants. We recruited 16 participants with hemiparesis and motor impairment due to stroke. Participants were included if (1) they had a first-time hemiparetic stroke recorded in the previous 2 years; (2) they obtained a physician's diagnosis of stroke that was confirmed based on the findings of neurological examinations and brain-imaging technologies (MRI or computed tomography (CT) scans); (3) they were aged between 20 and 85 years; (4) their proximal upper extremity on the more affected side was in Brunnstrom Stages II–VI; (5) they had no cognitive dysfunction, as measured using the Mini-Mental State Examination (MMSE ≥ 20) [23]; and (6) they were willing to participate in the study and sign the informed consent form. We excluded volunteers (1) with unstable vital signs; (2) who exhibited irreversible contracture of any joints of the impaired upper extremities; (3) who experienced a surgery, fracture, arthritis, or pain that may influence the recovery of upper-extremity function; (4) who exhibited spasticity (>2 on the modified Ashworth scale); (5) with uncontrolled poststroke seizures; and (6) who had experienced a heart attack in the previous 3 months. The Institutional Review Board of Taipei Veterans General Hospital, Taiwan, approved the consent procedure. The participant demographics are described in Table 1.

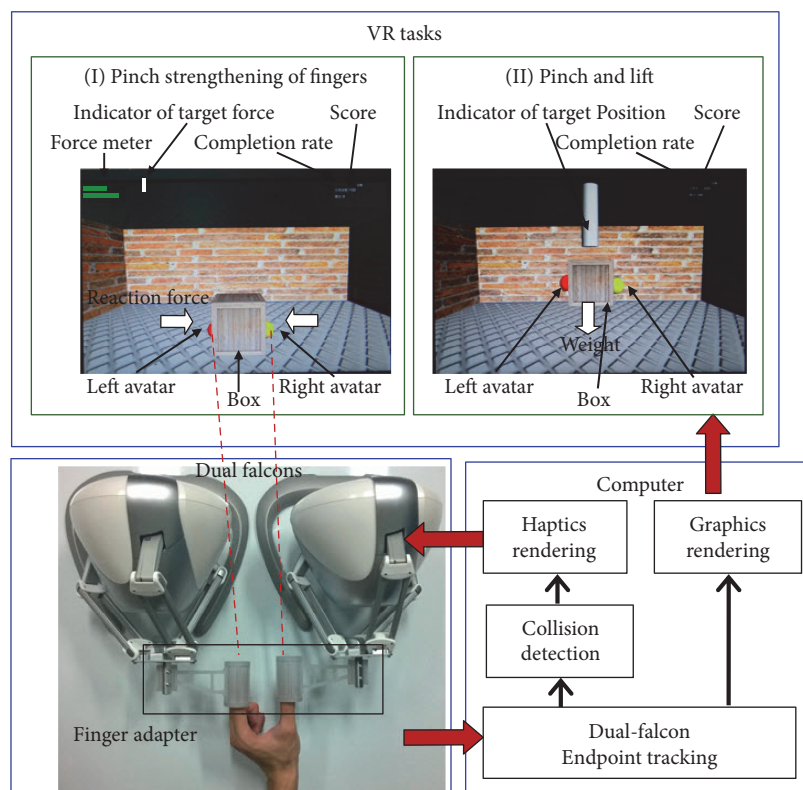


FIGURE 1: System architecture.

2.3. Intervention. An experienced occupational therapist supervised the haptics-based VR rehabilitation. The participants attended 30 min stroke-rehabilitation sessions three times per week for eight weeks, and all participants completed the 24 training sessions. To avoid fatigue, consecutive training sessions were conducted 24 hours apart. Each VR training session involved practicing the two VR tasks, the pinch-strengthening, and pinch-and-lift tasks. The pinch-strengthening task was performed 20 times using the thumb and each finger. The pinch-and-lift task was performed 20 times each using the thumb and the index finger, and the thumb and the middle finger. When performing the VR tasks, the participants were seated with their forearms resting on a height-adjustable table, shoulder in slight abduction, elbow at 90° flexion, and the forearm in a neutral position. Following each attempt, the occupational therapist increased the task difficulty according to the participant's abilities. As their ability increased, the level of difficulty was gradually increased. Clinical assessments were performed by an occupational therapist, with over 3 years of experience, who was not involved in treating the patients. Assessments were conducted three days before training (0 week), within three days after training (eight-week endpoint), and at a one-month follow-up session (12-week endpoint).

2.4. Measurements. The Fugl-Meyer assessment (FMA) [24] featuring wrist and hand portions was used to evaluate motor impairment (maximal score = 24). To measure upper-extremity function, we used the Wolf motor function test (WMFT) [25] that features four items that require distal

control (*lift pencil, lift paper clip, stack checker, and turn a key in lock*; max = 20) and the Test Evaluant les Membres superieurs des Personnes Agees (TEMPA) [26] that features four items also involving distal control (*prehension: handling coins, picking up, and moving small objects; precision of fine motor movements: handling coins, picking up, and moving small objects*; -12~0). The Box and Blocks test (BBT) [27] was used to evaluate manual dexterity as measured by the number of blocks moved from one side to the next. Strength was measured using handheld dynamometers (JAMAR [28]). System usability was evaluated through Users' Technology Acceptance questionnaire [29–31], which includes dimensions of usefulness, ease of use, intention to use, and playfulness. Each item in the questionnaire was rated using a 5-point Likert scale. Finally, kinematic and kinetic data were recorded for the two fingertips using position and force in three dimensions.

2.5. Analysis Methods. Statistical analysis was performed on scores of clinical measurements at pretests, posttests, and follow-up in order to investigate the efficacy of the proposed system. The Wilcoxon rank sum test was applied in the statistical analysis of paired samples. The statistical tool SPSS™ was used to perform the statistical analysis.

3. Results

3.1. Clinical Measures. Efficacy is used to determine if an intervention produces the expected result under ideal (often laboratory) environments or circumstances. To investigate

TABLE 1: Demographic data of each participant.

ID	Sex	Age	Stroke duration (month)	Hand dominance	Type of stroke	Lesion side	Lesion location	Brunnstrom stage (distal)
1	F	82	1	R	Ischemic	L	MCA	3
2	M	72	15	R	Ischemic	R	PCA	3
3	M	68	12	R	Hemorrhage	R	PCA	4
4	M	53	2	R	Hemorrhage	L	MCA	2
5	M	59	1	R	Ischemic	L	MCA	5
7	M	39	16	R	Hemorrhage	R	MCA	3
8	M	60	18	R	Hemorrhage	R	MCA	2
9	M	65	8	R	Ischemic	R	MCA	4
10	F	38	5	R	Hemorrhage	R	PCA	4
11	M	58	4	R	Ischemic	L	MCA	5
13	F	44	11	L	Ischemic	R	MCA	4
15	F	61	4	R	Ischemic	L	MCA	4
16	F	33	6	R	Ischemic	L	MCA	2
33	M	28	14	L	Hemorrhage	R	MCA	3
34	M	69	3	R	Hemorrhage	R	PCA	6
35	F	60	1	R	Ischemic	L	MCA	2

TABLE 2: Results of Wilcoxon rank sum test on clinical measures: pretest versus posttest ($N = 16$).

Measure	Pretest mean (SD)	Posttest mean (SD)	z value	Significance
FMA	7.69 (5.97)	10.31 (7.35)	-2.994	<0.01
TEMPA	-9.63 (2.75)	-8.44 (3.29)	-2.422	<0.01
WMFT	9.13 (5.55)	10.75 (4.77)	-2.283	<0.05
BBT	13.00 (13.68)	16.06 (15.06)	-2.810	<0.01
JAMAR	7.71 (6.48)	10.36 (7.81)	-1.707	<0.05

the efficacy of the proposed system, the scores of the pretests and posttests of the clinical measurements were analyzed (Table 2). The results indicated that the progress was statistically significant in FMA, TEMPA, WMFT, BBT, and JAMAR (all $P < 0.05$), with the progression rate of the scores being 34%, 12%, 18%, 24%, and 34%, respectively. Moreover, we analyzed the scores of the pretest and the follow-up test to assess the retention of the training obtained using the VR system presented here (Table 3); these results also indicated statistically significant progress in FMA, TEMPA, BBT, and JAMAR, with the scores progressing by 30%, 8%, 19%, and 24%, respectively. Although not significant ($P = 0.17$), the WMFT mean scores at the follow-up test were higher than those at the pretest, with the progression rate being 6%.

The participants in this study were divided into groups according to their conditions so that the effect of using the VR system could be investigated in relation to each condition. First, the participants were grouped according to the duration since the first stroke occurred: acute, 0–3 months ($n = 5$); subacute, 4–6 months ($n = 4$); and chronic, 7 or more months ($n = 7$). The results of the clinical measurements obtained for each group at pretest, posttest, and follow-up are presented in Figure 2. Participants in the acute-stage group showed statistically significant progress

TABLE 3: Results of Wilcoxon rank sum test on clinical measures: pretest versus follow-up ($N = 16$).

Measure	Pretest mean (SD)	Follow-up mean (SD)	z value	Significance
FMA	7.69 (5.98)	10.00 (7.29)	-2.455	<0.01
TEMPA	-9.63 (2.75)	-8.81 (3.47)	-1.916	<0.05
WMFT	9.13 (5.55)	9.68 (4.6)	-0.954	0.17
BBT	13.00 (13.68)	15.44 (13.93)	-2.242	<0.05
JAMAR	7.71 (6.48)	9.59 (7.42)	-1.733	<0.05

in scores from pretest to posttest in FMA, TEMPA, and BBT, and they further showed statistically significant preservation of the training effect from pretest to follow-up in FMA, BBT, and JAMAR. Participants at the subacute stage showed statistically significant progress from pretest to posttest in the scores of FMA, TEMPA, WMFT, and JAMAR, whereas participants in the chronic stage showed statistically significant BBT progress at both posttest and follow-up with respect to pretest. Second, the participants were grouped according to the sides of lesion and hand dominance, which were either coside (right and right or left and left) or alternated side (right and left or left and right) and were denoted as same side (SS) and different side (DS), respectively (SS: $N = 7$; DS: $N = 9$). The results of the clinical measurements obtained for each group at pretest, posttest, and follow-up are presented in Figure 3. In the DS group, significant progress from pretest to posttest was observed across all 5 measures, whereas in the SS group, statistically significant progress was identified in BBT at both posttest and follow-up with respect to the pretest.

3.2. *Synchronization of Kinematic and Kinetic Data to Interpret Behavior.* The kinematic data (positions in 3D) and kinetic data (force in 3D) of the two fingertips were

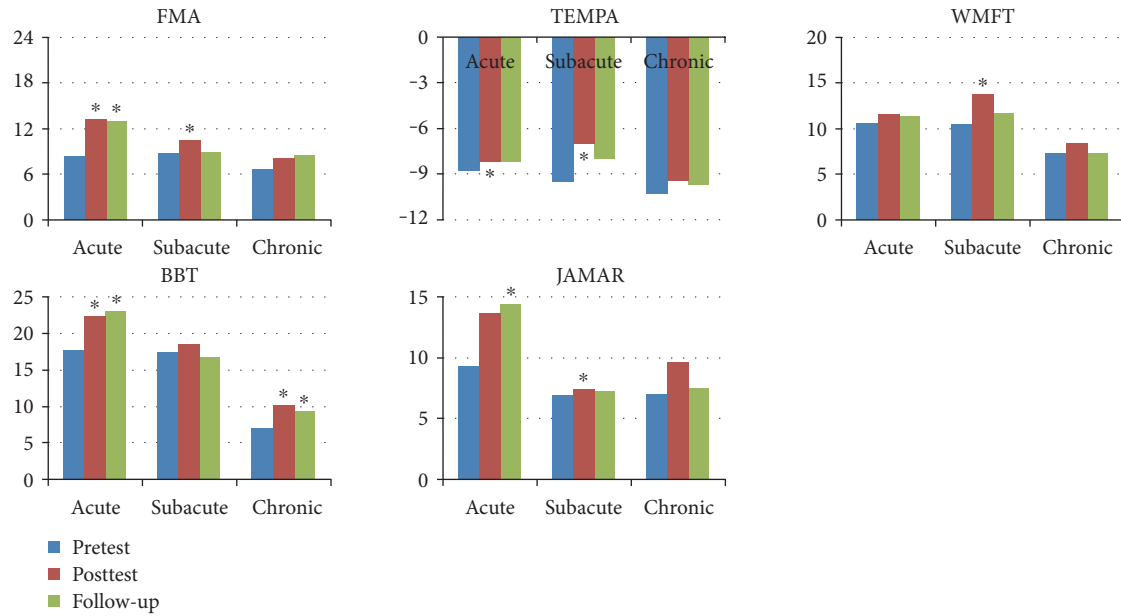


FIGURE 2: Group result: duration since stroke first hit (* significance of P value less than 0.05).

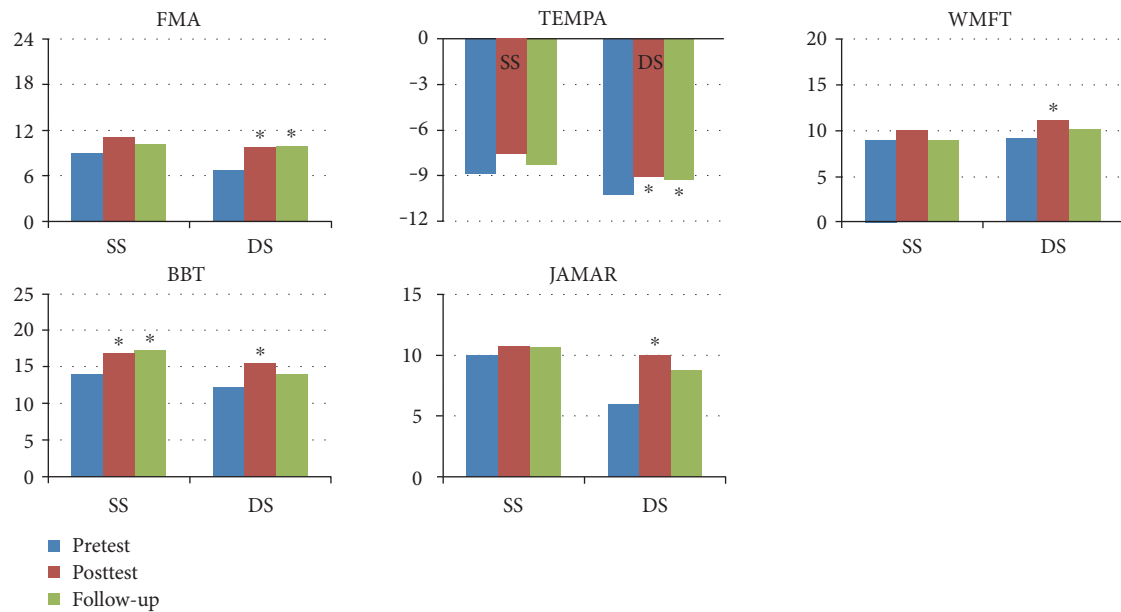


FIGURE 3: Group result: combination of lesion side and hand dominance. SS: lesion side and hand-dominance side are the same; DS: lesion side and hand-dominance side are different (* significance of P value less than 0.05).

synchronized along the same timeline to divide compound behaviors into several monobehavioral phases to facilitate their interpretation. A sample dataset acquired while participants were performing the two VR tasks is presented in Figure 4. In the pinch-strengthening task, two monobehavioral phases were detected (Figure 4(a)). The first phase started at the beginning of the task and ended when the two fingers were concurrently in contact with the target cube and the reaction forces were perceived to be horizontal. At this point, the second phase began, in which the participant gradually increased the strength of the two fingers until

the strength required for this trial was reached. In the pinch-and-lift task, three monobehavioral phases were detected (Figure 4(b)). The first phase was similar to the first phase in the pinch-strengthening task. During the second phase, the participant gradually increased the pinch strength to enhance the friction applied and overcome the cube weight so as to lift the target cube, marking the end of the second phase. While experiencing the reaction force and the cube weight during the third phase, the participant gradually moved the target cube upward until it reached the required height set in this trial.

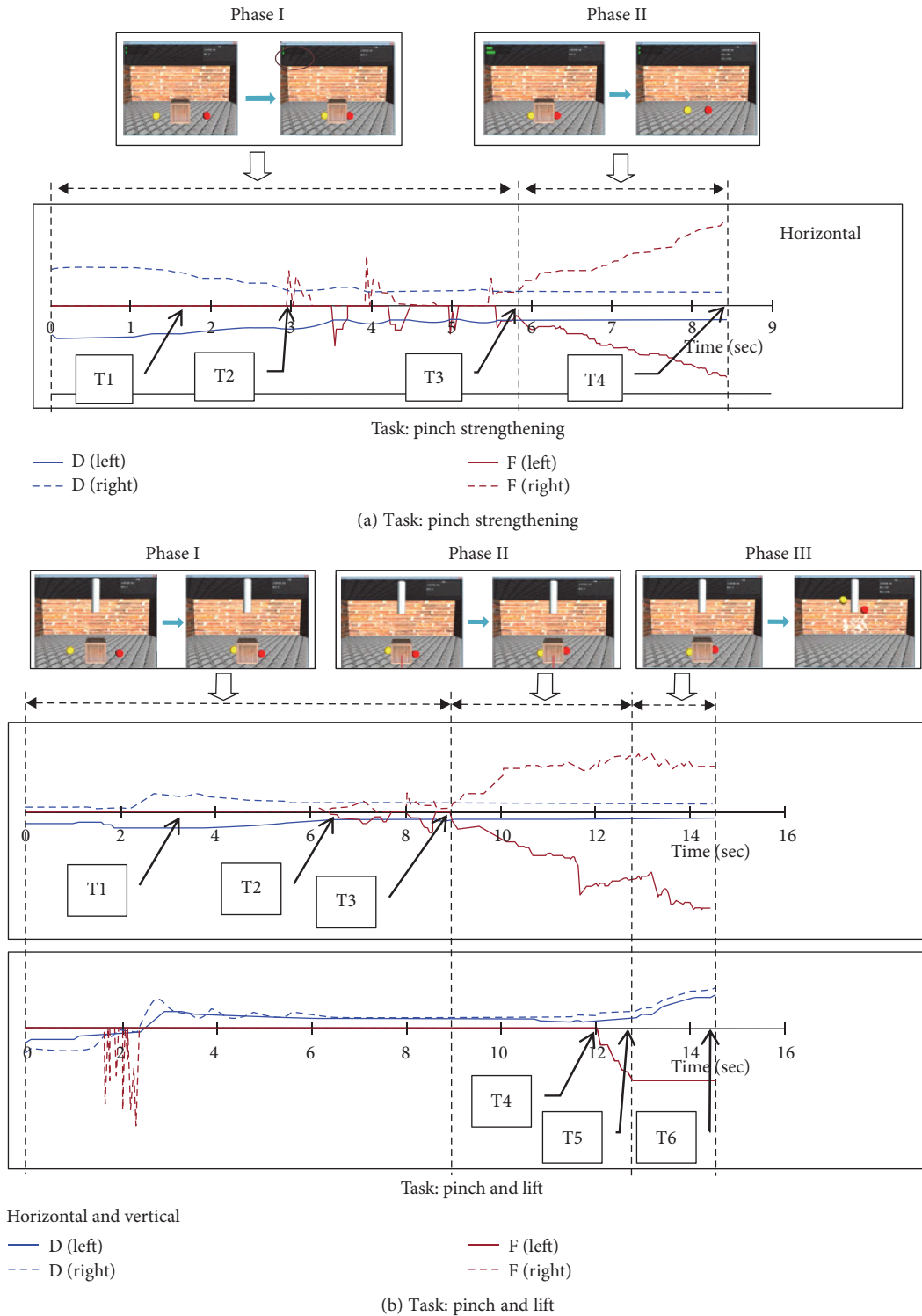


FIGURE 4: Behavior interpretation from synchronized kinematic and kinetic data being changed over time.

3.3. System Usability. The results of system usability evaluation, which featured four dimensions, were all higher than 4.0 points (Table 4), indicating that the participants considered the system to be useful, playful, easy to use, and that they strongly intended to continue using this VR system in rehabilitation.

4. Discussion

The key element addressed in this system was the haptic-enhanced simulation that was integrated with VR tasks to facilitate fine motor rehabilitation. We focused on 3 questions when conducting this study: (1) what are the types of

TABLE 4: Results of user usability evaluation.

	Usefulness	Playfulness	Intention to use	Ease of use
Mean (SE)	4.35 (0.55)	4.47 (0.61)	4.85 (0.28)	4.19 (0.53)

haptic system proposed previously to support fine motor rehabilitation? This addressed whether the type of system developed here was novel; (2) how might the haptic system be applied to the upper extremity while working coordinately with VR? This addressed how the haptics applied in this study might be more effective in fine motor rehabilitation than that which has been applied previously; and (3) what is the cost of existing haptic systems that support fine motor rehabilitation? This addressed whether the system developed in this study has the potential to be used widely in clinics.

Regarding the types of haptic system used for fine motor rehabilitation in previous studies, diverse haptic systems were proposed, in which force sensation was provided using a pneumatic glove [32, 33], a hand exoskeleton [16, 34, 35], a full-scale arm-like robotic exoskeleton [35–37], a cable-enabled glove [33], or a hand-held stylus [38]. Compared with the designs used in these studies, the design of our system and the included VR tasks is novel and distinct because the design integrated *dual* robot arms that required 2 fingers to work synchronously (i.e., the dual robot arms worked coordinately), and therefore the pinch task had to be completed precisely. Regarding the manner in which haptic systems are applied to the upper extremity while working with VR, 3 conditions can be identified in previous studies: (1) no haptics (pure VR) [39]; (2) haptics applied to the arm [35–37]; and (3) haptics applied to the fingers or the hand [32–35, 38]. In the case where no haptics was applied [39], statistically significant progress was reported in the FMA scores of stroke patients specifically in the acute phase. However, our results showed significant progress in FMA scores of patients in all 3 phases: acute ($N = 5$), subacute ($N = 4$), and chronic ($N = 7$); thus, the proposed system featuring force sensation appears to be more effective in treating stroke populations of all phases than previous systems were in doing so. In the cases in which haptics was applied to the arm, in one study [36], statistically significant progress in WMFT was reported, but the study lacked the other measurements obtained in our study. Another study [37] reported no significant progress in WMFT and BBT, but we measured significant progress in these scores in our study. Based on these results, we conclude that a system in which haptics is applied to fingers might be more effective when used for fine motor rehabilitation, as compared with a system in which haptics is applied to the arm only. Lastly, with regard to haptics being applied to the hand or fingers, previous studies conducted using a hand exoskeleton [16, 34, 35] and a hand-held exoskeleton [38] reported results in the form of descriptive statistics. However, one study [32] reported significant progress in FMA and BBT scores, which agrees with the results of our study. Compared with the aforementioned studies, the results of this study provide stronger evidence (statistically significant progress in FMA, TEMPA, WMFT,

BBT, and JARMAR) supporting the view that haptics applied to fingers, as in the case of the system presented here, might be more effective when used in fine motor rehabilitation than haptics applied to the arm alone. Regarding the cost issue, the haptic system presented here costs less than US\$ 500, which is considerably less than the cost of systems used in the studies listed in the preceding paragraph. Furthermore, the robot arm Novint Falcon is an off-the-shelf product that can be purchased from numerous retailers. Thus, our new VR system can potentially be used more widely than other systems in clinics and even in home-based applications.

In addition to the overall results of the participants discussed thus far, we collected results after dividing the participants into groups based on a variety of selected conditions to compare the effects of using the system within groups or between groups under specific conditions. The first condition selected was the duration since the first hit of stroke. From a clinical perspective, progress made in the acute phase of stroke is considered to be more apparent than that in other phases because of spontaneous recovery. This agrees with our results because we identified statistically significant progress from pretest to posttest and follow-up across all measures except WMFT. By contrast, the progress in the chronic phase is generally considered to be less obvious than that in other phases. However, the BBT results obtained in this study showed that statistically significant progress occurred in the chronic phase from the pretest to both the posttest and the follow-up. Among the 5 clinical measures, BBT is considered to be the most relevant to hand functions, and thus our results suggest that the proposed system facilitates the recovery of fine motor function in stroke patients in the chronic phase. The second condition was the combinations of lesion side and hand-dominance side. Clinically, progress is typically considered to be more definitive if the lesion side is distinct from the side of hand dominance than if the sides are the same, because the paretic side is the same as the hand-dominance side that exhibits superior functions before the stroke. This agrees with our results because statistically significant progress from pretest to posttest was identified across all measures. Conversely, progress may not be readily discernible if the lesion side is the same as the side of hand dominance. However, our results showed statistically significant progress in BBT scores from pretest to both posttest and follow-up when the lesion side was the same as the hand-dominance side. This result indicates that the proposed system may contribute to the progress of fine motor function in patients with lesion and hand dominance on the same side.

Based on our results, we also conclude that using the proposed system featuring haptic simulations applied directly to fingers and repetitively practicing the pinch tasks may be effective in treating a patient with harsh conditions such as a chronic stroke phase or a coside of lesion and hand dominance. The 16 stroke patients who were recruited in this clinical trial completed 24 30 min training sessions without complaints, and the system presented no severe technical setbacks, indicating that the rehabilitation system can be used effectively and safely. The participants' acceptance scores of the proposed system were high, and interviews conducted

with all participants confirmed their acceptance of this new technology applied in stroke rehabilitation. One of the participants was apprehensive nervous when performing the VR tasks for the first time, but showed an increase in confidence upon noticing progress. Another participant reported becoming completely engaged in the tasks and noticing pain less during the tasks, because a substantial amount of attention was devoted to enjoying playing the VR games.

A limitation of the study is that the number of participants (16) recruited in the clinical trial was small; consequently, the preliminary results presented in this paper must be further verified by performing clinical trials of a comparatively larger scale. Moreover, the design of this study hinged on the capabilities of the 2 robot arms, such as the maximal force output, the working zone, and the degrees of freedom, which limited the diversity of the tasks that could be developed.

5. Conclusion and Future Research

In this paper, we have described a novel haptic-enhanced VR system featuring haptic simulation that was developed to facilitate the long-term poststroke recovery of upper-extremity motor function. The results of the clinical trial performed using this system showed that all clinical measures examined (FMA, TEMPA, FMA, BBT, and JAMAR) exhibited statistically significant progress, indicating that the proposed system effectively promotes fine motor rehabilitation. Specifically, the results presented here reveal that this new VR system is also effective in treating certain harsh conditions such as a chronic stroke phase and a coside of lesion and hand dominance. By synchronizing kinematic and kinetic data, various behavioral phases are clearly interpreted. Moreover, measures of system usability indicate that the participants in this study strongly intend to continue using the proposed system in rehabilitation. In future work, a clinical trial larger than the one described here could be used to verify the preliminary results of this study. Furthermore, the prosperous rich kinematic and kinetic data gathered in clinical trials could be analyzed using advanced computational techniques to develop new assessment methods.

Conflicts of Interest

The authors declare that there is no conflict of interest regarding the publication of this article.

References

- [1] W. Rosamond, K. Flegal, K. Furie et al., "Heart disease and stroke statistics—2008 update: a report from the American Heart Association Statistics Committee and Stroke Statistics Subcommittee," *Circulation*, vol. 117, no. 4, pp. e25–146, 2008.
- [2] G. Kwakkel, B. J. Kollen, J. van der Grond, and A. J. Prevo, "Probability of regaining dexterity in the flaccid upper limb: impact of severity of paresis and time since onset in acute stroke," *Stroke*, vol. 34, pp. 2181–2186, 2003.
- [3] H. M. Feys, W. J. De Weerd, B. E. Selz et al., "Effect of a therapeutic intervention for the hemiplegic upper limb in the acute phase after stroke: a single-blind, randomized, controlled multicenter trial," *Stroke*, vol. 29, pp. 785–792, 1998.
- [4] T. S. Olsen, "Arm and leg paresis as outcome predictors in stroke rehabilitation," *Stroke*, vol. 21, pp. 247–251, 1990.
- [5] V. M. Parker, D. T. Wade, and R. Langton Hewer, "Loss of arm function after stroke: measurement, frequency, and recovery," *International Rehabilitation Medicine*, vol. 8, pp. 69–73, 1986.
- [6] D. T. Wade, R. Langton-Hewer, V. A. Wood, C. E. Skilbeck, and H. M. Ismail, "The hemiplegic arm after stroke: measurement and recovery," *Journal of Neurology, Neurosurgery & Psychiatry*, vol. 46, pp. 521–524, 1983.
- [7] G. Bard and G. G. Hirschberg, "Recovery of voluntary motion in upper extremity following hemiplegia," *Archives of Physical Medicine and Rehabilitation*, vol. 46, pp. 567–572, 1965.
- [8] T. E. Twitchell, "The restoration of motor function following hemiplegia in man," *Brain*, vol. 74, pp. 443–480, 1951.
- [9] I. Faria-Fortini, S. M. Michaelsen, J. G. Cassiano, and L. F. Teixeira-Salmela, "Upper extremity function in stroke subjects: relationships between the international classification of functioning, disability, and health domains," *Journal of Hand Therapy*, vol. 24, pp. 257–264, 2011.
- [10] J. M. Blennerhassett, L. M. Carey, and T. A. Matyas, "Grip force regulation during pinch grip lifts under somatosensory guidance: comparison between people with stroke and healthy controls," *Archives of Physical Medicine and Rehabilitation*, vol. 87, pp. 418–429, 2006.
- [11] J. M. Blennerhassett, T. A. Matyas, and L. M. Carey, "Impaired discrimination of surface friction contributes to pinch grip deficit after stroke," *Neurorehabilitation and Neural Repair*, vol. 21, pp. 263–272, 2007.
- [12] S. H. You, S. H. Jang, Y. H. Kim et al., "Virtual reality-induced cortical reorganization and associated locomotor recovery in chronic stroke: an experimenter-blind randomized study," *Stroke*, vol. 36, pp. 1166–1171, 2005.
- [13] S. H. Jang, S. H. You, M. Hallett et al., "Cortical reorganization and associated functional motor recovery after virtual reality in patients with chronic stroke: an experimenter-blind preliminary study," *Archives of Physical Medicine and Rehabilitation*, vol. 86, no. 11, pp. 2218–2223, 2005.
- [14] E. J. Plautz, G. W. Milliken, and R. J. Nudo, "Effects of repetitive motor training on movement representations in adult squirrel monkeys: role of use versus learning," *Neurobiology of Learning and Memory*, vol. 74, pp. 27–55, 2000.
- [15] D. L. Nelson, K. Konosky, K. Fleharty et al., "The effects of an occupationally embedded exercise on bilaterally assisted supination in persons with hemiplegia," *American Journal of Occupational Therapy*, vol. 50, pp. 639–646, 1996.
- [16] S. V. Adamovich, G. G. Fluet, A. Mathai, Q. Qiu, J. Lewis, and A. S. Merians, "Design of a complex virtual reality simulation to train finger motion for persons with hemiparesis: a proof of concept study," *Journal of Neuroengineering and Rehabilitation*, vol. 6, no. 1, p. 28, 2009.
- [17] S. V. Adamovich, A. S. Merians, R. Boian et al., "A virtual reality based exercise system for hand rehabilitation post-stroke: transfer to function," *The 26th Annual International Conference of the IEEE Engineering in Medicine and Biology Society*, vol. 7, pp. 4936–4939, 2004.
- [18] A. S. Merians, D. Jack, R. Boian et al., "Virtual reality-augmented rehabilitation for patients following stroke," *Physical Therapy*, vol. 82, no. 9, pp. 898–915, 2002.

- [19] J. Broeren, M. Rydmark, and K. S. Sunnerhagen, "Virtual reality and haptics as a training device for movement rehabilitation after stroke: a single-case study," *Archives of Physical Medicine and Rehabilitation*, vol. 85, no. 8, pp. 1247–1250, 2004.
- [20] M. R. Golomb, B. C. McDonald, S. J. Warden et al., "In-home virtual reality videogame telerehabilitation in adolescents with hemiplegic cerebral palsy," *Archives of Physical Medicine and Rehabilitation*, vol. 91, no. 1, pp. 1–8.e1, 2010.
- [21] M. S. Cameirao, S. B. Badia, E. D. Oller, and P. F. Verschure, "Neurorehabilitation using the virtual reality based Rehabilitation Gaming System: methodology, design, psychometrics, usability and validation," *Journal of Neuroengineering and Rehabilitation*, vol. 7, no. 1, p. 48, 2010.
- [22] <http://www.novint.com>.
- [23] M. F. Folstein, S. E. Folstein, and P. R. McHugh, "'Mini-mental state'. A practical method for grading the cognitive state of patients for the clinician," *Journal of Psychiatric Research*, vol. 12, no. 3, pp. 189–198, 1975.
- [24] A. R. Fugl-Meyer, L. Jaasko, I. Leyman, S. Olsson, and S. Steglind, "The post-stroke hemiplegic patient. 1. a method for evaluation of physical performance," *Scandinavian Journal of Rehabilitation Medicine*, vol. 7, no. 1, pp. 13–31, 1975.
- [25] D. M. Morris, G. Uswatte, J. E. Crago, E. W. Cook 3rd, and E. Taub, "The reliability of the wolf motor function test for assessing upper extremity function after stroke," *Archives of Physical Medicine and Rehabilitation*, vol. 82, no. 6, pp. 750–755, 2001.
- [26] B. Nedelec, K. Dion, J. A. Correa, and J. Desrosiers, "Upper extremity performance test for the elderly (TEMPA): normative data for young adults," *Journal of Hand Therapy*, vol. 24, no. 1, pp. 31–43, 2011.
- [27] J. Desrosiers, G. Bravo, R. Hebert, E. Dutil, and L. Mercier, "Validation of the Box and Block Test as a measure of dexterity of elderly people: reliability, validity, and norms studies," *Archives of Physical Medicine and Rehabilitation*, vol. 75, no. 7, pp. 751–755, 1994.
- [28] Jamar Dynamometer Lafayette Instrument Company, PO Box 5729, Lafayette, IN 47903.
- [29] F. D. Davis, R. P. Bagozzi, and P. R. Warshaw, "User acceptance of computer technology: a comparison of two theoretical models," *Management Science*, vol. 35, pp. 982–1003, 1989.
- [30] V. Venkatesh, "Determinants of perceived ease of use: integrating control, intrinsic motivation, and emotion into the technology acceptance model," *Information Systems Research*, vol. 11, pp. 342–365, 2000.
- [31] K. L. Nowak and F. Biocca, "The effect of the agency and anthropomorphism on users' sense of telepresence, copresence, and social presence in virtual environments," *Presence: Teleoperators and Virtual Environments*, vol. 12, pp. 481–494, 2003.
- [32] L. Connelly, Y. Jia, M. L. Toro, M. E. Stoykov, R. V. Kenyon, and D. G. Kamper, "A pneumatic glove and immersive virtual reality environment for hand rehabilitative training after stroke," *IEEE Transactions on Neural Systems and Rehabilitation Engineering*, vol. 18, no. 5, pp. 551–559, 2010.
- [33] D. G. Kamper, R. V. Kenyon, X. Luo, T. Kline, K. Stubblefield, and H. C. Fischer, "Hand rehabilitation following stroke: a pilot study of assisted finger extension training in a virtual environment," *Topics in Stroke Rehabilitation*, vol. 14, no. 1, pp. 1–12, 2007.
- [34] G. G. Fluet, A. S. Merians, Q. Qiu et al., "Robots integrated with virtual reality simulations for customized motor training in a person with upper extremity hemiparesis," *Journal of Neurologic Physical Therapy*, vol. 36, no. 2, pp. 79–86, 2012.
- [35] A. Merians, E. Tunik, G. Fluet, Q. Qiu, and S. Adamovich, "Innovative approaches to the rehabilitation of upper extremity hemiparesis using virtual environments," *European Journal of Physical and Rehabilitation Medicine*, vol. 45, no. 1, pp. 123–133, 2009.
- [36] A. S. Merians, G. G. Fluet, Q. Qiu et al., "Robotically facilitated virtual rehabilitation of arm transport integrated with finger movement in persons with hemiparesis," *Journal of Neuroengineering and Rehabilitation*, vol. 8, no. 1, p. 27, 2011.
- [37] N. N. Byl, G. M. Abrams, E. Pitsch et al., "Chronic stroke survivors achieve comparable outcomes following virtual task specific repetitive training guided by a wearable robotic orthosis (UL-EXO7) and actual task specific repetitive training guided by a physical therapist," *Journal of Hand Therapy*, vol. 26, no. 4, pp. 343–352, 2013.
- [38] J. Broeren, M. Rydmark, A. Bjorkdahl, and K. S. Sunnerhagen, "Assessment and training in a 3-dimensional virtual environment with haptics: a report on 5 cases of motor rehabilitation in the chronic stage after stroke," *Neurorehabilitation and Neural Repair*, vol. 21, no. 2, pp. 180–189, 2007.
- [39] M. da Silva Cameirão, i. Bermúdez, S. Badia, E. Duarte, and P. F. Verschure, "Virtual reality based rehabilitation speeds up functional recovery of the upper extremities after stroke: a randomized controlled pilot study in the acute phase of stroke using the rehabilitation gaming system," *Restorative Neurology and Neuroscience*, vol. 29, no. 5, pp. 287–298, 2011.

Research Article

Development of a Blood Pressure Measurement Instrument with Active Cuff Pressure Control Schemes

Chung-Hsien Kuo,^{1,2} Chun-Ju Wu,¹ Hung-Chyun Chou,¹ Guan-Ting Chen,¹ and Yu-Cheng Kuo¹

¹*Department of Electrical Engineering, National Taiwan University of Science and Technology, Taipei, Taiwan*

²*Department of Biomedical Engineering, National Defense Medical Center, Taipei, Taiwan*

Correspondence should be addressed to Chung-Hsien Kuo; chkuo@mail.ntust.edu.tw

Received 29 March 2017; Revised 31 July 2017; Accepted 29 August 2017; Published 3 October 2017

Academic Editor: David Moratal

Copyright © 2017 Chung-Hsien Kuo et al. This is an open access article distributed under the Creative Commons Attribution License, which permits unrestricted use, distribution, and reproduction in any medium, provided the original work is properly cited.

This paper presents an oscillometric blood pressure (BP) measurement approach based on the active control schemes of cuff pressure. Compared with conventional electronic BP instruments, the novelty of the proposed BP measurement approach is to utilize a variable volume chamber which actively and stably alters the cuff pressure during inflating or deflating cycles. The variable volume chamber is operated with a closed-loop pressure control scheme, and it is activated by controlling the piston position of a single-acting cylinder driven by a screw motor. Therefore, the variable volume chamber could significantly eliminate the air turbulence disturbance during the air injection stage when compared to an air pump mechanism. Furthermore, the proposed active BP measurement approach is capable of measuring BP characteristics, including systolic blood pressure (SBP) and diastolic blood pressure (DBP), during the inflating cycle. Two modes of air injection measurement (AIM) and accurate dual-way measurement (ADM) were proposed. According to the healthy subject experiment results, AIM reduced 34.21% and ADM reduced 15.78% of the measurement time when compared to a commercial BP monitor. Furthermore, the ADM performed much consistently (i.e., less standard deviation) in the measurements when compared to a commercial BP monitor.

1. Introduction

With the rapid development of the economy, people's eating and living habits are changing. Less exercise and high-calorie foods gradually threaten human health [1]. In recent years, many reports and studies indicated that the ages of chronic patients are significantly reduced. Hypertensions are the precursors of many chronic diseases, such as strokes, heart diseases, kidney diseases, and retinopathies. Therefore, regular measurement of blood pressure has become one of the most important references of health.

Blood pressure measurement approaches have been widely discussed. Nitzan et al. [2] proposed a cuff-based automatic measurement of SBP which was based on the simultaneous measurement of photoplethysmography

(PPG) signals [3] on the fingers of both hands. The PPG-based measurement directly detected the opening of the arteries under the cuff and provided accurate measurements of SBP. Song et al. [4] proposed a new cuff unit which improved the phenomenon of venous congestion for the measurement of the finger artery, and it was suitable for noninvasive and long-term monitoring. Due to the convenience of measuring finger arteries [5, 6], a lot of relative researches were proposed. However, the accuracy could be a concern. Lee et al. [7] proposed a calibrated method [8] which decreased the errors of different circumferences of the fingers of the subjects.

Moreover, Van Moer et al. [9] proposed a simplified method to obtain SBP and DBP. Based on the oscillometric method, blood pressure waveforms were analyzed in the frequency domain to filter out the harmonics and

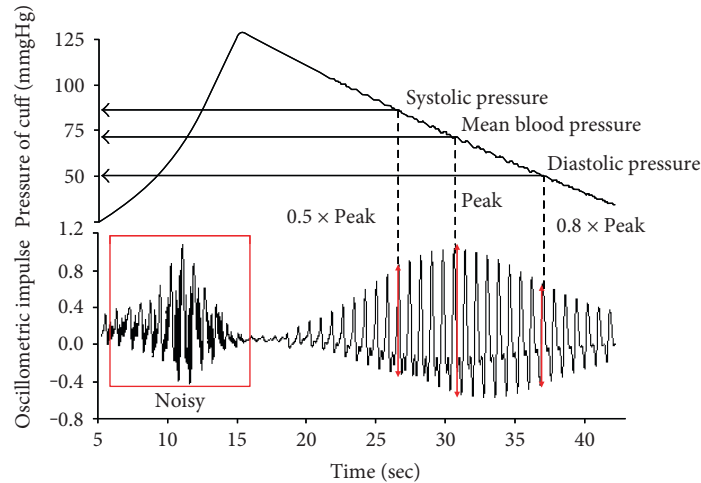


FIGURE 1: Cuff pressure waveform of oscillometric method.

intermodulation products. In their work, the accurate estimations of SBP and DBP were obtained from oscillometric waveforms. Wang et al. [10] presented a model-based fuzzy logic controller for continuously noninvasive BP waveform monitoring. The model-based fuzzy logic controller was applied to track unknown desired trajectories and to find the optimal coupling condition where the maximum compliance of the arterial vessel occurred.

The oscillometric method is the most common approach [11, 12] to be applied to electrical BP measurement instruments. It has the advantages of noninvasive measurement which requires less professional skills. Therefore, the oscillometric method is suitable for daily health monitoring [13, 14] and long-term measurements [15, 16]. Practically, the user may place a sphygmomanometer cuff around the upper arm. The oscillations caused by heart pumping are changed with the altered pressure in the cuff. The observed pressure oscillations are measured with an electronic pressure sensor. When the cuff pressure is close to the mean blood pressure (MBP), the peak of oscillometric curve would occur.

In general, the SBP and DBP are corresponding to the pressure of 0.5 times and 0.8 times of oscillometric peak, as shown in Figure 1. The estimation of SBP and DBP from oscillometric waveform is important. Lim et al. [17] proposed an improved measurement of blood pressure in terms of extracting the characteristic features from the cuff oscillometric waveform. Their study employed the multiple linear regression (MLR) and the support vector regression (SVR) for the relationship discovery. Moreover, Koohi et al. [18] presented a dynamic threshold algorithm to evaluate trustworthiness of the estimated blood pressure in oscillometry.

However, for conventional oscillometry, a linear active inflating cycle and an inactive deflating cycle were used. Although the inflecting pumping speed is one of the major concerns of a noisy signal, the disturbances and noises are also related to the air turbulences and electrical signal noise generated from pumping motors during the air pumping

stage, as shown in Figure 1. With such interference, the determination of BP characteristics would be challenging for conventional oscillometry. In other words, the active inflating cycle contains pumping air turbulence; hence, the active inflating cycle cannot be directly used for precisely determining the BP characteristics. As a consequence, conventional oscillometry measures and determines the BP characteristics at the inactive deflating cycle. For example, the cuff is desired to inflate to a pressure which is in excess of SBP, such as 160 mmHg, and then, it is released below DBP with a linear trajectory in every measurement. The duration of each measurement is taken above 30 seconds. Such a mechanism results in a longer measure time of BP characteristics.

Therefore, this paper proposes a nonlinear trajectory tracking control approach in the inflating and deflating cycles without using conventional pumps. Compared with conventional electronic BP instruments, the novelty of the proposed BP measurement approach is to utilize a variable volume chamber which actively and stably alters the cuff pressure during inflating or deflating cycles. The variable volume chamber is operated with a closed-loop pressure control scheme, and it is activated by controlling the piston position of a single-acting cylinder driven by a screw motor. Therefore, the variable volume chamber could significantly eliminate the air turbulence during the air injection stage when compared to an air pump mechanism.

Furthermore, the proposed active BP measurement approach is capable of measuring BP characteristics during the inflating cycle. Two modes of air injection measurement (AIM) and accurate dual-way measurement (ADM) were proposed, where the AIM mode is desired to significantly reduce the measurement time and the ADM mode is desired not only to reduce the measurement time but also to improve the measurement consistency and precision which can be evaluated in terms of statistical standard deviation. The details are described in the next section.

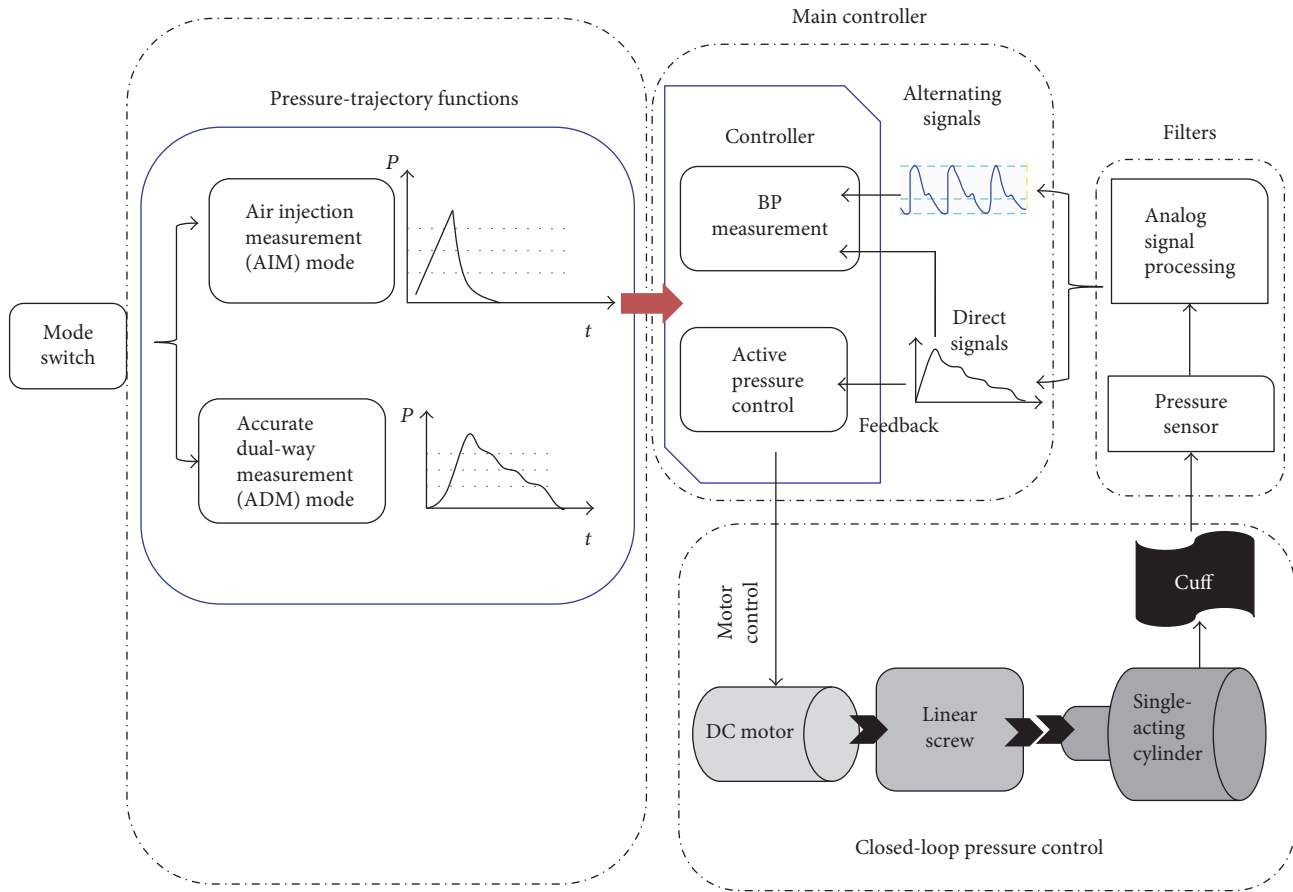


FIGURE 2: System architecture of the proposed active BP measurement approach.

Finally, this paper is organized as follows. Section 2 describes the system architecture. Different measurement modes, pressure-trajectory planning, BP measurement algorithm, and active pressure control are introduced in this section. The implementation, including the mechanical design, signal processing, and controller is stated in Section 3. In Section 4, the proposed approach is evaluated with a number of experiments, and a commercial BP instrument is used for comparison; a summary of our study is also conducted. Finally, conclusions and future works are addressed in Section 5.

2. System Architecture

The system architecture of the proposed active BP measurement approach is shown in Figure 2. It is composed of a single-acting cylinder, a linear screw, a DC motor, and a sphygmomanometer cuff. The stationary single-acting cylinder and the linear screw replace the function of a disturbing air pump which is adopted for most commercial instruments. The single-acting cylinder connects with the cuff through a low elastic rubber tube to form a variable volume chamber. The chamber volume is changed by altering the piston position of a single-acting cylinder which is connected to a linear screw. It is noted that the linear screw is driven by a DC

motor. Meanwhile, the changing volume alters the pressure in the cuff. In order to implement a closed-loop pressure control system, a pressure sensor which provides feedback pressure signals is equipped. The signals include alternating signals and direct signals. The controller further deals with the measured signals for BP characteristic recognitions (SBP and DBP) and the closed-loop nonlinear pressure trajectory control in both inflating and deflating cycles. It is noted that the pressure-trajectory functions represent nonlinear pressure trajectory functions for activating the AIM and ADM modes. The details are described in the next subsection.

2.1. Introduction of Different Measurement Modes. As described in Introduction, two measurement modes of AIM and ADM were used. The trajectories of pressure for each mode are shown in Figure 3. The measurement modes are switched according to different measurement purposes. The operations of these two modes are described as follows:

- (1) AIM (air injection measurement) mode: this mode is desired to measure the blood pressure characteristics in the air injection stage. Practically, a linear and stable inflating cycle is generated from a volume-variable single-acting cylinder for BP

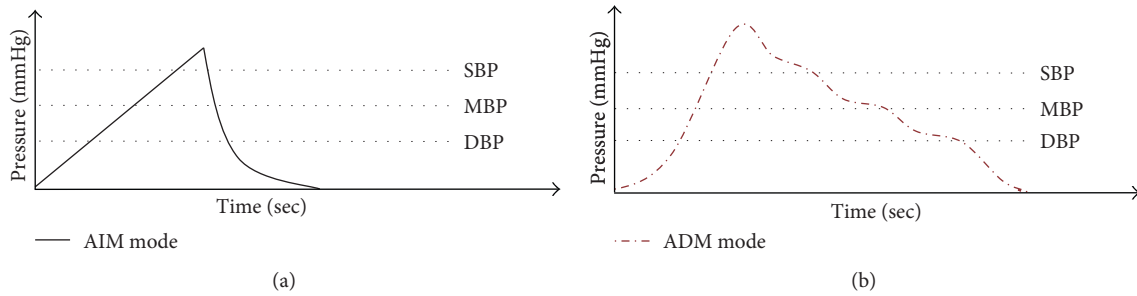


FIGURE 3: Different measurement modes of this paper: (a) AIM mode; (b) ADM mode.

characteristic measurement; hence, it overcomes the drawback of the conventional oscillometry that the BP characteristics do not determine during inflating cycle. It is noted that the disturbances and noises of conventional BP monitors are related to the air turbulences and electrical signal noise generated from pumping motors during the air pumping stage. With such interference, the determination of BP characteristics would be challenging during air pumping cycle for conventional oscillometry. On the other hand, because of the introduction of stable and stationary air injection of the AIM mode, the cuff pressure is linearly increased. The alternating signal indicated in Figure 2 is processed continuously to detect the DBP and SBP. When the SBP is detected, the air is fast extracted to reduce the measurement time. This mode presents a fast BP measurement solution.

- (2) ADM (accurate dual-way measurement) mode: the ADM uses a nonlinear inflating and deflating cycles, and the design of nonlinear tracking control in the inflating and deflating cycles aims at reducing the measurement time and the measurement resolution of the oscillometry as well. As shown in Figure 3(b), the ADM contains a fast ramp up inflecting cycle and a variable resolution deflecting cycle. The fast ramp up inflecting cycle determines three rough BP characteristics with a low resolution and fast speed operation. Then, the three rough BP characteristics help the generation of nonlinear deflation cuff pressure trajectory in the continued variable resolution deflecting cycle. As a consequence, more precise BP characteristics can be found due to a higher resolution of slow inflection curve near the region of rough BP characteristics. At the same time, the increasing of trajectory slope during the far rough BP characteristic region is desired to reduce the measurement time.

2.2. Pressure-Trajectory Control of ADM BP Measurement. In this subsection, a specific pressure trajectory for achieving the active cuff pressure control of the ADM mode is discussed. Basically, the pressure trajectory is formed with 5-time intervals (i.e., T1 to T5 segments). In order to

achieve efficient BP measurements, three different characteristic functions are applied to compose the active pressure trajectory, including sigmoid functions, cosine functions, and third order polynomial functions. As shown in Figure 4, the trajectory of pressure for a complete BP measurement is divided into five stages, that is, from T1 to T5. T1 is the stage of air injection, and T2 to T5 are the stages of air extraction. T1 is used to determine three rough characteristic BP characteristics, including the segment of systolic pressure (SSP), the segment of mean blood pressure (SMP), and the segment of diastolic pressure (SDP). These three rough BP characteristics altered the beginnings and ends of functions of the time segments of T2 to T5. Thus, the trajectories of pressure are automatically adjusted according to each measurement. The decreases of pressures are gentle at the stages which are close to the characteristic points of BP (i.e., roughly detected DBP, MBP, and SBP). Contrarily, the pressure curve segments which are far from characteristic points of BP decrease fast. These five-time segments are categorized as three types of functions, and they are described as follows:

- (1) Fast air injection period (T1): In this period, the air is injected to the cuff quickly to roughly obtain the DBP, MBP, and SBP. The pressure curve in this period is desired to be fast increased and smooth. Because the air is injected to the cuff through a DC motor-driven cylinder chamber, a third order polynomial function is suitable for this case. The third order polynomial function provides a gentle slope increasing rate at the beginning and ending of the curve segment so that the DC motor may work smoothly without inducing vibration interference. In addition to the beginning and ending, the curve exhibits fast increasing of the pressure. Because the DBP, MBP, and SBP appeared in the fast increasing pressure duration, the detection of DBP, MBP, and SBP would lose resolution and accuracy. Therefore, the fast air injection period is to roughly obtain the DBP, MBP, and SBP so that a specific air release pressure trajectory (i.e., from T2 to T5) can be desired to improve the accuracy of detecting DBP, MBP, and SBP as well as to reduce the measurement time. Equation (1) shows the third order polynomial function, where h is the amplitude; T is the period

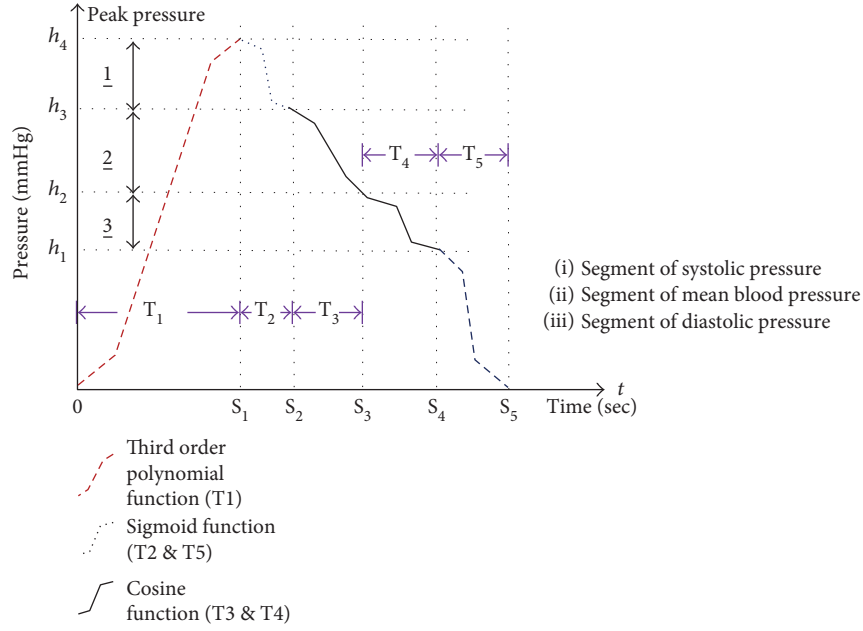


FIGURE 4: Pressure control curve of BP measurement.

of function; t is the time. It is noted that $T = S_1$ and $h = h_4$ in this case.

$$p(t) = \frac{-6h}{T^3} \left(\frac{t^3}{3} - \frac{t^2 T}{2} \right). \quad (1)$$

- (2) Non-BP characteristic periods (T2 and T5): In these two periods, there is not any BP characteristic appears. Therefore, the pressure trajectories are designed to be smooth at the beginning and end as well as to be fast at the middle of the period. The design purpose is to reduce the vibration of the motor and to reduce the time. As a consequence, the sigmoid function is applied to the stages of T2 and T5 which are far from characteristic BP points. Therefore, the characteristic of greater slope is suitable for fast air extraction. Equation (2) is the increasing function (S_d) and the decreasing function, where h is the amplitude; T is the period of function; t is the time; t_b is the start time of the period. It is noted that $T = (S_2 - S_1)$ or $(S_5 - S_4)$; $h = (h_4 - h_3)$ or h_1 ; $t_b = S_1$ or S_4 in this case.

$$s_d(t) = \frac{h}{1 + e^{2\pi(2((t-t_b)/T)-1)}}. \quad (2)$$

- (3) BP characteristic periods (T3 and T4): The pressure trajectories in these two periods are important because BP characteristics will be recognized. The trajectory must be smooth and gentle so that the precision of BP characteristic recognition could be improved. The cosine function is applied to the period of T3 and T4 which are close to characteristic BP points. The cosine function has a smaller slope change which is made use of going through the

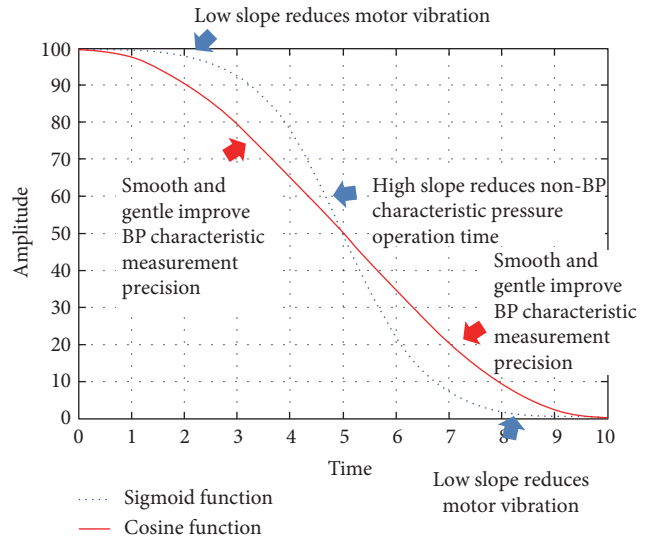


FIGURE 5: Trajectories of sigmoid function and cosine function.

characteristic BP segments. Equation (3) shows the decreasing cosine function, where h is the amplitude; T is the period of function; t is the time. It is noted that $T = (S_3 - S_2)$ or $(S_4 - S_3)$; $h = (h_3 - h_2)$ or $(h_2 - h_1)$; $t_b = S_2$ or S_3 in this case.

$$c_d(t) = \frac{h}{2} \cos\left(\frac{\pi(t-t_b)}{T}\right) + \frac{h}{2}. \quad (3)$$

2.3. Comparison of Sigmoid and Cosine Functions. To illustrate the uses of sigmoid and cosine functions in the aforementioned periods, Figure 5 demonstrates their trajectories.

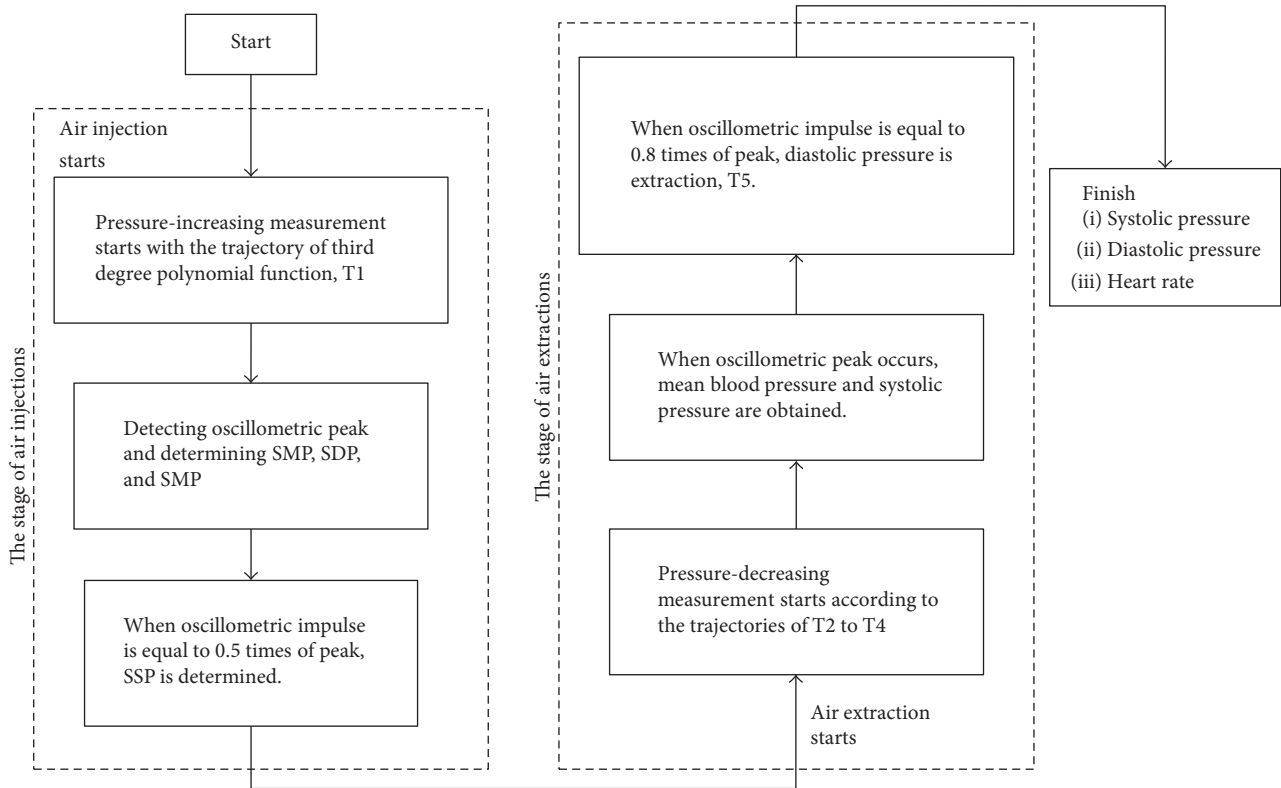


FIGURE 6: Flow chart of proposed BP measurement.

Within specific durations and amplitudes, there are greater changes of slopes in the sigmoid function than in the cosine function in the middles of trajectories. Therefore, sigmoid functions are applied to the noncharacteristic BP segments, and cosine functions are applied to recognize the BP characteristics. In addition, both functions have gentle changes of slopes at the beginnings and the ends. It prevents the DC motor from violent changes of speeds.

2.4. Measurement of BP. The proposed BP measurement approach is based on the oscillometric method. When the pressure of cuff is close to MBP, the peak of oscillometric curve occurs. Then, SBP and DBP could be obtained with the corresponding amplitudes of oscillometric pulses. However, there are five modes which are designed in this paper. Except the pressure-increasing measurement mode, other modes obtain BP during the stage of air extraction. Therefore, the algorithm of BP measurement must meet the switch of different modes. Thus, the BP measurements are able to obtain in both stages of air injections and air extractions.

The oscillometric pulses are detected from altering signals. The MBP which is the peak of oscillation needs to be recognized first. The SBP and DBP are obtained according to the oscillometric pulses of 0.8 times and 0.5 times of the amplitude of oscillometric peak. Before MBP, the pressure of cuff is increasing that means the air injection is activated, and the BP is obtained during the stage of air injection. Contrarily, before MBP, the pressure of cuff is decreasing that means the air extraction is activated, and the BP is obtained

during the stage of air extraction. If the pressure-increasing measurement mode is adopted, the DBP is recognized at the oscillometric pulse of 0.8 times of oscillometric peak. Then, the SBP is recognized at the oscillometric pulse of 0.5 times of oscillometric peak later. If another mode is adopted, the SBP is recognized at the oscillometric pulse of 0.5 times of oscillometric peak. Then, the DBP is recognized at the oscillometric pulse of 0.8 times of oscillometric peak later.

It is noted that the oscillometric peak setting is not time dependent, and it is cuff pressure dependent. Because of using precise closed-loop cuff pressure control scheme, the determination of BP characteristics would be independent of inflation/deflation speed and subject population.

2.5. Active Cuff Pressure Control. The proposed active pressure control is implemented based on a PID controller. Figure 6 shows the flow chart of the proposed BP measurement. The targeted trajectory of pressure which is generated by the system is the input signal, and the pressure sensor which connects with the cuff is the feedback sensor. The PID controller generates PWM signals to the DC motor according to the errors as well as altering the position of piston. At the stage of T1, the system increases the pressure of cuff with a fast speed which is greater than 15 mmHg. In the meanwhile, the oscillometric method is applied to determine the SSP, SMP, and SDP. This procedure determines characteristic functions of extracted stages. The system increases the pressure of cuff until in excess of SBP, and then the system goes to the stage of air extraction. The stage of air extraction is composed of T2 till T5 stages.

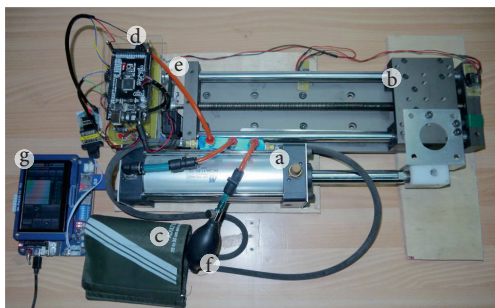


FIGURE 7: Picture of the proposed BP measurement device, including (a) single-acting cylinder; (b) linear screw; (c) cuff; (d) pressure sensor and analog circuit; (e) DC motor, timing wheel and timing belt; (f) bulb; and (g) monitor.

At the beginning, because T2 stage is far from the characteristic segment, the sigmoid function is made use of the command signal to decrease the pressure of cuff quickly. On the other hand, T3 and T4 stages include all of the characteristic points. Therefore, the cosine function is made use of controlling the change of pressure. Finally, T5 stage is the end of air extraction, and the sigmoid function is made use of releasing the pressure of cuff. To the pressure-increasing measurement mode, each measurement is finished at the stage of air injection. Therefore, measurement results are obtained at T1 stage and the system fast releases the pressure of cuff that skips the stages of T2 to T5.

3. Implementation of Active Blood Pressure Measurement Approach

The pressure of cuff is measured by a pressure sensor. The signals of measured pressure are divided into direct signals and alternating signals. The direct signal which is obtained after a low-pass filter represents the current pressure of cuff. Therefore, the direct signal provides not only BP measurement results but also feedback signals of the controller. The alternating signal is obtained after a band-pass filter. Based on the oscillometric method, oscillometric amplitudes are the important features to detect the SBP and the DBP. When measurements start, the system generates predefined pressure trajectories as the input command. According to the feedback signal of pressure sensor, the controller sends PWM signals to the DC motor and alters the position of single-acting cylinder. The pressure of cuff is changed in terms of altering the volume of chamber. In the meanwhile, the characteristic BP segments are obtained at the air injection stage. The characteristic BP segments adjust the pressure trajectory of air extraction stage to achieve efficient performances.

3.1. Design of Proposed BP Measurement Device. As shown in Figure 7, a single-acting cylinder with 63 mm in inner diameter and 150 mm in stroke is used. When the piston of the cylinder moves toward the air vent which connects with the cuff, the volume of air in the chamber is compressed. This movement injects the air of chamber into the cuff and

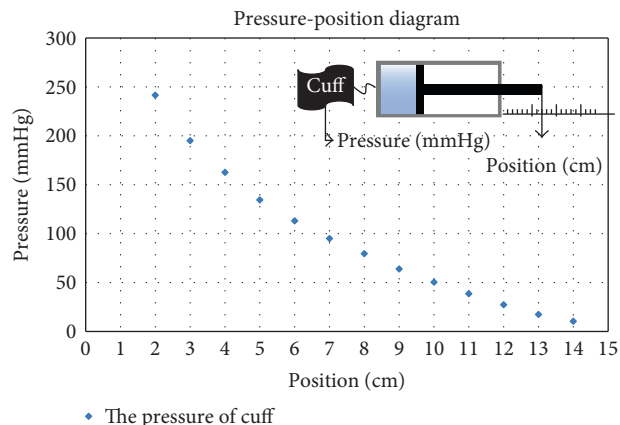


FIGURE 8: Pressure-position diagram.

increases the pressure. Contrarily, when the piston moves away from the air vent, the air of cuff is extracted and the pressure is decreased.

The single-acting cylinder uses preinjected air in the volume-variable chamber. The closed-loop cuff pressure control is achieved in terms of activating a DC screw motor. The DC screw motor injects the air with relatively stable during the changes of cuff pressure when compared to disturbed air pumping mechanism. In addition, the feedback pressure sensor eliminates the air leaking problems when tracking a specific cuff pressure trajectory. In case of the large amount of air leakage, the screw motor position and cuff pressure feedback can be detected and injected manually with a bulb that was indicated in Figure 7(f).

The pressure-position diagram of proposed device is shown in Figure 8. In Figure 8, when the position of piston is at 30 mm, the pressure of cuff is about 200 mmHg which is higher than the normal SBP. Therefore, the volume of the selected single-acting cylinder is suitable for this study. In addition, Teflon tapes are affixed to any connections, such as tubes and air vents, in order to prevent the air from leaking. The piston connects with the slide of linear screw. The linear screw is driven by a DC motor. The DC motor with type Faulhaber 2643 series was used, and it is capable of providing 28 mN-m in torque with 24 volts. It transfers the rotary motions to the linear screw through timing wheels and a timing belt. It is noted that the timing wheel and timing belt were formed as a transmission mechanism. The belt and circular wheel were formed with teeth so that they can make sure no slipping effects during mechanical transmission.

3.2. Signal Processing of Pressure Signal. The proposed BP measurement system is equipped with a pressure sensor, Honeywell SCC05DN. The sensory range is from 0 mmHg to 250 mmHg, and the output signal is from 25 mV to 26 mV. The measured pressure signals include direct signals and alternating signals. In order to obtain the particular frequencies of signals, an analog signal processing circuit is implemented. The flow chart of analog signal processing is shown in Figure 9. First, the instrumentation amplifier, a preamplifier, is applied to set the gain of signal

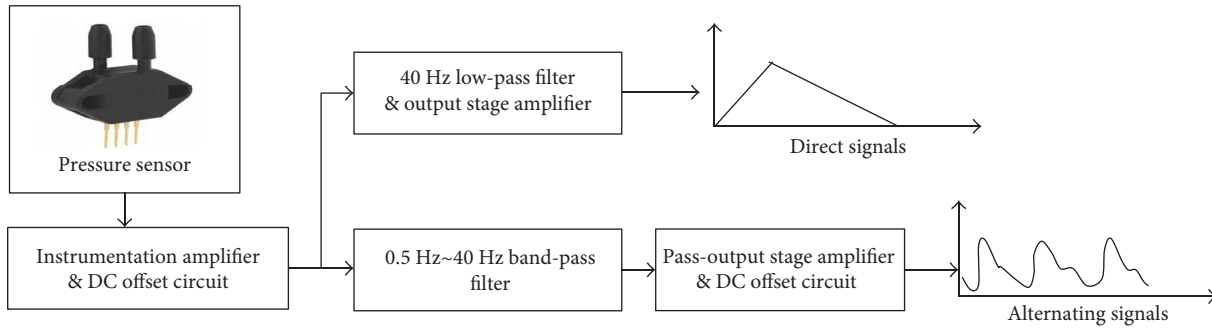


FIGURE 9: The analog signal processing of measured pressure signals.

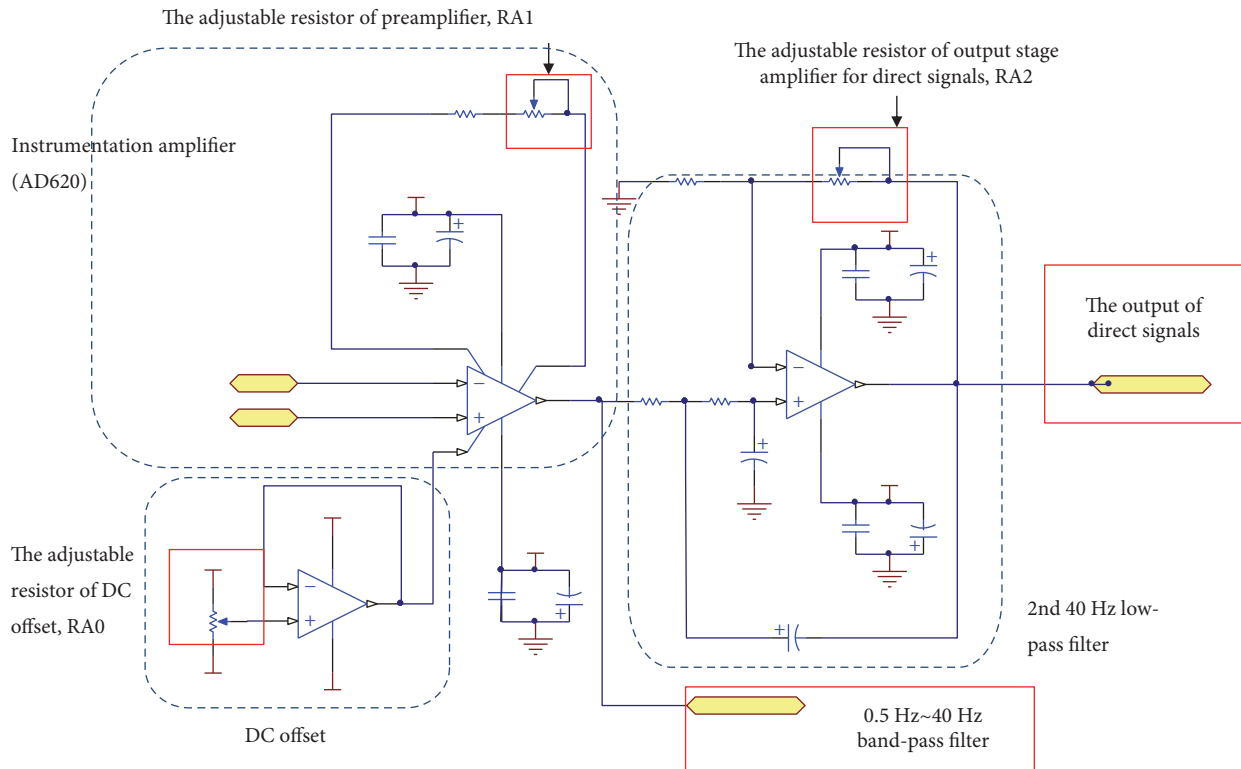


FIGURE 10: Analog signal processing circuit of direct signals.

to 45. There are advantages of high signal to noise ratio and high common-mode rejection ratio. It is noted that the selected instrumentation amplifier outputs the signal from -5V to 5V , and the signal is read by an analog to digital converter (ADC) interface. Therefore, a reference terminal potential of the amplifier defines the zero output voltage. The implemented analog circuit is shown in Figure 10. The adjustable resistors of RA0 and RA1 are for adjusting the voltage offset and the gain of preamplifier. Table 1 lists the resistor values and the gains of analog signal processing circuit shown in Figures 10 and 11.

In order to obtain direct signals, a 40 Hz 2nd order Sallen-Key low-pass filter is designed to remove the high-frequency noise, as shown in Figure 10. The adjustable resistor, RA2, is for adjusting the gain of output stage

amplifier. The filtered signal further sets the gain of signal to 2. After detecting the direct signal, the curve fitting approach is applied to find the transformations of pressures and ADC values. A commercial pressure meter is made use of measuring the actual pressure, and the corresponding ADC value is recorded. The curve fitting function is able to be obtained according to experimental results, as shown in Figure 12.

To alternating signals, a band-pass filter with the band from 0.5 Hz to 40 Hz is designed to filter out unwanted signals, as shown in Figure 11. The normal heart beat ranges from 1 Hz to 1.7 Hz (60 bpm to 100 bpm), and the frequency of environment noises is 60 Hz. Therefore, the band-pass filter is composed of a 0.5 Hz 2nd order Sallen-Key high-pass filter and a 40 Hz 2nd order Sallen-Key low-pass filter. The

TABLE 1: The resistor values of implemented analog circuit.

Number	Resistor value	Function	Gain
RA1	10 k Ω	Adjusting the gain of preamplifier	45
RA2	1.86 k Ω	Adjusting the gain of direct signal of output stage amplifier	1.86
RA4	90.8 k Ω	Adjusting the gain of alternating signal of output stage amplifier	90

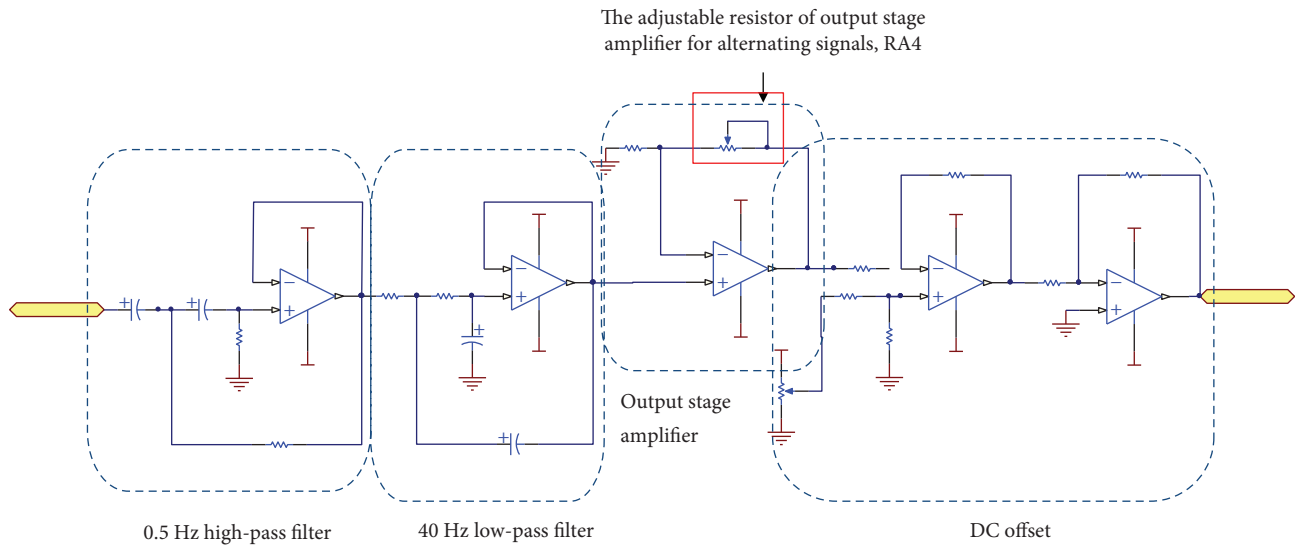


FIGURE 11: The analog signal processing circuits of alternating signals.

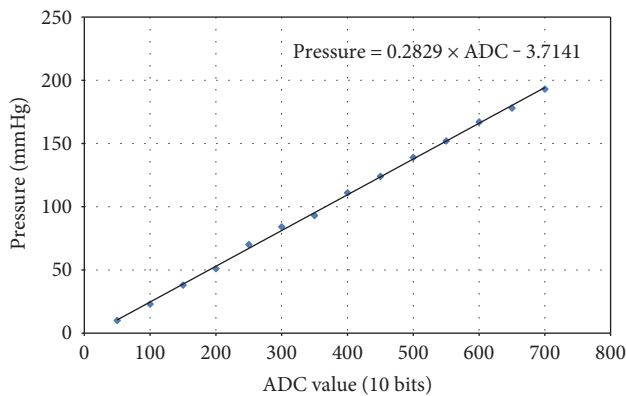


FIGURE 12: The curve fitting of pressures and ADC values.

arterial signals are obtained by the band-pass filter. The amplitudes of output signals are approximately from 1 mV to 20 mV. Therefore, an output stage amplifier sets the gain of signal to 90, and the output signal ranges from 0 volts to 5 volts.

3.3. Controller of Active BP Measurement. An 8-bit AVR microcontroller is employed as a main controller. There are 15-channel 10-bit A/D converters and 10-channel 1 MHz PWM output interfaces. The main controller deals with the measured pressure signals which were processed after the analog circuits. The signals including direct signals and alternating signals are further used as the feedback signals and

oscillometric signals for proposing the active pressure control and the deriving algorithm for BP measurement. The controller generates PWM (pulse width modulation) signals to control the speed of DC motor and to alter the position of piston. Then, the cuff pressure is adjusted according to measured pressures and desired pressures. It is noted that the mentioned BP measurement modes and algorithms are implemented in a main controller to achieve the purpose of a real-time control.

3.4. Design of DC Motor Driver Module. The main control generates PWM signals to control the DC motor. However, the voltage levels of PWM signals which are generated by the main controller are 5 volts. In addition, the insufficient currents cannot actuate the DC motor. Therefore, a DC motor driver with type L6201 is introduced to transform the voltage level to 24 volts. The maximum current output of the motor driver is 1 A, and the operating frequency reaches 100 kHz. Therefore, the specification of the selected motor driver meets the required operating frequency of DC motor, 20 kHz. Because the electromagnetic interference (EMI) which is caused by the motor affects the performance of circuit, an optical coupler is employed to prevent the main controller from disturbance, as shown in Figure 13.

4. Experiment and Results

Several experiments are arranged to evaluate the performance of the proposed active BP measurement approach. First, the system responses of different parameters in the PID controller

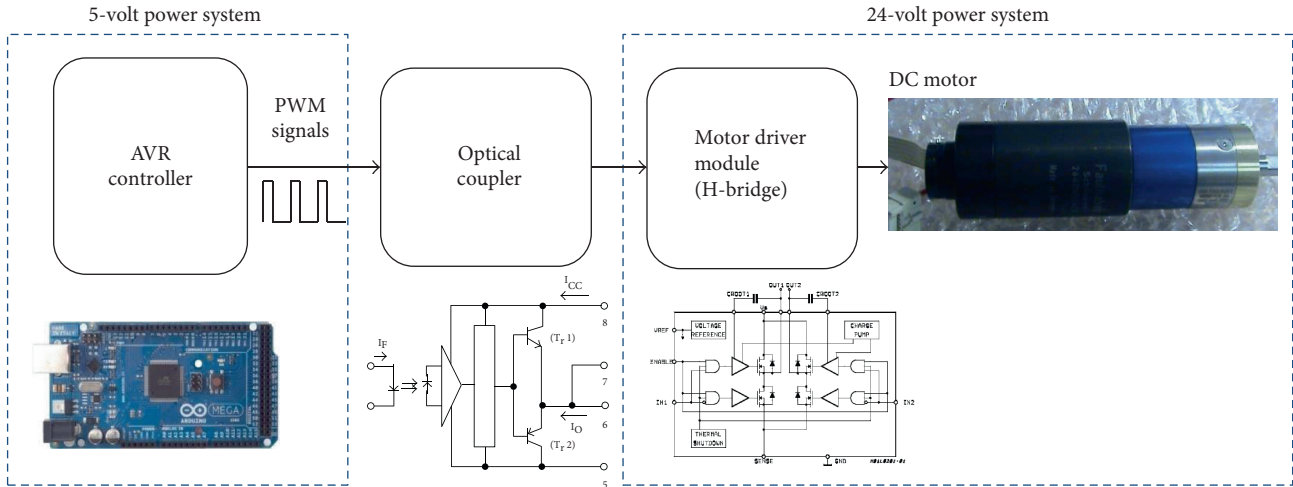


FIGURE 13: Architecture of DC motor driver module.

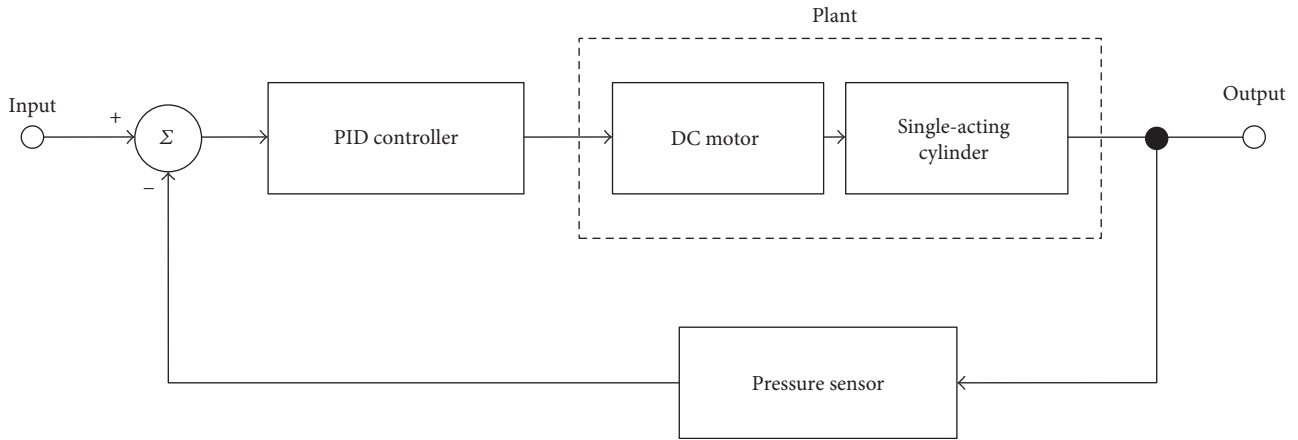


FIGURE 14: The block diagram of the active pressure control.

algorithm are observed. Second, the control of desired pressure trajectory is verified to evaluate the performance of the main control. Third, different measurement modes are executed to verify the BP measurement algorithm. Finally, five subjects are employed to evaluate the proposed BP measurement approach, and a commercial electronic BP measurement instrument is further evaluated for comparison.

4.1. Experiments of Active Cuff Pressure Control. The block diagram of the active pressure control is shown in Figure 14. In order to evaluate the performance of the controller, the step response with different control parameters is observed. Each step response diagram is shown from Figures 15, 16, and 17.

Table 2 lists the step response of each control parameter. From the experimental result, P is increased to shorten the response time and I is adjusted to eliminate the steady state error. The PID parameters determine the performance of pressure control and directly affect measurement results. From Table 2, the PID controller with parameters of $P = 60$, $I = 0.003$, and $D = 8$ has shorter response time and smaller

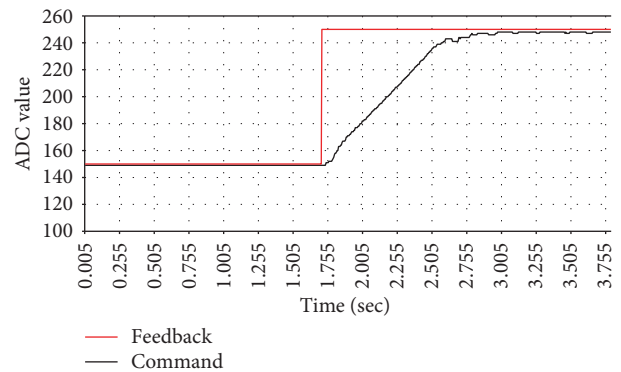
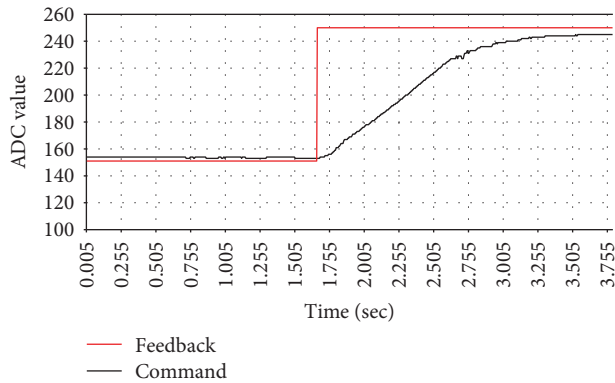
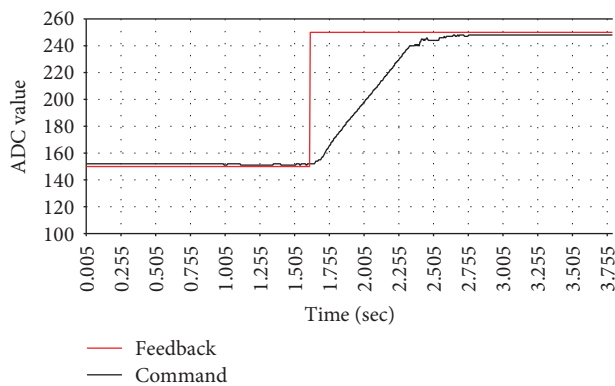


FIGURE 15: The step response of $P = 30$, $I = 0.0015$, and $D = 8$.

steady state error than the other parameters. These parameters are selected for the following experiments.

4.2. Verification of Active Cuff Pressure Control. The proposed BP measurement approach includes AIM and ADM measurement modes. In this experiment, the ADM mode is

FIGURE 16: The step response of $P = 60$, $I = 0.0015$, and $D = 8$.FIGURE 17: The step response of $P = 60$, $I = 0.0030$, and $D = 8$.

selected to verify the performance of PID controller with respect to response time and pressure feedback. The ADM mode includes all of the required trajectories of pressure waveforms from T1 to T5 in a measurement. Therefore, the result covers all of the verifications of five measurement modes. As shown in Figure 18, the blue curve is the desired pressure and the red curve is the measured pressure. The controlled functions are changed according to different measurement stages, as being plotted with the black line. Because of the response time, the desired pressure and the measured pressure are not equal. The response time was approximately from 0 sec to 1 sec, and the errors ranged from 5 mmHg to 10 mmHg.

4.3. Verification of BP Measurement. Based on the above ADM mode experiment and verification, the proposed measurement modes of AIM and ADM are further examined by integrating BP measurement algorithms. The AIM mode experiment is shown in Figure 19. The BP measurement result is obtained at the stage of air injection, and then the cuff is deflated. The blue curve indicates the measured pressure; the red curve is the oscillometric impulse; the recognized BP characteristics are indicated with red circles with SBP, MBP, and DBP symbols. For a complete measurement of AIM mode experiment setting in Figure 19, it took less than 20 s to obtain SBP. The ADM mode experiment is shown in Figure 20. In this experiment,

TABLE 2: The step responses of different PID parameters.

	$P = 30,$ $I = 0.0015,$ $D = 8$ (Figure 14)	$P = 60,$ $I = 0.0015,$ $D = 8$ (Figure 15)	$P = 60,$ $I = 0.0030,$ $D = 8$ (Figure 16)
Response time (sec)	1.7	1.0	1.0
Steady state error (ADC)	10.0	5.0	3.0

it took 34 s to finish a complete ADM mode measurement. However, to improve the AIM mode accuracy, the linear trajectory could be desired as a slower pressure increasing curve. Similarly, to reduce the ADM mode measurement time, the nonlinear trajectory could be also desired. The new setting will be used for comparison with a commercial BP monitor.

4.4. In the Comparison with Commercial Electronic BP Device. In order to verify the feasibility and performance of proposed AIM and ADM modes, a commercial electronic BP instrument (with type: Microlife BP A200) was employed for comparisons.

Five healthy subjects were asked to proceed continuously with 8-time BP measurements. SBP, DBP, and measurement time were recorded in each experiment. There is a one-minute interval between two measurements to avoid the problem of losing arterial compliance. The arrangement of the experiment is designed as Figure 21. At the beginning, each subject is measured by a commercial electronic BP device for three times. Then, the proposed ADM mode is executed for the next two measurements. The AIM mode provides the 6th and 7th experiments. Finally, the commercial electronic BP instrument provided the last one measurement.

Table 3 summarized the measurement results of the abovementioned experiments. Compared with the commercial instrument, there was a difference of 5 mmHg in average between the commercial device and the proposed ADM mode and a difference of 15 mmHg in average between the commercial device and the AIM mode. In addition, the average measurement time significantly decreased. The commercial device is about 38 seconds; the ADM mode is about 32 seconds; and the AIM mode is 25 seconds. According to the above healthy subject experiment results, the AIM reduced 34.21% and the ADM reduced 15.78% of the measurement time when compared to a commercial BP monitor.

On the other hand, the standard deviation of measurements of the same healthy subject at the same time was also evaluated to examine the performance of precision. With this experiment setting, a young healthy subject, 24 years old, was investigated. The same commercial BP monitor was used for the comparisons with AIM and ADM modes. Three different methods were examined for 11 times to obtain statistics performance. The results are shown in Table 4. It is noted that the time courses of the pressure trajectory were the same as the experiments

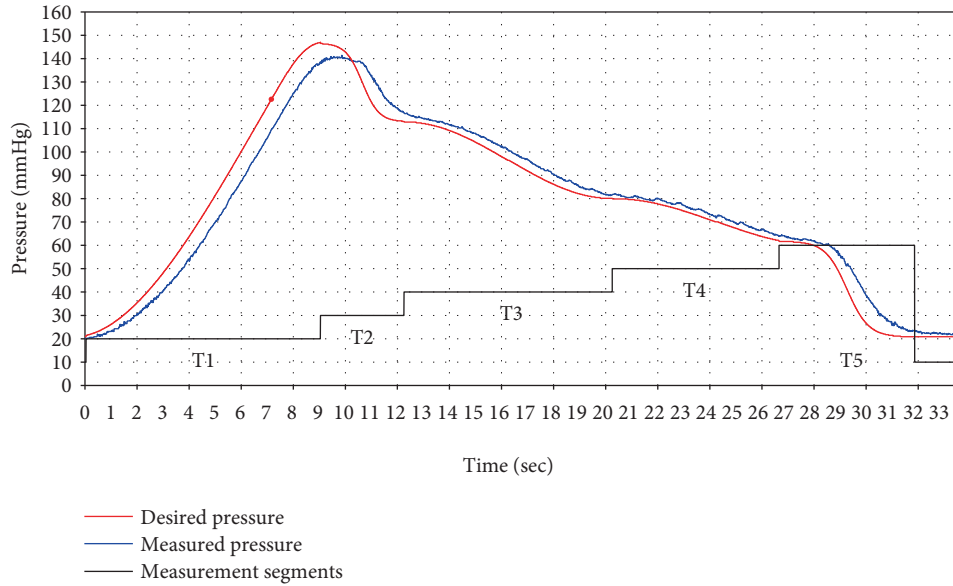


FIGURE 18: The trajectories of desired pressure and measured pressure (ADM mode).

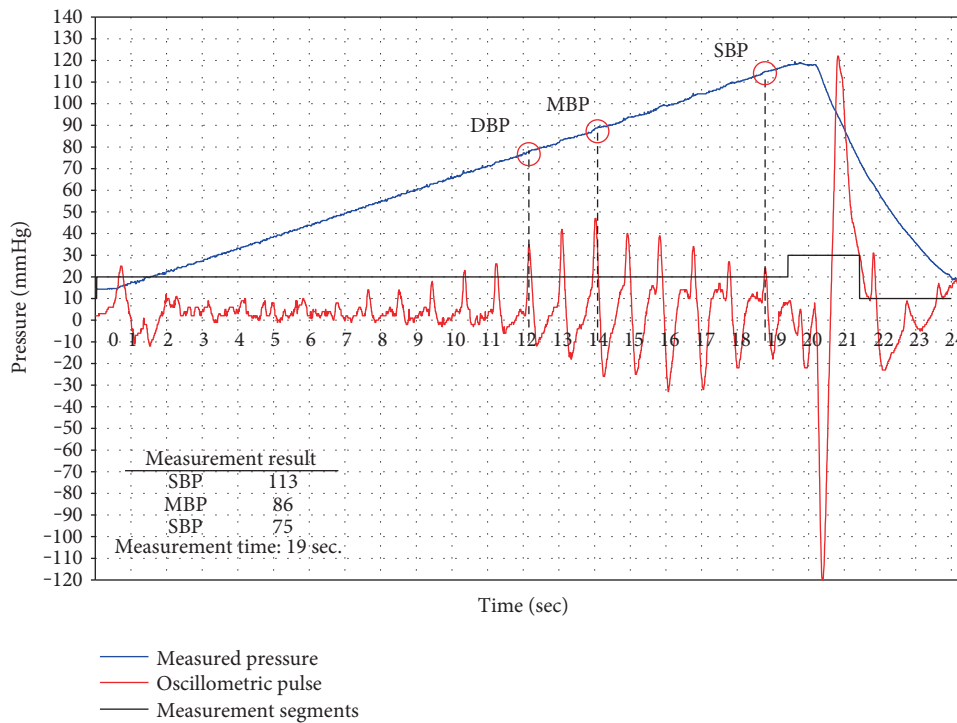


FIGURE 19: The measurement result of the AIM mode.

shown in Table 3. Apparently, the ADM performed much consistently (i.e., less standard deviation) in the measurements when compared to a commercial BP monitor. The AIM performed a little worse performance in the standard deviation when compared to a commercial BP monitor.

It is noted that this experiment setting is not for the BP accuracy comparison, because our study was based on home-made circuits and machines. The circuit and

mechanical drive designs were not certificated. Hence, bias and interference would be a concern. Hence, the statistical standard deviation evaluation would be a method to examine the benefits from nonlinear variable pressure control trajectory for improving the resolution within the near BP characteristic regions.

In summary, according to the experiment results, the benefits of the proposed active variable volume chamber method are the following:

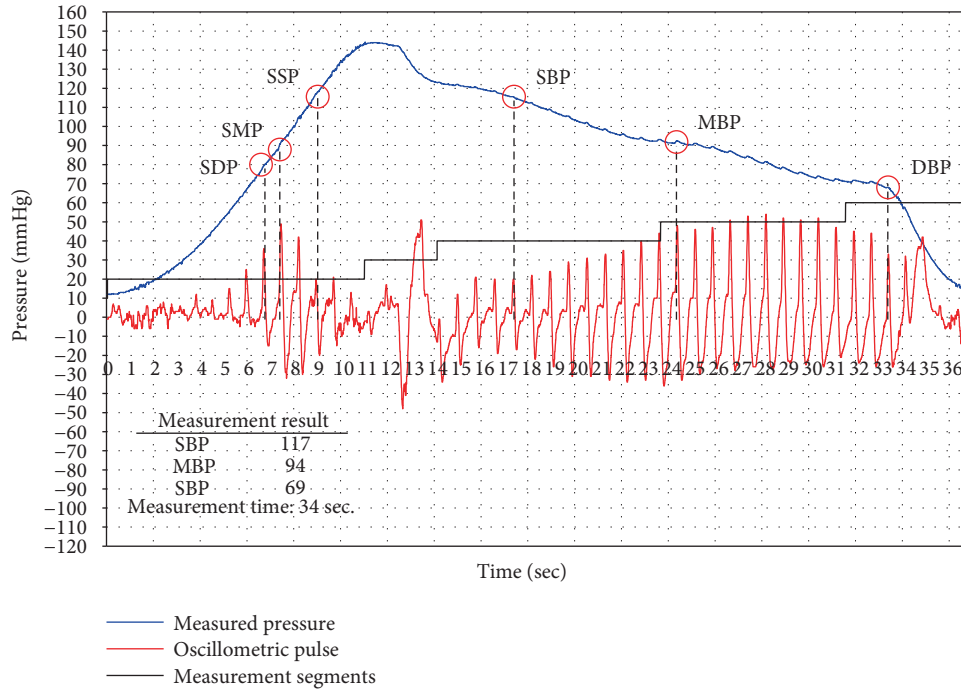


FIGURE 20: The measurement result of ADM mode.

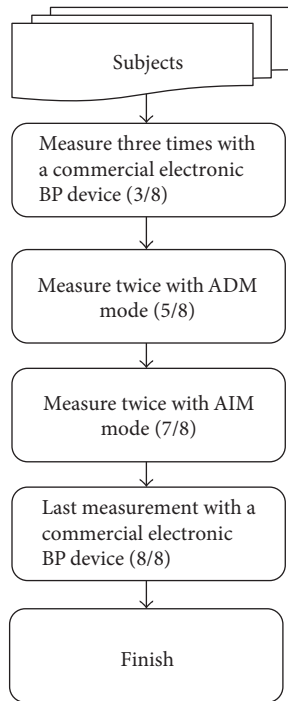


FIGURE 21: The flow chart of BP measurement experiment.

- (1) The active variable volume chamber method could produce stationary injection air so that it can obtain the BP characteristics during injecting stage to reduce the measurement time.
- (2) The active variable volume chamber method may design air injecting and releasing pressure curves to

discover the characteristics of BP curve in a time-efficient manner.

- (3) Such an approach could be used for the development of automated blood pressure measurements [19, 20].
- (4) Medical mechatronics integration would bring novel healthcare application which considers the techniques of the biomedical signal processing of cuff pressure sensors as well as the control of motor-activated variable volume cuff chamber [21].

5. Conclusions and Future Works

In this paper, a BP measurement approach based on an active control scheme of cuff pressure is proposed. It automatically adjusted the trajectories of pressure to achieve a highly efficient measurement performance. Compared with conventional BP instruments, the dedicated processes of cuff inflation and deflation resulted in a longer measurement time. An actuated single-acting cylinder provides the targeted pressure of cuff by altering the position of piston. It significantly eliminated the air disturbances during air pump. According to the characteristic BP segments, the functions of trajectories are automatically generated to achieve the considerations of both measuring time and resolution. The single-acting cylinder is actuated by a DC motor and a linear screw. The active pressure control is implemented in terms of a closed-loop pressure control scheme. The experiments verified the system performance. According to the healthy subject experiment results, the AIM reduced 34.21% and the ADM reduced 15.78% of measurement time when compared to a commercial BP

TABLE 3: Measurement results of proposed and commercial BP device of five healthy subjects (unit: mmHg).

SBP/DBP mmHg Method	Subject 1	Subject 2	Subject 3	Subject 4	Subject 5	Average measurement time
Commercial electronic BP device (1st measurement)	115/77	132/61	113/74	103/53	107/78	
Commercial electronic BP device (2nd measurement)	117/77	133/53	107/64	89/51	99/63	
Commercial electronic BP device (3rd measurement)	116/74	137/60	100/62	87/48	101/64	38
Commercial electronic BP device (8th measurement)	121/82	123/65	105/59	87/52	105/67	
Average	116/77	131/59	106/64	91/51	103/68	
ADM mode (4th measurement)	114/75	126/70	114/66	91/64	107/60	
ADM mode (5th measurement)	119/80	125/71	109/67	84/47	110/71	32
Average	116/77	125/70	111/66	87/55	108/65	
AIM mode (6th measurement)	131/66	125/65	129/80	94/52	123/68	
AIM mode (7th measurement)	121/75	139/70	114/65	86/53	112/65	25
Average	126/70	132/66	121/72	90/52	117/66	

TABLE 4: Statistics results of proposed and commercial BP device of a healthy subject with 11 trials (unit: MMHG).

	Mean SBP	SBP STDEV	Mean DBP	DBP STDEV
MicroLife	107.36	4.17	70.45	3.64
ADM mode	108.54	3.72	68.36	3.25
AIM mode	112.72	4.22	67.27	3.82

monitor. The standard deviation of measurements of the same healthy subject at the same time was also evaluated to examine the performance of precision. The ADM performed much consistently (i.e., less standard deviation) in the measurements when compared to a commercial BP monitor.

In the future, the control parameters of system are optimized with respect to characteristic models, such as the systems of single-acting cylinder and cuff. Thus, the stability and efficiency of control system could be further improved. Meanwhile, the real patient with an IRB application will be done to examine the clinical feasibility. Besides, processing the verification with IEC EN 1060-4 standard will be the next plan of this work.

Conflicts of Interest

The authors declare no conflict of interest.

References

- [1] R. Anthony, L. Carlene, G. Thomas, and V. Thoe, "The growing burden of risk from high blood pressure, cholesterol, and bodyweight," in *Disease Control Priorities in Developing Countries*, pp. 851–868, World Bank, Washington (DC), 2006.
- [2] M. Nitzan, A. Patron, Z. Glik, and A. T. Weiss, "Automatic noninvasive measurement of systolic blood pressure using photoplethysmography," *Biomedical Engineering Online*, vol. 8, p. 28, 2009.
- [3] G. Fortino and V. Giampa, "PPG-based methods for non invasive and continuous blood pressure measurement: an overview and development issues in body sensor networks," in *2010 IEEE International Workshop on Medical Measurements and Applications*, pp. 10–13, Ottawa, Canada, April 2010.
- [4] Y. Song, S. Gao, A. Ikarashi, and K. Yamakoshi, "A new cuff unit for measuring instantaneous blood pressure at the finger artery by local pressurization," in *2009 3rd International Conference on Bioinformatics and Biomedical Engineering*, pp. 1–4, Beijing, China, June 2009.
- [5] H. Shimazu, H. Ito, and H. Kobayashi, "Idea to measure diastolic arterial pressure by volume oscillometric method in human fingers," in *Proceedings of Medical and Biological Engineering and Computation*, pp. 549–554, Tokyo, Japan, 1986.
- [6] M. Nogawa, M. Ogawa, T. Yamakoshi, S. Tanaka, and K. Yamakoshi, "Adaptive control with self-tuning for non-invasive beat-by-beat blood pressure measurement," in *2011 Annual International Conference of the IEEE Engineering in Medicine and Biology Society*, pp. 4344–4347, Boston, MA, USA, August 2011.
- [7] J. Y. Lee, E. Y. Choi, H. J. Jeong, K. H. Kim, and J. C. Park, "Blood pressure measurement using finger cuff," in *2005 IEEE Engineering in Medicine and Biology 27th Annual Conference*, pp. 3575–3577, Shanghai, China, September 2005.
- [8] F. S. Cattivelli and H. Garudadri, "Noninvasive cuffless estimation of blood pressure from pulse arrival time and heart rate with adaptive calibration," in *2009 Sixth International Workshop on Wearable and Implantable Body Sensor Networks*, pp. 114–119, Berkeley, CA, USA, June 2009.
- [9] W. Van Moer, L. Lauwers, D. Schoors, and K. Barbé, "Linearizing oscillometric blood-pressure measurements: (non)sense?" *IEEE Transactions on Instrumentation and Measurement*, vol. 60, no. 4, pp. 1267–1275, 2011.
- [10] J. J. Wang, C. T. Lin, S. H. Liu, and Z. C. Wen, "Model-based synthetic fuzzy logic controller for indirect blood pressure measurement," *IEEE Transactions on Systems, Man, and Cybernetics, Part B (Cybernetics)*, vol. 32, no. 3, pp. 306–315, 2012.
- [11] H. S. Oh, Y. J. Chee, J. S. Lee, I. Y. Kim, S. I. Kim, and Y. S. Kim, "The modified step-wise deflation method in blood pressure measurement," in *2008 Computers in Cardiology*, pp. 169–172, Bologna, Italy, September 2008.
- [12] K. Barbé, W. V. Moer, and L. Lauwers, "Oscillometric blood pressure measurements: a signal analysis," *Journal of Physics: Conference Series*, vol. 238, no. 1, 2010.

- [13] G. Lopez, H. Ushida, K. Hidaka, M. Shuzo, and I. Yamada, "Continuous blood pressure measurement in daily activities," in *SENSORS, 2009 IEEE*, pp. 827–831, Tokyo, Japan, 2009.
- [14] X. R. Ding, N. Zhao, G. Z. Yang et al., "Continuous blood pressure measurement from invasive to unobtrusive: celebration of 200th birth anniversary of Carl Ludwig," *IEEE Journal of Biomedical and Health Informatics*, vol. 20, no. 6, pp. 1455–1465, 2016.
- [15] M. M. Islam, F. H. M. Rafi, A. F. Mitul, and M. Ahmad, "Development of a noninvasive continuous blood pressure measurement and monitoring system," in *2012 International Conference on Informatics, Electronics & Vision (ICIEV)*, pp. 1085–1090, Dhaka, Bangladesh, May 2012.
- [16] C. H. Chang and Y. T. Zhang, "Continuous and long-term arterial blood pressure monitoring by using h-shirt," in *2008 International Conference on Information Technology and Applications in Biomedicine*, pp. 267–269, Shenzhen, China, May 2008.
- [17] P. K. Lim, S. C. Ng, W. A. Jassim et al., "Improved measurement of blood pressure by extraction of characteristic features from the cuff oscillometric waveform," *Sensors*, vol. 15, pp. 14142–14161, 2015.
- [18] I. Koohi, S. Ahmad, I. Batkin, V. Groza, S. Shirmohammadi, and H. R. Dajani, "Dynamic threshold algorithm to evaluate trustworthiness of the estimated blood pressure in oscillometry," *IEEE Instrumentation & Measurement Magazine*, vol. 19, no. 5, pp. 26–35, 2016.
- [19] W. J. Verberk, S. Omboni, A. Kollias, and G. S. Stergiou, "Screening for atrial fibrillation with automated blood pressure measurement: research evidence and practice recommendations," *International Journal of Cardiology*, vol. 203, pp. 465–473, 2016.
- [20] M. Nitzan, "Automatic noninvasive measurement of arterial blood pressure," *IEEE Instrumentation & Measurement Magazine*, vol. 14, no. 1, pp. 32–37, 2011.
- [21] G. T. Chen, *Development of an Embedded BP Measurement Instrument with Active Cuff Pressure Control Schemes*, [Master Thesis], Department of Electrical Engineering, National Taiwan University of Science and Technology, Taipei, Taiwan, 2012.

Research Article

Analysis of the Biceps Brachii Muscle by Varying the Arm Movement Level and Load Resistance Band

Nuradebah Burhan,¹ Mohammad ‘Afif Kasno,² Rozaimi Ghazali,¹ Md Radzai Said,³ Shahrum Shah Abdullah,⁴ and Mohd Hafiz Jali¹

¹Center for Robotics and Industrial Automation, Faculty of Electrical Engineering, Universiti Teknikal Malaysia Melaka, Hang Tuah Jaya, 76100 Durian Tunggal, Malaysia

²Faculty of Engineering Technology, Universiti Teknikal Malaysia Melaka, Hang Tuah Jaya, 76100 Durian Tunggal, Malaysia

³Faculty of Mechanical Engineering, Universiti Teknikal Malaysia Melaka, Hang Tuah Jaya, 76100 Durian Tunggal, Malaysia

⁴Department of Electric and Electronics, Malaysia-Japan International Institute of Technology, Universiti Teknologi Malaysia, International Campus, Jalan Semarak, 54100 Kuala Lumpur, Malaysia

Correspondence should be addressed to Mohammad ‘Afif Kasno; mohammad.afif@utem.edu.my

Received 7 April 2017; Revised 30 June 2017; Accepted 1 August 2017; Published 12 September 2017

Academic Editor: Yi-Hung Liu

Copyright © 2017 Nuradebah Burhan et al. This is an open access article distributed under the Creative Commons Attribution License, which permits unrestricted use, distribution, and reproduction in any medium, provided the original work is properly cited.

Biceps brachii muscle illness is one of the common physical disabilities that requires rehabilitation exercises in order to build up the strength of the muscle after surgery. It is also important to monitor the condition of the muscle during the rehabilitation exercise through electromyography (EMG) signals. The purpose of this study was to analyse and investigate the selection of the best mother wavelet (MWT) function and depth of the decomposition level in the wavelet denoising EMG signals through the discrete wavelet transform (DWT) method at each decomposition level. In this experimental work, six healthy subjects comprised of males and females (26 ± 3.0 years and BMI of 22 ± 2.0) were selected as a reference for persons with the illness. The experiment was conducted for three sets of resistance band loads, namely, 5 kg, 9 kg, and 16 kg, as a force during the biceps brachii muscle contraction. Each subject was required to perform three levels of the arm angle positions (30° , 90° , and 150°) for each set of resistance band load. The experimental results showed that the Daubechies5 (db5) was the most appropriate DWT method together with a 6-level decomposition with a soft heursure threshold for the biceps brachii EMG signal analysis.

1. Introduction

The National Institutes of Health (NIH), through the National Centre for Medical Rehabilitation Research (NCMRR) located in the United States, published a rehabilitation research plan in 1993 due to the increase in the range of disabilities among Americans affecting daily activities, work, and communication [1]. The rehabilitation research was aimed at improving, restoring, and developing the disabilities of the body or functions of the body system. This can help workers to recover physically and vocationally and, finally, return to the work area. In the rehabilitation method, the first assessment is necessary to identify the

current condition of the patient’s disability and his/her ability before the illness. It also includes a biopsychosocial model that emphasizes the physical functionality factor, the level of mobilization, and the physiological and environmental conditions, as well as identifies the needs of the patient on returning to work.

Biceps brachii muscle illness is a common physical disability that requires rehabilitation exercises in order to launch the movement and strengthen the weak biceps brachii muscle. The biceps brachii muscle condition can be measured by electromyography (EMG) [2], which helps to analyse the muscle activity signal produced by the desired muscle. The muscle activity signal is generated by an

electrical signal that originates from the activation of the muscle fibres by a motor unit. It can be detected and measured by using EMG electrodes.

The EMG electrodes are of two types. The surface EMG (sEMG), which is commonly used in biomedical techniques, is known as a noninvasive method, while the needle EMG is an invasive method. The sEMG method is a convenient EMG measurement method as it can be easily implemented without any medical certificate, where the sEMG electrodes that are used can be placed on the desired skin surface to record the activity of the muscle [3]. However, the detection of the EMG signals is a complex process that is easily affected by a combination of numerous noise signals, the motion artefact, and the internal structure of the human body, such as the skin formation, velocity of the blood flow, and thickness of the fatty tissue [4]. It shows the recorded EMG signals, called the raw EMG signals, that contain information about the muscle and several noises during the EMG measurement. In order to obtain useful information from the EMG signals, several approaches in terms of feature extraction must be considered when analysing the performance of the EMG signal.

Feature extraction is the main part in signal processing in order to eliminate the affected noise or undesired part and to obtain the useful information in the EMG signals. Feature extraction can be categorized into three methods, namely, for the extraction of time domain (TD), frequency domain (TF), and time-frequency domain (TFD) features. Previous studies have mentioned that a stationary sEMG signal depends on many factors such as the contraction of the muscle under the application of a constant force, where the sEMG signal would be considered as stationary, which is a TD feature [5]. In the meantime, the sEMG signal is also considered as nonstationary because it is contained in various frequency components [6]. Thus, wavelet transform, as a TFD feature, is the best feature extraction technique for analysing the sEMG in both the time and frequency domains.

Several authors have described the EMG signal analysis performance and their validation of the biceps brachii muscle with different ranges of age, protocols, and electrode placements on the desired muscle. For example, the monitoring of an athlete's performance in muscle strength exercises focuses on the use of a dumbbell as a resistance to muscle contraction [7] in order to increase the strength of the biceps brachii muscle. A previous study discussed and compared the effect of electromyography on the biceps brachii muscles of male and female subjects. The comparisons were based on the root mean square and mean values [8]. Many studies have attempted to analyse the contraction signals of the biceps brachii muscle in three different age groups, namely, adolescents (younger age), vicenarians (middle age), and tricenarians (elderly age). In their research, the comparison of the electromyographic biceps brachii muscle activity was based on differences in the root mean square (RMS) and mean absolute value (MAV), which are the most commonly accepted features that are used to define the amplitude of electromyography signals [9, 10]. Some researchers discussed the placement of the electrodes on the biceps brachii muscle

TABLE 1: Physical characteristics of subjects.

Gender	Age (years)	Weight (kg)	Height (cm)	BMI (kg/cm)
Male	24	70	172	23.5
	25	68	169	23.8
	27	69	170	23.9
Female	23	55	157	22.3
	25	58	160	22.7
	26	54	159	21.4

during the EMG measurement. The best location for the EMG electrodes is in the area between the innervation zone (IZ) and the tendon to obtain high-quality and stable sEMG signals [11, 12].

This shows that previous researches into electromyography concentrated more on the performance of the biceps brachii muscle with regard to several factors based specifically on age and gender. Others clarified the role of the biceps brachii muscle in shoulder elevation and elbow flexion and extension movements [13, 14]. These were examined based on several variable factors such as the type of external load, contraction, and elbow joint angles.

Thus, this research was inspired to focus on analysing the electromyography signals from the biceps brachii muscle for resistance band rehabilitation exercises. The EMG measurement was made during the isometric muscle contraction for three angles at the arm level. This study was to investigate the difference in the sEMG signals on the muscles of vicenarians during the resistance band rehabilitation exercises in terms of gender and types of loads during muscle contraction at three angles at the arm level. A fixed sampling rate of 1000 Hz and a wireless EMG pre-amplifier were used.

2. Materials and Method

2.1. Subjects. Six healthy subjects, who were right-hand dominant, participated in this study. The six healthy subjects were categorized based on gender into three healthy male subjects and three healthy female subjects. All the subjects were vicenarians between the ages of 23 to 27 years. According to investigations in previous works, vicenarian subjects are within the best range of age as references for the human body in EMG measurements, where the muscles of those in middle age have grown gradually and a higher amplitude of EMG signals can be obtained during the EMG measurement process [15]. The normal body mass index (BMI) was one of the preferred physical characteristics of the subjects that was considered in this study. Table 1 shows the physical characteristics of all the subjects.

2.2. Experimental Setup and Protocols. A wireless Z03 EMG preamplifier with surface recording of the ground by Motion Lab Systems Inc. (Baton Rouge, LA, USA) was used for the EMG signal recording. The EMG preamplifier is a compact device with 12 mm disks with an interelectrode distance of 18 mm and one reference contact (12 × 3 mm) bar separating the sensors. Medical-grade stainless steel was used as the

contact material for the electrodes in this experiment. The EMG preamplifier had a gain at $1\text{ kHz} \times 300 \pm 1\%$, CMRR $> 100\text{ dB}$ at 65 Hz , input protection from radio frequency interference (RFI) filters, and electrostatic discharge (ESD), while the power supply range of this device was between $\pm 5\text{ Volts}$ and $\pm 15\text{ Volts}$.

Some protocols had to be considered before the start of the experiment. First, the subjects had to be free of any muscular disease and avoid strenuous exercise on the biceps brachii muscle for two days prior to the EMG measurement. Second, the subjects needed to perform 5 minutes of warm-up stretching exercises with the lifting and lowering of weights, with an interval of at least 2 minutes between muscle contractions to avoid the possibility of muscle fatigue. The third protocol was the clarification about the procedure for the placement of the electrodes and the skin preparation. It was necessary to prepare the skin by cleaning the desired skin area using 70% isopropyl alcohol and shaving the hair, if necessary, in order to reduce the electrode-skin impedance [16]. The preferred placement of the EMG electrodes on the biceps brachii muscle, as suggested in previous works, is in the middle of the biceps brachii muscle, known as the belly muscle, as it shows a significantly higher amplitude [17]. All the protocols were designed to minimize the motion artefact, crosstalk, and internal noise during the EMG measurement.

This experiment consisted of three sets of resistance band loads of 5 kg, 9 kg, and 16 kg that were used as a force during the biceps brachii muscle contractions. Each subject was required to stand up straight and perform three levels of arm angle positions (30° , 90° , and 150°) for each set of resistance band loads. The arm angle position was measured using a Medigauge electronic digital goniometer. The subjects had to hold the resistance band for 10 seconds and then take a break for a time interval of 2 minutes for each movement of the arm level. The procedure was repeated 10 times per set of resistance band loads. This is illustrated in Figure 1, which shows the subject holding the resistance band for 10 seconds when the angle at the arm level was at 90° . The resistance band is one of the preferred tools in biceps brachii rehabilitation exercises, where it is currently being used in rehabilitation centres to train patients to build up the strength of their biceps brachii muscle after surgery or injury.

2.3. EMG Signal Processing. In the experimental setup, a compact wireless EMG preamplifier device was used to supply the input signal to an NI USB-6009 data acquisition (DAQ) device from National Instruments, where the raw signal was recorded at a sampling rate of 1000 Hz . The signal acquired from the DAQ device acted as a signal source for the LabVIEW 2016 model. Subsequently, the recorded EMG signal was processed by filtering and extracting the useful signals with the LabVIEW WA Detrend VI and LabVIEW Wavelet Denoise Signal. The discrete wavelet transform (DWT) approach was implemented in the EMG signal analysis. Based on the previously mentioned work, the DWT

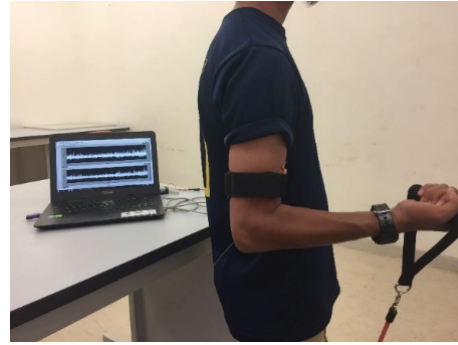


FIGURE 1: EMG data being recorded when angle at the arm level is at 90° .

was better than the continuous wavelet transform (CWT) approach, which did not yield a redundant analysis [16].

The DWT algorithm uses a filtering technique that consists of a shifted and scaled version of a certain function called a mother wavelet transform (MWT) function, $\psi(t)$ [18]. The MWT is shifted by time (b) and scaled by a factor (a), as in

$$\text{DWT}_{a,b}(f) = \frac{1}{\sqrt{a}} \int f(t) \psi\left(\frac{t-b}{a}\right) dt. \quad (1)$$

In this method, the DWT will decompose a signal into different frequency bands by passing it through two filters, namely, a low-pass filter (h) and a high-pass filter (g) at each decomposition level. Both filters are associated with the scaling function, φ , and the MWT function, ψ , where the scaling function is related to the low-pass filter and the MWT function is related to the high-pass filter [19], which can be shown through the following equations:

$$\begin{aligned} \varphi &= 2 \sum_{n=0}^{N-1} h(n) \varphi(2t-n), \\ \psi &= 2 \sum_{n=0}^{N-1} g(n) \psi(2t-n). \end{aligned} \quad (2)$$

These equations will be followed by downsampling by the factor of 2 in order to obtain the successive DWT filtering of the time domain signal. The output of the downsampled low-pass filter produces an approximation coefficient, cA_i , whereas the downsampled high-pass filter produces the detailed coefficient, cD_i , of the depth decomposition level, i . The equations for the filters can be expressed by

$$\begin{aligned} cA_i(k) &= \sum_{n=0} cA_{i-1}(n) h(2k-n), \\ cD_i(k) &= \sum_{n=0} cA_{i-1}(n) g(2k-n). \end{aligned} \quad (3)$$

2.4. Mother Wavelet and Decomposition Level Selection. In the denoising signal, several common MWT functions, such as Daubechies, Coiflet, and Symlet, are used. The selection of the best wavelet function and depth of

decomposition is required to produce a perfect reconstruction and better signal analysis [17]. The best MWT function and decomposition level were determined by calculating the signal to noise ratio (SNR) and root mean square error (RMSE), as given below [19].

$$\text{SNR (dB)} = 10 \log_{10} \left(\frac{\sum_{n=1}^N x[n]^2}{\sum_{n=1}^N (\hat{x}[n] - x[n])^2} \right), \quad (4)$$

$$\text{RMSE} = \sqrt{\frac{1}{N} \sum_{n=1}^N (\hat{x}[n] - x[n])^2},$$

where $x[n]$ is the noise-free EMG signal and $\hat{x}[n]$ is known as the denoised signal, while N is the number of signal samples. In this study, the value of N was 10000.

The SNR is defined as the ratio of the variance of the noise-free signal to the mean square error between the noise-free signal and the denoised signal, and it is the measurement of the signal strength relative to the background noise. It is measured in decibels (dB). The RMSE indicates the absolute measure of fit, which evaluates the closer of the observed data points to the predicted values.

2.5. Statistical Analysis. In this study, a statistical analysis was applied to the EMG signals and was executed using the MATLAB software. All the filtered EMG signals were analysed in terms of the average (Avg), standard deviation (SD), and root mean square (RMS). The Avg, SD, and RMS were obtained by using the statistical equations as follows:

$$\text{average (Avg)}(\bar{x}) = \frac{1}{N} \sum_{i=1}^N x_i,$$

$$\text{standard deviation (SD)}(\sigma) = \sqrt{\frac{1}{N} \sum_{i=1}^N (x_i - \bar{x})^2}, \quad (5)$$

$$\text{root mean square (RMS)} = \sqrt{\frac{1}{N} \sum_{i=1}^N x_i^2},$$

where x_i is the noise-free signal collected and N is the number of signal samples.

3. Results and Discussion

In this experiment, the biceps brachii EMG signals of the subjects were obtained at a six-level decomposition coefficient through the DWT method. Seven subbands were involved, namely, cD1, cD2, cD3, cD4, cD5, cD6, and cA6, which represented the frequency range from the band limit of the EMG signal. The selection of a suitable decomposition level was necessary to extract the useful information and analyse the EMG signal by using the DWT method. Other than that, the threshold function and limit were also the main factors in ensuring that the useful information of the EMG signal would be able to be extracted using the

TABLE 2: SNR and RMSE results with respect to the decomposition level.

Decomposition level	SNR (dB)	RMSE (* 10 ⁻³)
1	57.056	2.80
2	56.946	2.83
3	56.945	2.83
4	56.946	2.80
5	56.960	2.80
6	56.992	2.80
7	56.919	2.83
8	56.901	2.87
9	56.872	2.90
10	56.901	2.87
11	56.901	2.87
12	56.906	2.87
13	56.901	2.87

WT denoising technique. Based on that, the heursure threshold, with a soft thresholding method, was proposed to analyse the EMG signal. Table 2 presents the SNR and RMSE results with respect to the decomposition level by using the Daubechies5 (db5) and heursure thresholding method. The results for both the SNR and RMSE values showed the best performance at the 6-level decomposition through the DWT method at each level, where the highest SNR value and lowest RMSE value were obtained. The highest SNR value showed the strength of the EMG signal that was acquired. The lowest value of the RMSE illustrated a better fit of the signal data.

Consequently, the best SNR and RMSE values were required to determine the suitable MWT function at the 6-level decomposition of the EMG signal analysis. The MWT functions that were investigated in previous studies, such as Daubechies, Coiflet, and Symlet, have their own suitability that depends on the types of signals in the biomedical field that need to be analysed, where the Daubechies2 (db2) is more appropriate for the electroencephalography (EEG) smoothing signal, the Daubechies4 (db4), Coiflet3 (coif3), Coiflet4 (coif4), and Coiflet5 (coif5) are able to improve the electrocardiography (ECG) detection signal in their applications, and the Daubechies5 (db5) is convenient for use in the removal of noise from the EMG signal [20–24]. This can be further strengthened with the SNR and RMSE results for the db5 as the optimal MWT in Table 3, where it is shown that the db5 with a 6-level decomposition and soft heursure threshold through the DWT method is suitable for the biceps brachii EMG signal analysis.

The EMG denoising technique, using the DWT method with the appropriate MWT function (db5) and depth of the decomposition level (6-level), was implemented in the rehabilitation application focusing on biceps brachii illness. The efficacy of the EMG denoising technique used was determined by calculating the SD values for the subjects in every given task. The results of the EMG signal analysis

TABLE 3: SNR and RMSE results with respect to wavelet types.

Wavelet types	SNR (dB)	RMSE (* 10 ⁻³)
Daubechies2 (db2)	54.1161	3.93
Daubechies3 (db3)	56.1163	3.13
Daubechies4 (db4)	56.7373	2.93
Daubechies5 (db5)	56.9924	2.80
Coiflet2 (coif2)	56.8161	2.90
Coiflet3 (coif3)	57.0431	2.80
Coiflet4 (coif4)	56.9870	2.83
Coiflet5 (coif5)	57.0415	2.83
Symlet2 (sym2)	56.8161	2.90
Symlet3 (sym3)	56.1163	3.13
Symlet4 (sym4)	56.6773	2.93
Symlet5 (sym5)	57.0152	2.80

TABLE 4: Results of three male subjects for 5 kg.

Gender	Angles	Statistical values		
		Avg	SD	RMS
Male 1	30°	2.0001	0.0312	2.0003
	90°	2.0001	0.0511	2.0008
	150°	2.0006	0.0549	2.0013
Male 2	30°	2.0000	0.0060	2.0000
	90°	2.0000	0.0142	2.0001
	150°	2.0000	0.0093	2.0000
Male 3	30°	2.0000	0.0123	2.0001
	90°	2.0000	0.0214	2.0001
	150°	2.0001	0.0347	2.0004

TABLE 5: Results of three male subjects for 9 kg.

Gender	Angles	Statistical values		
		Avg	SD	RMS
Male 1	30°	2.0001	0.0299	2.0003
	90°	2.0001	0.0480	2.0007
	150°	2.0001	0.0664	2.0013
Male 2	30°	2.0000	0.0077	2.0000
	90°	2.0000	0.0111	2.0000
	150°	2.0000	0.0105	2.0000
Male 3	30°	2.0000	0.0188	2.0001
	90°	2.0001	0.0299	2.0003
	150°	1.9999	0.0357	2.0002

were classified according to the gender. It consisted of three types of resistance band loads, namely, 5 kg, 9 kg, and 16 kg. Each set of resistance band loads contained three different angles of the arm level. Tables 4, 5, and 6 show the results for the male subjects, whereas the results of the statistical values for the female subjects are presented in Tables 7, 8, and 9.

TABLE 6: Results of the three male subjects for 16 kg.

Gender	Angles	Statistical values		
		Avg	SD	RMS
Male 1	30°	1.9995	0.0686	2.0007
	90°	2.0000	0.0509	2.0006
	150°	1.9999	0.0695	2.0011
Male 2	30°	2.0000	0.0078	2.0000
	90°	2.0000	0.0121	2.0000
	150°	2.0000	0.0102	2.0000
Male 3	30°	2.0000	0.0326	2.0003
	90°	2.0000	0.0371	2.0004
	150°	2.0000	0.0670	2.0011

TABLE 7: Results of three female subjects for 5 kg.

Gender	Angles	Statistical values		
		Avg	SD	RMS
Male 1	30°	2.0000	0.0097	2.0001
	90°	2.0000	0.0135	2.0000
	150°	2.0000	0.0207	2.0001
Male 2	30°	2.0000	0.0177	2.0002
	90°	1.9999	0.0256	2.0000
	150°	2.0000	0.0306	2.0003
Male 3	30°	2.0000	0.0057	2.0000
	90°	2.0000	0.0088	2.0000
	150°	2.0000	0.0089	2.0000

TABLE 8: Results of three female subjects for 9 kg.

Gender	Angles	Statistical values		
		Avg	SD	RMS
Male 1	30°	2.0000	0.0111	2.0000
	90°	2.0000	0.0192	2.0001
	150°	1.9999	0.0366	2.0002
Male 2	30°	2.0000	0.0248	2.0002
	90°	2.0000	0.0187	2.0001
	150°	2.0000	0.0199	2.0000
Male 3	30°	2.0000	0.0063	2.0000
	90°	2.0000	0.0143	2.0001
	150°	2.0000	0.0129	2.0000

The tables above show that the SD values had a smaller range, where the SD range for the male subjects was from 0.006 to 0.0695 and the SD range for the female subjects was from 0.005 to 0.0624. This indicated the clustered data of the EMG signals produced during the rehabilitation exercise. The lowest SD in the statistical data in this experiment showed that the data had a good performance. The good performance of the statistical data in this experiment was shown in the regression performance for both genders. Figures 2, 3, and 4 present the regression results of the male subjects, while Figures 5, 6, and 7 show

TABLE 9: Results of three female subjects for 16 kg.

Gender	Angles	Statistical values		
		Avg	SD	RMS
Male 1	30°	2.0000	0.0276	2.0002
	90°	2.0000	0.0425	2.0004
	150°	1.9999	0.0568	2.0007
Male 2	30°	2.0001	0.0369	2.0004
	90°	2.0003	0.0624	2.0012
	150°	2.0001	0.0326	2.0003
Male 3	30°	1.9999	0.0176	2.0000
	90°	2.0001	0.0225	2.0002
	150°	2.0000	0.0228	2.0001

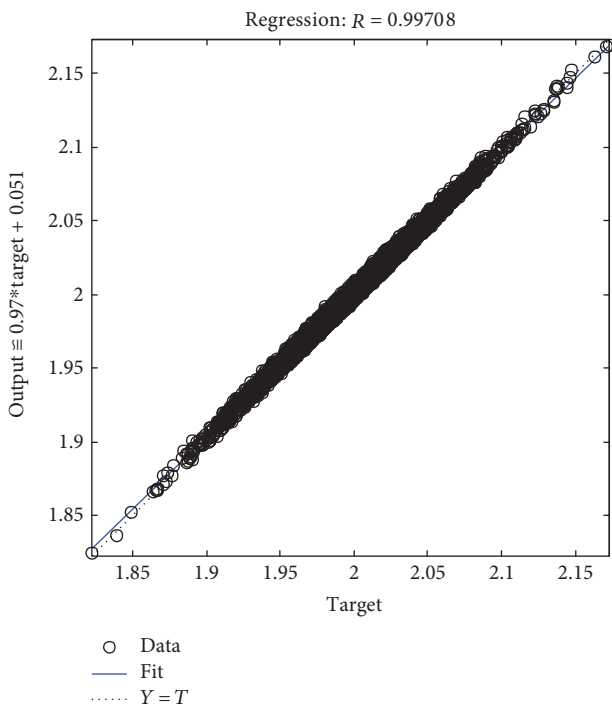


FIGURE 2: Male linear regression for 5 kg.

the regression results for the female subjects for three different load resistance bands when the arm angle was at 30°. The regression, R , in each load resistance band for both genders was above 0.92. The regression plots displayed the perfect fit of the data, where the data fell along a 45° line, thereby indicating that the data obtained were equal to the targets. This indicated a good accuracy performance of the data obtained by using the appropriate db5 as a MWT function and a 6-level decomposition through the DWT method in the EMG denoising. The best performance of the denoising EMG signals acquired helped to obtain a better feature extraction and classification of the EMG signals. Consequently, it helped to classify the EMG patterns of the three different angles of the arm level in this rehabilitation application.

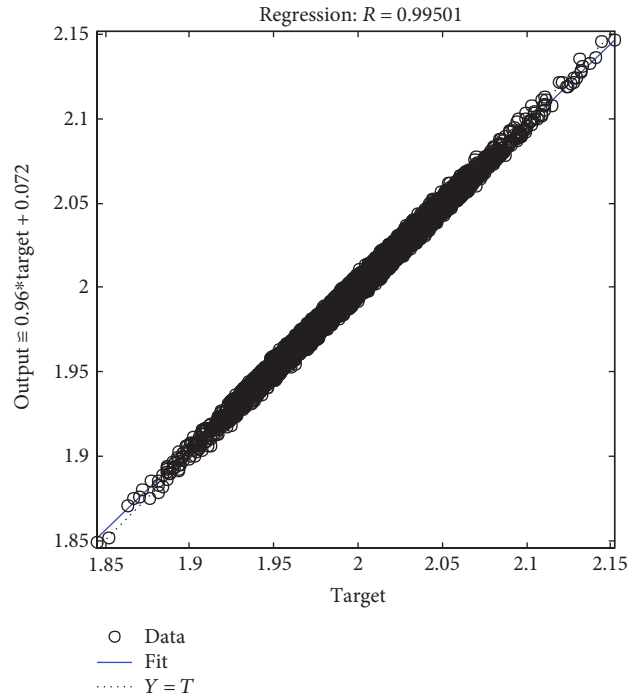


FIGURE 3: Male linear regression for 9 kg.

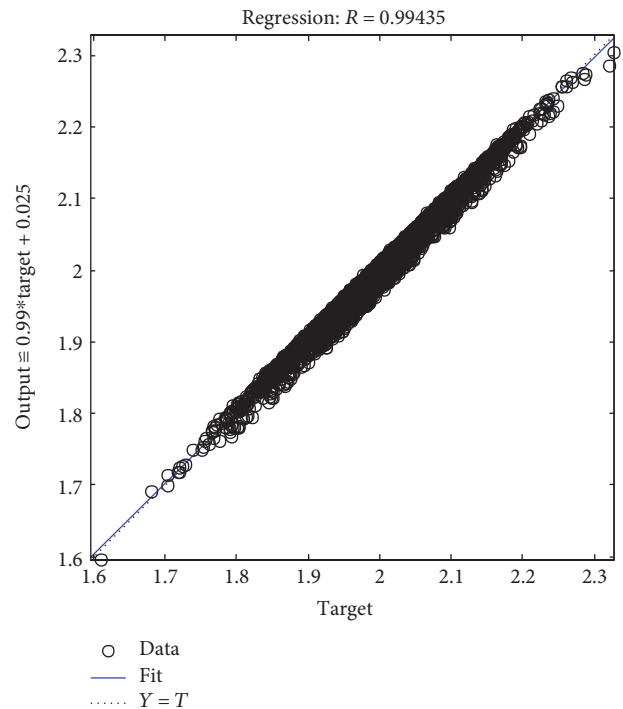


FIGURE 4: Male linear regression for 16 kg.

4. Conclusion

In this study, the compatibility of the three common MWT functions, namely, Daubechies, Coiflet, and Symlet, were selected for analysis to determine an optimal MWT function in order to obtain the best performance for the denoising of

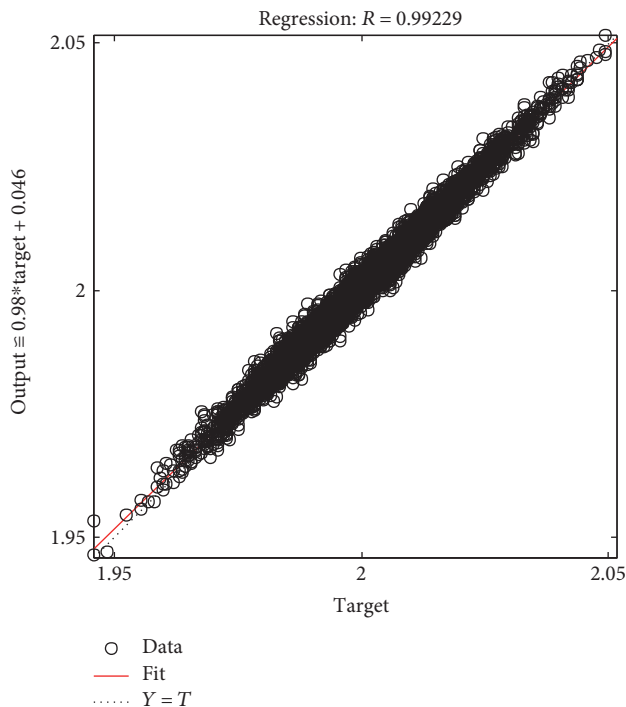


FIGURE 5: Female linear regression for 5 kg.

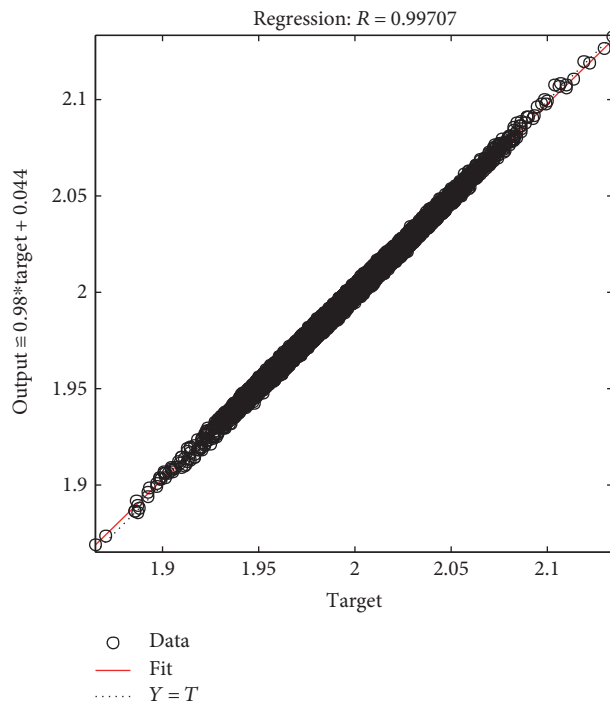


FIGURE 7: Female linear regression for 16 kg.

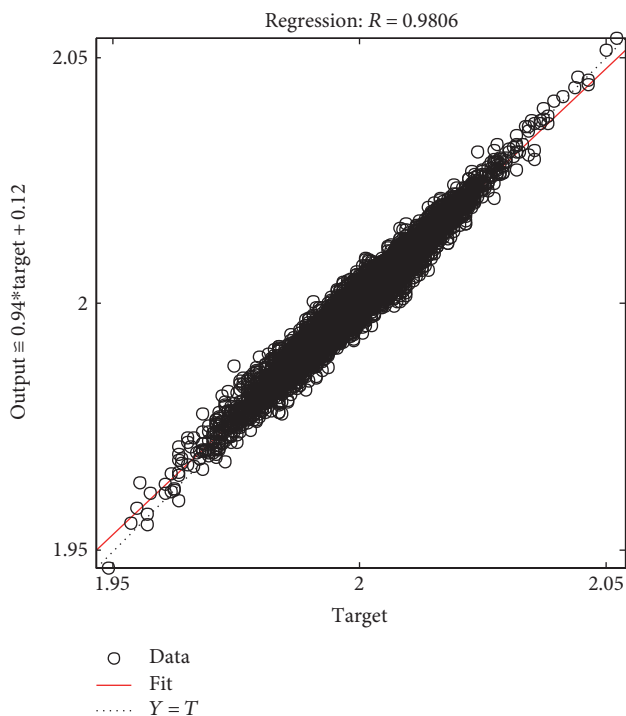


FIGURE 6: Female linear regression for 9 kg.

the EMG signals. This experiment was able to successfully select the optimal MWT function and depth of the decomposition level with the best performance of the EMG signal denoising with the EMG datasets of the six subjects. Based on the analysis in this study, it was concluded that the “db5” with a “6-level decomposition” is more appropriate

for denoising the EMG signal of the biceps brachii muscle in order to obtain a better performance on the feature extraction and classification technique of the EMG signal in the rehabilitation application.

Conflicts of Interest

This funding did not lead to any conflict of interests regarding the publication of this manuscript.

Acknowledgments

The authors would like to thank the Ministry of Education (MOE), Centre for Research and Innovation Management (CRIM), and Universiti Teknikal Malaysia Melaka (UTeM) for sponsoring this project. This project is funded under Research Acculturation Grant Scheme (RAGS) Grant no. RAGS/1/2015/TK05/FTK/03/B0012.

References

- [1] A. O'Mara, J. H. Rowland, and T. N. Greewell, “National Institutes of Health research plan on rehabilitation,” *Archives of Physical Medicine and Rehabilitation*, vol. 98, no. 4, pp. 1–4, 2017.
- [2] M. Z. Jamal, “Signal acquisition using surface EMG and circuit design considerations for robotic prosthesis,” in *Computational Intelligence in Electromyography Analysis - A Perspective on Current Applications and Future Challenges*, pp. 427–448, 2012.
- [3] M. H. Jali, I. Ibrahim, Z. H. Bohari, M. F. Sulaima, and M. N. M. Nasir, “Classification of arm movement based on upper limb muscle signal for rehabilitation device,” *Journal*

- of Theoretical and Applied Information Technology*, vol. 68, no. 1, pp. 125–137, 2014.
- [4] C. J. De Luca, L. Donald Gilmore, M. Kuznetsov, and S. H. Roy, “Filtering the surface EMG signal: movement artifact and baseline noise contamination,” *Journal of Biomechanics*, vol. 43, no. 8, pp. 1573–1579, 2010.
- [5] A. Phinyomark, F. Quaine, S. Charbonnier, C. Serviere, F. Tarpin-bernard, and Y. Laurillau, “Feature extraction of the first difference of EMG time series for EMG pattern recognition,” *Computer Methods and Programs in Biomedicine*, vol. 117, no. 2, pp. 247–256, 2014.
- [6] F. Bai, T. M. Lubecki, C. M. Chew, and C. L. Teo, “Novel time-frequency approach for muscle fatigue detection based on sEMG,” in *2012 IEEE Biomedical Circuits and Systems Conference. Intell. Biomed. Electron. Syst. Better Life Better Environment. BioCAS 2012 - Conference Publications*, pp. 364–367, 2012.
- [7] Z. Taha, C. Ming, N. U. Ahamed, S. Joseph, and S. F. S. Omar, “Performance analysis in strength training: an innovative instrumentation,” *Procedia Engineering*, vol. 147, pp. 455–460, 2016.
- [8] N. U. Ahamed, Z. md yusof, M. Alqahtani, O. Altwijri, M. Rahman, and K. Sundaraj, “Gender effects in surface electromyographic activity of the biceps brachii muscle during prolonged isometric contraction,” *Procedia Computer Science*, vol. 61, pp. 448–453, 2015.
- [9] N. U. Ahamed, Z. Taha, M. Alqahtani, O. Altwijri, M. Rahman, and A. Deboucha, “Age related differences in the surface EMG signals on adolescent’s muscle during contraction,” in *IOP Conference Series: Materials Science and Engineering*, vol. 114, pp. 1–6, 2015.
- [10] N. U. Ahamed, M. Alqahtani, O. Altwijri, M. Rahman, and K. Sundaraj, “Age-related EMG responses of the biceps brachii muscle of young adults,” *Biomedical Research*, vol. 27, no. 3, pp. 787–793, 2016.
- [11] H. J. Hermens, B. Freriks, C. Disselhorst-Klug, and G. Rau, “Development of recommendations for SEMG sensors and sensor placement procedures,” *Journal of Electromyography and Kinesiology*, vol. 10, no. 5, pp. 361–374, 2000.
- [12] A. Rainoldi, G. Melchiorri, and I. Caruso, “A method for positioning electrodes during surface EMG recordings in lower limb muscles,” *Journal of Neuroscience Methods*, vol. 134, no. 1, pp. 37–43, 2004.
- [13] S. Charlotte, F. Anneliese, and C. Disselhorst-klug, “The role of biceps brachii and brachioradialis for the control of elbow flexion and extension movements,” *Journal of Electromyography and Kinesiology*, vol. 28, pp. 67–75, 2016.
- [14] D. Landin, J. Myers, M. Thompson, R. Castle, and J. Porter, “The role of the biceps brachii in shoulder elevation,” *Journal of Electromyography and Kinesiology*, vol. 18, no. 2, pp. 270–275, 2008.
- [15] N. U. Ahamed, K. Sundaraj, R. B. Ahmad, M. Rahman, and M. A. Islam, “Analysis of right arm biceps brachii muscle activity with varying the electrode placement on three male age groups during isometric contractions using a wireless EMG sensor,” *Procedia Engineering*, vol. 41, pp. 61–67, 2012.
- [16] M. H. Jali, I. M. Ibrahim, M. F. Sulaima, W. M. Bukhari, T. Ahmad Izzuddin, and M. Na’im Nasir, “Features extraction of EMG signal using time domain analysis for arm rehabilitation device,” *International Conference on Mathematics, Engineering and Industrial Applications. 2014 (ICoMEIA 2014)*, vol. 1660, no. 1, pp. 1–9, 2015.
- [17] N. Uddin, K. Sundaraj, M. Alqahtani, O. Altwijri, M. A. Ali, and M. A. Islam, “EMG-force relationship during static contraction: effects on sensor placement locations on biceps brachii muscle,” *Technology and Health Care*, vol. 22, no. 4, pp. 505–513, 2014.
- [18] M. R. Canal, “Comparison of wavelet and short time Fourier transform methods in the analysis of EMG signals,” *Journal of Medical Systems*, vol. 34, pp. 91–94, 2010.
- [19] N. K. Al-qazzaz, S. Hamid, B. Mohd, and S. A. Ahmad, “Signal analysis during a working memory task,” *Sensors*, vol. 15, no. 11, pp. 29015–29035, 2015.
- [20] K. Veer, “A technique for classification and decomposition of muscle signal for control of myoelectric prostheses based on wavelet statistical classifier,” *Measurement*, vol. 60, pp. 283–291, 2015.
- [21] A. Subasi, “Classification of EMG signals using combined features and soft computing techniques,” *Applied Soft Computing*, vol. 12, no. 8, pp. 2188–2198, 2012.
- [22] A. O. Andrade, A. B. Soares, S. J. Nasuto, and P. J. Kyberd, *EMG Decomposition and Artefact Removal*, 2012.
- [23] S. F. Omar, S. Yussof, and T. Islam, “Finding the optimum level of wavelet decomposition for reducing noise in wireless communication,” *Australian Journal of Basic and Applied Sciences*, vol. 5, no. 11, pp. 1212–1217, 2011.
- [24] B. Liu, Y. Sera, N. Matsubara, K. Otsuka, and S. Terabe, “Signal denoising and baseline correction by discrete wavelet transform for microchip capillary electrophoresis,” *Electrophoresis*, vol. 24, no. 18, pp. 3260–3265, 2003.

Research Article

Development of an Automatic Dispensing System for Traditional Chinese Herbs

Chi-Ying Lin and Ping-Jung Hsieh

Department of Mechanical Engineering, National Taiwan University of Science and Technology, Taipei City, Taiwan

Correspondence should be addressed to Chi-Ying Lin; chiying@mail.ntust.edu.tw

Received 5 April 2017; Revised 21 June 2017; Accepted 5 July 2017; Published 7 September 2017

Academic Editor: Yi-Hung Liu

Copyright © 2017 Chi-Ying Lin and Ping-Jung Hsieh. This is an open access article distributed under the Creative Commons Attribution License, which permits unrestricted use, distribution, and reproduction in any medium, provided the original work is properly cited.

The gathering of ingredients for decoctions of traditional Chinese herbs still relies on manual dispensation, due to the irregular shape of many items and inconsistencies in weights. In this study, we developed an automatic dispensing system for Chinese herbal decoctions with the aim of reducing manpower costs and the risk of mistakes. We employed machine vision in conjunction with a robot manipulator to facilitate the grasping of ingredients. The name and formulation of the decoction are input via a human-computer interface, and the dispensing of multiple medicine packets is performed automatically. An off-line least-squared curve fitting method was used to calculate the amount of material grasped by the claws and thereby improve system efficiency as well as the accuracy of individual dosages. Experiments on the dispensing of actual ingredients demonstrate the feasibility of the proposed system.

1. Introduction

Traditional Chinese medicine (TCM) can be divided into herbal decoctions and commercial extracts [1]. The former involves boiling TCM herbs to obtain a liquid for direct administration, whereas the latter involves artificial processing, such as drying, after the boiling process to produce a powder. Commercial extracts are easier to produce, transport, and administer. Their price is also more competitive. In contrast, herbal decoctions must be formulated by patients and the herbs tend to be more expensive. As a result, commercial extracts are preferred by many practitioners. Whether herbal decoctions and commercial extracts differ with regard to efficacy remains a topic of academic debate [2, 3]. Most TCM prescriptions require the boiling of multiple medicinal herbs followed by complex solubilizing, precipitation, adsorption, suspension, and chemical reactions to create new substances with enhanced efficacy, reduced potency, or reduced toxicity. Commercial extracts are mixtures of boil-free granules that have not undergone complex chemical reactions [4, 5]. The production process destroys many volatile substances and necessitates the

addition of excipients (mainly starch), which reduces the concentration of the herbal extracts. Furthermore, many TCM practitioners are accustomed to prescribing herbal decoctions in accordance with the medication compliance of their patients and then adjusting the prescriptions according to their constitution and specific symptoms. As a result, herbal decoctions remain an important part of clinical TCM.

Statistics compiled by the HPSO/CNA on pharmacist negligence [6] indicate that between 2002 and 2011, 43.8% of pharmacist negligence involved dispensing the wrong drug, and 31.5% involved dispensing the wrong dosage. Furthermore, 57.9% of all deaths caused by pharmacist negligence were caused by overdose, which resulted in USD 10,454,468 in compensation for damages. The most common reasons for dispensing errors include excessive work volume (21%), insufficient pharmacy staff (12%), time restrictions (11%), overwork (11%), and interruptions during dispensing (9.4%) [7]. Dispensing errors and medical staff shortages led to the development and wide-scale implementation of automated dose dispensing (ADD) systems [8–12]. According to Pedersen et al. [13], over 53% of the hospitals in Canada and 89% of those in the US are currently using ADD systems.

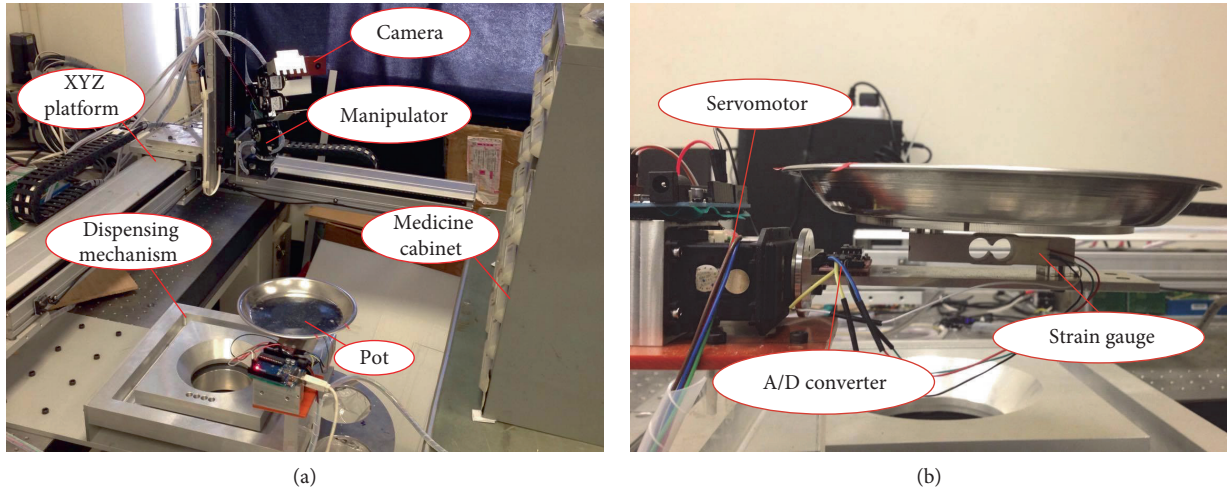


FIGURE 1: System setup. (a) Front view. (b) System used for weighing of herbs.

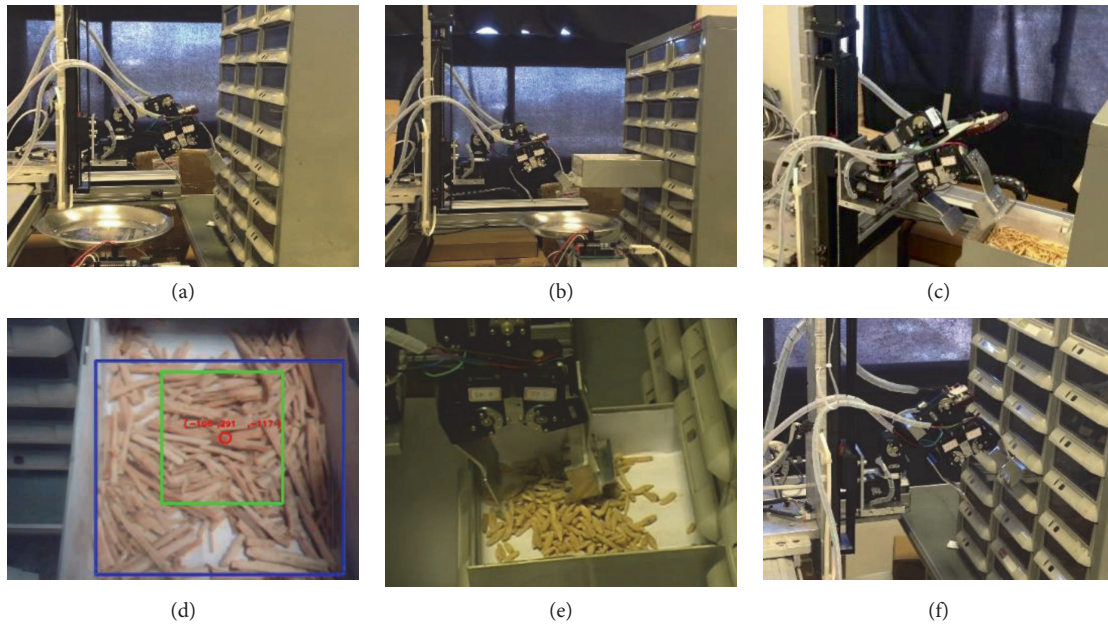


FIGURE 2: System in action. (a) Arm moving to location of herb drawer. (b) Medicine cabinet being opened. (c) Camera scanning the distribution of herbs in the drawer. (d) Determination of ideal gripping position. (e) Arm retrieving herb. (f) Medicine cabinet being closed.

Studies have proven that ADD systems can lower the chance of dispensing errors [14–16], enhance overall efficiency [14, 17], and even improve space usage [18, 19]. In contrast, most TCM pharmacies store medicinal herbs in cabinets and rely on the manual retrieval and weighing of herbs, which tends to be inefficient and arduous. As a result, patients must wait longer to pick up their prescriptions and dispensing errors are common. Several years ago, HollySys developed an ADD system for the scientific concentration of herbal medicines in hospitals [20]. The ability of that system to identify drugs automatically helps to prevent dispensing mistakes; however, errors still occurred in 10% of the samples weighing more than 5 g. Song et al. [21] constructed a dispensing system for 400 types of commercial

extracts. The system comprises multiple workstations and conveyor belts arranged in a parallel configuration. That system is able to fill several prescriptions at the same time and package medicines automatically.

Unfortunately, those dispensing systems are applicable only to commercial extracts. No existing scheme has been developed to automate the retrieval and dispensing of materials for herbal decoctions. This is the first study to develop such a system. The proposed solution uses a robotic arm-based ADD system in conjunction with image recognition technology. We also designed a user-friendly human-machine interface for inputting prescriptions, including the names and weights of each herb. The system automatically dispenses the medicines in the form of packets. Simulations

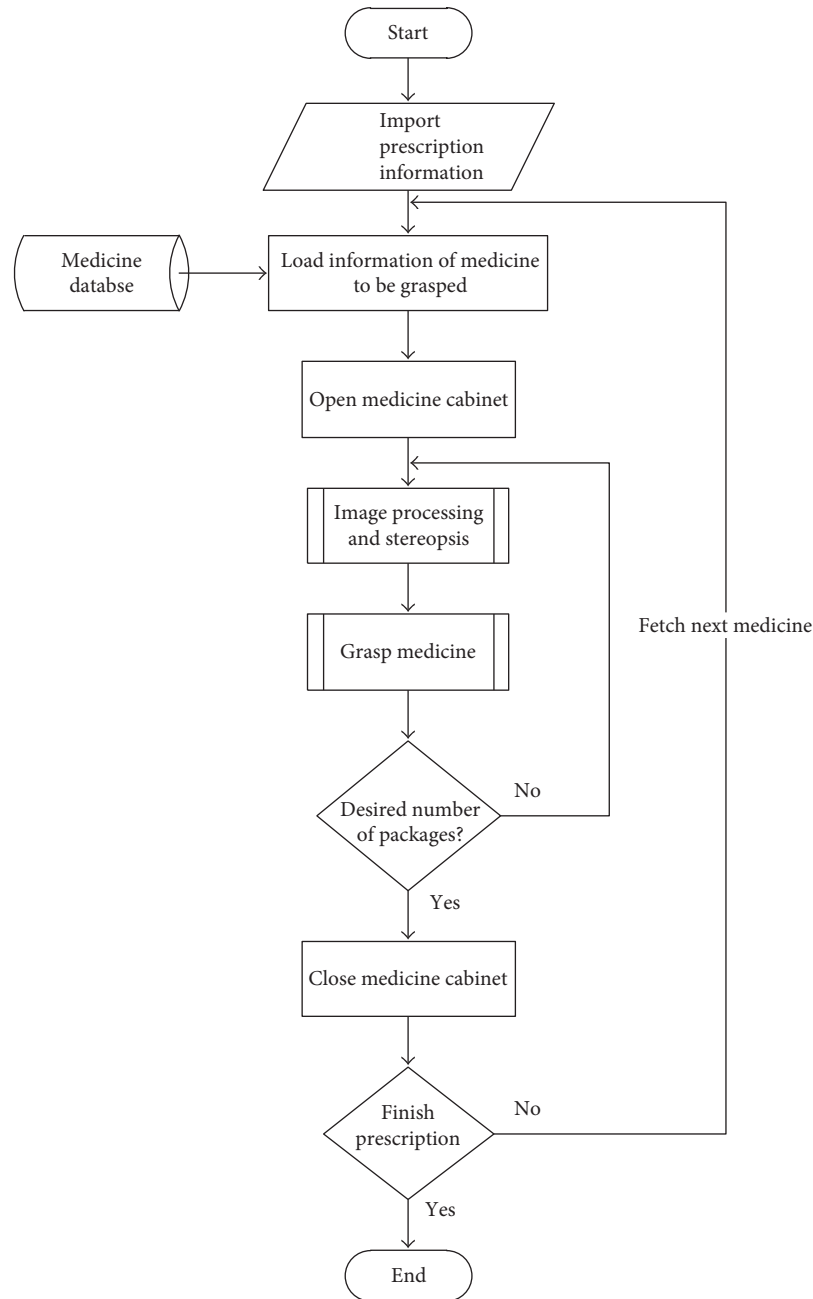


FIGURE 3: System flowchart.

were used to emulate the actual motions involved in retrieving herbs from cabinets in TCM pharmacies. The retrieval of herbs alters the distribution of ingredients in cabinet drawers, thereby altering the optimal retrieval location for the robotic arm. Thus, we employed machine vision to estimate the optimal location for retrieval. Unlike powdered herbs, the amount of which can be controlled using a flow control valve [21], most of the materials in herbal decoctions are irregular in size and shape. Thus, we employed a robotic claw for the retrieval of herbs. We employed the least-squares (LS) method to obtain the parameters for the retrieval equation used to calculate the weight of the herb and the size of the

claw aperture. Repeated performance of retrieval trials enabled the iterative optimization of the equation. We then compared this approach with two other methods that do not use iterative refinement. Experimental results demonstrate that the proposed approach can indeed enhance the retrieval accuracy and execution efficiency of the ADD system.

2. Methodology

2.1. Prototype System. Figure 1(a) presents a front view of the system, which uses an XYZ linear motion platform and a 3

degrees of freedom (DOF) robotic arm, which was designed in-house. The XYZ platform is responsible for large-stroke motions using an EzM-56L-A servomotor (manufactured by FASTECH) as an actuator with an encoder resolution of 10,000/Rev. The effective operating range of the platform in the X and Y directions is 500 mm × 500 mm with a screw lead of 10 mm/Rev. The effective operating range in the Z direction is 400 mm with screw lead of 5 mm/Rev. The main tasks of the 3 DOF robotic arm are the opening of cabinet drawers and the retrieval of herbs. Servomotors manufactured by ROBOTIS were installed at the joints of the arm. MX-106 servomotors were used for the first and second axes, which resulted in resolution of 0.087°. RX-64 servomotors are used for the third axis and the claw, resulting in resolution of 0.29°. The tracking of targets using the robotic arm requires an understanding of the external environment, such as posture, location, and color; therefore, we installed a binocular stereo camera on the third axis to estimate the location of the target. The weight of the herbs was measured using a TAL220 strain gauge (manufactured by HT Sensor), which can measure up to 5 kg. We also used an HX711 24-bit A/D conversion chip to enhance measurement resolution, as shown in Figure 1(b). A computer is used to issue commands pertaining to the location of the XYZ platform and run the image processing algorithm. An Arduino board is used to acquire readings from the strain gauge and send them to the computer via an RS-232 serial communication port for subsequent analysis.

2.2. System Flow. Figures 2 and 3 illustrate the system in action as well as details of the various procedures. After the user inputs the names and weights of the herbs and the number of packets needed, the system accesses information pertaining to the desired herbs in a database that was created beforehand. This information includes the location of the drawer in which the herb is stored, an image of the herb, and the relationship between the weight of the herb and width of the claw used to retrieve it. The robotic arm then moves to the designated drawer and pulls it open, as shown in Figures 2(a) and 2(b). The camera scans the distribution of the herbs in the drawer and processes the image to determine the optimal retrieval location, as shown in Figures 2(c) and 2(d). The red circle in Figure 2(d) indicates the optimal retrieval location derived via image processing. The system retrieves the quantity of the herb required to fill a designated number of packets, as shown in Figure 2(e). The drawer is then closed, as shown in Figure 2(f). The entire process (as shown in Supplementary Material available online at <https://doi.org/10.1155/2017/9013508>) is repeated until all of the herbs required for a given order have been retrieved.

In the above process, a database is used to establish the relationship between the size of the claw aperture and amount (weight) of the herb to be retrieved. This is meant to enhance retrieval accuracy and the overall robustness of the system when dealing with a wide range of herbs. To further enhance the efficiency of herb retrieval, we also calculate the discrepancy between the retrieved weight and target weight and set a threshold of acceptable error. The width of

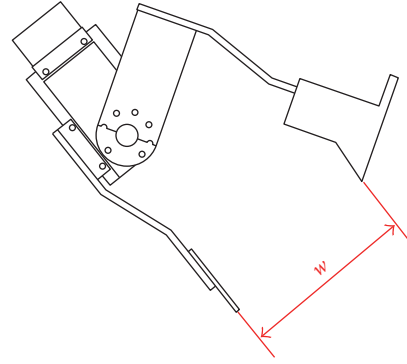


FIGURE 4: Schematic diagram showing the width of the claw w .

the claw can then be adjusted to compensate for errors in measuring the weight of the herbs.

2.3. Claw Width. Herbs vary greatly in their size, shape, and unit weight. Even the same type of herb may differ considerably with regard to shape. To enable the adjustment of claw width during retrieval, we first derive the optimal relationship between the width of the claw and the weight of each type of herb and the results of which are stored in a database. As shown in Figure 4, the width of the claw is defined as the distance w indicated in the side view of the designed claw.

Three methods are used to estimate the relationship between the width of the claw and the weight of the herb: linear interpolation, curve fitting, and iterative refinement. The first method involves using a database to determine a weight range for a given herb and then applying linear interpolation to calculate the width of the claw needed to obtain the designated quantity of the herb. Suppose that the designated weight of the herb g and width of the claw w fall between two adjacent data points (g_i, w_i) and (g_{i+1}, w_{i+1}) . Therefore, g and w fulfill the following equation:

$$g = g_i + \frac{w - w_i}{w_{i+1} - w_i} \times (g_{i+1} - g_i). \quad (1)$$

The curve fitting method assumes that the herbs are evenly distributed within their drawers and fits a polynomial equation to obtain the relationship between the width of the claw and the weight of the herb. We performed curve fitting using least-squares regression (LSR) based on the retrieval results in the database and adopted a first-order polynomial as follows:

$$w = ag + b, \quad (2)$$

where a and b are constants obtained via curve fitting. Both of the aforementioned methods employ the database established beforehand. Any major errors associated with the measurement data in the database affect the width of the claw and the actual retrieval results. Thus, we also developed an iterative refinement method to update estimates of how far the claw should be opened. Based on curve fitting, the proposed approach calculates the R -squared value and

Input: Stipulated number of iterations I , current number of iterations i , previous retrieval equation $y_1(x)$, current retrieval equation $y_2(x)$, and corresponding R -squared values R_1 and R_2

Output: Target retrieval equation $y(x)$

- (1) Designate retrieval weight, with 1 g as sampling point, retrieval from 5 g to 15 g;
- (2) Calculate retrieval equation $y_1(x)$ using LSR (Eq. (2));
- (3) Retrieve designated quantity (weight) of herb using $y_1(x)$;
- (4) Calculate corresponding R -squared value R_1 based on retrieval results and formulate new retrieval equation $y_2(x)$;
- (5) Repeat Steps 3 and 4 using $y_2(x)$ and obtain R -squared value R_2 ;

if $R_2 > R_1$, $y_1(x) = y_2(x)$;
 Current number of iterations $i = i + 1$;
if $i < I$, go to step 3;
else, $y(x) = y_1(x)$, **return** $y(x)$;

ALGORITHM 1: Iterative refinement method.

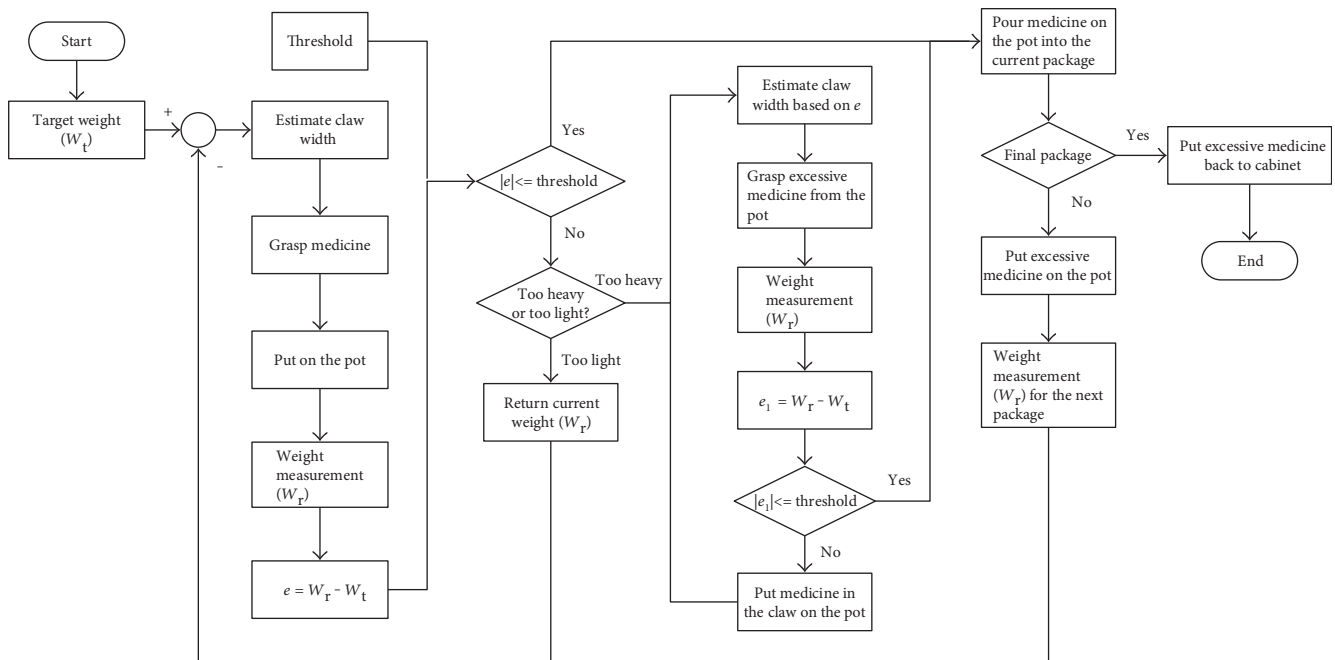


FIGURE 5: Proposed herb retrieval and dispensation process.

revises the retrieval equation repeatedly until reaching an acceptable R -squared value. The details are presented in Algorithm 1, where $y_1(x)$ and $y_2(x)$ denote the previous and current retrieval equations established using LSR and R_1 and R_2 are the corresponding R -squared values. If R_2 is greater than R_1 , then the current retrieval equation $y_2(x)$ is deemed superior and is thus used to replace the previous retrieval equation $y_1(x)$; otherwise, the retrieval equation is not changed. When the current number of iterations i reaches the designated number of iterations I , then the experiment is terminated and the latest retrieval equation $y(x)$ is used to estimate the width of the claw for herb retrieval.

To minimize the unavoidable effects of weight error during the herb retrieval process, the system calculates the discrepancy between the target weight (W_t) and the weight of the herbs on the weighing pan (W_r). This is done after

each retrieval to determine whether to continue or stop the retrieval of that particular herb. The procedure is detailed in Figure 5 and Supplementary Material. After calculating the current weight error ($e = W_r - W_t$), the system determines whether the absolute value of e is within the preset error threshold. If W_t has reached the designated weight, then the herbs on the weighing pan are automatically poured into bags on the turntable below, thereby ending the retrieval process. If the absolute value of e falls outside the error threshold, then there are two possible situations: too heavy and too light. The system begins by estimating the width of the claw based on e . If the retrieved sample is too light, then the system retrieves more of that material and sends back the current W_r value to continue retrieval of the same herb. If the retrieved sample is too heavy, then the claw is used to remove a quantity of the herb proportional to the excess

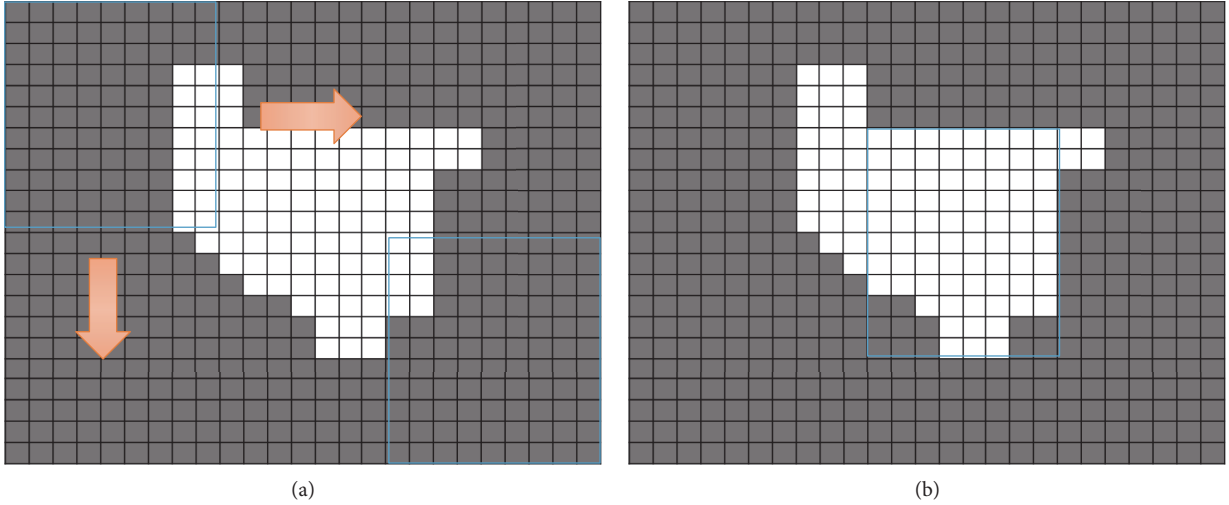


FIGURE 6: Herb density estimation. (a) Scanning method: from left to right and from top to bottom. (b) Final result with the blue frame as the ROI.

weight. The weight error e_1 ($e_1 = W_r - W_i$) is calculated again, and the above process is repeated until the value of e_1 falls within the preset error threshold. The material remaining on the weighing pan is loaded into bags. The system then determines whether it is currently engaged in filling the last packet. If so, then the herbs currently held in the claw are returned to the drawer. If not, then the claw places the herbs on the weighing pan, measures the current W_r value, and sends it back for the next retrieval. If the error (e) falls within the preset threshold, then the retrieval process is concluded.

2.4. Image Processing. The location from which herbs can be retrieved changes every time a drawer is accessed. Thus, we employed two cameras to capture images and applied a series of preprocessing procedures to enable stereo vision monitoring. Preprocessing included blurring, color filtering, image binarization, and region of interest (ROI) estimation. The principle of parallax is used to create a stereo vision relationship for use in estimating the three-dimensional coordinates of the target retrieval location. We adopted the HSV format for color filtering: that is, hue (H), saturation (S), and lightness (V), with the range of the color channels serving as boundaries. Image pixels that fall within the preset HSV range are retained and the rest are filtered out. Image binarization involves setting the areas within the threshold as white and those outside the threshold as black. This accelerates the process by reducing computational complexity. Machine vision is used to identify areas in which the herbs are most densely distributed to which the claw is directed. The width of the claw is adjusted according to the designated weight of the herb. Therefore, we used the width of the claw to determine the corresponding ROI, which is used to calculate the pixel area of each region in the preprocessed image from left to right and from top to bottom, as shown in Figure 6(a) and Supplementary Material. The system selects the largest area as the target retrieval region. Figure 6(b) presents an example of the scanning results, in which the white regions indicate areas that are retained after color filtering and the black regions are regions that have been filtered out. The blue

frame indicates the ROI, and the range of which is determined by the width of the claw. During retrieval, the robotic arm regards the center of the ROI as the target retrieval location. After obtaining the coordinates of the center, the stereo vision relationship is used to convert the coordinates into world coordinates of the target location.

2.5. Stereopsis. An appropriate coordinate system must first be established to calculate the correct location of the herb and obtain the spatial geometric relationships among the herbs, camera, and robotic arm in order to facilitate herb retrieval. We defined three coordinate systems for the various objects: world coordinates (x_w , y_w , and z_w), camera coordinates (x_c , y_c , and z_c), and pixel coordinates (u_p and v_p). The conversion relationships are shown in Figure 7. For the pixel coordinates, the upper left corner of the images of herbs serves as the origin for use in describing the location of the target object on the image plane, whereas the coordinates for the center of the camera serve as the origin from which to describe the location of the target object. For the world coordinates, a point in the space is designated as the origin used to describe the absolute locations of various objects. The location of the target must be converted into world coordinates in order for the robotic arm to engage in tracking motions. In the conversion relationship above, the world coordinates are first converted into camera coordinates and then into pixel coordinates.

The conversion relationship between the pixel coordinates and the world coordinates can be described as follows:

$$s \begin{bmatrix} u_p \\ v_p \\ 1 \end{bmatrix} = \begin{bmatrix} f & 0 & 0 & u_0 \\ 0 & f & 0 & v_0 \\ 0 & 0 & 1 & 0 \end{bmatrix} \begin{bmatrix} \mathbf{R}_{3 \times 3} & \mathbf{T}_{3 \times 1} \\ \mathbf{0}_{1 \times 3} & 1 \end{bmatrix} \begin{bmatrix} x_w \\ y_w \\ z_w \\ 1 \end{bmatrix}, \quad (3)$$

where s is a gain value; u_p and v_p are the coordinates of the target as described by the pixel coordinate system; and x_w , y_w , and z_w indicate the location of the target in the world

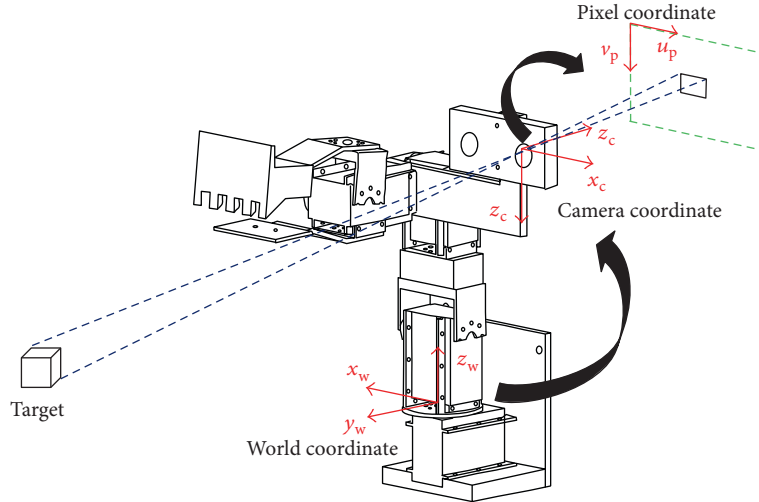


FIGURE 7: Coordinate system for stereopsis.

TABLE 1: D-H parameters for the camera coordinate system.

i	α_i	a_i (mm)	d_i (mm)	θ_i
1	90°	0	50.6	θ_1
2	0°	107	0	θ_2
3	0°	39	0	θ_3
4	-90°	50	135	$\theta_4(-90^\circ)$
5	180°	0	12	$\theta_5(-90^\circ)$

coordinate system. f represents the focal length of the camera; u_0 and v_0 are the coordinates of the center of the camera, the parameters of which can be found via standard camera calibration [22]. $\mathbf{R}_{3 \times 3}$ and $\mathbf{T}_{3 \times 1}$ are the external parameters of the camera, respectively, denoting the rotation matrix and translation vector of the world coordinate with regard to the camera coordinates. In this study, the camera was installed on the third axis of the robotic arm, which means that the conversion relationship between the coordinate systems changes as the arm moves. Thus, a camera coordinate system must be defined to calculate the external parameters. Based on robotics theory, we constructed a D-H table (as shown in Table 1) to define the camera coordinate system shown in Figure 8, where α_i represents a constant twist angle; a_i denotes the vertical distance between the z axes of adjacent coordinate systems, generally equal to the link length; d_i is the joint offset; and θ_i represents the joint angle.

Based on this D-H table, we derived the conversion relationship using (4), where \mathbf{E} is referred to as the external parameter of the camera in this study; $C_1 = \cos \theta_1$, $S_1 = \sin \theta_1$, $C_{23} = \cos(\theta_2 + \theta_3)$, $S_{23} = \sin(\theta_2 + \theta_3)$, and ${}^{i-1}\mathbf{A}_i$ is the matrix of conversion between the joints; θ_1 , θ_2 , and θ_3 denote the amount of rotation in each joint in the robotic arm, indicating the current posture of the arm; θ_4 is the angle between frame 3 and frame 4 in Figure 8; θ_5 is the angle between frame 4 and frame 5, which does not change with the posture of the arm and is therefore constant. This conversion matrix makes it possible to convert the target

location estimated in the camera coordinate system into coordinates in the coordinate system of the robotic arm. The conversion relationship is as shown in (5), where \mathbf{P}_r and \mathbf{P}_c , respectively, represent the locations of the target as described by the coordinate system of the robotic arm and the camera coordinate system.

$$\mathbf{E} = {}^0\mathbf{A}_1 {}^1\mathbf{A}_2 {}^2\mathbf{A}_3 {}^3\mathbf{A}_4 {}^4\mathbf{A}_5$$

$$= \begin{bmatrix} -S_1 & -C_1 S_{23} & -C_1 C_{23} & -a_5 S_1 + d_5 C_1 C_{23} + \\ C_1 & -S_1 S_{23} & -S_1 C_{23} & d_4 S_1 + a_4 C_1 S_{23} + \\ 0 & -C_{23} & S_{23} & a_3 C_1 C_{23} + a_2 C_1 C_2 \\ 0 & 0 & 0 & -a_5 C_1 + d_5 S_1 C_{23} + \\ & & & d_4 C_1 + a_4 S_1 S_{23} + \\ & & & a_3 S_1 C_{23} + a_2 S_1 C_2 \\ & & & -d_5 S_{23} + a_4 C_{23} - \\ & & & a_3 S_{23} - a_2 S_2 + d_1 \\ & & & 1 \end{bmatrix}, \quad (4)$$

$$\mathbf{P}_r = \mathbf{E} \mathbf{P}_c. \quad (5)$$

3. Results

TCM practitioners prescribe traditional formulas (prescriptions with fixed compositions of particular ingredients) or make up their own formulas. In this experiment aimed at demonstrating the feasibility of the proposed ADD system, we selected the traditional formula referred to as Yi Guan Jian (一貫煎) [23]. As shown in Figure 9, this formula includes six herbs: Dwarf Lilyturf Tuber, Radix Glehniae, Barbary Wolfberry, Chinese Angelica, Dried Rehmannia Root, and Szechwan Chinaberry. As can be seen, these herbs vary widely in size, shape, and color. Table 2 presents the formula of this prescription. The unit ‘‘mace’’ is commonly used for prescriptions in TCM.

As shown in Figure 10 and the Supplementary Material, we designed a user-friendly human-machine interface to

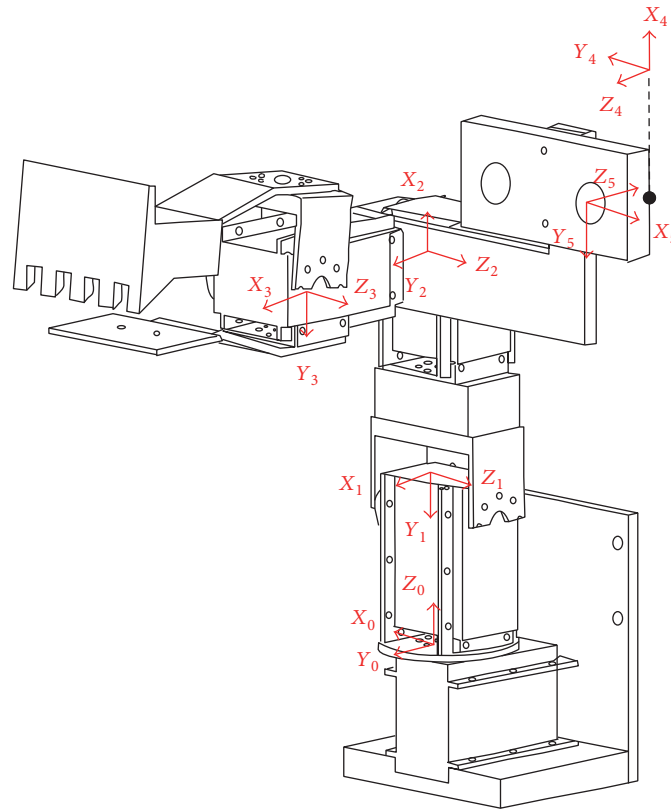


FIGURE 8: Camera coordinate system (frames 0–3: motor rotation axis; frame 4: left camera location; and frame 5: center of left camera).

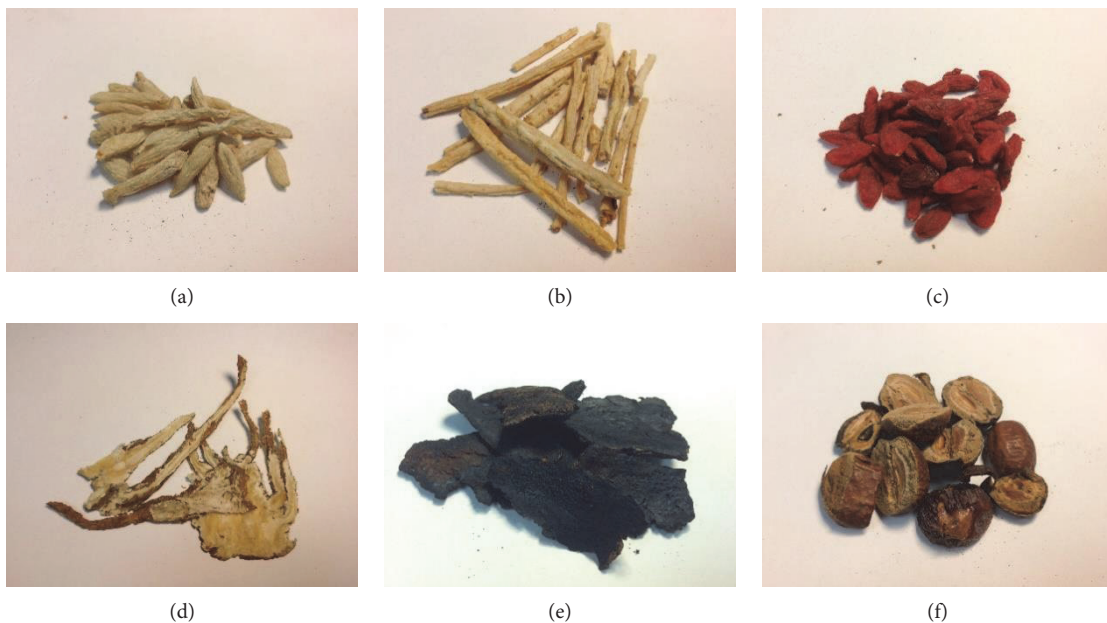


FIGURE 9: Photos showing the ingredients of Yi Guan Jian: (a) Dwarf Lilyturf Tuber, (b) Radix Glehniae, (c) Barbary Wolfberry, (d) Chinese Angelica, (e) Dried Rehmannia Root, and (f) Szechwan Chinaberry.

enter the ingredients of prescriptions. The fields on the right display the target medicine, target weight, and target number of packets. The current weight and current amount represent the weight that the system has retrieved and the number of

packets that have been processed. The action currently being performed by the system is also displayed in the current action field to enable monitoring by the user and facilitate debugging. As each packet is filled, the system lists each

TABLE 2: Ingredients of Yi Guan Jian.

Medicine	Quantity (mace)	Medicine	Quantity (mace)
Dwarf Lilyturf Tuber	3 mace	Chinese Angelica	3 mace
Radix Glehniae	3 mace	Dried rehmannia root	7 mace
Barbary Wolfberry	4 mace	Szechwan Chinaberry	1.5 mace

1 mace (錢): 3.125 g.

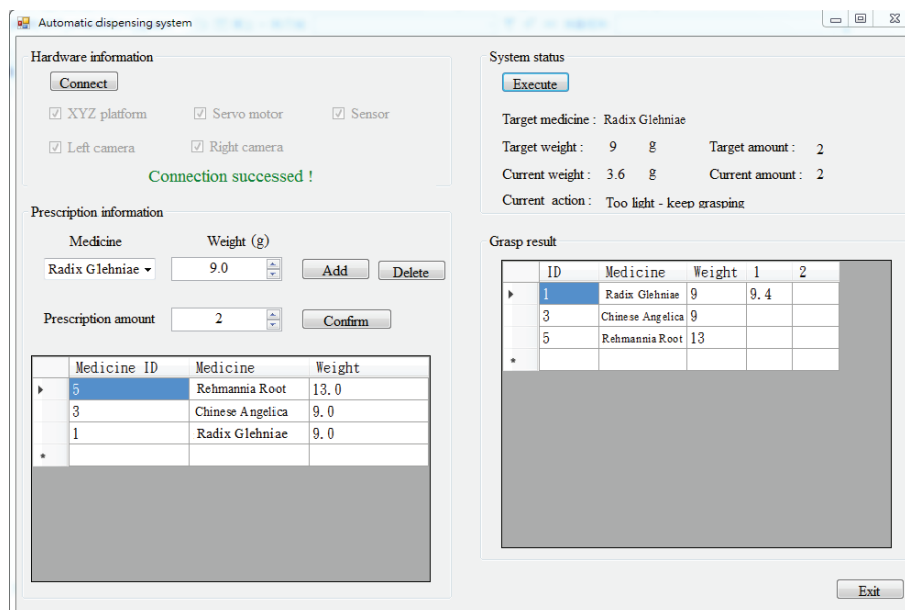


FIGURE 10: Human-machine interface for the automatic dispensing system.

completed retrieval in the table in the lower right corner of the window, so that users can monitor the system's current progress. Below, we examine the database and the results obtained during the retrieval process. The database contains information pertaining to the relationship between the width of the claw and the weight of the herb for each type of herb. These values were derived using (1) linear interpolation, (2) LSR curve fitting, or (3) iterative refinement. We analyzed the retrieval results achieved using these methods for use in assessing the feasibility of the proposed ADD system.

3.1. Estimation of Grasp Volume. The purpose of this experiment was to investigate the accuracy of the system with regard to the volume of materials retrieved. We set the width of the claw at 40 mm, 55 mm, 70 mm, 85 mm, 100 mm, and 115 mm prior to performing retrieval motions. Using 1 g as the sampling point, the system performed retrieval tests for quantities ranging from 5 g to 15 g in order to establish a herb retrieval database. We then used linear interpolation, LSR curve fitting, and iterative refinement to estimate the corresponding relationships between the width of the claw and the weight of the herb. Finally, we calculated the R -squared value of the retrieval results for comparison and analysis. For the sake of convenience, we use the retrieval results of Chinese Angelica in Figure 11 as an example. Figure 11(a) presents the weight of the herbs corresponding to the width

of the claws from 40 mm to 115 mm at intervals of 15 mm. Figures 11(b) and 11(c) show the relationships between the weight of the herb and the width of the claw derived using linear interpolation and LSR, based on the results in Figure 11(a). Figure 11(d) presents the retrieval equation obtained after applying the LSR-based refinement method through three iterations (the algorithm mentioned in Section 2.3). In Figures 11(b), 11(c), and 11(d), the solid lines in the figures represent the claw estimation relationship, and the asterisks (*) show the actual herb retrieval results derived using said relationships. As can be seen in Figure 11(b), most of the retrieval results calculated from the width of the claws using linear interpolation do not fall along the linear line that was estimated, and the errors present no fixed trend. A comparison of Figures 11(b) and 11(c) revealed that LSR curve fitting could be used to reduce retrieval errors; however, many of the weights would still be far from the ideal weights. Figure 11(d) clearly shows that using the iterative refinement method to revise the retrieval equation estimated using LSR curve fitting can produce retrieval results that are very close to the values estimated using retrieval equation, that is, greatly reducing retrieval errors.

Table 3 shows the R -squared values derived from the retrieval results using the three methods. Clearly, curve fitting (method 2) achieved better R -squared values (all greater than 0.8) than did linear interpolation (method 1),

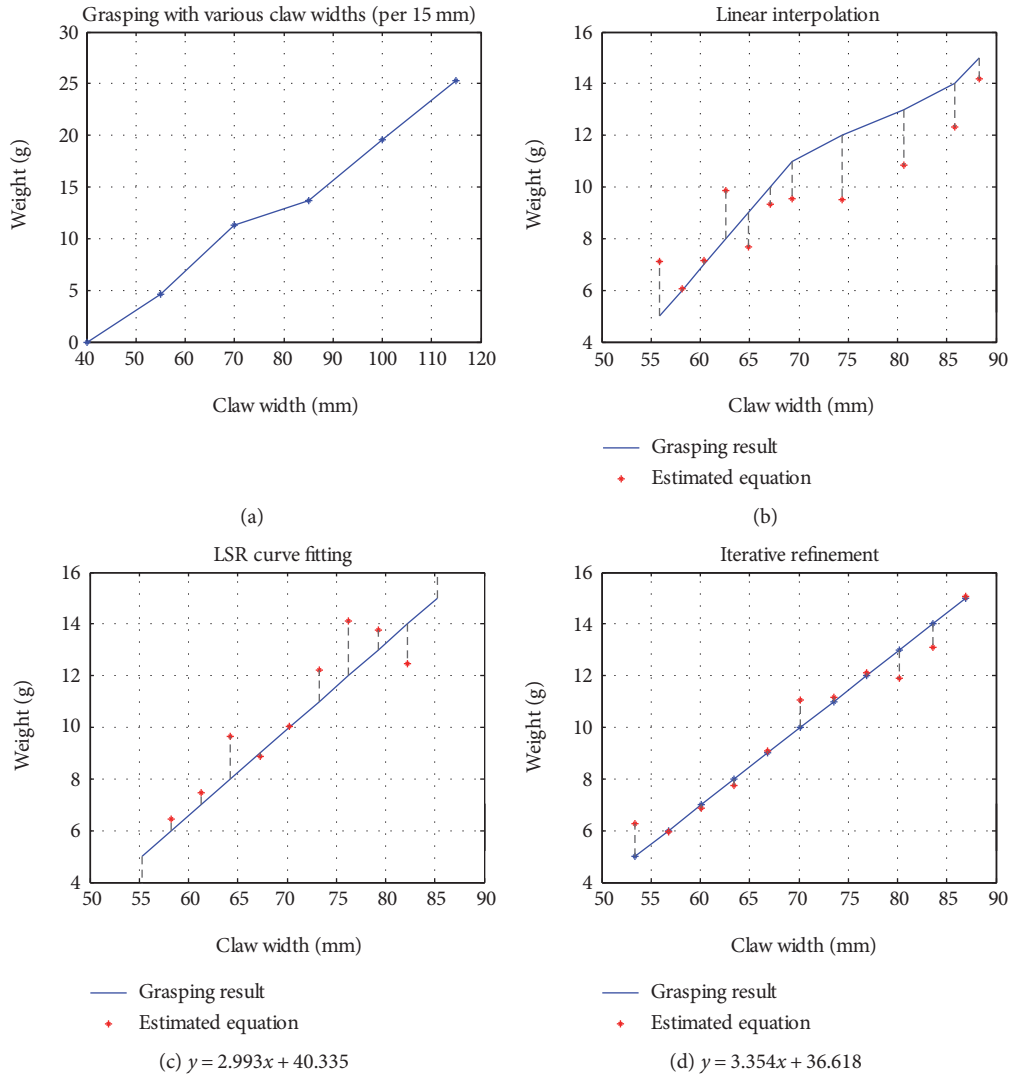


FIGURE 11: Estimation of grasping amount—Chinese Angelica. (a) Grasping with claws of various width (from 40 mm to 115 mm/per 15 mm). (b) Grasp estimates obtained using linear interpolation using the data in (a). (c) Grasp estimates obtained using LSR curve fitting with the data in (a). (d) Grasp estimates obtained based on LSR curve fitting after refinement (three iterations).

TABLE 3: Comparison of *R*-squared values using three methods (method 1: linear interpolation; method 2: LSR curve fitting; and method 3: iterative refinement).

Herbal medicine	Method 1	Method 2	Method 3
1 (Dwarf Lilyturf Tuber)	0.7737	0.8861	0.9617
2 (Radix Glehniae)	0.6281	0.8254	0.9382
3 (Barbary Wolfberry)	0.8886	0.8151	0.9172
4 (Chinese Angelica)	0.5452	0.8493	0.9464
5 (Dried Rehmannia Root)	0.8382	0.8481	0.9490
6 (Szechwan Chinaberry)	0.8316	0.9065	0.9417

regardless of the type of herb. The *R*-squared values from iterative refinement (method 3) were all greater than 0.9, nearing 1 for Dwarf Lilyturf Tuber. Due to the fact that the

herbs were distributed unevenly, differences in the size and shape tend to result in different equations after curve fitting. Nonetheless, iterative refinement can improve the accuracy of retrieval equations obtained using curve fitting.

3.2. *Analysis of System Performance.* To examine the operating efficiency and accuracy of the proposed system, we went to an actual TCM pharmacy and had the pharmacist manually prepare five packets of Yi Guan Jian. We then used the width of the claws estimated using the three methods to analyze the performance of the ADD system. The acceptable error threshold was set to 2 g, that is, a retrieval weight within ± 2 g of the target weight was considered acceptable. Table 4 compares the manual retrieval results and the retrieval results of the proposed system. The average error, standard deviation of error, and max error were calculated after multiple measurements using an electronic scale (resolution 0.1 g).

TABLE 4: System performance analysis using five packets of herbs (medicine 1: Dwarf Lilyturf Tuber; medicine 2: Radix Glehniae; medicine 3: Barbary Wolfberry; medicine 4: Chinese Angelica; medicine 5: Dried Rehmannia Root; and medicine 6: Szechwan Chinaberry).

Herbal medicine	1	2	3	4	5	6
Quantity (g)	9	9	13	9	20	4.5
<i>Measured by pharmacist (five doses)</i>						
Average error (g)	0.91	0.91	0.4	0.93	0.44	0.98
Standard deviation of error (g)	1.02	1.45	0.65	1.24	0.57	1.41
Max error (g)	2.9	1.2	1.3	1.5	0.8	1.7
Executing time	9 min 27 s					
<i>Proposed dispensing system: linear interpolation method (five doses)</i>						
Average error (g)	0.92	1.12	1.2	1.16	1.08	1.06
Standard deviation of error (g)	1.02	1.28	1.35	1.37	1.32	1.23
Max error (g)	1.6	1.8	1.9	2.3	1.9	1.7
Number of average grasping (times)	1.6	1.6	1.6	1.4	2	1.2
Executing time	20 min 38 s					
<i>Proposed dispensing system: LSR curve fitting method (five doses)</i>						
Average error (g)	1.5	1.46	1.04	1	1.18	0.74
Standard deviation of error (g)	1.23	1.24	1.12	0.95	1.31	0.91
Max error (g)	2.3	2.3	1.4	2	2.4	1.6
Number of average grasping (times)	1.8	1.4	1.4	1.4	1.8	1.4
Executing time	20 min 11 s					
<i>Proposed dispensing system: iterative refinement method (five doses)</i>						
Average error (g)	0.64	0.9	0.94	0.72	1.14	0.72
Standard deviation of error (g)	0.81	1.01	1.04	0.91	0.93	0.82
Max error (g)	1.1	1.4	1.8	2.1	2.2	1.3
Number of average grasping (times)	1.2	1.2	1.4	1.2	1.6	1.2
Executing time	18 min 1 s					

Table 4 shows that errors greater than 2g occurred in some cases. This was because the weight measurements were obtained using a strain gauge and the herbs were poured into the bag when the error values were less than the preset threshold. Following the retrieval process, the herbs in the bag were then weighed using a scale. The limited resolution of the strain gauge was the cause of the measurement error. Examination of the results revealed more pronounced retrieval errors with Chinese Angelica and Dried Rehmannia Root. This was because these two parts of herbs come in large pieces that are difficult for the excavator bucket-like claw to retrieve, particularly when the herb pieces are not arranged neatly. Our results clearly revealed uneven retrieval errors when manually dispensing Barbary Wolfberry and Dried Rehmannia Root. This is because pharmacists usually use a traditional Chinese scale (low resolution) to obtain rough values of scale readings and then rely on experience for subsequent dispensation processes. Therefore, the error results may vary every time that experiments are performed by different pharmacists or with different prescriptions. In terms of average error, setting an error threshold was shown to reduce retrieval errors. Nevertheless, a comparison of the results from the three methods still revealed some differences. With iterative refinement, the average error and standard deviation of error all remained at approximately

1g, unlike those resulting from the other two methods (linear interpolation and curve fitting) and the manual method. Note that these errors could be further reduced by setting a smaller error threshold and/or using more advanced herb retrieval methods. Nevertheless, the proposed approach did not improve all of the retrieval results (such as those for Dried Rehmannia Root). This was because herb retrieval was set to proceed continuously in our experiment. The distribution of herbs in the drawer changed each time it was accessed, and sometimes the more elongated herbs were moved into positions that were difficult to access using the claw. This affected the depth of retrieval as well as the retrieval results for the next packet. Overall, iterative refinement was shown to reduce the average number of retrievals needed to complete a packet and thus the time required to complete an order. However, the total time needed was still significantly longer than manual retrieval. This may be due to the fact that we adopted an XYZ platform and a robotic arm to perform large-stroke motions. Insufficient structural rigidity resulted in shaking, which hindered the retrieval process. Furthermore, limitations in the moving speed meant that retrievals could not be performed quickly. Nevertheless, the experimental results demonstrate the accuracy and feasibility of the proposed approach.

4. Conclusions

This study proposed a robotic arm-based ADD system with machine vision to assist in the collection of ingredients for herbal decoctions. Experiments involving the collection of five packets of a prescription containing six types of herbs were conducted to demonstrate the feasibility of the proposed automated process and retrieval algorithm. Experimental results indicate that obtaining an appropriate retrieval equation for the width of the claw and retrieval weight using iterative refinement is an effective approach to enhancing retrieval accuracy and improving the operating efficiency of the system. Retrieval apparatus designed to simulate human fingers and structural enhancements to the system could further improve the operating speed and efficiency of the system. The inclusion of image-based machine learning technology to determine the optimal width of the claw and robotic arm decisions may also serve as solutions for the retrieval of herbs with complex shapes.

Conflicts of Interest

The authors declare no conflict of interest.

Acknowledgments

The authors would like to thank the Ministry of Science and Technology, Taiwan, for providing financial support of this research under Grant no. MOST 104-2221-E-011-037. They are also thankful to Dr. Fan-Pey Chen from the Institute of Traditional Medicine, National Yang-Ming University, Taipei City, Taiwan, for providing the research motivation of this work.

References

- [1] Ministry of Health and Welfare, "The comparative researches between traditional herbal decoction and commercial extract," 2013, <http://dep.mohw.gov.tw/DOCMAP/fp-719-30754-108.html>.
- [2] K. Ried and K. Stuart, "Efficacy of traditional Chinese herbal medicine in the management of female infertility: a systematic review," *Complementary Therapies in Medicine*, vol. 19, no. 6, pp. 319–331, 2011.
- [3] L. Logo, "Herbal treatments vs western medicine," 2017, <http://www.livestrong.com/article/449539-herbal-treatments-vs-western-medicine/>.
- [4] Q. Zhou, J. Tao, H. Song et al., "Chinese herbal medicine Kuntai capsule for treatment of menopausal syndrome: a systematic review of randomized clinical trials," *Complementary Therapies in Medicine*, vol. 29, pp. 63–71, 2016.
- [5] Research Papers Center, "Advantages and disadvantages of Chinese medicine formulations and recommendations particles," 2011, <http://eng.hi138.com/medicine-papers/>.
- [6] CNA/Healthcare Providers Service Organization Pharmacist Liability, "2013 pharmacist liability," 2013, http://www.hpso.com/Documents/pdfs/Pharmacist_Claim_Report_2013.pdf.
- [7] A. Beso, B. D. Franklin, and N. Barber, "The frequency and potential causes of dispensing errors in a hospital pharmacy," *Pharmacy World and Science*, vol. 27, no. 3, pp. 182–190, 2005.
- [8] Stichting Farmaceutische Kengetallen, "On pharmaceutical care in the Netherlands (Facts and Figures 2012)," 2012, <https://www.sfk.nl/english/f-f-2012>.
- [9] K. Johnell and J. Fastbom, "Multi-dose drug dispensing and inappropriate drug use: a nationwide register-based study of over 700,000 elderly," *Scandinavian Journal of Primary Health Care*, vol. 26, no. 2, pp. 86–91, 2009.
- [10] J. Sinnemaki, S. Sihvo, J. Isojarvi, M. Blom, M. Airaksinen, and A. Mantyla, "Automated dose dispensing service for primary healthcare patients: a systematic review," *Systematic Reviews*, vol. 2, no. 1, 2013.
- [11] J. S. Bell, M. Vaananen, H. Ovaskaninen, U. Narhi, and M. S. Airaksinen, "Providing patient care in community pharmacies: practice and research in Finland," *Annals of Pharmacotherapy*, vol. 41, no. 6, pp. 1039–1046, 2007.
- [12] A. B. Larsen and L. S. Haugbole, "The impact of an automated dose-dispensing scheme on user compliance, medication understanding, and medication stockpiles," *Research in Social and Administrative Pharmacy*, vol. 3, no. 3, pp. 265–284, 2007.
- [13] C. A. Pedersen, P. J. Schneider, and D. J. Scheckhoff, "ASHP national survey of pharmacy practice in hospital settings: dispensing and administration-2011," *American Journal of Health-System Pharmacy*, vol. 69, no. 9, p. 768, 2012.
- [14] B. D. Franklin, K. O'Grady, L. Voncina, J. Popoola, and A. Jacklin, "An evaluation of two automated dispensing machines in UK hospital pharmacy," *International Journal of Pharmacy Practice*, vol. 16, no. 1, pp. 47–53, 2008.
- [15] L. Fanning, N. Jones, and E. Manias, "Impact of automated dispensing cabinets on medication selection and preparation error rates in an emergency department: a prospective and direct observational before-and-after study," *Journal of Evaluation in Clinical Practice*, vol. 22, no. 2, pp. 156–163, 2016.
- [16] K. C. Cheung, M. L. Bouvy, and P. A. D. Smet, "Medication errors: the importance of safe dispensing," *British Journal of Clinical Pharmacology*, vol. 67, no. 6, pp. 676–680, 2009.
- [17] A. C. Lin, Y. C. Huang, G. Panches, and Y. Chen, "Effect of a robotic prescription-filling system on pharmacy staff activities and prescription-filling time," *American Journal of Health-System Pharmacy*, vol. 64, no. 17, pp. 1832–1839, 2007.
- [18] R. Fitzpatrick, P. Cooke, C. Southall, K. Kaudhar, and P. Waters, "Evaluation of an automated dispensing system in a hospital pharmacy dispensary," *The Pharmaceutical Journal*, vol. 274, 2005.
- [19] S. Goundrey-Smith, "Pharmacy robots in UK hospitals: the benefits and implementation issues," *The Pharmaceutical Journal*, vol. 280, pp. 599–602, 2008.
- [20] H. Sys, "Traditional Chinese Medicine Dispenser MD6100," 2017, <http://www.hollysys.com.sg/>.
- [21] Z. Song, X. Yang, J. Wang, H. Xue, and J. Zhang, *Automatic Deploying System for Single-Ingredient Pellet Formulas of Traditional Chinese Medicines*, In International Conf. Robotics and Biomimetics, Shenzhen, China, 2013.
- [22] R. Tsai, "A versatile camera calibration technique for high-accuracy 3D machine vision metrology using off-the-shelf TV cameras and lenses," *IEEE Journal on Robotics and Automation*, vol. 3, no. 4, pp. 323–344, 1987.
- [23] BoiMed Central, "Yiguanjian decoction and its ingredients inhibit angiogenesis in carbon tetrachloride-induced cirrhosis mice," 2013.

Research Article

Realization of a CORDIC-Based Plug-In Accelerometer Module for PSG System in Head Position Monitoring for OSAS Patients

Wen-Yen Lin,^{1,2} Wen-Cheng Chou,³ Tsu-Hui Shiao,⁴ Guang-Ming Shiao,⁴
Chin-Shan Luo,^{4,5} and Ming-Yih Lee^{2,6}

¹Department of Electrical Engineering, Center for Biomedical Engineering, Chang Gung University, Taoyuan, Taiwan

²Division of Cardiology, Department of Internal Medicine, Chang Gung Memorial Hospital, Linkou, Taoyuan, Taiwan

³Department of Electrical Engineering, Chang Gung University, Taoyuan, Taiwan

⁴Department of Chest Medicine, Taipei Veterans General Hospital, Taipei, Taiwan

⁵Division of Pulmonary Medicine, Department of Internal Medicine, Shuang Ho Hospital, Taipei Medical University, New Taipei City, Taiwan

⁶Graduate Institute of Medical Mechatronics, Center for Biomedical Engineering, Chang Gung University, Taoyuan, Taiwan

Correspondence should be addressed to Ming-Yih Lee; leemiy@mail.cgu.edu.tw

Received 7 April 2017; Revised 29 June 2017; Accepted 4 July 2017; Published 20 August 2017

Academic Editor: Yi-Hung Liu

Copyright © 2017 Wen-Yen Lin et al. This is an open access article distributed under the Creative Commons Attribution License, which permits unrestricted use, distribution, and reproduction in any medium, provided the original work is properly cited.

Overnight polysomnography (PSG) is currently the standard diagnostic procedure for obstructive sleep apnea (OSA). It has been known that monitoring of head position in sleep is crucial not only for the diagnosis (positional sleep apnea) but also for the management of OSA (positional therapy). However, there are no sensor systems available clinically to hook up with PSG for accurate head position monitoring. In this paper, an accelerometer-based sensing system for accurate head position monitoring is developed and realized. The core CORDIC- (COordinate Rotation DIgital Computer-) based tilting sensing algorithm is realized in the system to quickly and accurately convert accelerometer raw data into the desired head position tilting angles. The system can hook up with PSG devices for diagnosis to have head position information integrated with other PSG-monitored signals. It has been applied in an IRB test in Taipei Veterans General Hospital and has been proved that it can meet the medical needs of accurate head position monitoring for PSG diagnosis.

1. Introduction

Obstructive sleep apnea syndrome (OSAS) is common in our community and is characterized by repetitive, short-duration blockages of the upper airways during sleep, resulting in episodic cessation of breathing (apnea) or reduction in airflow (hypopnea) that may lead to frequent arousals, disrupted sleep structures, excessive daytime sleepiness, intermittent hypoxemia, and many other systemic effects. Sleep apnea is estimated to occur in up to 24% of middle-aged men and 9% of middle-aged women [1]. Fortunately, clinical studies reported that the remission from apnea syndrome was diagnosed from the patients with mild OSAS. That finding can relieve the problem of sleep apnea. The reason of the

remission might be caused by the change of body or head position. Studies showed that lying on one's side or the lateral decubitus position reduces the number of apneic events as compared to lying on one's back or supine sleeping position [2, 3]. Sleeping positions were suggested to have correlation with the sleeping problems. However, there is no scientific evidence to support this clinical observation.

Currently, overnight polysomnography (PSG) is the standard diagnostic procedure for OSAS. Some pilot studies showed that monitoring of head position is crucial [4, 5] not only for the diagnosis (positional sleep apnea) but also for the management of OSAS (positional therapy). However, the existing PSG is incapable of measuring head position with high accuracy for the study of remission. In fact, the

researchers had to use the existing body position sensor of PSG, which usually is mounted on the trunk, and had the sensor mounted on the head for the detection of head position in order to find the correlation between head position and the remission of the OSAS. The body position sensor only identifies the position into 8 segments for 0° , -45° , -90° , -135° , -180° , -225° , -270° , and -315° ranges. Recently, some studies proposed new techniques to monitor sleeping body position. By using load cells placed under the supports of a bed, the individual's lying position was classified for the detection of sleep apnea [6, 7]. Moreover, a textile-based ECG system was developed for the determination of the sleeping body position [8]. Eight electrodes were multiplexed in the system and supported by a foam pad to ensure good contact as well as comfort. By measuring and analyzing the ECG signals, both the heart rate and sleeping body position could be determined. The aforementioned techniques only measured the sleeping body position but not the head position. The correlation between the head position and remission had not yet been investigated scientifically due to the lack of accurate head position monitoring tools for the study. Indeed, the researchers require a system which is capable of measuring the head position (orientation) with $1^\circ \sim 2^\circ$ accuracy to hook up with PSG for further studies on the correlation between head position and the remission of OSAS patients.

In this work, a novel head position monitoring system was developed for the study of the correlation between head position and remission of OSAS. The system had the advantages of low power, low system cost, light in weight, and real-time monitoring and fulfilled the clinical requirement that eliminates the disturbance of the subjects. It can be integrated with current PSG to perform real-time diagnosis with accurate head and body position information provided. In this system, 3-axis digital accelerometers were used for the measurement of head position. However, the calculation of head tilting angle from the mathematical formulas is time-consuming and cannot be applied to in-line and real-time applications. In order to shorten the time cost of calculating the angles, a novel CORDIC- (COordinate Rotation DIgital Computer-) based low-complexity and less-memory tilting sensing algorithm was used [9]. As a matter of fact, the computation time of the CORDIC-based algorithm was almost only 1/4 of the calculations from the mathematical formulas on the microcontroller used. Therefore, the embedded system could finish all tasks within every sampling period including the collection of raw data from the accelerometers, calculation of head position, and transmission of data from the microcontroller to the PSG. Hence, the system successfully performed head position monitoring in an in-line and real-time manner. Finally, a practical clinical demonstration was conducted to show the realization of using the system for the study of the correlation between head position and remission of OSAS.

2. Materials and Methods

2.1. Head Position Monitoring for OSAS Patients. The typical movements of the head include inclinations (nodding), and

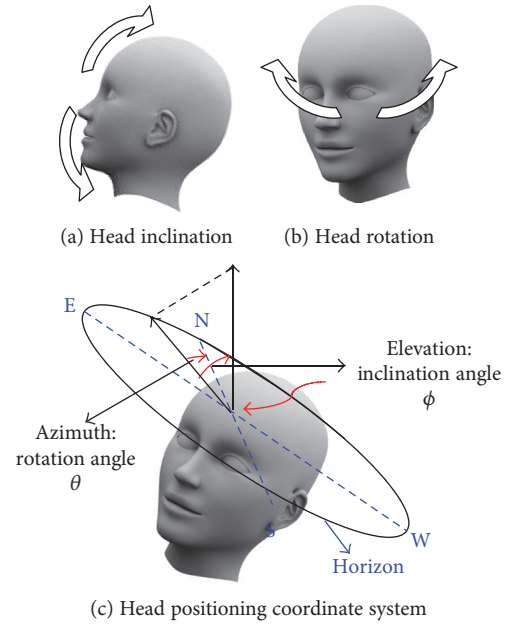


FIGURE 1: Head movements: (a) inclination, (b) rotation, and (c) head positioning coordinate system.

the rotations are shown in Figures 1(a) and 1(b). In a traditional spherical coordinate system, the azimuth (rotation angle) of the object is defined as the angle between the direction of the projected object on the horizon and the north. The elevation (inclination angle) defines the angle between the direction of the object and the zenith. Intuitively, the head position can be represented by its rotation angle and inclination angle when we apply the direction of the forehead in the spherical coordinate system of the earth, as shown in Figure 1(c). In this system, accelerometers were used for the measurement of head position. Inclination or tilt angle sensing can be determined by the gravity vector and its projection on the axes. Depending on the number of axes available in the accelerometer, different inclination or tilt angles can be defined and calculated.

2.2. Accelerometer-Based Tilting Sensing. When a 3-axis accelerometer is used for inclination sensing, the raw data read from accelerometer are the projections of the gravity vector on the three axes, x , y , and z (A_x , A_y , and A_z), in the rectangular coordinate system of the motion domain. To understand the orientation of the accelerometer, we can represent the gravity vector in the spherical coordinate system, $(\rho, \theta, \text{and } \varphi)$, where ρ is the length of the gravity vector, that is, $1g$, θ is the angle between the x -axis and the projected gravity vector on the x - y plane, where φ is the angle between the gravity vector and x - y plane. As a matter of fact, to retrieve the orientation information using the accelerometer is to perform domain transformation from the rectangular coordinate system in the motion domain of the measured raw data from the accelerometer to the spherical coordinate system in the angular domain as shown in Figure 2. The transformation equations between these two coordinate systems can be expressed in

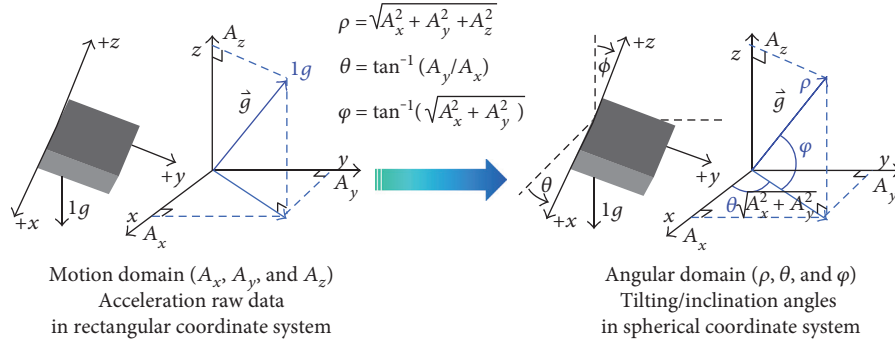


FIGURE 2: Angles of the spherical coordinate system and domain transformation.

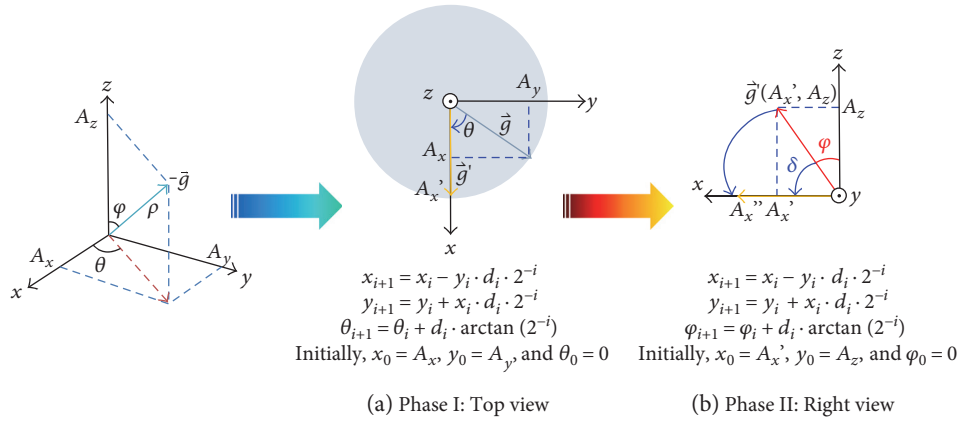


FIGURE 3: The computation process of CORDIC-based tilt sensing algorithm.

$$\begin{aligned}
 A_x &= \rho \cos \varphi \cdot \cos \theta, \\
 A_y &= \rho \cos \varphi \cdot \sin \theta, \\
 A_z &= \rho \sin \varphi,
 \end{aligned} \tag{1}$$

where $-\pi/2 \leq \varphi \leq \pi/2$ and $-\pi \leq \theta \leq \pi$. So, given a reading from 3D accelerometer data (A_x , A_y , and A_z), we can calculate the two angles φ and θ as

$$\begin{aligned}
 \theta &= \arctan\left(\frac{A_y}{A_x}\right) + \sigma \cdot \lambda \cdot \pi, \\
 \varphi &= \arctan\left(\frac{A_z}{\sqrt{A_x^2 + A_y^2}}\right).
 \end{aligned} \tag{2}$$

The term of $\sigma \cdot \lambda \cdot \pi$ added in θ is to have it converted into $-\pi \leq \theta \leq \pi$ range since the original arctan function only produces $-\pi/2 \leq \theta \leq \pi/2$ range, where $\sigma = 0$, if $A_x \geq 0$; otherwise, $\sigma = 1$. $\lambda = 1$, if $A_y \geq 0$; otherwise, $\lambda = -1$.

2.3. CORDIC-Based Tilting Sensing Algorithm. The calculations of these trigonometric functions are usually complicated; therefore, long computation time is required by low-cost and low-power microcontroller. Hence, most research works adopted offline computations [10], streaming the raw data to PC/PDA for computation [11–13], and table look up [14]. However, the offline computation approach could

not identify the tilting information in real time and in the system. Even if the streaming approach could retrieve the orientation information in real time, it could not perform the calculations in the system. Therefore, these two approaches were not able to produce the in-line and real-time orientation information and could not be integrated into existing PSGs for real-time diagnosis. Even worse, the streaming approach may raise concerns of excessive RF signal transmission. Table look up approach required huge memory space for table storage, and higher system cost was induced. Huge memory space is not feasible on typical microcontrollers which usually only have few hundred Kbytes or even less of flash or ROM on chip. Based on the existing technologies, the system is not capable of performing early detection, delivering early warning and, hence, is not capable of taking early actions. Therefore, an intelligent and low-complexity CORDIC-(COordinate Rotation DIGital Computer-) based tilting angle identification algorithm based on the 2D CORDIC [15] operations is proposed for saving the computation power. This can perform the computation in (2) with only basic adders and binary shifters for rotation of a 2D vector through a sequence of simple elementary rotations.

The algorithm is to calculate the angle between a 3D vector and one of the three axes. Taking the identification of the angle φ , for example, Figure 3 illustrates the process of the algorithm. The algorithm is conducted in two phases. Phase I, Figure 3(a), is to rotate the $-\vec{g}$ projected vector on the x -

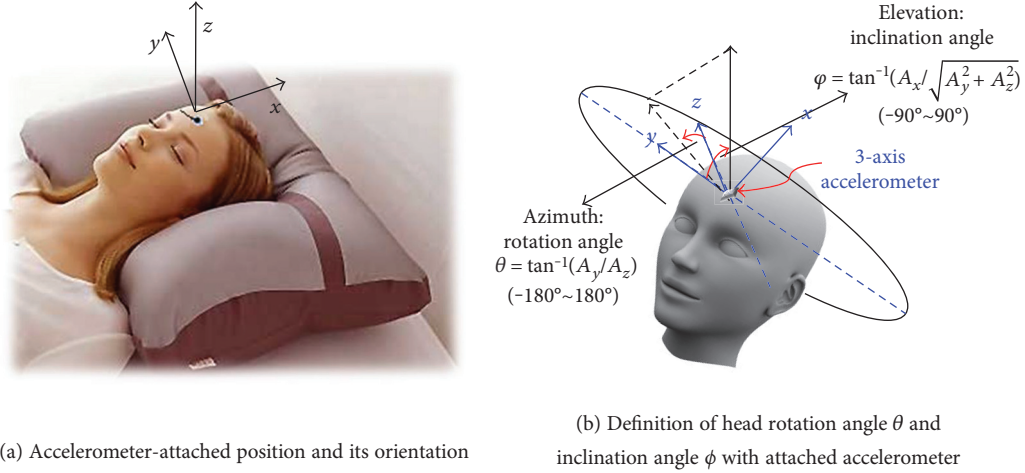


FIGURE 4: (a) Attached accelerometer on the forehead and the orientation. (b) Definition of the head position angles accordingly.

plane and have it aligned to the x -axis and forms g' vector as looking from the pointing direction of the z -axis (top view). The rotation is performed by 2D CORDIC on the x - y plane with the initial 2D vector (A_x, A_y) and the final vector $(A_x', 0)$. The iterative equations are shown in Figure 3(a), and the rotated angle θ and $A_x' = \sqrt{A_x^2 + A_y^2}$ are accrued.

Phase II, as shown in Figure 3(b), is to rotate the g' vector on the x - z plane and have it aligned to the x -axis, as looking from the pointing direction of the y -axis (right side). The rotation is performed by 2D CORDIC on the x - z plane with the initial 2D vector (A_x', A_z) and have it aligned to the x -axis. The iterative equations are shown in Figure 3(b), and the rotated angle δ is accrued through CORDIC operations and $\varphi = \pi/2 - \delta$. As you can see, the tilt angle, φ , is obtained with simple shifting and addition operations only by this proposed algorithm.

2.4. System Design and Realization

2.4.1. Definition of Head Position Angles. In the proposed sensing system, an accelerometer is attached to the forehead of the subject mounted with 3M™ Micropore™ Surgical Tape in the orientation shown in Figure 4(a), where x -axis points toward the head of the head, y -axis points to the right-hand side of the body, and z -axis points to the front of the head. With the accelerometer attached to the forehead to comply with the defined orientation, the head would rotate along the x -axis. Therefore, the rotation angle θ and the inclination angle φ can be calculated as in (3) for a different orientation compared with those in (2). It is also represented in Figure 4(b).

$$\begin{aligned} \varphi &= \arctan\left(\frac{A_x}{\sqrt{A_y^2 + A_z^2}}\right), \\ \theta &= \arctan\left(\frac{A_y}{A_z}\right) + \sigma \cdot \lambda \cdot \pi, \end{aligned} \quad (3)$$

where $\sigma = 0$, if $A_z \geq 0$; otherwise, $\sigma = 1$. $\lambda = 1$, if $A_y \geq 0$; otherwise, $\lambda = -1$.

2.4.2. System Realization. The overall system consists of front-end sensing subsystem and back-end data conversion subsystem. The front-end subsystem is the accelerometer sensor with a microcontroller for data acquisition and tilting angle transformation in digital formats. The angle information is then passed to the back-end subsystem for signal conversion into analog voltage signals to be hooked up with the PSG devices. Digital information has to be converted into analog signals because the tilting information has to be integrated with the PSG devices through their AUX inputs which are available for most of the PSG devices. Depending on how the data can be passed from front-end to back-end, the system can be realized as a wired system or a wireless system.

2.4.3. Wired Sensing System Implementation. The wired system block diagram is shown in Figure 5 and mainly consisted of a microcontroller unit (MCU; ADuC7020; Analog Devices Inc.) and accelerometer modules (ADXL345, Analog Devices Inc.). The system was integrated into the PSG (Alice 5; Philips Respironics Inc.) for in-line and real-time application. The firmware executed on the MCU was developed in C language under the software of uVision4 IDE. The MCU core clock was set at 10.44 MHz. The accelerometer module was an ultralow-power high-performance 3-axis digital accelerometer. It has the sensitivity of 3.9 mg/LSB with a $\pm 2g$ range and an on-chip low-pass filter for the removal of high-frequency noise. The communication between the accelerometers and MCU was through an I2C bus on a wired cable. The sampling rate of the accelerometer was set to be 100 Hz, and therefore, the MCU received the rectangular coordination $(A_x, A_y, \text{ and } A_z)$ of vector $(-1g)$ from a 3-axis digital accelerometer for every 10 ms. The data were then transformed to the angular domain for tilting angle identifications. Four channels of on-chip digital-to-analog converters (DACs) were included in the MCU and converted the in-line calculated angles into analog voltages representing the inclination information. Then, the

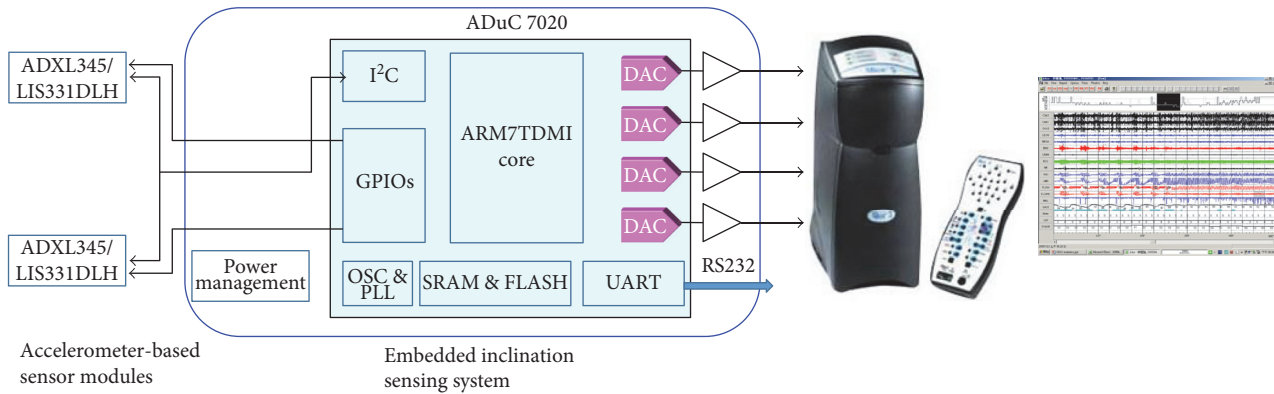


FIGURE 5: The system block diagram of a wired sensing system.

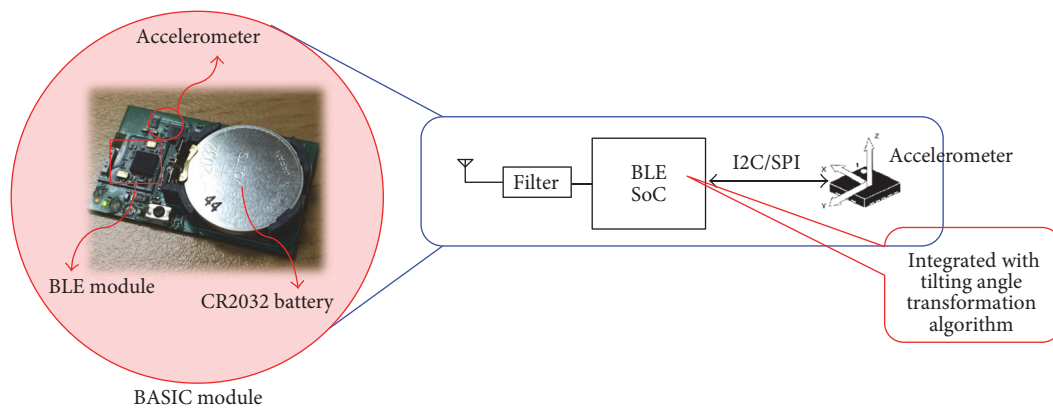


FIGURE 6: BASIC module and its block diagram.

information was directly transferred to the auxiliary inputs of the PSG for the study of remission of the patient with OSAS. This is the system that has been implemented for the IRB tests.

2.4.4. Wireless Sensing System Implementation. If the tilting information of the head is transmitted wirelessly to the back-end data conversion subsystem and hooked up to the PSG, then it is the wireless sensing system. With this implementation, a front-end sensing subsystem could be attached on the forehead of the subject and without any cable connected to the PSG. In this front-end sensing subsystem, a module named “BASIC” was developed. BASIC stands for BLE-enabled Accelerometer-based Sensing In a Chip-packaging and is a fusion of A, B, and C technologies which are the accelerometer-based inertial sensing, Bluetooth low-energy (BLE) technology, and CORDIC-based tilting angle transformation algorithm. It is an integration of the accelerometer with the BLE module with CORDIC-based tilting angle transformation algorithm realized in the SoC of the BLE module. So, the module is capable of transmitting the tilting information according to the configured orientation over the air wirelessly by itself. The photo of the BASIC module and its block diagram is shown in Figure 6. With this module attached to the forehead of the subject, there will be no wired connection from the sensing front-end to the data

conversion back-end which is then attached to the PSG device. The back-end system can be simply modified from Figure 5 using a BLE module to receive the transmitted data from the wireless sensing front-end subsystem, for example, the BASIC module; then, the received data are filled into the DACs inside the MCU for signal conversion and hooked up to the PSG device.

3. Results

In this section, the accuracy of the CORDIC-based tilting sensing algorithm-converted information is analyzed by comparing the angle calculated using mathematical equations as in (3). Then, the accuracy of the proposed sensing system was tested with a three-axis rotation platform to measure its actual accuracy under a precise controlled environment. Finally, the results of the system applied in a clinical IRB test is shown to prove the usability of the system for an unmet medical need.

3.1. Precision of the CORDIC-Based Tilting Sensing Algorithm. Validation of the algorithm accuracy was performed to show its precision. The number of iterations executed in the CORDIC-based algorithm can greatly impact the accuracy. Generally, the more iterations executed, the better accuracy can be obtained. But, the trade-off is to

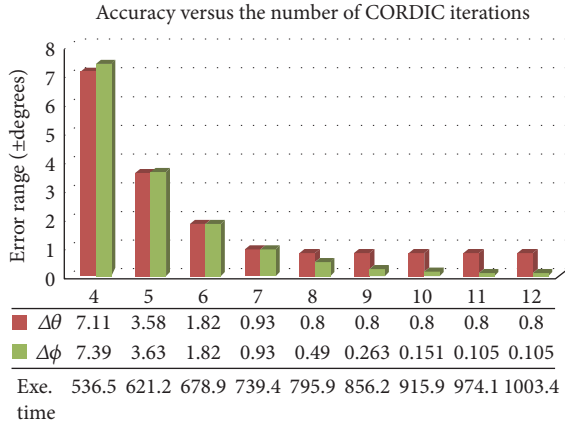
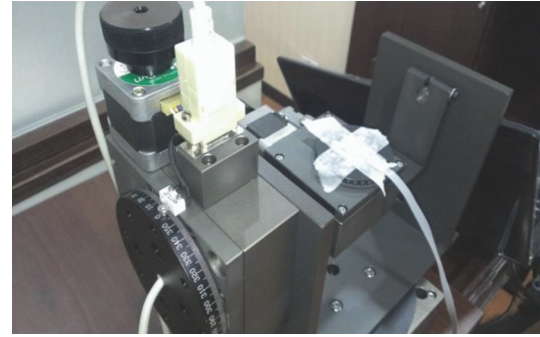


FIGURE 7: Accuracy and timing cost evaluation with varied number of iterations in CORDIC operations.

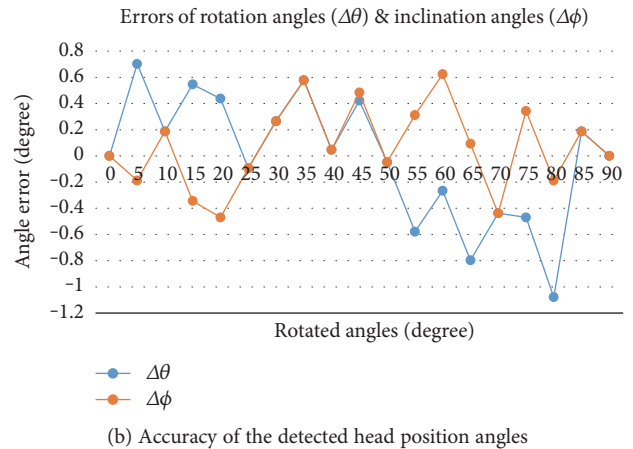
increase the computation time. An optimization was performed to find the number of iteration with acceptable accuracy and computation time. Hereby, different numbers of iterations from 4 to 12 were tested and compared with those of the calculated angles from the offline mathematical calculations. The results are summarized in Figure 7. It indicated that to meet the medical requirement of accuracy at 1°~2°, an acceptable accuracy of ±0.8 degrees for rotation angles and ±0.49 degrees for inclination angle was calculated by 8 iterations with the computation time of 795.9 ms. Such computation time was still much faster than the one from the original trigonometric calculation.

3.2. Accuracy of the Sensing System with an Accelerometer. The accuracy of the sensing system with the actual accelerometer was confirmed through testing on a controllable three-axis rotation platform (with a tri-axis step motor controller, TL-3T, from Tanlian E-O Co. Ltd.), as shown in Figure 8(a). The accelerometer sensing module being tested was placed at the center of the platform. During such testing, the tilting angles of the platform are controlled using precise step motors on the *x*-axis, *y*-axis, and *z*-axis with a resolution of 0.0025 degrees per step. In addition, the tilting angle of the platform is controlled incrementally and thoroughly. The calculated results from the proposed algorithm were then compared with the tilting setting of the platform. The accuracy analysis over the 0°~90° range is shown in Figure 8(b). The validation results show that the maximum error of the tilting angles transformed by the algorithm was within 1.08 degrees for the rotation angle and 0.6 degrees for the inclination angle. This kind of accuracy actually still can meet with the physician’s requirement which is 1°~2° of accuracy for the study.

3.3. System Applied in the Institutional Review Board (IRB) Tests. This study was reviewed and approved by the Institutional Review Board (IRB) of the Taipei Veterans General Hospital with 130 subjects participated. In the test, two sensors with the proposed system were attached to the subject’s forehead for head position monitoring and the other one was attached to the subject’s chest for body position monitoring



(a) The 3-axis rotation platform with module being tested

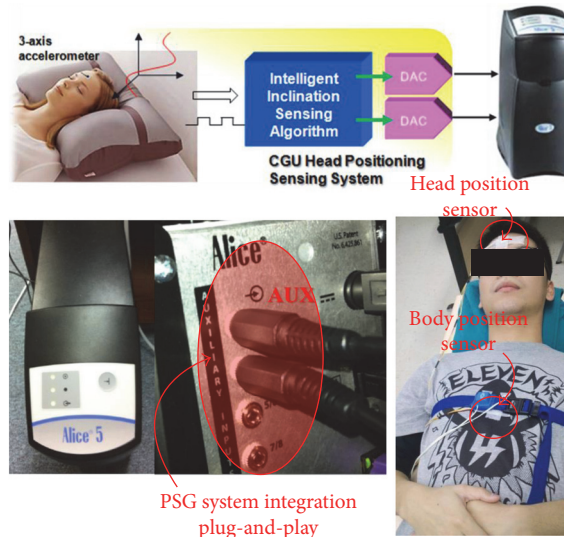


(b) Accuracy of the detected head position angles

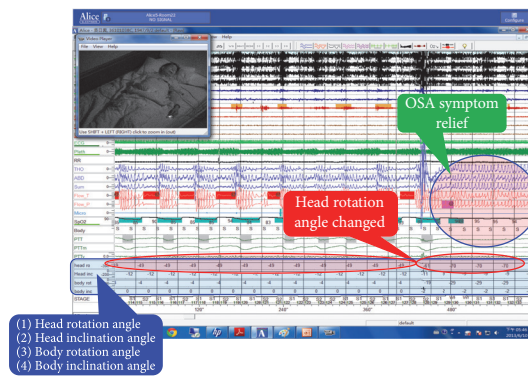
FIGURE 8: (a) The 3-axis rotation platform. (b) Errors of rotation angles and inclination angles of the proposed system.

as shown in Figure 9(a). Figure 9(b) shows the PSG screen captured with the head and body position angle information integrated. This captured screen also catches the scenario that the patient had the head rotation angle changed just before remission from OSAS happened.

As indicated above, one sensor with the proposed sensing system was also attached to the chest for body position monitoring. Since the PSG system was also hooked up with its existing body position sensor which can only provide very rough resolutions classified by 45 degrees (i.e., 0°, -45°, -90°, -135°, -80°, -225°, -270°, and -315° ranges) into 8 sleep positions, a comparison of the body position from these two sensors is provided in Figure 10, where Figure 10(a) shows the details of the body position angle from two sensors, the existing body position sensor (Alice), and the CGU-proposed sensing system (CG) in this study, and Figure 10(b) shows the differences from these two. In this comparison, the epoch in the *x*-axis of both Figures 10(a) and 10(b) represents a 30-second time period which is a standard unit of time used in clinical sleep study. Data were from the PSG of one patient’s overnight sleep test. In Alice (the PSG used in this study), the sampling rate for body position sensor is 1 Hz, and the CGU-proposed sensing system in this study could achieve the sampling rate of 100 Hz. Hence, the 1st data point of every one second from the proposed sensing system was used to compare with the data from existing body position sensors. The position angles shown in Figure 10 were recorded whenever there was apnea/hypopnea that

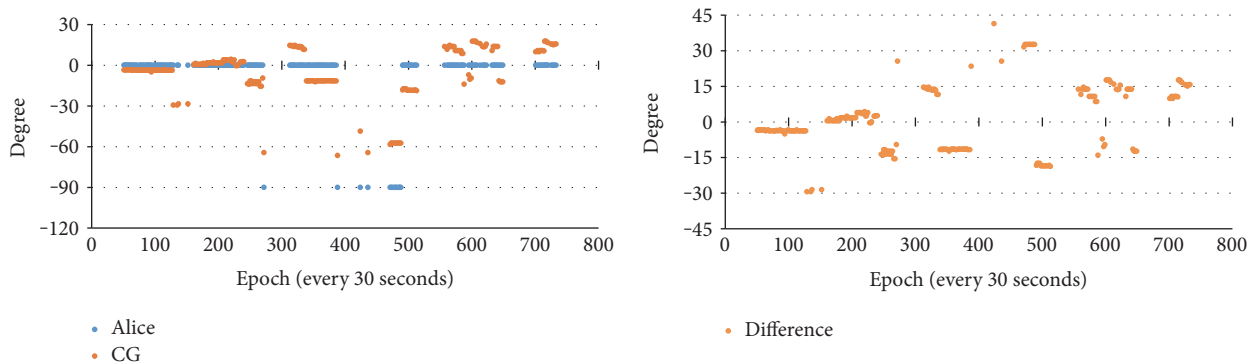


(a) Setup of the sensing system



(b) PSG signal screen captured with head and body position information integrated

FIGURE 9: PSG screen captured with head and body position angle information integrated.



(a) Body position comparison between the existing body position sensor (Alice) and CGU-proposed sensing system (CG)

(b) Differences of body position sensing from the existing body position sensor (Alice) and CGU-proposed sensing system (CG)

FIGURE 10: Body position comparison of the existing body position sensor (Alice) and CGU-proposed sensing system (CG).

occurred; therefore, data points in Figure 10 were not continuous. It can be observed that the sensing system proposed in this study delivered higher resolution of the position angles comparing with the existing body position sensor of the

PSG system which had been used by other researchers [4, 5] for the study of head position-related issues on OSAS patients when a higher resolution of head position-sensing system was not yet available for clinical diagnosis.

TABLE 1: Statistics information of body position comparison for Figure 10.

Statistics of angle difference	Value
Average of absolute differences	10.50°
Standard deviation of absolute differences	8.02°
Maximum difference	41.38°
Minimum difference	-29.40°

Table 1 shows the statistics information of the body position comparison shown in Figure 10. It can be observed that the body position angle differences between the existing body position sensor and the CGU sensing system described in this study are ranging from -29.40° to 41.38° with the average of the absolute differences at 10.50° and a standard deviation of 8.02° . Even by subtracting the maximum error, 1.08° , in the rotation angle, of the CGU sensing system found in Section 3.2 validated with a commercially available controllable rotation platform, the differences of the angles reported by the existing body position sensor are still pretty significant compared with the actual angles. It can be concluded that using the existing body position sensor is not accurate enough to deliver the head position information due to its low resolution. In fact, the CGU sensing system proposed in this study can deliver more accurate position (orientation) information of the desired portion of the body, including the head. Hence, it is more suitable for the remission study of OSAS patients correlated with the head position.

4. Discussion

4.1. Limitations of Using Accelerometer-Based Inclination Sensing for Head Positioning. There are also some limitations using accelerometer-based inclination sensing for head positioning:

- (i) The accuracy of accelerometer-based inclination sensing basing upon the assumption of measured net force is gravitational acceleration only. If the object attached to the accelerometer has significant continuous movements, then the measured acceleration vector from the accelerometer will be the combination of the movement force with the gravitational acceleration. Fortunately, the head movements during sleeping are typically occasional and gentle. Therefore, once the head movements stop, the accurate head position information could be retrieved through accelerometer-based inclination sensing.
- (ii) If in case the measured gravity vector in accelerometer is almost aligned to one of the axes and if the subject rotates along that axis, then the accelerometer is not able to differentiate the rotation angle. This situation happens when the subject sits up or even stands up, such that the gravity vector in the accelerometer is aligned to the x -axis, as shown in Figure 11(a). Under this circumstance, the projected gravity vector on the y - z plane is 0 ($A_y = A_z = 0$). As

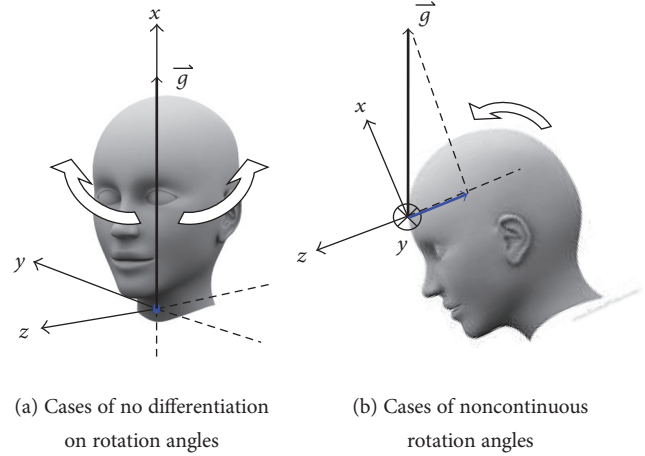


FIGURE 11: Special cases for accelerometer-based inclination sensing of head positioning monitoring.

a result, it is not able to calculate the rotation angle θ as in (3). However, the system is supposed to detect head position when the subject is sleeping, and when the situation happens, the subject could not be sleeping. Therefore, this is the case of no interest for sleeping diagnosis.

- (iii) When the subject leans forward, the head position will be like the figure shown in Figure 11(b). In this case, the A_z reading from the accelerometer will be negative and $A_y \approx 0$. As described in (3), to extend the rotation angle θ to cover the whole 360° range, the term of $\sigma \cdot \lambda \cdot 180$ is used for the adjustment. Since $A_z < 0$, and $A_y \approx 0$, so, even with small changes of A_y , it results in the sign changes of A_y . Consequently, the calculated rotation angle θ will be jumping between $+180^\circ$ and -180° . This phenomenon is also observed in our study. However, this is a case of no interest since this situation happens when the subject sits up and leans forward. Under this circumstance, the subject is not in a normal sleeping mode.

4.2. Error Ingredient of the Proposed Sensing System. In the accuracy validation of the proposed sensing system, the errors of rotation angles and inclination angles are actually larger than the errors shown in the precision analysis of the CORDIC-based tilting sensing algorithm alone. This is because the overall errors of the sensing system also include the errors from the accelerometer itself besides the errors contributed by the algorithm. Even though the data from the accelerometer were calibrated, the data from the accelerometer still contains some noise as well as the mechanical structure of the accelerometer. During the system validation, it can be observed that the 3 axes of the accelerometer were not perpendicular to each other. This would add to the overall errors of the proposed sensing system using accelerometers.

5. Conclusions

This study presents the design and development of a sensing system for head position monitoring. The system has been realized and was proved to be able to plug-and-play into most of the PSG devices used in hospitals and clinical sleep institutions for the diagnosis of OSAS patients. A CORDIC-based tilting sensing algorithm was also implemented in the system to reduce the burdens of high computability required, such that the cost of the system can be reduced. The system has been carefully verified with the performance analysis of the tilting sensing algorithm and accuracy validation through a precise controlled rotation platform. The system was proved to meet the medical needs of doctors on providing accurate head position information for their study of remission in OSAS patients.

Disclosure

The funding sponsors had no role in the design of the study; in the collection, analyses, or interpretation of data; in the writing of the manuscript; and in the decision to publish the results.

Conflicts of Interest

The authors declare that there is no conflict of interest regarding the publication of this paper.

Acknowledgments

This work was supported in part by the Ministry of Science and Technology, Taiwan (under Grant nos. NSC 101-2325-B-075-007, NSC 102-2325-B-075-004, MOST 105-2221-E-182-079, MOST 105-2627-E-182-001, and MOST 105-2745-8-182-002) and CGU fund BMRPC50 and BMRP138.

References

- [1] T. Young, M. Palta, J. Dempsey, J. Skatrud, S. Weber, and S. Badr, "The occurrence of sleep-disordered breathing among middle-aged adults," *The New England Journal of Medicine*, vol. 328, pp. 1230–1235, 1993.
- [2] R. D. Cartwright, "Effect of sleep position on sleep apnea severity," *Sleep*, vol. 7, pp. 110–114, 1984.
- [3] C. F. George, T. W. Millar, and M. H. Kryger, "Sleep apnea and body position during sleep," *Sleep*, vol. 11, pp. 90–99, 1988.
- [4] E. R. Van Kesteren, J. P. van Maanen, A. A. J. Hilgevoord, D. M. Laman, and N. de Vries, "Quantitative effects of trunk and head position on the apnea hypopnea index in obstructive sleep apnea," *Sleep*, vol. 34, pp. 1075–1081, 2011.
- [5] R. J. Schwab, "A quantum advance in PSG recordings: the importance of head position in mediating the AHI," *Sleep*, vol. 34, p. 985, 2011.
- [6] Z. T. Beattie, C. C. Hagen, and T. L. Hayes, "Classification of lying position using load cells under the bed," in *2011 Annual International Conference of the IEEE Engineering in Medicine and Biology Society (EMBC)*, pp. 474–477, Boston, MA, USA, August–September 2011.
- [7] Z. T. Beattie, C. C. Hagen, M. Pavel, and T. L. Hayes, "Classification of breathing events using load cells under the bed," in *2009 Annual International Conference of the IEEE Engineering in Medicine and Biology Society*, pp. 3921–3924, Minneapolis, MN, USA, 2009.
- [8] C. M. Yang, C. M. Chou, S. G. Chen et al., "Sleeping ECG and body position monitoring system," in *2009 Annual International Conference of the IEEE Engineering in Medicine and Biology Society (EMBC)*, pp. 1856–1859, Minneapolis, MN, USA, September 2009.
- [9] W.-T. Liao, W.-C. Chou, W.-Y. Lin, K. F. Lei, W.-W. Tsai, and M.-Y. Lee, "CORDIC-based inclination sensing algorithm using three-axis accelerometer-based inertial sensors," in *2011 4th International Conference on Biomedical Engineering and Informatics (BMEI 2011)*, pp. 705–709, Shanghai, China, October 2011.
- [10] R. J. Nevins, N. G. Durdle, and V. J. Raso, "A posture monitoring system using accelerometers," in *IEEE Canadian Conference on Electrical and Computer Engineering, 2002 (CCECE 2002)*, vol. 2, pp. 1087–1092, Winnipeg, MB, Canada, 2002.
- [11] E. Farella, A. Pieracci, L. Benini, and A. Acquaviva, "A wireless body area sensor network for posture detection," in *Proceedings of 11th IEEE Symposium on Computers and Communications (ISCC '06)*, pp. 454–459, Cagliari, Italy, June 2006.
- [12] W. T. Huang, C. N. Hung, C. C. Tuan, C. C. Chen, Y. J. Chang, and Y. Y. Chen, "Novel design of interactive caption and recognition postures within the wearable and non-vision system over wireless sensor network," in *2010 International Conference on Complex, Intelligent and Software Intensive Systems (CISIS)*, pp. 752–757, Krakow, TBD, Poland, February 2010.
- [13] H. R. Silva, J. A. Afonso, P. C. Morim, P. M. Oliveira, J. H. Correia, and L. A. Rocha, "Wireless hydrotherapy smart-suit network for posture monitoring," in *IEEE International Symposium on Industrial Electronics (ISIE 2007)*, pp. 2713–2717, Vigo, Spain, June 2007.
- [14] P. Cech, J. Dlouhy, M. Cizek, I. Vicha, and J. Rozman, "Software for automatic head position monitoring," in *19th International Conference on Radioelektronika, 2009 (RADIOELEKTRONIKA '09)*, pp. 31–34, Bratislava, Slovakia, April 2009.
- [15] J. E. Volder, "The CORDIC trigonometric computing technique," *IRE Transactions on Electronic Computers*, vol. EC-8, no. 3, pp. 330–334, 1959.

Research Article

Research on Safety and Compliance of a New Lower Limb Rehabilitation Robot

Yongfei Feng,¹ Hongbo Wang,¹ Hao Yan,¹ Xincheng Wang,¹ Zhennan Jin,¹ and Luige Vladareanu²

¹Parallel Robot and Mechatronic System Laboratory of Hebei Province, Key Laboratory of Advanced Forging & Stamping Technology and Science of Ministry of Education, Yanshan University, Qinhuangdao 066004, China

²Institute of Solid Mechanics of Romanian Academy, 010141 Bucharest, Romania

Correspondence should be addressed to Hongbo Wang; hongbo_w@ysu.edu.cn

Received 19 March 2017; Revised 16 May 2017; Accepted 7 June 2017; Published 26 July 2017

Academic Editor: Yi-Hung Liu

Copyright © 2017 Yongfei Feng et al. This is an open access article distributed under the Creative Commons Attribution License, which permits unrestricted use, distribution, and reproduction in any medium, provided the original work is properly cited.

The lower limb rehabilitation robot is an application of robotic technology for stroke people with lower limb disabilities. A new applicable and effective sitting/lying lower limb rehabilitation robot (LLR-Ro) is proposed, which has the mechanical limit protection, the electrical limit protection, and the software protection to prevent the patient from the secondary damage. Meanwhile, as a new type of the rehabilitation robots, its hip joint rotation ranges are different in the patient sitting training posture and lying training posture. The mechanical leg of the robot has a variable workspace to work in both training postures. So, if the traditional mechanical limit and the electrical limit cannot be used in the hip joint mechanism design, a follow-up limit is first proposed to improve the compatibility of human-machine motion. Besides, to eliminate the accident interaction force between the patient and LLR-Ro in the process of the passive training, an amendment impedance control strategy based on the position control is proposed to improve the compliance of the LLR-Ro. A simulation experiment and an experiment with a participant show that the passive training of LLR-Ro has compliance.

1. Introduction

Cerebral vascular disease, hemiplegic, and paraplegia may cause limb motor dysfunction. Based on the nerve rehabilitation theory, patients could recover through the specialized rehabilitation training [1]. The lower limb rehabilitation robot is an application of robotic technology for people with lower limb disabilities [2]. In recent years, research on the lower limb rehabilitation robots has become an active topic [3, 4]. Several kinds of lower limb rehabilitation robots have been developed. Those can be divided into the trainers with single degree of freedom [5], wearable trainers [6], suspended gait trainers [7, 8], and sitting/lying gait trainers [9]. Because of the specificity of the lower limb rehabilitation robot, it has high demand on the safety and compliance. There is still a lack of widespread randomized clinical trials of the lower limb rehabilitation robots in the hospitals. The safety and compliance have been key issues for robot design and control.

Rehabilitation robotic is the interdisciplinary science. Most of the rehabilitation robots are based on medical rehabilitation principle, modeling on body parameters of normal people, and the lack of the unknown design error, model uncertainty, and parameter self-correction [10]. Based on security considerations, the electrical limit switch is installed on the robots. However, it cannot fully guarantee the patient in the whole training process. Erol and Sarkar used an automatic release rectifier controller on PUMA 560 to provide a quick release of the electromagnet that is fixed on the robot, so as to ensure that the affected limb can be quickly withdrawn from the rehabilitation equipment [11]. Tejima and Stefanov [12] have designed a reflex mechanism that is similar to a biological reflex. When the machine detects unexpected force, it will make a back reaction to prevent collision damage. Some of rehabilitation robots are equipped with special vision-based proximity sensors that perceive the human body and automatically stop the robot when they

move too closely toward the user [13]. ViGRR is also to ensure safety by releasing the user from the robot. The footplate is magnetically attached and can be released on demand to mitigate safety risk [14]. The above methods ensure the safety of the patients to some extent. But the realization of these methods is just based on the stability of the electrical system of the rehabilitation robot. When the electrical system is in the unsteady state, the safety of the patient without controlling ability of limb motion may suffer huge risks. So, the mechanical limit protection has to be designed in the rehabilitation robot. However, the sitting/lying lower limb rehabilitation robot as a new type of mechanism [15, 16], its hip joint ranges are different in the sitting training posture and lying training posture. So, the mechanical leg of this type robot has a variable workspace. The traditional mechanical and electrical limit is no longer applicable, and a follow-up mechanical-electrical limit protection is first proposed.

Besides, the mechanical limit and electrical limit protections only aim to prevent the accident from the outside world. They are powerless to deal with the human body's own discomfort and muscle spasm. The interactive force control between robot and patient is a very important aspect in the research of lower limb rehabilitation robot. An interactive control method with active compliance characteristics can avoid the limb and the robot to generate a confrontation, due to the abnormal muscle activity, such as convulsion and tremor. Yang's team controls the upper limb rehabilitation robot by impedance control strategy based on the position, and the control structure is a double-closed loop [17]. Duschau-Wicke et al. used impedance control method to build the virtual wall around the ideal training path to ensure the activity of the lower limb [18]. The impedance control could achieve the dynamic relationship between the force and position and has a good flexibility and security. According to the impedance control strategy based on the position, an amendment impedance control strategy is proposed in this paper to improve the compliance of rehabilitation robot, and its effectiveness is verified by the experiment.

2. Materials and Methods

2.1. Innovative Design of the LLR-Ro. The LLR-Ro contains the movable seat, the left mechanism leg module, the right mechanism leg module, the touch screen, and the control box as shown in Figure 1. The left mechanism leg module and the right mechanism leg module are bilateral symmetry. Each module has a mechanical leg, which has the hip, knee, and ankle joint in the human body sagittal. The mechanical leg is the most important part of the prototype as shown in Figure 2. In order to satisfy people with different height from 1500 mm to 1900 mm, the lengths of the thigh and calf of the LLR-Ro could be changed automatically. The sensing system contains sensors to measure joint rotations and estimate the torque and force produced by the patients. The torque sensors are installed on the location of the joint axis, which can directly acquire joint torque values.

As the LLR-Ro is a typical human-machine system, the limb safety of the patient is the most important principle to be considered in its design. LLR-Ro has the mechanical limit,



FIGURE 1: The prototype of the LLR-Ro.

the electrical limit, and the software protection to prevent the patient from the secondary damage. The design of the mechanical limit mainly takes advantage of the mechanical structure to limit the motion range of joints. Limit switches are installed on extreme position of the hip joint, knee joint, and ankle joint to realize the electrical limit. Patient information will be recorded into the control system during the human-machine interaction. Then, the actuators will control the DC servo motors moving in the motor-designated scope to realize software limit protection.

2.2. The Design of the Hardware Control System. Based on the functions of the LLR-Ro, the hardware control system contains the central control module, the human-machine interactive system, the sensor feedback system, and the motion control system as shown in Figure 3. The central control module mainly runs the control software and receives the operational order from the human-machine interactive system. The human-machine interactive system displays the control software interface and feeds back the training conditions. The motion control system receives the motion control commands from the central control module, realizes the motor closed-loop control and feeds back the joint real motion condition to the central control module. The sensor feedback system acquires the sensor information and achieves the sensor state.

2.3. The Follow-Up Limit Design of the LLR-Ro. To meet the needs of the patient with different recovery stages, the back angle of the movable seat could be altered from 110° to 170° to help the patient realize sitting and lying training posture. However, there is a safety angle between the thigh and the upper part of the body in both sitting posture training and lying posture training as shown in Figure 4. If the upper part of the body is at the dotted line position and the thigh is at the full line position, it would bring the patient a secondary damage. So, the mechanical leg in the sitting posture training and the lying posture training has different training workspaces. If the traditional mechanical limit and the electrical limit

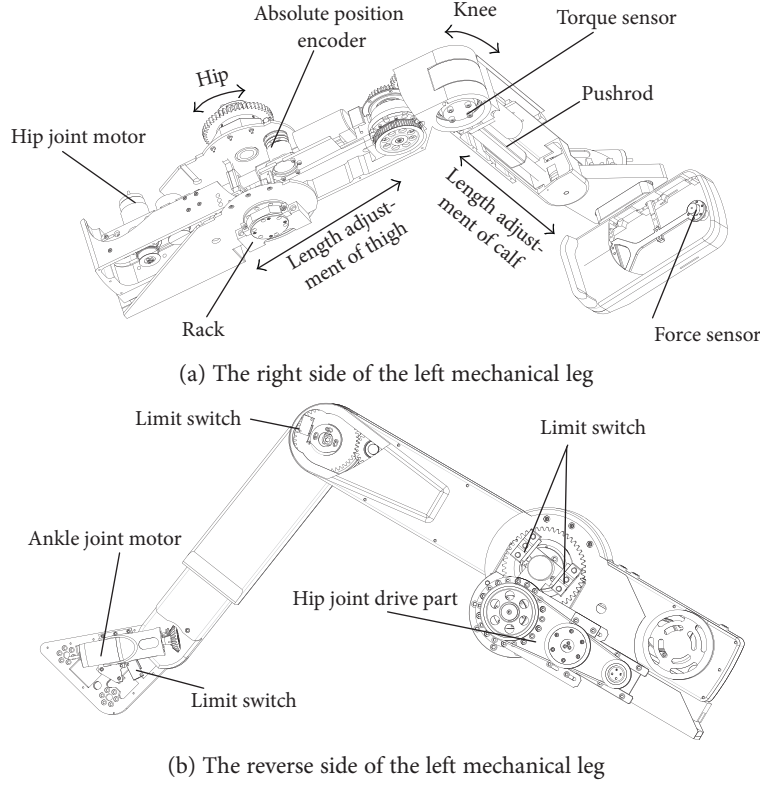


FIGURE 2: The detailed design of LLR-Ro leg mechanism.

cannot be used in this hip joint design, then a follow-up limit is proposed to solve this problem.

In order to prevent the mechanism leg squeezing in the patient when the seat back angle is adjusted, the angle between the back and the mechanical leg will be limited at $45^\circ \sim 170^\circ$. The design of the seat back adjustment takes advantage of the link mechanism with linear actuator as shown in Figure 5(a). Figure 5(b) shows the simplified model of the seat. l_{ZT} is the length of the linear actuator. Point A and point C are fixed on the seat rack. θ_{C3} , θ_{D2} , θ_{D4} , θ_{D6} , l_{CA} , and l_{CB} are the constant. θ_{D5} equals 45° .

Based on the geometry relationship,

$$\begin{aligned}\theta_{C1} &= \arccos \frac{l_{BC}^2 + l_{CA}^2 - l_{ZT}^2}{2l_{BC}l_{CA}} \\ \theta_{C2} &= 360 - \theta_{C1} - \theta_{C3} \\ \theta_{D1} &= 180 - \theta_{C2} \\ \theta_{D3} &= 360 - \theta_{D2} - \theta_{D1}.\end{aligned}\quad (1)$$

The seat back angle could be gotten as

$$\theta_{ZY} = \theta_{D3} - \theta_{D4}, \quad (2)$$

and then, the max value of the hip joint would be obtained.

$$\theta_{1\max} = 540 - \theta_{D2} - \theta_{D4} - \theta_{C3} - \arccos \frac{l_{BC}^2 + l_{CA}^2 - l_{ZT}^2}{2l_{BC}l_{CA}} - \theta_{D5}. \quad (3)$$

Equations (1) and (2) are the relationship between the seat back angle and the linear actuator; (1) and (3) are the relationship between the max value of the hip joint and the linear actuator.

The follow-up limit design of the hip joint mechanism will also adapt the link mechanism with linear actuator as shown in Figure 6. Point O is the center of the hip joint; l_{XT} is the length of the linear actuator; point G and point E are fixed on the mechanism rack; and point I is the hip joint limit switch trigger point. The line segment IF represents the mechanical limit rod. l_{IF} , l_{GE} , l_{EF} , l_{IJ} , and θ_{G2} are the constant. Coordinate system is established, where O is the origin point, x is the horizontal direction, and y is the vertical direction.

Based on the geometry relationship,

$$\begin{aligned}\theta_{G1} &= \arccos \frac{l_{XT}^2 + l_{GE}^2 - l_{EF}^2}{2l_{XT}l_{GE}} \\ \theta_{G3} &= \theta_{G1} - \theta_{G2}.\end{aligned}\quad (4)$$

Then the coordinates of point $I(x_1, y_1)$ could be obtained if

$$\begin{aligned}x_1 &= x_G + l_{XT} \cos \theta_{G3} \\ y_1 &= y_G - l_{XT} \sin \theta_{G3} + l_{IF}.\end{aligned}\quad (5)$$

The angle θ_{O1} could be gotten if

$$\theta_{O1} = \arctan \frac{l_{IJ}}{\sqrt{x_1^2 + y_1^2}}. \quad (6)$$

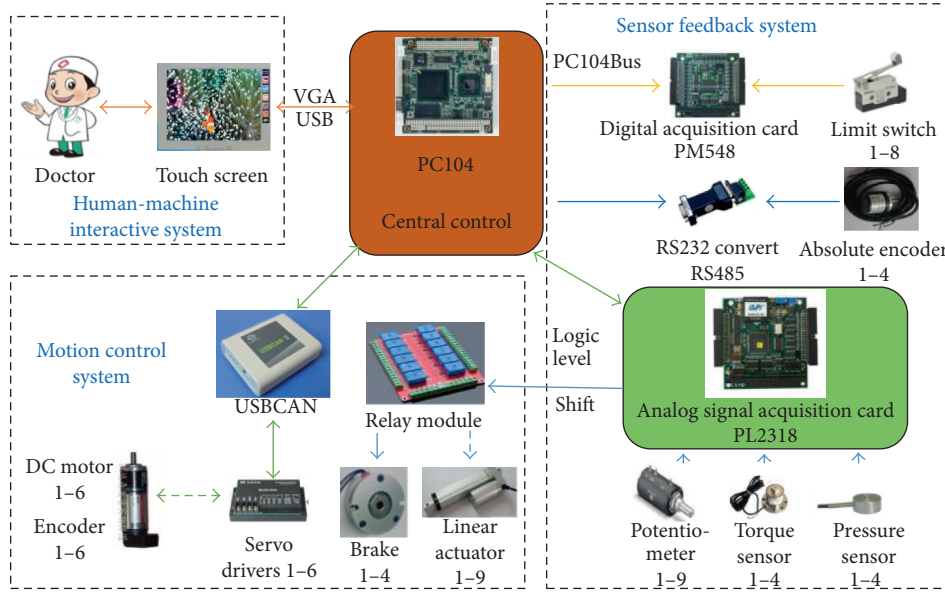


FIGURE 3: The structure of the hardware control system.

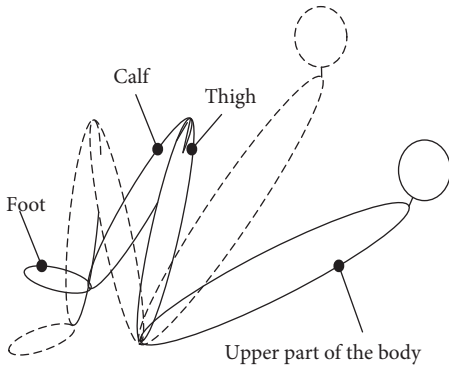


FIGURE 4: Training posture sketch of the patient.

The relationship between the maximum value of the hip joint angular position with the length of the linear actuator will be calculated.

$$\theta_{1\max} = 180 - \theta_{O_2} - \theta_{O_1} = \arctan \frac{y_F + l_{IF}}{x_F} - \arcsin \frac{l_{II}}{\sqrt{x_F^2 + (y_F + l_{IF})^2}}, \quad (7)$$

where

$$\begin{aligned} x_F &= x_G + l_{XT} \cos \left(\arccos \frac{l_{XT}^2 + l_{GE}^2 - l_{EF}^2}{2l_{XT}l_{GE}} - \theta_{G_2} \right) \\ y_F &= y_G - l_{XT} \sin \left(\arccos \frac{l_{XT}^2 + l_{GE}^2 - l_{EF}^2}{2l_{XT}l_{GE}} - \theta_{G_2} \right). \end{aligned} \quad (8)$$

Combining (2), (3), and (7), the relationship between the seat back angle and the length of linear actuator on the follow-up limit device could be achieved. When the

seat back angle is changed, the max limit position of hip joint will be calculated.

2.4. The Control Compliance of the LLR-Ro. Most of passive training control strategies of the rehabilitation robot are designed in accordance with the strategy of industry robots as shown in Figure 7. In the passive training process, the LLR-Ro drives the patient lower limb along a certain trajectory. However, the passive training is mainly suitable for the patients in the early phase of their illness. At this phase, patient lower limbs have large muscle tone. If the patient feels uncomfortable and his legs move achingly while the mechanism leg of the LLR-Ro still in motion, the patient leg would be hurt again. So, the research on the motion compliance of the LLR-Ro is necessary.

The LLR-Ro also adapts the impedance control strategy based on position control to realize accuracy position control. The impedance control strategy is shown in Figure 8.

The position correction ΔX will be obtained through the force F in the impedance control model. The impedance control model is introduced by

$$\begin{aligned} M_d \Delta \ddot{X} + B_d \Delta \dot{X} + K_d \Delta X &= F \\ F &= F_{PM} + G_P + G_R, \end{aligned} \quad (9)$$

where M_d , B_d , and K_d are the target inertia matrix, the damping matrix, and the stiffness matrix, respectively; ΔX is the position correction of the mechanism leg; F_{PM} is the contact force from the patient muscle tone; and G_P and G_R represent the weight from the patient lower limb and LLR-Ro mechanical leg, respectively.

It can be obtained through the Russ transform:

$$\Delta X(s) = \frac{F(s)}{M_d s^2 + B_d s + K_d}. \quad (10)$$

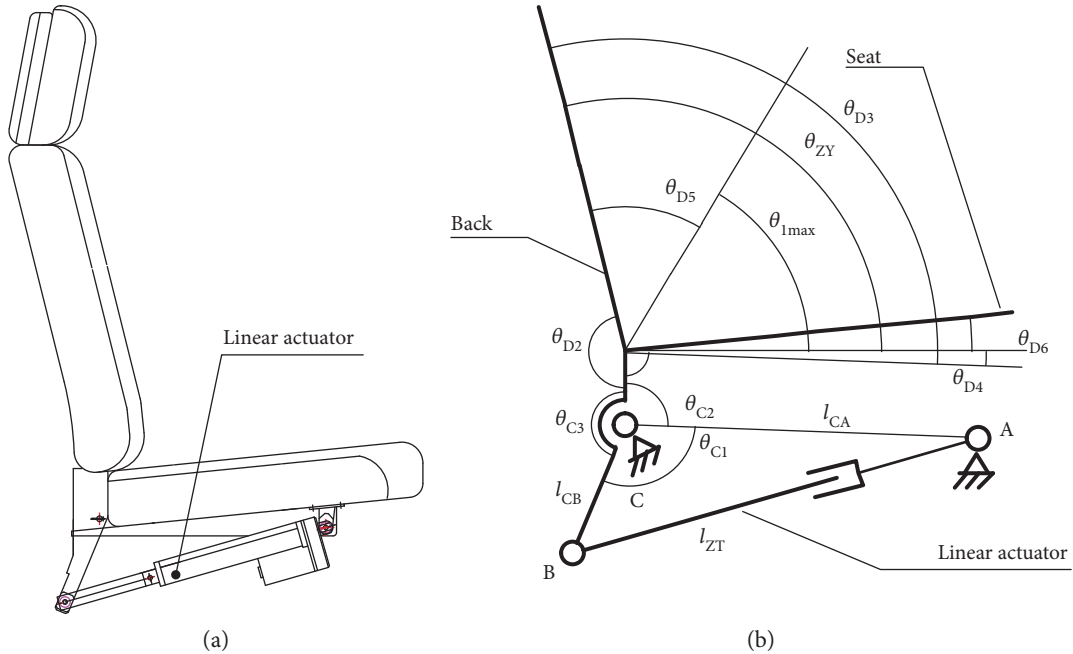


FIGURE 5: The design of the seat. (a) The structure of the prototype; (b) the simplified model of the seat.

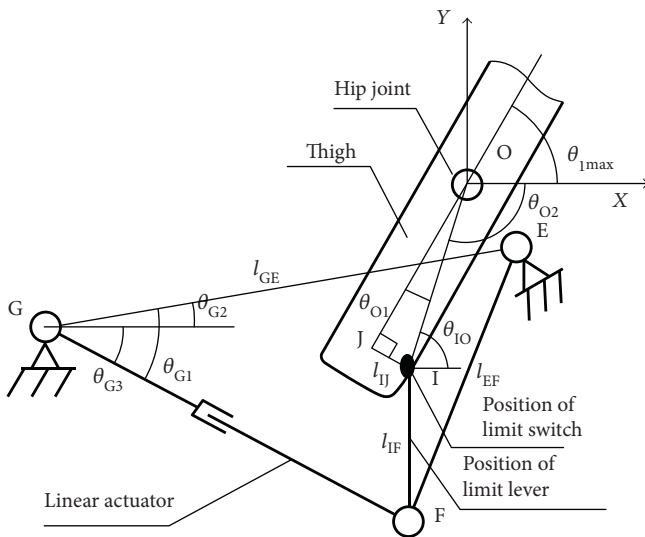


FIGURE 6: The design of the follow-up limit.

When the patient feels uncomfortable and has no ability to move with the robot along the trajectory during the training, the contact force F_{PM} from the patient muscle tone will be bigger. Based on the above impedance control strategy to realize the compliance in the motion along the preplan trajectory, we also need to change the end point force to position the adjustment amount through the impedance control model. The impedance control strategy will be modified to the new amendment impedance control strategy to suit the rehabilitation training as shown in Figure 9. This new control strategy contains two parts, including the traditional impedance control loop in the dashed frame and the opposite direction correction control loop out of the dashed frame. The two parts are connected through a switch block.

When the force F_{PM} equals zero, the amendment impedance control strategy is just as the common impedance control strategy to make the robot move along the preplan trajectory. If the force F_{PM} does not equal to zero, the opposite direction correction control loop is closed. The contact force will be converted to position correction through the impedance control model. The actual position X_a adds the position correction ΔX to get the amendment trajectory X_d . The LLR-Ro moves along the amendment trajectory until the contact force F_{PM} equals to zero, then the LLR-Ro shuts down. The physician will check the patient security to determine the next training program.

2.5. Approximate Calculation of the Force from Patient Accident Force. As the length of the foot is very short relative to the calf and thigh, in the passive training, the ankle joint moves in a small motion range and it will be planned separately. In this paper, the ankle joint of LLR-Ro mechanical leg is fixed. There are torque sensors installed on the hip joint and knee joint of the mechanical leg to measure the LLR-Ro joint torques. The measured torques contain three parts, F_{PM} , G_p , and G_R . Because of the length adjustment of the mechanical leg and the transmission parts installed on the mechanical leg with a nonuniform distribution, the position of the centroid is difficult to determine. So, it cannot use the dynamics directly to calculate the torques generated by the weight of the mechanism leg. However, the LLR-Ro moves in a low velocity and steady state, and the effect from dynamics can be ignored. The torques generated by the weights of the mechanical leg and patient leg will be calculated through the statics. The statics model is shown in Figure 10. G_{R1} represents the weight of the mechanical leg thigh, and G_{R2} represents the weight of the mechanical leg calf and foot, respectively. l_{c1} and l_{c2} represent the distance from the spindle to the calf plus foot centroid and thigh

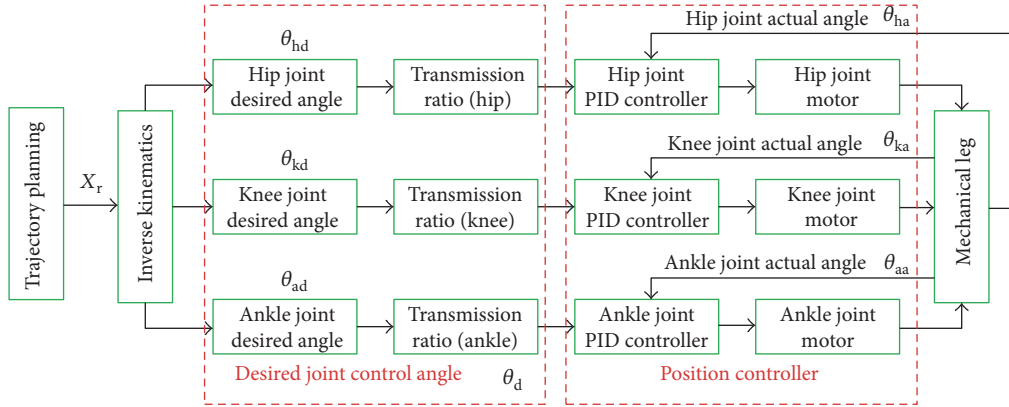


FIGURE 7: The passive training control based on PID method.

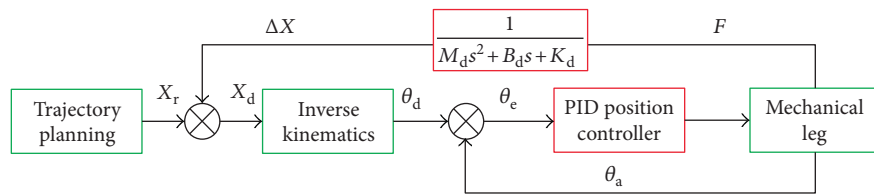


FIGURE 8: The LLR-Ro impedance control model.

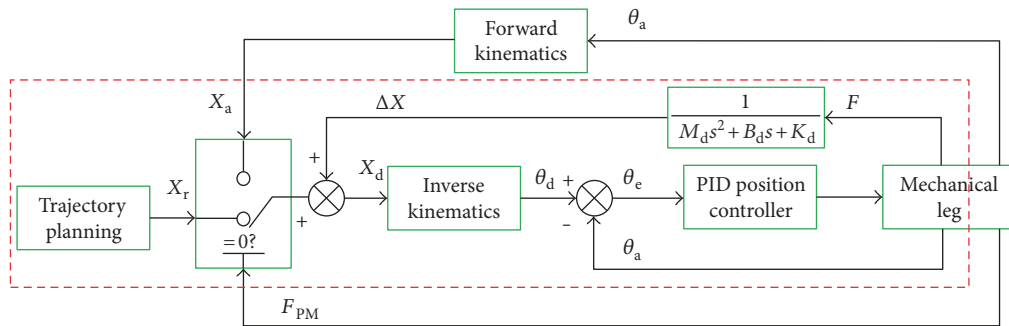


FIGURE 9: The amendment impedance control strategy.

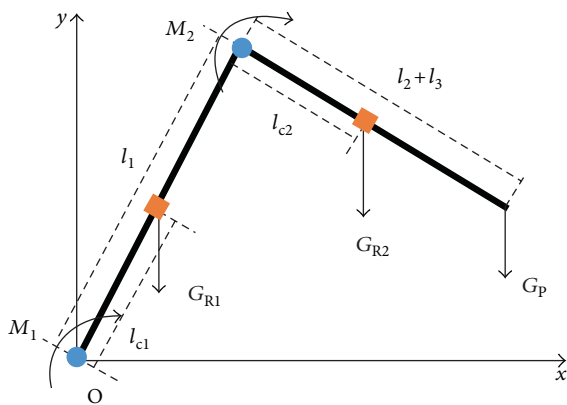


FIGURE 10: The statics model to calculate the torques.

centroid, respectively. The knee torque generated from the weight of LLR-Ro mechanical leg calf as well as patient leg and the hip torque generated from the weight of mechanical leg as well as patient leg could be calculated through the joint torque sensors, respectively.

$$\begin{aligned} M_{2z} &= G_{R2} l_{c2} \cos(\theta_1 + \theta_2) + G_p l_2 \cos(\theta_1 + \theta_2) = B \cos(\theta_1 + \theta_2) \\ M_{1z} &= G_{R1} l_{c1} \cos \theta_1 + (G_{R2} + G_p) l_1 \cos \theta_1 + M_2 = A \cos \theta_1 + M_2. \end{aligned} \quad (11)$$

The values of A and B will be changed when the length of the mechanical leg is varied. It could be calculated through the experiment. When the patient exerts force F_{PM} on the end of mechanism leg, the torques M_{1P} and M_{2P} would be generated at the hip joint and knee joint. F_{PM} could be seen as a component force from F_x and F_y .

TABLE 1: Geometric parameters of the movable seat and mechanical leg rack.

Name	Geometric parameters		
Movable seat	$\theta_{C3} = 157^\circ$	$\theta_{D2} = 166^\circ$	$\theta_{D4} = -3^\circ$
	$\theta_{D5} = 45^\circ$	$l_{CA} = 324.7 \text{ mm}$	$l_{CB} = 129 \text{ mm}$
Mechanical leg rack	$(x_G, y_G) = (-560 \text{ mm}, -235 \text{ mm})$	$(x_E, y_E) = (64 \text{ mm}, -81 \text{ mm})$	$l_{EF} = 350 \text{ mm}$
	$l_{IF} = 150 \text{ mm}$	$l_{IJ} = 27.5 \text{ mm}$	—

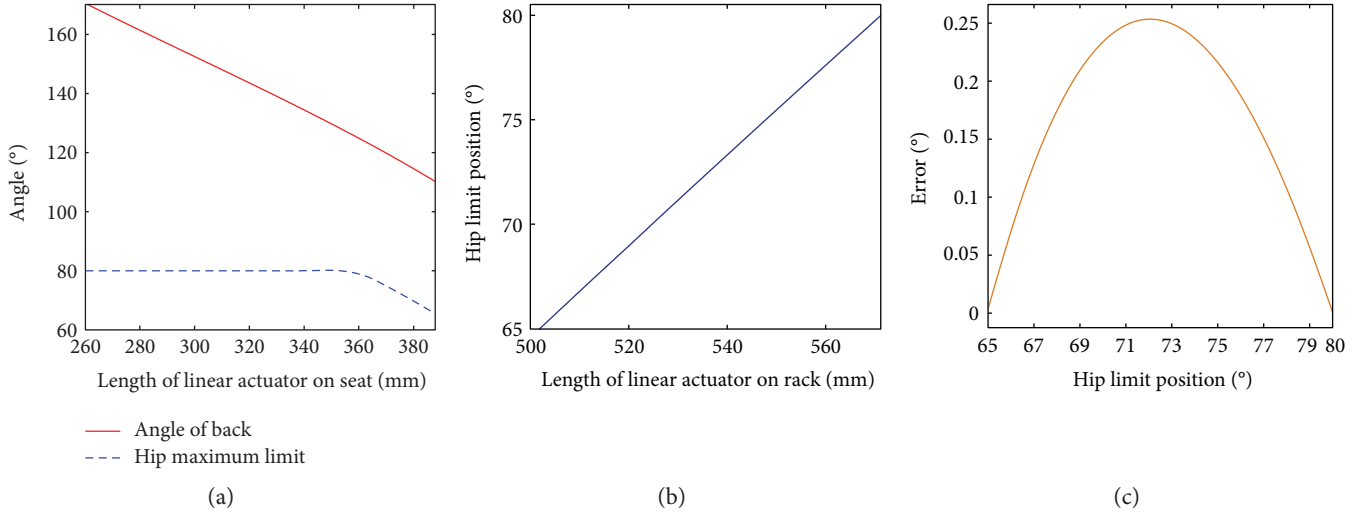


FIGURE 11: Results of the follow-up limit experiment. (a) The relationship between length of linear actuator on seat and angle of seat back as well as hip maximum limit position; (b) the relationship between length of linear actuator on rack and actual hip maximum limit position; (c) the error of hip maximum limit position.

F_x and F_y are the forces along the horizontal direction and vertical direction.

$$\begin{bmatrix} M_{1P} \\ M_{2P} \end{bmatrix} = \begin{bmatrix} -l_1 \sin \theta_1 - l_2 \sin(\theta_1 + \theta_2) & l_1 \cos \theta_1 + l_2 \cos(\theta_1 + \theta_2) \\ -l_2 \sin(\theta_1 + \theta_2) & l_2 \cos(\theta_1 + \theta_2) \end{bmatrix} \cdot \begin{bmatrix} F_x \\ F_y \end{bmatrix} = J^T(q) \begin{bmatrix} F_x \\ F_y \end{bmatrix}, \quad (12)$$

where $J^T(q)$ is the Jacobin matrix transposition.

The contact force could be calculated as follows:

$$F_{PM} = \begin{bmatrix} F_x \\ F_y \end{bmatrix} = (J^T(q))^{-1} \begin{bmatrix} M_{1P} \\ M_{2P} \end{bmatrix} = (J^{-1}(q))^T \begin{bmatrix} M_{1P} \\ M_{2P} \end{bmatrix}, \quad (13)$$

where

$$(J^{-1}(q))^T = \frac{1}{l_1 l_2 \sin \theta_2} \begin{bmatrix} l_2 \cos(\theta_1 + \theta_2) - l_1 \cos \theta_1 - l_2 \cos(\theta_1 + \theta_2) \\ l_2 \sin(\theta_1 + \theta_2) - l_1 \sin \theta_1 - l_2 \sin(\theta_1 + \theta_2) \end{bmatrix}. \quad (14)$$

At this time, the actual torque of the hip joint M_{1t} and the actual torque of the knee joint M_{2t} are measured by the

torque sensors, and we could get the torques exerted by the patient as follows:

$$\begin{aligned} M_{1P} &= M_{1t} - M_{1z} \\ M_{2P} &= M_{2t} - M_{2z}. \end{aligned} \quad (15)$$

At last, the contact force F_{PM} from the patient muscle tone could be calculated through (13) and (15).

3. Results

3.1. The Functional Verification Experiment of the Follow-up Limit. Based on the mechanical design of the movable seat and mechanical leg rack, the geometric parameters in Section 2.3 are given in Table 1. The follow-up limit includes the mechanical limit and electrical limit protections. Both limit protections have the same limit position. When the mechanical leg reaches the hip joint maximum limit position, the limit switch will change its signal and stop the mechanical leg moving. According to the range of the seat back angle, the hip joint maximum limit position could be changed from 65° to 125° . However, the hip joint maximum position is designed at 80° . So, the hip joint maximum limit position is designed from 65° to 80° .

Based on (3) and (7), when the linear actuator l_{ZT} on the seat is changed, the linear actuator l_{XT} on the mechanical leg rack is varied correspondingly. The hip joint maximum limit

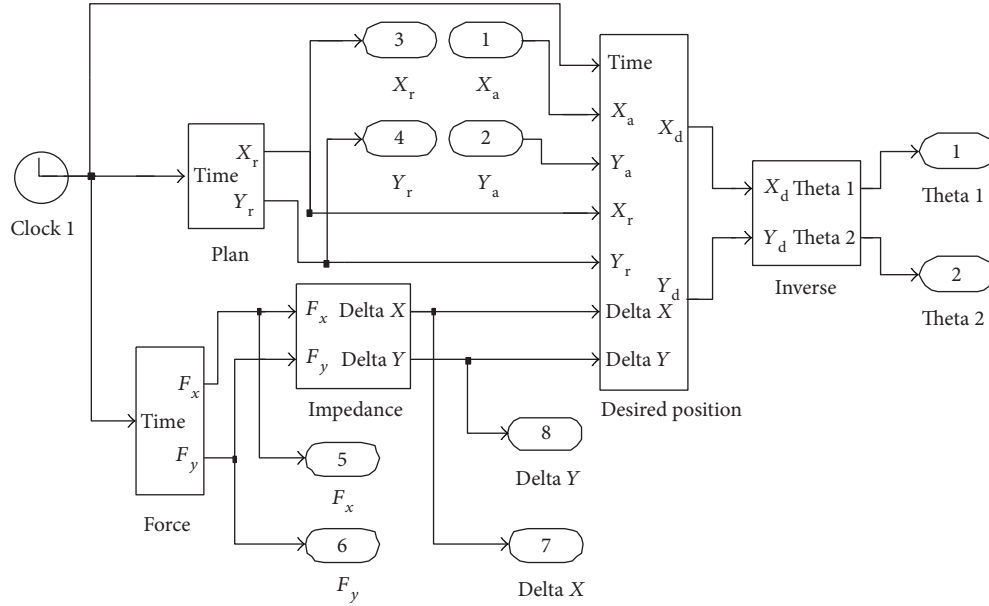


FIGURE 12: The simulation model of the amendment impedance control strategy.

position is measured through angulometer. The results are recorded in Figure 11. Figure 11(a) shows the relationship between length of linear actuator on seat and angle of seat back as well as theoretical hip maximum limit position. Figure 11(b) shows the relationship between length of linear actuator on rack and actual hip maximum limit position. Figure 11(c) shows the error of hip maximum limit position.

3.2. Simulation Experiment of the Amendment Impedance Control Strategy. The theoretical simulation has been researched through MATLAB as shown in Figure 12. In this simulation, the values of G_p and G_R are designed as zero. F_{PM} is seen as a component force from F_x and F_y . F_x and F_y are supposed to be given as below:

$$F_x = \begin{cases} 0 & t < 3s \\ \sin t + 0.3 \sin 2t - 0.2 \sin 4t & 3s \leq t \leq 4.5s \\ 0 & 4.5s < t, \end{cases} \quad (16)$$

$$F_y = \begin{cases} 0 & t < 3s \\ \cos t + 0.4 \cos 3t - 0.3 \cos 5t & 3s \leq t \leq 4.5s \\ 0 & 4.5s < t. \end{cases} \quad (17)$$

The inputs of the force block are from (16) and (17). Plan block is simulated to get the training trajectory. The impedance block could realize the force transferred as position correction. The inputs of desired position block are from the outputs of plan block and impedance block. The function of inverse block is designed to get each joint position to drive the motors. In this simulation experiment, plan block is the input of a linear trajectory. The positions of the start point and end point are (362.16, 131.36) and (758.69, -30.66), respectively. The parameters M_d , B_d , and K_d are given as follows:

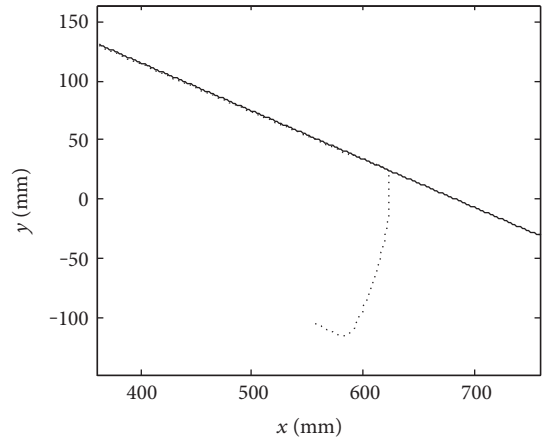


FIGURE 13: The planning trajectory and trajectory after corrected.

$$M_d = \begin{bmatrix} 0.0625 \\ 0.0625 \end{bmatrix}, B_d = \begin{bmatrix} 5 \\ 5 \end{bmatrix}, K_d = \begin{bmatrix} 100 \\ 100 \end{bmatrix}. \quad (18)$$

The simulation planning trajectory and corrected trajectory are obtained as shown in Figure 13. The curves of the forces F_x and F_y and the correction values along x -axis Δx and y -axis Δy are obtained as shown in Figure 14.

3.3. Preliminary Experiment of the Amendment Impedance Control Strategy. In order to verify the innovative design of the prototype and the amendment impedance control strategy, a preliminary experiment is conducted. The experiment is held at the Intelligent Rehabilitation Robot Laboratory in Yanshan University. Before the experiment, approval for all studies is obtained from Yanshan University

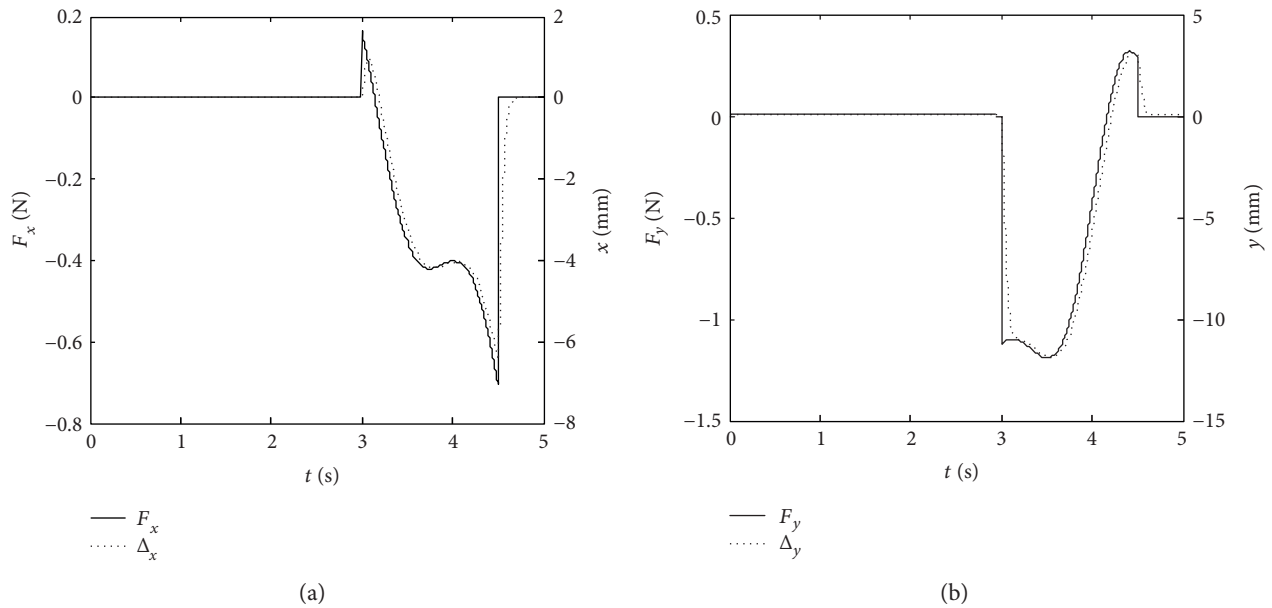


FIGURE 14: The simulation comparison between the contact force and the position correction. (a) The curves of the force F_x and the correction value along x -axis Δx ; (b) the curves of the force F_y and the correction value along y -axis Δy .



FIGURE 15: The process of the participant doing the passive rehabilitation training.

Ethics Committee, and all the experiment information is introduced to the participant and an informed consent form is signed by the participant. The participant in this experiment is a healthy person, and his left leg is put on the mechanical leg of the LLR-Ro as shown in Figure 15. The participant thigh length $l_1 = 350$ mm and the calf length $l_2 = 350$ mm. At the start of the rehabilitation training, the participant is in a relaxed state moving with the LLR-Ro. Based on (11), the values of A and B are obtained 15.47 N·m and 17.43 N·m, respectively.

Then, the participant force on the mechanism leg suddenly to imitate the participant at uncomfortable state. The software will calculate the contact force through the torque sensors on the mechanism leg. The contact force would be transformed from the joint torques. If the force along the x -axis or y -axis is beyond $(-2\text{N}, 2\text{N})$, the LLR-Ro will be in the amendment impedance control strategy based on the position control to adjust the end trajectory until the contact force is back in $(-2\text{N}, 2\text{N})$ and the mechanism leg stops.

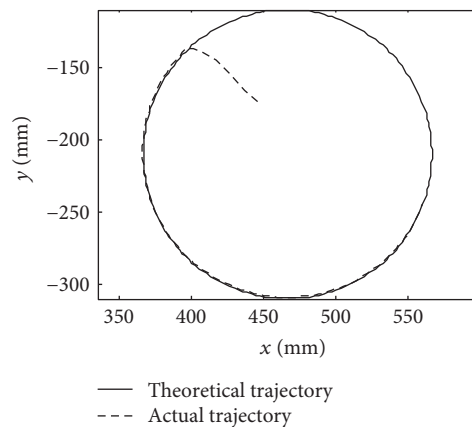


FIGURE 16: The theoretical and actual motion curves of the mechanism leg end point.

The impedance model is applied on the digital control with data discretization. When $m = 0.0625$, $b = 5$, and $k = 200$, the transfer function is discretized through the zero-order holder. Sampling time is 150 ms, and the discrete time transfer function could be obtained as

$$G(z) = \frac{0.00499z + 7.728e - 06}{z^2 - 0.000413z + 4.264e - 08}. \quad (19)$$

The difference equation could be gotten as

$$x(k) = 0.004958x(k-1) - 0.000006144x(k-2) + 0.009826f(k-1) + 0.000124f(k-2). \quad (20)$$

The initial values are $x(1) = x(2) = 0$, $f(1) = f(2) = 0$. The experiment will use a circle trajectory. The center is

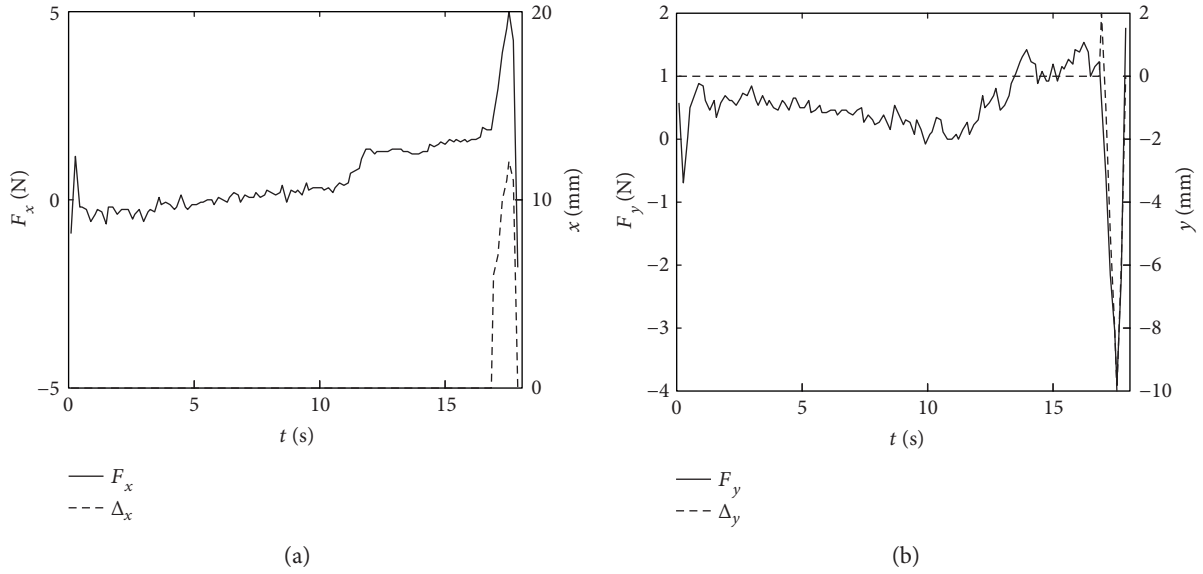


FIGURE 17: The comparison between the contact force and the position correction. (a) The comparison between the contact force and the position correction along x -axis; (b) the comparison between the contact force and the position correction along y -axis.

$(x_0, y_0) = (466.48, -209.83)$ as shown in Figure 16, and the radius is $r = 100$ mm.

From the experiment, we could obtain that the force along x -axis and the position correction versus time and the force along y -axis and the position correction versus time are shown in Figure 17.

4. Discussion

The follow-up limit experiment is conducted. Figure 11 shows that when the angle of seat back is changed, the hip maximum limit position will be varied accordingly. Although there is an error between the actual hip maximum limit position and the theoretical hip maximum limit position, the largest error is 0.25° and could be acceptable. The design of follow-up limit is feasible. However, this experiment just used limit switch and conducted with a small hip joint speed. Maybe the fast hip joint speed would destroy the linear actuator on the rack. The destructive experiment of the follow-up limit will be verified in the future.

It is necessary to conduct a simulation experiment before the experiment with human participation. From Figures 13 and 14, the curves of correction values along x -axis and y -axis have the same changing trend with the forces F_x and F_y . In the first three seconds, the forces F_x and F_y equal to zero, the position correction values are zero, and the mechanical leg end point moves along the circular trajectory. During the time at 3 s~4.5 s, the forces vary below and beyond zero, the position corrections can follow the variations of forces very fast, and the mechanical leg end moves along the correctional trajectory. When the time is at 4.5 s~5 s, the position corrections turn into zero as the forces F_x and F_y are reducing to zero. Then, the mechanical leg end stops moving. The above simulation process shows that when the patient

accident forces emerge, LLR-Ro will decrease the forces through position corrections of the mechanical leg end. This control strategy makes LLR-Ro realize good compliance to make the passive training safe.

The environments of the simulation experiment and an experiment with a participant are a little different. The simulation one ignores the weights from patient leg and mechanical leg. Besides, the simulation experiment also neglects the errors from the mechanical leg assemble and sensor errors. The improvement of the experiment with a participant is considering the errors, and patient muscular tone F_{PM} is limited at $(-2N, 2N)$. If F_{PM} is beyond the limited range, LLR-Ro will generate position corrections.

From Figures 16 and 17, when the force F_{PM} is in the allowable range, the mechanism leg moves along the preplan trajectory. However, when it is beyond the allowable range, the mechanism leg will do the amendment impedance control based on the position. The results are almost same with the simulation experiment. From the experiment results, the amendment impedance control strategy is feasible. From Figure 15, the LLR-Ro could help the volunteer realize passive training. It proves that the mechanism design of the LLR-Ro is feasible and safe.

In the future, the authors will do the research on the active training based on the impedance control strategy, the clinic verification of the LLR-Ro, and biocooperative control strategy. The rehabilitation training patterns are automatically achieved through the intelligent human-machine-cooperative control system. Applying high-tech methods like biomechanical information and patient physiological information, the evaluation system of rehabilitation efficacy of LLR-Ro will be established. Based on the patient training state, LLR-Ro could changed the training parameters by itself during one rehabilitation training pattern.

5. Conclusions

A new intelligent lower limb rehabilitation robot (LLR-Ro) is proposed. It can help patients recover lower limb disabilities. Because of the specificity of the lower limb rehabilitation robot, the safety and compliance are researched. The LLR-Ro has a variable workspace. If the traditional mechanical limit and the electrical limit cannot be used in the design, then a follow-up limit is proposed to solve this problem. To prevent the patient from the secondary damage in the passive training, an amendment impedance control strategy based on the position control is proposed to improve the compliance of the LLR-Ro. The simulation experiment and experiment with a participant verify that the control strategy is feasible and the mechanical design of LLR-Ro is safe.

Conflicts of Interest

The authors declare that they have no conflicts of interest.

Acknowledgments

This work was supported by the China Science and Technical Assistance Project for Developing Countries (KY201501009), the Hundred Talents Program of Hebei Province, and the National Construction High Level University Government-Sponsored Graduate Student Project (Certificate no. 201608130106).

References

- [1] W. Q. Wang, Z. G. Hou, L. Cheng et al., "Toward patients' motion intention recognition: dynamics modeling and identification of iLeg—an LLRR under motion constraints," *IEEE Transactions on Systems, Man, and Cybernetics: Systems*, vol. 46, pp. 980–992, 2016.
- [2] N. Koceska, S. Koceski, F. Durante, P. B. Zobel, and T. Raparelli, "Control architecture of a 10 DOF lower limbs exoskeleton for gait rehabilitation," *International Journal of Advanced Robotic Systems*, vol. 10, pp. 1–11, 2013.
- [3] R. Lu, Z. Li, C. Y. Su, and A. Xue, "Development and learning control of a human limb with a rehabilitation exoskeleton," *IEEE Transactions on Industrial Electronics*, vol. 61, pp. 3776–3785, 2014.
- [4] I. Díaz, J. J. Gil, and E. Sánchez, "Lower-limb robotic rehabilitation: literature review and challenges," *Journal of Robotics*, vol. 2011, Article ID 759764, 11 pages, 2011.
- [5] K. Chen, Y. Z. Zhang, J. G. Yi, and T. Liu, "An integrated physical-learning model of physical human-robot interactions with application to pose estimation in bikebot riding," *International Journal of Robotics Research*, vol. 35, pp. 1459–1476, 2016.
- [6] D. Dan, S. Y. Qiu, Z. Guan, C. Shi, and Z. Li, "Development of an exoskeleton robot for lower limb rehabilitation," in *International Conference on Advanced Robotics and Mechatronics*, pp. 312–317, Macau, China, August 2016.
- [7] X. N. Wang, T. Lu, S. J. Wang, J. Gu, and K. Yuan, "A patient-driven control method for lower-limb rehabilitation robot," in *International Conference on Mechatronics and Automation*, pp. 908–913, Harbin, China, August 2016.
- [8] B. M. Fleerkotte, B. Koopman, J. H. Buurke, E. H. van Asseldonk, H. van der Kooij, and J. S. Rietman, "The effect of impedance-controlled robotic gait training on walking ability and quality in individuals with chronic incomplete spinal cord injury: an explorative study," *Journal of Neuroengineering and Rehabilitation*, vol. 11, pp. 1–15, 2014.
- [9] A. Mehmet Arif and A. Erhan, "The design and control of a therapeutic exercise robot for lower limb rehabilitation: physiotherobot," *Mechatronics*, vol. 21, pp. 509–522, 2011.
- [10] L. Marchal-Crespo and D. J. Reinkensmeyer, "Review of control strategies for robotic movement training after neurologic injury," *Journal of Neuroengineering and Rehabilitation*, vol. 6, pp. 1–15, 2009.
- [11] D. Erol and N. Sarkar, "Intelligent control framework for robotic rehabilitation after stroke," in *IEEE International Conference on Robotics and Automation*, pp. 1238–1243, Piscataway, USA, April 2007.
- [12] N. Tejima and D. Stefanov, "Fail-safe components for rehabilitation robots—a reflex mechanism and fail-safe force sensor," in *9th International Conference on Rehabilitation Robotics*, pp. 456–460, Piscataway, USA, June–July 2005.
- [13] K. Kawamura, R. A. Peters, M. W. Wilkes, W. A. Alford, and T. E. Rogers, "ISAC: foundations in human-humanoid interaction," *IEEE Intelligent Systems and their Applications*, vol. 15, pp. 38–45, 2000.
- [14] K. J. Chisholm, K. Klumper, A. Mullins, and M. Ahmadi, "A task oriented haptic gait rehabilitation robot," *Mechatronics*, vol. 24, pp. 1083–1091, 2014.
- [15] H. B. Wang, X. H. Shi, H. T. Liu, L. Li, Z. Hou, and H. Yu, "Design, kinematics, simulation, and experiment for a lower-limb rehabilitation robot," *Proceedings of the Institution of Mechanical Engineers, Part I: Journal of Systems and Control Engineering*, vol. 225, pp. 860–872, 2011.
- [16] H. B. Wang, D. Zhang, H. Lu et al., "Active training research of a lower limb rehabilitation robot based on constrained trajectory," in *2015 International Conference on Advanced Mechatronic Systems (ICAMEchS)*, pp. 22–24, Beijing, China, August 2015.
- [17] Y. Yang, L. Wang, J. Tong, and L. Zhang, "Arm rehabilitation robot impedance control and experimentation," in *Proceedings of the IEEE International Conference on Robotics and Biomimetics*, pp. 914–918, Kunming, China, December 2006.
- [18] A. Duschau-Wicke, J. von Zitzewitz, A. Caprez, L. Lunenburger, and R. Riener, "Path control: a method for patient-cooperative robot-aided gait rehabilitation," *IEEE Transactions on Neural Systems and Rehabilitation Engineering*, vol. 18, pp. 38–48, 2010.

Research Article

Mechanical Bed for Investigating Sleep-Inducing Vibration

Hitoshi Kimura, Akisue Kuramoto, Yuma Inui, and Norio Inou

Department of Mechanical and Control Engineering, Tokyo Institute of Technology, Tokyo, Japan

Correspondence should be addressed to Hitoshi Kimura; kimura@mech.titech.ac.jp

Received 24 February 2017; Revised 19 May 2017; Accepted 1 June 2017; Published 9 July 2017

Academic Editor: Yi-Hung Liu

Copyright © 2017 Hitoshi Kimura et al. This is an open access article distributed under the Creative Commons Attribution License, which permits unrestricted use, distribution, and reproduction in any medium, provided the original work is properly cited.

In running cars or trains, passengers often feel sleepy. Our study focuses on this physiological phenomenon. If a machine can reproduce this phenomenon, it is feasible to put a person, such as an insomnia patient or an infant, to sleep without any harmful effects. The results of our previous study suggest that low-frequency vibration induces sleep. This report describes a new mechanical bed for inducing sleep and discusses the effects of different vibration conditions. The new bed has two active DOFs in the vertical and horizontal directions to examine the anisotropy of sensation. The bed includes three main parts: a vertical driver unit, a horizontal driver unit, and a unique 2-DOF counterweight system to reduce driving force and noise. With regard to motion accuracy, the maximum motion error in the vertical direction lifting 75 kg load was only 0.06 mm with a 5.0 mm amplitude of a 0.5 Hz sinusoidal wave. The results of excitation experiments with 10 subjects showed a significant difference in sleep latency between the conditions with vibration and without vibration. Furthermore, the average latency with insensible vibration (amplitude=2.4 mm) was shorter than that with sensible vibration (amplitude=7.5 mm). These results suggest the ability of appropriate vibration to induce sleep.

1. Introduction

The control of sleeping time is essential to modern society. The development of an effective method to induce sleep without harmful effects will bring remarkable benefits for insomnia patients, babies, and employees that work non-standard shifts (e.g., long-distance drivers). To realize a sleep-inducing method, this study focuses on the phenomenon wherein passengers often fall asleep in running cars or trains. Conceivable sleep-inducing factors in mechanical environments include light, temperature, sound, vibration, and oxygen density. In our previous study, a tendency is observed where the low-frequency vibration of a running train make people fall asleep [1]. This paper describes a new mechanical bed designed to elucidate the detailed vibration conditions necessary to induce sleep. Various mechanical cradles designed to help babies sleep are commercially available; however, few studies have investigated the relationship between vibration and sleep induction. Although many studies and the ISO have defined

uncomfortable vibration [2–4], few studies have discussed comfortable vibration [5]. Kitado et al. suggested that the vibration of running trains with 1/f fluctuation has a sleep-inducing effect [6, 7]. The authors have investigated the relationship between sleeping passengers and the vibration of running trains to identify effective vibration for inducing sleep [8]. In that study, the authors did not find a significant relationship between the number of sleeping passengers in running trains and the 1/f fluctuation of their vibration; however, the results suggested that low-frequency vibration, less than 2.0 Hz, tended to induce sleep. The results also showed that a certain magnitude of jerk (i.e., more than 0.2 m/s^3) disturbs sleep [9, 10]. Thus, our past study indicated that smooth vibration without jerking is required for a mechanical environment to induce sleep. This conclusion is in agreement with studies showing that large jerks impair the comfortableness of vehicles [11, 12]. To reproduce a sleep-inducing environment with a simple mechanism, the authors examined several subjects with a 1-DOF exciter bed [13]. The results

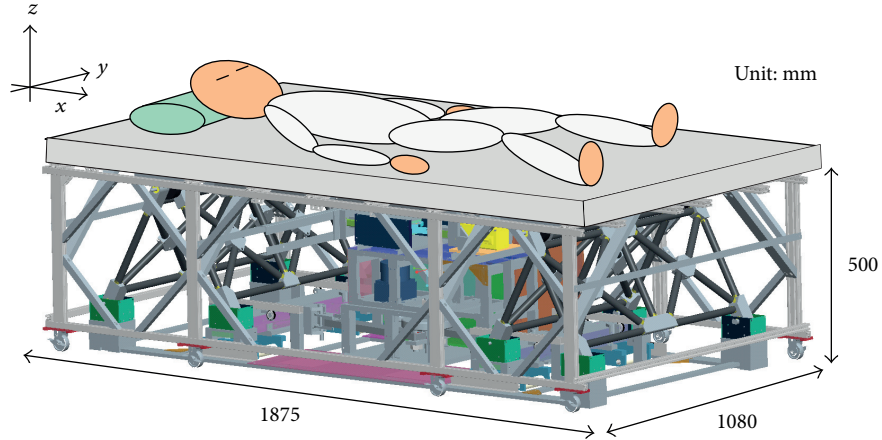


FIGURE 1: Schematic of the new mechanical bed.

showed that a frequency of 0.5 Hz and no fluctuation were optimal conditions to induce sleep. Altmann reports that vibrations with frequency less than 2.0 Hz have a possibility of resonance at a part of the body depending on the subject's posture; however, the resonance vanishes at about 0.5 Hz [14]. A research of motion sickness reported by O'Hanlon et al. showed that 0.2 Hz vibration caused sickness which recovered at about 0.5 Hz [15]. Of course, there remain unknown factors about the relationship between vibration and feeling; these studies agree that 0.5 Hz vibration is not uncomfortable. However, our bed could not examine the anisotropy of body sensation. Thus, this study aims to investigate the detailed conditions of vibration that effectively induces sleep. This paper describes a new prototype mechanical bed that has two active DOFs in the horizontal and vertical directions. The bed has a unique counterweight system with two passive DOFs to decrease the required motor torque and operating noise. Experiments in which sleep latencies were measured on the basis of brain waves under several excitation conditions were conducted with 10 subjects.

2. Mechanism of the New Mechanical Bed

2.1. Design of the Overall Structure. The mechanical bed is designed to stimulate a human body within two directions (horizontal and vertical). Accurate and quiet motion is necessary because this study also aims to determine the vibrational conditions that induce sleep. Since the vertical driving mechanism must lift the subject, the required force would be enormous with a normal mechanism. Although the required force for horizontal motion is lower than that for vertical motion, the movement of the center of mass (hereafter referred to as COM) will cause errors in the vibrational motion and result in large operating noise. To avoid these problems, the authors designed a new counterweight system to generate both vertical and horizontal motion using one weight. This counterweight system decreases the forces required for vertical motion and the COM's movement. The resulting new mechanical bed comprises three main mechanisms: a vertical

driving unit, a horizontal driving unit, and a counterweight system. Figure 1 shows the overall structure of the bed. Hereafter, this paper uses the Cartesian coordinate system shown in Figure 1.

2.2. Vertical Driving Unit. Figure 2 shows the driving mechanism for vertical vibration. The driving mechanism comprises a pair of pantograph mechanisms connected to a slider crank mechanism. The slider crank is driven by the motor, and the pantograph works to elevate the bed frame. The pantograph mechanisms are arranged centrosymmetrically with the motor axis serving as the symmetric center. Within this mechanism, the bed frame is supported by passive wheels at the four corners to achieve stable motion.

The force required for motion in the vertical direction F_v is represented by the following equation:

$$F_v = \frac{m(g + a_v)}{4 \tan \theta}, \quad (1)$$

where m is the total mass of vibrational motion including the human subject and bed frame, g and a_v are the accelerations of gravity and in the vertical direction, respectively, and θ is the angle of the toggle mechanism linkage shown in Figure 3. The motor torque τ can be derived from F_v and the kinematics as follows:

$$\tau = \frac{2F_v l_3}{r} \left(\sin \alpha + \frac{l_3 \sin 2\alpha}{2\sqrt{l_2^2 - l_3^2 \sin^2 \alpha}} \right), \quad (2)$$

where r is the reduction ratio of the gearhead of the motor and l_n ($n = 1, 2, 3$) is the link length, as shown in Figure 3. Assuming that the maximum weight of a subject is 100 kg, the maximum required torque is approximately 2.0 Nm. The actual required force is considerably smaller than this maximum torque because the total vertical load, which includes the human body and the bed frame, is supported by a counterweight mechanism, as will be described later. From the viewpoint of safety, this study adopts a stepping motor with sufficient torque to generate 12.0 Nm. Thus, the

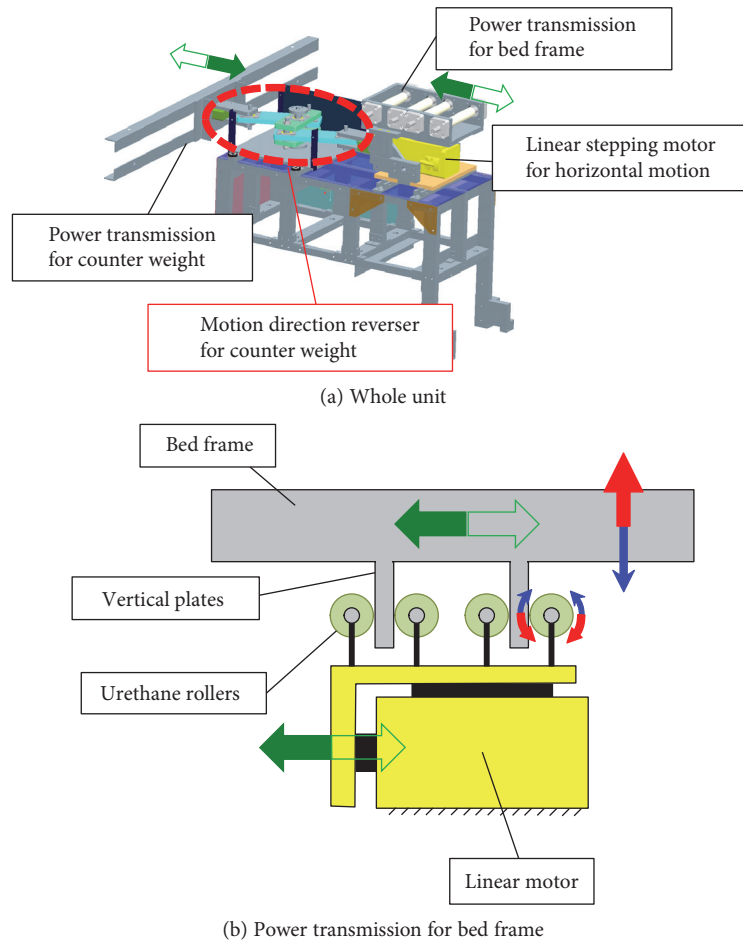


FIGURE 4: Schematic of the horizontal driving unit.

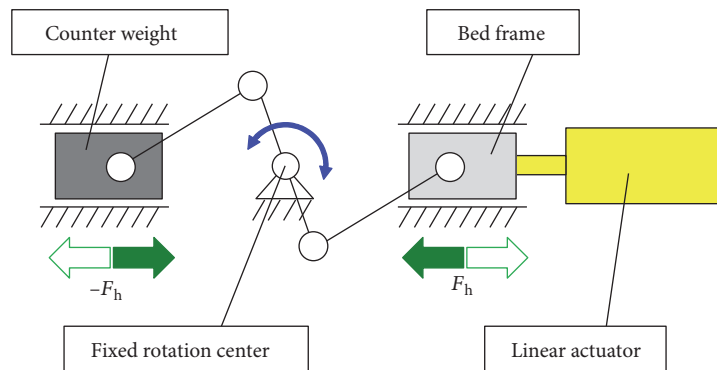


FIGURE 5: Kinematic diagram of the horizontal driving mechanism.

directions. A microprocessor unit (MPU) independently controls each motor driver, and the frequency and amplitude are variable during the bed excitation. On the basis of our previous research and ISO standards [2, 3], simple vibration of sinusoidal wave with large amplitude tends to cause motion sickness. Although the vibrations of running cars or trains include more than 10 mm amplitude, it is obvious that sleeping is almost impossible under a continuous large amplitude. Authors also confirmed that a sinusoidal vibration with

an amplitude of 10 mm or more causes the subject to get motion sickness with another mechanical bed. In addition, a vibration with a frequency of 2.0 Hz or more may not contribute to induce sleep [8]. This tendency is intuitive referring that the natural frequencies of lymph in semicircular canals is about 1.0 to 2.0 Hz [2]. Thus, for each direction, the maximum amplitude and frequency is defined as 10 mm and 2.0 Hz, respectively. Figure 8(a) shows the difference between the command and actual motion in the vertical direction

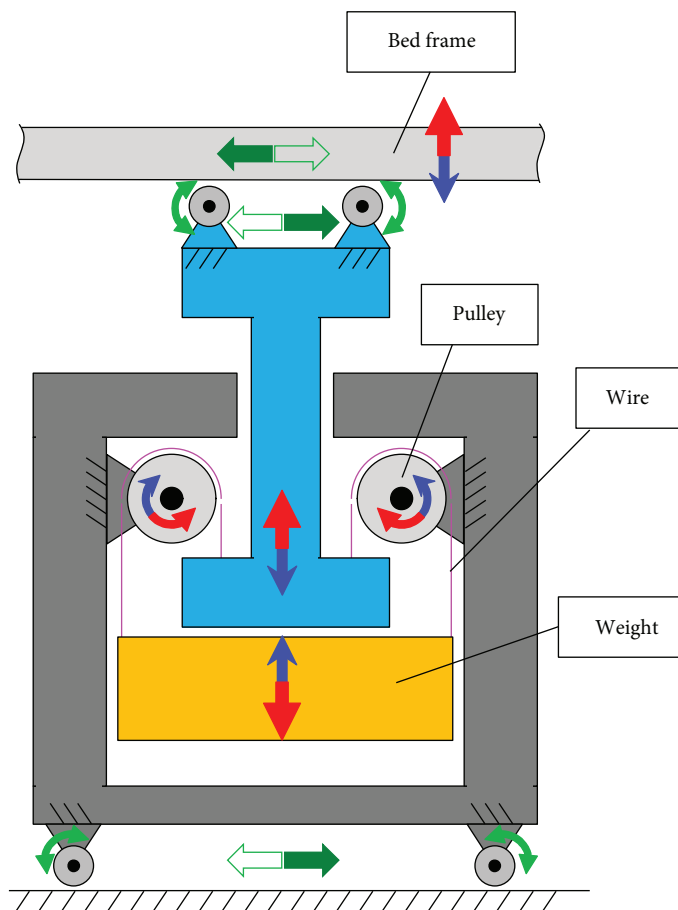


FIGURE 6: Schematic of counterweight unit.

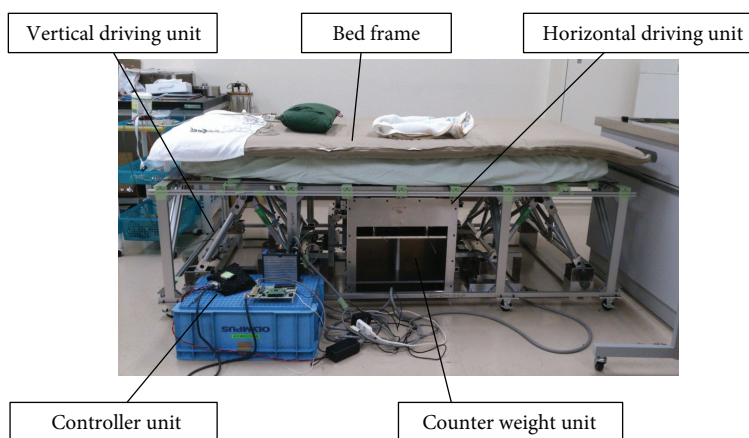


FIGURE 7: Overview of prototype 2-DOF bed.

without load. The actual motion of the bed frame was measured using a KEYENCE laser displacement sensor IA2000. Two sensors are fixed on the ground, and the displacements of the bed frame are measured in both horizontal and vertical directions with high accuracy. The motion accuracy was also confirmed without load and with 75 kg load of human body. The maximum error of the vertical motion is less than 0.06 mm under a sine wave vibration with an amplitude of

5.0 mm at 0.5 Hz (Figure 8(b)). In terms of a machine which can drive the human body, this motion error is extremely small. Meanwhile, the maximum error of the horizontal motion is 0.28 mm with 75 kg human body, which is larger than that of the vertical direction (Figure 8(c)). The horizontal motion error might be caused by urethane rollers for driving force transmitter (Figure 4(b)) which has a certain flexibility for noise reduction. However, even the maximum

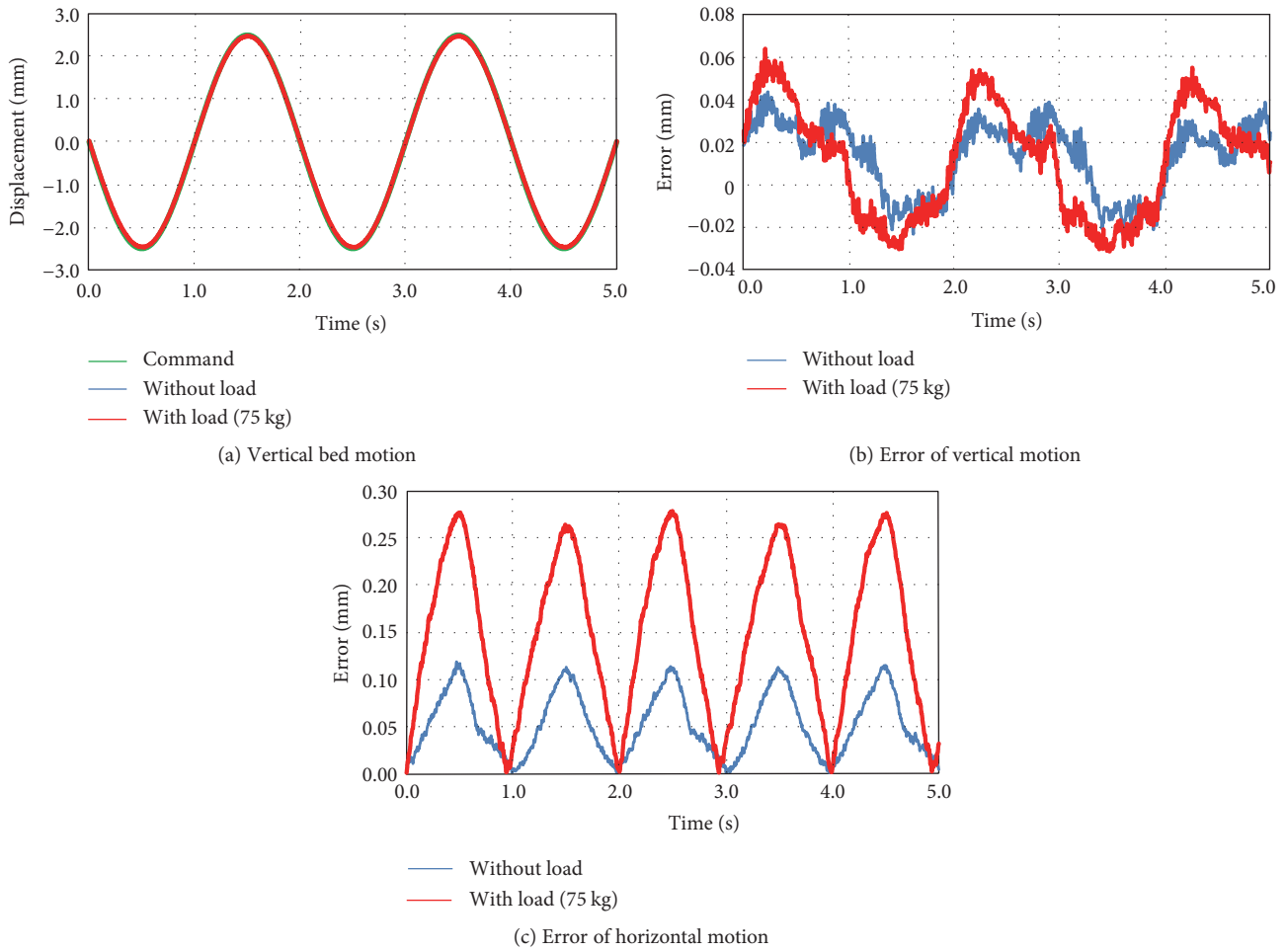


FIGURE 8: Motion accuracy of the bed (5.0 mm amplitude at 0.5 Hz).

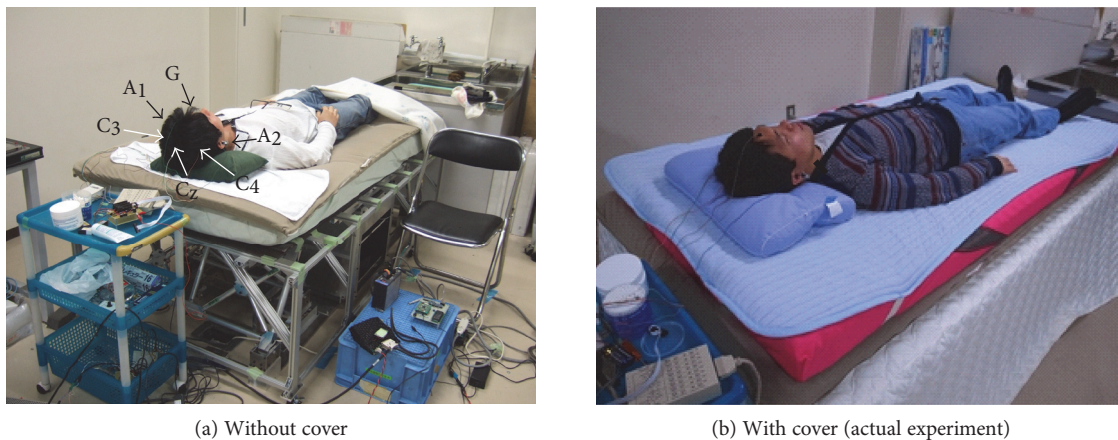


FIGURE 9: Overview of the excitation experiment.

error in the horizontal direction is less than 0.3 mm and this is enough accuracy for a sleep-inducing experiment. The error of horizontal motion might be reduced by replacing the urethane rollers with stiff parts.

3.2. Excitation of Subjects. The 2-DOF mechanical bed is able to provide 2-DOF motion; however, 2-DOF motion includes

infinite variation of trajectories. It is not easy to narrow down the candidates of 2-DOF motions without considering the effect of 1-DOF vibration. Based on this reason, this study focuses on the effect of 1-DOF vibration as the first step.

In the first step of the experiment, the excitation frequency was kept at 0.5 Hz because this was determined to be the optimal frequency to induce sleep using the previous

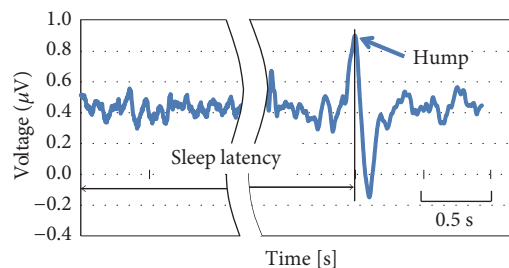


FIGURE 10: Definition of sleep latency based on brain waves.

1-DOF exciter bed [13]. Using a cover that wraps around the excitation mechanism, the noise was approximately 43 dB. Although the noise level was very low compared to the environment of daily living (45 dB) [16], all subjects use earplugs because the sound of the motor may be offensive to some subjects.

Ten healthy men aged between 21 and 27 were recruited as subjects in this experiment. The eligibility criteria included (1) no history of sleep disorders and (2) no motion sickness. The experimental protocol adhered to the ethical standards of Tokyo Tech and was authorized by the committee (#A14014). The tested excitation amplitudes were 0, 2.4, 5.0, and 7.5 mm in each direction. Because the amplitude of the previous 1-DOF bed was 2.4 mm, this study also used 2.4 mm instead of 2.5 mm as the amplitude. The subjects were excited in the horizontal or vertical direction to investigate the anisotropy of body sensing, and sleep latency was measured from the subjects' brain waves. The subjects' sensory perceptions of the bed were also collected using a questionnaire.

The brain wave is measured by general electrode made of silver metal with brain-wave amplifier BA1008 manufactured by Digitex Lab. The output voltage is amplified 100,000 times with this system. Sampling rate is 200 Hz and band-pass filter from 1.5 to 30 Hz is applied to the signal. The frequency band is defined for measurement of brainwaves α (8–14 Hz), β (14–38 Hz), δ (0.5–4 Hz), and θ (4–8 Hz). These waves are generally used as the indicator of the stages including REM. Low-frequency waves are not very important in our study because the brain waves with low frequency such as δ and θ are observed on the deep sleep stages 3 and 4. This study focuses on the sleep latency and does not deal with such deep stages. As is well known in the art, hump and K-complex are characteristic waveforms indicating the early stage of sleep. This study adopted these waveforms as the indicators of sleep. Rechtschaffen and Kales method [17], a standard of brain wave discrimination, is used to identify the waveforms.

In order to avoid sleep disturbance, the number of electrodes should be suppressed as little as possible. This study measured the brain waves of Cz, C3, and C4 within the 10–20 method (general EEG method) [18]. The waves of 3-points provide sufficient information to detect hump and K-complex. The voltages of C3 and Cz are refereed by A1 (left earlobe). The voltage of C4 is refereed by A2 (right earlobe). The voltage of G is used to remove common noise. The overview of the experiment and the arrangement of the electrodes are shown in Figure 9. The mechanical

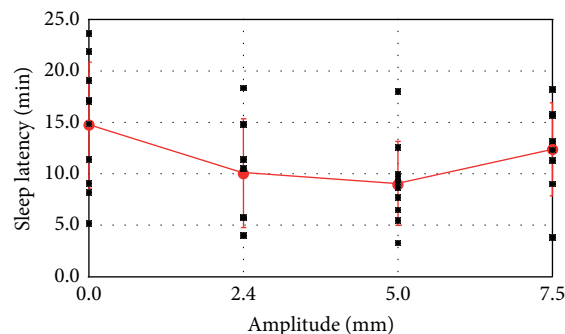


FIGURE 11: Average sleep latency with 0.5 Hz horizontal excitation.

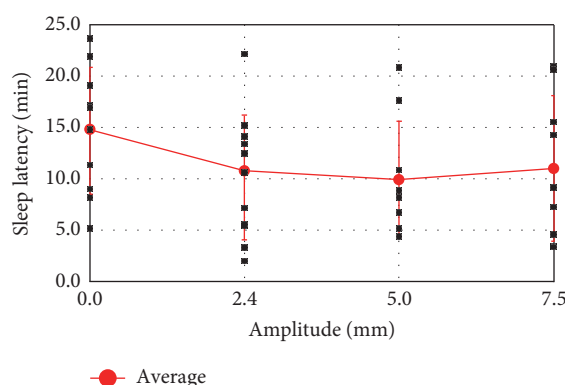


FIGURE 12: Average sleep latency with 0.5 Hz vertical excitation.

part of the bed is covered by a thick cloth to decrease the mechanical sound.

Herein, sleep latency is defined as the duration of time between the beginning of excitation and when the hump or K-complex is observed in the brain waves (Figure 10). Of course, the result of sleep latencies indicates different values every time. This study adopted an average value of the latencies, and the number of measurements was at least three times for each subject.

Average sleep latency was measured under excitation in the horizontal direction, and the results are shown in Figure 11. Without excitation, the average latency was 14.7 min. In contrast, under a 5.0 mm amplitude excitation, the average latency was 9.0 min. At an amplitude of 2.4 mm, the average latency was 10.1 min, although almost all of the subjects could not sense the excitation (based on the responses to the questionnaire). This latency obtained at a 2.4 mm excitation is almost the same as that observed at a 5.0 mm amplitude. In contrast, for excitation at an amplitude of 7.5 mm, the subjects reported that it was easy to feel the vibration. In addition, the corresponding average latency with the amplitude of 7.5 mm was 12.4 min, which is longer than the latencies with the amplitudes of 5.0 mm and 2.4 mm. This result suggests that low-amplitude vibration in the horizontal direction is effective for inducing sleep. This assumption supports the description of human exposure to whole-body vibration in ISO standards [2].

TABLE 1: Statistical results of sleep latencies using the Smirnov-Grubbs test.

	No exc.	Horizontal excitation			Vertical excitation		
Amplitude	0	2.4	5.0	7.5	2.4	5.0	7.5
Ave. latency [min]	14.7	10.1	9.0	12.4	10.8	9.9	11.0
Min. latency [min]	5.1	4.0	3.2	9.0	2.0	4.4	3.5
Max. latency [min]	21.9	18.3 (29.7)	18.0 (26.6)	15.6	15.2	17.6	21.0
Std. deviation	6.1	5.3	4.1	4.5	6.1	5.7	7.1
Variance	34.0	23.8	14.9	17.8	33.4	28.6	44.2
Conf. interval [%]	4.2	4.5	2.8	3.5	3.4	3.5	4.3
Sample number	10	7	10	8	11	9	9
Number of exclusion	2	3	2	3	1	2	1
Outliers in exclusion	0	1	1	0	0	0	0
Number of experiments	12	10	12	11	12	11	10

Values in parentheses are omitted as outliers.

TABLE 2: Acceleration values for each amplitude under 0.5 Hz sine wave.

Amplitude (mm)	2.4	5.0	7.5
Acceleration (mm/s^2)	12	25	37

The effect of excitation in the vertical direction was also examined, as shown in Figure 12. The average sleep latencies for vertical excitation at amplitudes of 2.4, 5.0, and 7.5 mm were 10.8, 9.9, and 11.0 min, respectively. The latency for 2.4 mm vertical excitation was also shorter than that for the no-excitation condition (14.7 min). As for horizontal excitation at 2.4 mm, the subjects reported that they could not feel the vertical excitation at 2.4 mm.

The statistical chart of the experimental results is shown in Table 1. The outliers were omitted from the analysis according to the Smirnov-Grubbs test [19]. The most important results are the average sleep latencies with and without excitation, which exhibit a significant difference.

Using statistical methods, this study aimed to detail the ability of excitation to induce sleep. Although the results for horizontal and vertical excitation were slightly different, no statistical significance was found. Furthermore, no significant differences in sleep latency were found among different amplitudes of excitation. The obtained data were then divided into two groups, that is, with and without excitation. These groups were compared using the F-test of equality of variances. The F -value was 1.30, and the critical value of the F -distribution was 2.06 under α of 0.05 (α = significance probability). These values indicate that the two groups have the same variance. The groups were then compared using two-sample t -tests assuming equal variance. The calculated t -value was 2.28, and the critical value of the t -distribution was 2.00 under α of 0.05. These results suggest that there is a significant difference between the excitation group and the no-excitation group in terms of average sleep latency. Moreover, the value of Cohen's d was 0.79. This value allows us to conclude that appropriate excitation had the effect of inducing sleep, although the statistical power was merely 0.62 due to the small number of subjects. With respect to detailed condition of the effective

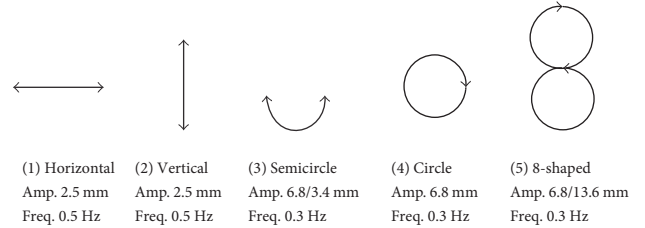


FIGURE 13: Examined trajectories of 2-DOF excitation.

excitation, we plan to increase the number of subjects in future studies.

As is well known, humans cannot feel his/her displacement but acceleration. A human detects vibration not only the semicircular canals but also each body part such as the pacinian corpuscle. ISO 2631 series [2, 3] describe the standards of whole body vibration. Appendix C of ISO 2631-1 describes that 15 mm/s^2 is the median of the least acceleration which a human who has exquisite sensitivity can feel [2]. On the basis of this description, 0.5 Hz sinusoidal wave with the amplitude of 5.0 mm generates 25 mm/s^2 (Table 2). This acceleration is on the borderline between sensible and insensible vibrations. Actually, the average sleep latencies of 2.4 mm and 5.0 mm are almost the same. Meanwhile, the acceleration is 37 mm/s^2 when the amplitude is 7.5 mm. In the worst case, the vibration causes motion sickness. From the results of the sensory test, a large acceleration does not induce sleep but causes an uncomfortable feeling. This tendency is natural even in view of daily life. Our result suggests a possibility that a sleep-inducing phenomenon correlates not only semicircular canals but whole body sensors such as the pacinian corpuscle. In other words, these organs might detect very small accelerations less than 25 mm/s^2 which humans cannot recognize, and affect inducing sleep. This assumption can explain the result.

In order to confirm the bed performance, this study also examined 2-DOF excitation. As a preliminary experiment, 5-trajectories including 1-DOF and 2-DOF motions are examined as shown in Figure 13. The maximum accelerations are the same value of 12 mm/s^2 for result comparison between the

trajectories. The 2-DOF trajectories are realized by calculated speed from differentiated trajectory. The speed of the bed is controlled by position command (the number of steps) at regular intervals because the bed is driven by stepping motors. For example, in the case of a circular motion with a radius A and rotation speed ω , the trajectory is expressed by position vector $\mathbf{p} = (A\cos\omega t, A\sin\omega t)$. However, it is impossible to realize the speed of $(d\mathbf{p}_x/dt, d\mathbf{p}_y/dt) = (-A\omega\sin\omega t, A\omega\cos\omega t)$ from the static state $((v_x, v_y) = (0, 0))$ directly. Coordinated accelerations in horizontal and vertical (x and y) directions are necessary to realize the 2-DOF motion. At first, the velocity in the vertical direction is accelerated from 0 to $A\omega\cos\omega t$. Meanwhile, the velocity in the horizontal direction is kept 0. When the vertical speed reaches $A\omega\cos\omega t$ ($t = 0$), the horizontal motion is started with the velocity of $-A\omega\sin\omega t$ ($=0$ when $t = 0$). With this method, a circular bed motion can be generated. Other 2-DOF motions are realized in the similar ways. Of course, by differentiation of the trajectory directly, obtaining the speed command is also possible. With 3 subjects, there was no clear difference of sleep latencies and questionnaire results between 1-DOF and 2-DOF motions. Increasing the number of subjects and statistical analysis are our future works.

4. Conclusion

We developed a new, active 2-DOF mechanical bed that excites the human body to induce sleep. In the prototype bed, a counterweight system decreases the required motor torque and driving noise, allowing it to achieve silent and smooth excitation. The vertical and horizontal excitation of the bed can be controlled independently. In both the horizontal and vertical directions, the motion error is almost only 0.02 mm for a sine wave with a frequency of 0.5 Hz and an amplitude of 5.0 mm. The brain waves of human subjects were measured both with and without excitation. Several amplitudes were examined by sinusoidal excitation at a constant frequency of 0.5 Hz in both the horizontal and vertical directions. Although an optimal amplitude of excitation was not identified, we observed an evident statistical difference in average sleep latency between the with- and without-excitation groups. Particularly, very low-amplitude vibrations also induce sleep although subjects cannot recognize the vibration. These results indicate that an effective vibration can induce sleep.

Conflicts of Interest

The authors declare that they have no conflicts of interest.

References

- [1] S. Namba, "Sleep disturbance caused by meaningful sounds and the effect of background noise," *Journal of Sound of Vibration*, vol. 277, pp. 445–452, 2004.
- [2] ISO2631-1, *Mechanical Vibration and Shock - Evaluation of Human Exposure to Whole-Body Vibration - Part 1: General Requirements*, 1997.
- [3] ISO10326-2, *Mechanical Vibration - Laboratory Method for Evaluating Vehicle Seat Vibration - Part 2: Application to Railway Vehicles*, 2001.
- [4] K. Yamazaki, "The effect of whole-body vibration on sleep," *Journal of Noise Control*, vol. 6, no. 3, pp. 21–26, 1982, (in Japanese).
- [5] T. Kawashima, "Study for comfortable swinging: comfortable swinging for active rocking chair," *Transactions of the JSME. C*, vol. 69, no. 677, pp. 219–226, 2003.
- [6] M. Kitado, K. Araki, T. Takahashi, H. Inabe, and T. Yanase, "Effect of whole body vibration applied with low level of acceleration on sleep onset-whole body vibration which utilizes the characteristic frequencies of vibration of electric trains and 1/f fluctuation pattern," *The Japanese Journal of Ergonomics*, vol. 35, no. 4, pp. 229–239, 1999, (in Japanese).
- [7] T. Musha, S. Sata, and M. Yamamoto, *Noise in Physical Systems and 1/f Fluctuation*, pp. 106–112, Kodansha Ltd, 1980, (in Japanese).
- [8] H. Kimura, M. Endo, M. Koseki, and N. Inou, "Sleep-inducing factors in mechanical environments," *Journal of Environment and Engineering*, vol. 5, no. 2, pp. 275–286, 2010.
- [9] T. Flash and N. Hogan, "The coordination of arm movements: an experimentally confirmed mathematical model," *The Journal of Neuroscience*, vol. 5, no. 7, pp. 1688–1703, 1985.
- [10] H. Seki and S. Tadakuma, "Velocity pattern generation for power assisted wheelchair based on jerk and acceleration limitation," in *31st Annual Conference of IEEE IECON 2005*, pp. 457–462, 2005.
- [11] H. Yoshida and N. Machida, "Studies on the effects of low frequency vibration to the human body-physiological effects of low frequency horizontal vibration-, congress of the international ergonomics association," in *Proceedings of the 10th IEA*, pp. 369–371, 1988.
- [12] N. Ma, F. Wang, K. Sagawa, and H. Inooka, "A real-time estimation system for the evaluation of riding comfort," *Proceedings of the 13th Bioengineering Conference*, pp. 254–255, 2001, 2001, (in Japanese).
- [13] H. Kimura, A. Kuramoto, Y. Inui, and N. Inou, "Sleep inducing factor in mechanical environment development of 2-DOF bed for precise excitation," *Annual Conference of System Integration (SI2013)*, 3C1–1, 2013, (in Japanese).
- [14] J. Altmann, "Acoustic weapons-a prospective assessment," *Science & Global Security, Taylor and Francis*, vol. 9, pp. 165–234, 2001.
- [15] J. F. O'Hanlon and M. E. McCauley, "Motion sickness incidence as a function of the frequency and acceleration of vertical sinusoidal motion," *Aerospace Medicine*, vol. 45, no. 4, pp. 366–369, 1974.
- [16] Adelaide Service SA Centre, *General Environmental Noise, Information Sheet*, pp. 1–4, 2013.
- [17] A. Rechtschaffen and A. Kales, *A Manual of Standardized Terminology, Techniques and Scoring System for Sleep Stages of Human Subjects*, Public Health Service, U.S. Government Printing Office, US, 1968, Washington, DC, 1968.
- [18] H. Jasper, "The ten-twenty electrode system of the International Federation," *Electroencephalography and Clinical Neurophysiology*, vol. 10, pp. 371–375, 1958.
- [19] F. Grubbs, "Sample criteria for testing outlying observations," *The Annals of Mathematical Statistics*, vol. 21, no. 1, pp. 27–58, 1950.